

May 2016

Crack Growth Mechanisms under Anti-Plane Shear in Composite Laminates

Allison Lynne Horner
Syracuse University

Follow this and additional works at: <http://surface.syr.edu/etd>

 Part of the [Engineering Commons](#)

Recommended Citation

Horner, Allison Lynne, "Crack Growth Mechanisms under Anti-Plane Shear in Composite Laminates" (2016). *Dissertations - ALL*. Paper 435.

This Dissertation is brought to you for free and open access by the SURFACE at SURFACE. It has been accepted for inclusion in Dissertations - ALL by an authorized administrator of SURFACE. For more information, please contact surface@syr.edu.

Abstract

The research conducted for this dissertation focuses on determining the mechanisms associated with crack growth in polymer matrix composite laminates subjected to anti-plane shear (mode III) loading. For mode III split-beam test methods were proposed, and initial evaluations were conducted. A single test method was selected for further evaluation. Using this test method, it was determined that the apparent mode III delamination toughness, G_{IIIc} , depended on geometry, which indicated a true material property was not being measured. Transverse sectioning and optical microscopy revealed an array of transverse matrix cracks, or echelon cracks, oriented at approximately 45° and intersecting the plane of the delamination. Subsequent investigations found the echelon array formed prior to the onset of planar delamination advance and that growth of the planar delamination is always coupled to echelon array formation in these specimens. The evolution of the fracture surfaces formed by the echelon array and planar delamination were studied, and it was found that the development was similar to crack growth in homogenous materials subjected to mode III or mixed mode I-III loading, although the composite laminate architecture constrained the fracture surface development differently than homogenous materials. It was also found that, for split-beam specimens such as those used herein, applying an anti-plane shear load results in twisting of the specimen's uncracked region which gives rise to a mixed-mode I-III load condition. This twisting has been related to the apparent mode III toughness as well as the orientation of the transverse matrix cracks. A finite element model was then developed to study the mechanisms of initial echelon array formation. From this, it is shown that an echelon array will develop, but will become self-limiting prior to the onset of planar delamination growth.

Crack Growth Mechanisms under Anti-Plane Shear in Composite Laminates

by

Allison Lynne Horner

B.S. University of Tulsa, 2011

M.S. Syracuse University, 2012

Dissertation

Submitted in partial fulfillment of the requirements for the degree of Doctor of
Philosophy in Mechanical and Aerospace Engineering.

Syracuse University

May 2016

Copyright © Allison Lynne Horner 2016

All rights reserved

Acknowledgements

First and foremost, I would like to thank my family for their support and encouragement over the years as I pursued my Doctor of Philosophy at Syracuse University. In particular, I am thankful for my husband Will Horner who has been positive and encouraging every step of the way, and even went so far as to move to upstate New York so I could follow my dreams.

I am indebted to my advisor, Dr. Barry Davidson, for the time, attention, and effort he contributed to my education and training. I always felt like we were on the same team, which not many graduate students can say about their advisor. I am grateful for the collaboration with Dr. Mike Czabaj and Dr. James Ratcliffe, the assistance of Dr. Ratcliffe and Dr. Jake Hochhalter in developing the skills required for finite element modeling, the continued mentoring Dr. Aaron Hall provided throughout my graduate education, and the inspiration from Dr. Jesse French to attend graduate school in the first place. Finally, I would like to thank the NSF Graduate Research Fellowship Program, Zonta International, and Syracuse University for funding my education and allowing me to focus entirely on my research for the past five years.

This work is dedicated to my son, Joel Christopher Horner, who, in the short amount of time he has been in this world, has already brought me more happiness than I can imagine.

Table of Contents

1. Introduction.....	1
2. Literature Review	4
2.1. Introduction.....	4
2.1.1. Delamination in Composites.....	4
2.1.2. Delamination Toughness	5
2.1.3. Mode III Delamination Toughness	5
2.1.4. Reviewed Topics.....	6
2.2. Mode III Testing of Composite Materials	8
2.2.1. Introduction.....	8
2.2.2. Early Mode III Tests	9
2.2.3. Edge Crack Torsion Test	11
2.2.3.1. Test Description	11
2.2.3.2. Critical Load for Delamination Growth Determination.....	13
2.2.3.3. G_{IIIc} Determination.....	15
2.2.3.4. Mode III Toughness Testing.....	19
2.2.4. Modified Split Cantilever Beam Test	19
2.2.4.1. Test Description	19
2.2.4.2. Critical Load for Delamination Growth Determination.....	21
2.2.4.3. G_{IIIc} Determination.....	23
2.2.4.4. Mode III Toughness Testing.....	25
2.2.5. Recently Introduced Mode III Tests	25
2.2.6. Conclusions from Mode III Toughness Testing	28
2.3. Mode III Testing of Homogenous Materials	29
2.3.1. Introduction.....	29
2.3.2. Pure Mode III Tests	30
2.3.3. Almost Pure Mode III Tests.....	31
2.3.4. Conclusions of Homogenous Mode III Testing.....	32
2.4. Mode I-III Testing of Homogenous Materials.....	33
2.4.1. Introduction.....	33
2.4.2. Fracture Theories	33

2.4.2.1.	Echelon Crack Orientation.....	34
2.4.2.2.	Crack Length and Segmentation Spacing	38
2.4.2.3.	Crack Front Rotation.....	39
2.4.2.4.	Fracture Surface Evolution	41
2.4.3.	Experimental Results	42
2.4.3.1.	Tension (Compression) – Torsion of Cylinder Tests.....	42
2.4.3.2.	Edge-Cracked Plates	45
2.4.3.3.	Geometry of Goldstein and Osipenko.....	47
2.4.4.	Summary	49
2.5.	Modeling of Anti-Plane Shear Fracture.....	50
2.5.1.	Introduction.....	50
2.5.2.	Perturbation Models.....	51
2.5.2.1.	Analytical Instability Investigations	51
2.5.2.2.	Numerical Instability Investigations	53
2.5.3.	Discrete Echelon Crack Models.....	55
2.5.4.	Summary	58
2.6.	Conclusions of Literature Review	59
3.	Objectives and Approach.....	60
3.1.	Introduction.....	60
3.2.	Objectives	60
3.3.	Experimental Approach.....	61
3.3.1.	Mode III Toughness Determination.....	61
3.3.2.	Dependence of Toughness on Geometry	62
3.3.3.	Growth Mechanisms in Anti-Plane Shear Loading	62
3.4.	Modeling Approach	64
3.4.1.	Delamination Growth Prediction Methodology.....	64
3.4.2.	Discrete Modeling of Echelon Cracks	66
3.5.	Dissertation Overview	67
3.6.	Conclusions.....	68
4.	Delamination Toughness Testing: Experiments and Analysis.....	70
4.1.	Introduction.....	70
4.2.	Test and Specimen Design.....	72
4.3.	Finite Element Modeling	76

4.3.1. Overview.....	76
4.3.2. Mesh and Boundary Conditions	77
4.3.3. Mesh Refinement Studies	79
4.4. Experimental Overview	80
4.4.1. Materials and Manufacturing Procedures	80
4.4.2. Fixture Design.....	82
4.4.3. Test Procedures.....	84
4.4.4. Material Property Determination	85
4.5. Evaluation of Baseline Configurations	85
4.5.1. FE Analyses for Baseline Configurations.....	85
4.5.2. Load versus Deflection Response.....	88
4.5.3. Onset of Delamination Growth.....	89
4.5.4. Post-Test C-Scan Results.....	91
4.6. Data Reduction Techniques	92
4.6.1. Compliance Calibration	93
4.6.1.1. Compliance Calibration Technique	93
4.6.1.2. Compliance Calibration of Tabbed Specimens.....	93
4.6.1.3. Untabbed Specimen Assessments.....	94
4.6.2. FE Based Method.....	95
4.6.2.1. G_{IIIc} Basis for Baseline Configurations.....	95
4.6.2.2. Determinations of G_{IIIc} of Baseline Configurations.....	96
4.7. Baseline Delamination Toughness Test Results.....	97
4.8. Dependence of Toughness on Delamination Length.....	99
4.8.1. FE Analysis.....	100
4.8.2. Experimental Investigation	101
4.8.3. Photomicroscopy.....	104
4.9. Conclusions.....	108
5. Fracture Surface Evolution.....	109
5.1. Introduction.....	109
5.2. Test Design	110
5.2.1. Specimen Design	110
5.2.2. Materials and Manufacturing Process.....	111
5.2.3. Fixture Design.....	115

5.2.4. Test and Evaluation Procedures.....	117
5.2.4.1. ERR Determination.....	117
5.2.4.2. Test Plan.....	119
5.3. Delamination Toughness Testing	122
5.3.1. Apparent Toughness Test Results.....	122
5.3.2. Delamination Toughness Photomicroscopy	124
5.4. Damage Progression Testing	125
5.4.1. Damage Progression Test Results.....	125
5.4.2. Damage Progression Photomicroscopy	126
5.4.2.1. 26-ply IM7/977-3 Specimens	126
5.4.2.2. 24-ply IM7/8552 Specimens.....	129
5.4.3. Analysis of Damage Progression	131
5.5. Extended Growth Testing	134
5.5.1. Extended Growth Test Results.....	134
5.5.2. Extended Growth X-ray CT and Photomicroscopy	134
5.5.2.1. 24-ply Specimens.....	134
5.5.2.2. 48-ply Specimens.....	137
5.5.3. Analysis of Extended Growth Testing	138
5.6. Effect of Materials and Laminate Architecture on Fracture Surface Development and Evolution.....	140
5.7. Implication for Mode III SST Testing	141
5.8. Conclusions.....	143
6. Effects of Split-Beam Specimen Twisting	145
6.1. Introduction.....	145
6.2. Test Design	147
6.2.1. Test Geometry and Specimen Preparation.....	147
6.2.2. Specimen Rotation Measurement	149
6.2.3. Transverse Crack Measurement.....	150
6.3. Analyses.....	150
6.3.1. Energy Release Rate and Mode Mixity	150
6.3.2. Apparent Toughness	153
6.3.3. Stress Intensity Factors	154
6.3.4. Transverse Crack Angle.....	155

6.4. Results.....	157
6.4.1. Apparent Toughness Tests	157
6.4.2. Effect of Geometry on Matrix Cracking.....	160
6.4.3. Matrix Crack Orientation.....	163
6.4.4. Effect of Geometry on Fracture Surface Evolution	166
6.4.5. Comparison of Composite Fracture Surface Evolution to Homogenous Materials	172
6.5. Application to Mode III Delamination Toughness Testing.....	173
6.6. Conclusions.....	175
7. Model Formulation and Validation.....	177
7.1. Introduction.....	177
7.2. Model Plans	177
7.2.1. Overall Goals of Modeling	177
7.2.2. Modeling Plans	178
7.2.3. Intended Model Details.....	179
7.3. Energy Release Rate Calculations	181
7.3.1. Straight Crack Fronts	182
7.3.2. Curved Crack Fronts.....	183
7.4. Model Validation.....	187
7.4.1. Model Benchmarks	187
7.4.2. Validation of Delamination Model	190
7.4.2.1. Geometry without Diagonal Partition.....	191
7.4.2.2. Geometry with Diagonal Partition	193
7.4.3. Validation of Echelon Crack Model	196
7.4.3.1. Pure Mode I Loading	197
7.4.3.2. Mixed Mode I-II/III Loading	199
7.4.4. Validation of Combined Model	201
7.4.4.1. Geometry with Only Echelon Crack.....	202
7.4.4.2. Geometry with Only Delamination.....	204
7.4.5. Validation of Ellipsoidal Echelon Cracks.....	206
7.4.6. Validation of Multiple Echelon Cracks	208
7.5. Final Model Details	210
7.6. Conclusions.....	210

8. Modeling of Echelon Crack Array Development.....	212
8.1. Introduction.....	212
8.2. Modeling Results for a Single Echelon Crack.....	212
8.2.1. Centered Circular Echelon Crack	213
8.2.1.1. Delamination Front Results	213
8.2.1.2. Echelon Crack Front Results	218
8.2.2. Semi-Ellipsoidal Echelon Crack.....	221
8.2.3. Offset Circular Echelon Crack.....	225
8.3. Modeling Results for Multiple Echelon Cracks	230
8.3.1. Three Centered Circular Echelon Cracks	230
8.3.2. Three Offset Circular Echelon Cracks	236
8.3.3. Three Centered Circular Echelon Cracks of Different Diameters	238
8.3.4. Five Centered Circular Echelon Cracks.....	241
8.4. Discussion.....	245
8.4.1. Initiation and Development of an Echelon Array	246
8.4.2. Effect of Increasing Crack Number on Development.....	250
8.4.3. Coupled Advance of an Echelon Array and the Planar Delamination.....	254
8.5. Conclusions.....	256
9. Conclusions and Future Work.....	258
9.1. Conclusions.....	258
9.2. Future Work.....	261
9.2.1. Mode III Delamination Toughness Test Development.....	261
9.2.2. Observation of the Initiation of Echelon Cracks.....	264
9.2.3. Modeling of Echelon Array Development.....	266
Appendix A. Tensile Test Procedure for Axial Modulus Determination	269
A.1. Specimen Preparation	269
A.1.1. Specimen Size	269
A.1.2. Tabbing for Extensometers	270
A.2. Test Setup.....	270
A.2.1. Grip Alignment	271
A.2.2. Specimen Insertion.....	272
A.2.3. Running Programs.....	273
A.3. Test.....	274

A.4. Data Reduction	275
Appendix B. Test Procedure for Shear Modulus Determination.....	276
B.1. Specimen Preparation.....	276
B.1.1. Plate Layup.....	276
B.1.2. Specimen Size	276
B.1.3. Strain Gage Application	277
B.2. Test Setup.....	278
B.2.1. Fixture Alignment	278
B.2.2. Specimen Insertion.....	279
B.2.3. Strain Gage Calibration.....	280
B.2.4. Running Programs.....	281
B.3. Test.....	281
B.4. Data Reduction.....	282
Appendix C. Derivation of Maximum Energy Release Rate Criterion for an Orthotropic Material	283
Appendix D. Derivation and Evaluation of Maximum Principal Tensile Stress Criterion for an Orthotropic Material	289
D.1. Maximum Principal Tensile Stress Criterion Derivation.....	289
D.2. Sensitivity to Material Properties and Constraint Conditions.....	291
D.3. Appropriate Material Properties and Constraint Condition for Comparison to Experimental Data.....	294
Appendix E. Full Results of Model Validation.....	296
E.1. Delamination Model without Diagonal Partition	296
E.1.1. Model Details	296
E.1.2. Results	300
E.1.3. Discussion.....	305
E.1.4. Conclusions	306
E.2. Delamination Model with Diagonal Partition	307
E.2.1. Model Details	307
E.2.2. Results	310
E.2.3. Discussion.....	315
E.2.3. Conclusions	316
E.3. Echelon Crack Model with Pure Mode I Loading.....	317

E.3.1. Model Details	317
E.3.2. Results	322
E.3.3. Discussion.....	323
E.3.4. Conclusions	325
E.4. Echelon Crack Model with Mixed Mode Loading.....	325
E.4.1. Model Details	325
E.4.2. Results	329
E.4.3. Discussion.....	332
E.4.4. Conclusions	333
E.5. Combined Model with Only Echelon Crack	334
E.5.1. Model Details	334
E.5.2. Results	339
E.5.3. Discussion.....	342
E.5.4. Conclusions	343
E.6. Combined Model with Only Delamination	343
E.6.1. Model Details	343
E.6.2. Results	347
E.6.3. Discussion.....	349
E.6.4. Conclusions	349
E.7. Ellipsoidal Echelon Crack Model.....	350
E.7.1. Model Details	350
E.7.2. Results	352
E.7.3. Discussion.....	353
E.7.4. Conclusions	353
E.8. Multiple Echelon Cracks Model.....	354
E.8.1. Model Details	354
E.8.2. Results	357
E.8.2.1. Delamination Only	357
E.8.2.2. Echelon Cracks Only	359
E.8.3. Discussion.....	361
E.8.4. Conclusions	362
References.....	363
Vita	380

List of Figures

Figure 2.1. Crack rail shear (CRS) geometry (Becht and Gillespie, 1988).	10
Figure 2.2. Split cantilever beam (SCB) geometry (Donaldson, 1988).	10
Figure 2.3. Edge crack torsion (ECT) geometry (de Morais et al., 2011).	12
Figure 2.4. Examples of ECT load-displacement plots with several possible “critical loads” noted (Ratcliffe, 2004).	13
Figure 2.5. Modified split cantilever beam (MSCB) geometry (Khoshravan and Moslemi, 2014).	21
Figure 2.6. Four point bending plate (4PBP) geometry (de Morais and Pereira, 2009B).	26
Figure 2.7. Six point edge crack torsion (6ECT) geometry (de Morais et al., 2011).	26
Figure 2.8. Shear torsion bending (STB) geometry (Davidson and Sediles, 2011).	28
Figure 2.9. Boundary element model geometry of Pham and Ravi-Chandar (2014) showing a disk-shaped daughter crack intersecting a planar parent crack and subjected to mixed mode I-III loading.	57
Figure 4.1. Mode III STB test. (a) Original orientation, (b) rotated 90° about x-axes.	71
Figure 4.2. Specimen with load tabs.	73
Figure 4.3. (a) Nomenclature and (b) edge delamination geometry.	75
Figure 4.4. FE model of STB test with inset view of near-tip mesh.	78
Figure 4.5. Test fixture setup. (a) SST front view, (b) side view, (c) STB back view.	82
Figure 4.6. ERR distributions for IM7/977-3. (a) G for P = 1500N. (b) G_{III}/G_{avg} . (c) G_{II}/G_{avg}	87
Figure 4.7. Typical load-deflection plots for STB and SST test specimen.	89
Figure 4.8. Typical post-test delamination front shapes from SST NE (a, b) and STB NE (c, d) specimens.	90
Figure 4.9. Toughness data for (a) IM7/977-3 and (b) T800S/3900-2B specimens.	99
Figure 4.10. ERR distributions as a function of delamination length for IM7/977-3 SST NE. .	101
Figure 4.11. Apparent G_{IIIc} versus delamination length for IM7/977-3 SST NE specimens.	102
Figure 4.12. Photomicrograph at the delamination front of specimen I10-8 with delamination length $a = 54$ mm.	105
Figure 4.13. Photomicrograph at the delamination front of specimen I10-10 with delamination length $a = 32$ mm.	106
Figure 4.14. Photomicrograph at the delamination front of specimen I10-4 with delamination length $a = 76$ mm.	106
Figure 5.1. SST test (a) loading, (b) method of load introduction.	112
Figure 5.2. SST specimen with load tabs.	113

Figure 5.3. SST test fixture setup (a) front view, (b) side view.	116
Figure 5.4. Typical load versus deflection plot.	120
Figure 5.5. Apparent G_{IIIc} vs. delamination length for IM7/977-3.	123
Figure 5.6. Photomicrograph of an IM7/977-3 delamination front, I13-7B, $a = 32$ mm, apparent $G_{IIIc} = 723$ J/m ²	124
Figure 5.7. Photomicrographs of IM7/977-3 delamination fronts, $a = 76$ mm. (a) I13-9T, 73% of apparent G_{IIIc} . (b) I14-3T, 88% of apparent G_{IIIc} . (c) I13-10T, 91% of apparent G_{IIIc} . ..	128
Figure 5.8. Photomicrographs of IM7/8552 delamination fronts, $a = 76$ mm. (a) J2-3, 75% of apparent G_{IIIc} . (b) J2-9, 100% of apparent G_{IIIc}	131
Figure 5.9. Images obtained from 24-ply SST specimen. (a) and (b) by optical microscopy, (c) – (f) by X-ray CT. Distances ahead of insert tip: (a) 0.5 mm, (b) 2 mm, (c) 2 mm, (d) 7 mm, (e) 11 mm, (f) 16 mm.	135
Figure 5.10. X-ray CT images from 48-ply SST specimen. Distances ahead of insert tip: (a) 6 mm, (b) 10 mm, (c) 14 mm.	138
Figure 5.11. Crack surface evolution data for $a = 32$ mm SST specimens. (a) Average transverse crack length. (b) Number of transverse cracks detected.	140
Figure 6.1. Schematic of SST test geometry and loading.	148
Figure 6.2. Photograph of masked, tabbed SST specimen with $a = 32$ mm.	149
Figure 6.3. Schematic showing orientation of SST specimen cross-section (a) before and (b) after deformation.	152
Figure 6.4. Plots of apparent G_c versus (a) specimen rotation at delamination tip, (b) mode mixity.	158
Figure 6.5. Plot of apparent G_c versus delamination length for 24-ply specimens.	159
Figure 6.6. Representative transverse section photomicrographs of 24-ply specimens with different delamination lengths (a) 32 mm, (b) 70 mm, (c) 127 mm, taken approximately 2 mm ahead of the Teflon insert tip.	162
Figure 6.7. Representative transverse section images of 24-ply specimens just ahead of the Teflon insert tip for different delamination lengths (a) 32 mm, (b) 70 mm, (c) 127 mm.	164
Figure 6.8. Ratio of experimentally measured transverse crack angles ($\theta_{\text{Experimental}}$) with predictions from maximum principal tensile stress criteria ($\theta_{\text{Theoretical}}$) versus mode ratio.	166
Figure 6.9. Crack surface evolution data for 24-ply specimen of three difference delamination lengths. Evolution of (a) matrix crack length, (b) number of crack groups.	168
Figure 6.10. Evolution of representative cracks from transverse sections of 24-ply specimens with delamination lengths of (a) 32 mm, (b) 70 mm, (c) 127 mm. Legend represents distance ahead of the Teflon insert tip from which each profile was taken.	171

Figure 7.1. (a) FE model geometry with a single echelon crack intersecting the delamination front in the center of the specimen. (b) Cross-sectional view with delamination front and echelon crack positions labeled.	180
Figure 7.2. Nodal force and displacement labels for eight noded solid element VCCT calculations.	183
Figure 7.3. Nodal force and displacement labels for eight noded solid elements with arbitrarily curved crack fronts (lower face omitted for clarity).	184
Figure 7.4. Definition of terms defining element area for a crack plane with a mesh that is not orthogonal to the crack front.	185
Figure 7.5. Schematics of models created for delamination validation (a) without diagonal partition, and (b) with diagonal partition.	191
Figure 7.6. ERR distributions comparing the FineMeshA-60 model and the simplified STB model. (a) G_I , (b) G_{II} , (c) G_{III} , (d) G	193
Figure 7.7. ERR distributions comparing the FineMeshB-82 model with a $t/20$ circular partition and the simplified STB model. (a) G_I , (b) G_{II} , (c) G_{III} , (d) G	195
Figure 7.8. Schematics of models created for delamination validation (a) pure mode I, (b) mixed-mode I-II/III.	196
Figure 7.9. ERR distributions for an embedded circular crack of size $t/5$ with mode mixity $G_I/G = 0.46$. Solid lines are for the analytical solution (Kassir and Sih, 1975), symbols are FE results.	199
Figure 7.10. Combined FE Model. Partitions shown were used with both delamination-only model and echelon crack-only model. The delamination front and the profile of the echelon crack are highlighted in the inset image.	200
Figure 7.11. ERR distributions for an embedded circular crack of size $t/20$ oriented at 45° in the combined model. Solid lines are for the analytical solution (Kassir and Sih, 1975), symbols are FE results.	204
Figure 7.12. ERR distributions for the delamination front in the combined model and the simplified STB model. (a) G_I , (b) G_{II} , (c) G_{III} , (d) G	205
Figure 7.13. ERR distributions for an embedded ellipsoidal crack with $a/c = 0.4$. Solid line is for the analytical solution (Newman and Raju, 1983), symbols are FE results.	207
Figure 7.14. Final model of a $t/20$ diameter echelon crack for use in Chapter 8. (a) Isometric view of model. (b) Edge-view of length-wise mesh with several stages of refinement. (c) Edge-view of width-wise mesh with 45° partition and element sizes from 0.012 mm to 0.6 mm. (d) 45° plane view of echelon crack with ordered element shapes surrounding crack tip. (e) Close-up 45° plane view of echelon crack (outlined in red) with 60 elements around the crack tip and 0.001 mm element length. Delamination plane also highlighted in red.	209
Figure 8.1. Echelon crack plane-view of model. Delamination and centered echelon crack shape highlighted.	214

Figure 8.2. ERRs on delamination front for centered circular echelon cracks of diameters $t/20$, $t/15$, $t/10$, $t/5$, and $t/3$. (a) G_I , (b) G_{II} , (c) G_{III}	215
Figure 8.3. ERRs on echelon crack front for centered circular echelon cracks of diameters $t/20$, $t/15$, $t/10$, $t/5$, and $t/3$. (a) G_I , (b) G_{II} , (c) G_{III} , (d) G	219
Figure 8.4. Echelon crack plane-view of model with delamination and semi-ellipsoidal echelon crack shape highlighted.	222
Figure 8.5. ERRs on delamination front for semi-ellipsoidal echelon cracks of nominal diameter $t/20$ with major ellipsoidal diameters of $1.0x$, $1.5x$, and $2.0x$. (a) G_{II} , (b) G_{III}	223
Figure 8.6. ERRs on echelon crack front for semi-ellipsoidal echelon cracks of nominal diameter $t/20$ with major ellipsoidal diameters of $1.0x$, $1.5x$, and $2.0x$. (a) G_I , (b) G_{II} , (c) G_{III}	225
Figure 8.7. Representation of idealized stages of echelon crack growth from a centered circular echelon crack to a semi-ellipsoidal echelon crack and then an offset circular echelon crack.	226
Figure 8.8. Echelon crack plane-view of model with delamination and offset circular echelon crack shape highlighted.	227
Figure 8.9. ERRs on delamination front for offset circular echelon cracks offset to $t/20$ position with echelon crack diameters of $t/20$, $t/16$, and $3t/40$. (a) G_{II} , (b) G_{III}	228
Figure 8.10. ERRs on echelon crack front for offset circular echelon cracks offset to $t/20$ position with echelon crack diameters of $t/20$, $t/16$, and $3t/40$. (a) G_I , (b) G_{II} , (c) G_{III}	229
Figure 8.11. ERRs on delamination front and echelon crack fronts for three centered circular echelon cracks of diameter $t/20$ and center-to-center crack spacing of one diameter. (a) Delamination front G_{II} and G_{III} , (b) Echelon crack front G_I , G_{II} , and G_{III}	231
Figure 8.12. ERRs on delamination front and echelon crack fronts for three centered circular echelon cracks of diameter $t/20$ and center-to-center crack spacing of two diameters. (a) Delamination front G_{II} and G_{III} , (b) Echelon crack front G_I , G_{II} , and G_{III}	234
Figure 8.13. ERRs on delamination front and echelon crack fronts for three centered circular echelon cracks of diameter $t/20$ and center-to-center crack spacing of three diameters. (a) Delamination front G_{II} and G_{III} , (b) Echelon crack front G_I , G_{II} , and G_{III}	235
Figure 8.14. ERRs on delamination front and echelon crack fronts for three offset circular echelon cracks of diameter $t/16$ and nominal offset position of $t/20$ and center-to-center crack spacing of three diameters. (a) Delamination front G_{II} and G_{III} , (b) Echelon crack front G_I , G_{II} , and G_{III}	237
Figure 8.15. ERRs on delamination front and echelon crack fronts for a middle $t/15$ circular echelon crack and two outside $t/20$ circular echelon cracks with center-to-center crack spacing of 2.5 center-crack diameters. (a) Delamination front G_{II} and G_{III} , (b) Echelon crack front G_I , G_{II} , and G_{III}	240
Figure 8.16. ERRs on delamination front and echelon crack fronts for five centered circular echelon cracks of diameter $t/20$ and center-to-center crack spacing of one diameter. (a) Delamination front G_{II} and G_{III} , (b) Echelon crack front G_I , G_{II} , and G_{III}	242

Figure 8.17. ERRs on delamination front and echelon crack fronts for five centered circular echelon cracks of diameter $t/20$ and center-to-center crack spacing of 2.5 diameters. (a) Delamination front G_{II} and G_{III} , (b) Echelon crack front G_I , G_{II} , and G_{III}	243
Figure 8.18. ERRs on delamination front and echelon crack fronts for five centered circular echelon cracks of diameter $t/20$ and center-to-center crack spacing of five diameters. (a) Delamination front G_{II} and G_{III} , (b) Echelon crack front G_I , G_{II} , and G_{III}	245
Figure 8.19. G_I on echelon crack front for progressive stages of growth starting at a $t/20$ centered circular crack.	249
Figure 8.20. Representation of idealized stage of echelon crack growth from an offset circular echelon crack to a fan shaped echelon crack.	249
Figure 8.21. Percent differences between multiple crack results and single crack result for centered circular $t/20$ echelon crack. (a) Peak G_I for three cracks, (b) average G_I for three cracks, (c) peak G_I for five cracks, (d) average G_I for five cracks.	252
Figure 8.22. G_I distribution flattening on echelon crack fronts shown for a single crack, three cracks with three diameters spacing, and five cracks with five diameters spacing.	253
Figure 8.23. G_I on echelon crack front for coupled planar delamination and echelon crack growth of a single echelon crack.	255
Figure A.1. E ₁₁ specimen with razor marked epoxy ready for testing.	270
Figure A.2. E ₁₁ grips installed in load frame.	272
Figure A.3. E ₁₁ specimen installed in grips with extensometers.	274
Figure B.1. G ₁₂ specimen with strain gages ready for testing.	277
Figure B.2. G ₁₂ fixture installed in load frame.	279
Figure B.3. G ₁₂ specimen installed in fixture.	280
Figure C.1. Stress field at Irwin slit-crack tip, showing rectangular coordinate components. ...	287
Figure C.2. Model for out-of-plane twisting crack extension.	288
Figure C.3. Maximum energy release rate criterion solution for IM7/8552 material properties and the assumption of $\epsilon_{zz} = 0$	288
Figure D.1. Stress field at Irwin slit-crack tip, showing rectangular coordinate components. ...	290
Figure D.2. General expression for stress state in y-z plane and Mohr's Circle representation. ...	291
Figure D.3. Maximum principal tensile stress criterion prediction for different material properties and constraint conditions.	293
Figure D.4. Plot of percent differences between different material property and constraint conditions for MPTS predictions.	293
Figure D.5. Ratio of experimental data to MPTS predictions for $\epsilon_{zz} = 0$ and different material properties.	295

Figure E.1. Linear-60 mesh. (a) edge-view of refined region. Refined region is 3mm long, i.e., it extends 1.5mm ahead and behind delamination tip. (b) edge-view of near-tip region with delamination tip elements highlighted.	298
Figure E.2. FineMesh-30 mesh. (a) edge-view of refined region. Refined region is 3mm long, i.e., it extends 1.5mm ahead and behind delamination tip. (b) edge-view of near-tip region with delamination tip elements highlighted.	299
Figure E.3. FineMeshA-60 mesh. (a) edge-view of refined region. Refined region is 3mm long, i.e., it extends 1.5mm ahead and behind delamination tip. (b) edge-view of near-tip region with delamination tip elements highlighted.	299
Figure E.4. RefineMesh-3X mesh. (a) edge-view of refined region. Refined region is 9mm long, i.e., it extends 4.5mm ahead and behind delamination tip. (b) edge-view of near-tip region with delamination tip elements highlighted.	299
Figure E.5. Plot of ERRs for Linear-30 model.	301
Figure E.6. Plot of ERRs for FineMesh-30 model.	302
Figure E.7. Plot of ERRs for RefinedMesh3X model.	302
Figure E.8. Plot of ERRs for FineMeshA-150 model.	303
Figure E.9. A66 F20-20 mesh. (a) edge-view of refined region, (b) edge-view of near-tip region, (c) diagonal partition-view of refined regions, (d) diagonal partition-view of near-tip region.	309
Figure E.10. B94 F5-60 mesh. (a) edge-view of refined region, (b) edge-view of near-tip region, (c) diagonal partition-view of refined regions, (d) diagonal partition-view of near-tip region.	310
Figure E.11. G_{II} distributions for models with diagonal partitions.	311
Figure E.12. G_{III} distributions for models with diagonal partitions.	312
Figure E.13. G distributions for models with diagonal partitions.	312
Figure E.14. G_I distributions for models with diagonal partitions.	313
Figure E.15. Echelon crack-view meshes created for mode I loading validation with $t/20$ diameter echelon crack and 60 elements around the crack tip (F20-60). (a) D0.1_X3, (b) D0.05_X7, (c) D0.05_X14, (d) D0.025_X14.	321
Figure E.16. Echelon crack-view meshes created for mode I loading validation with $t/5$ diameter echelon crack and 60 elements around the crack tip (F5-60). (a) D0.01_X5, (b) D0.04_X5, (c) D0.04_X18.	322
Figure E.17. Echelon crack-view meshes created for mixed mode loading validation with $t/5$ diameter echelon crack and 60 elements around the crack tip (F5-60). (a) D0.01_X5, (b) D0.04_X18.	329
Figure E.18. ERR distributions for mixed mode loading of embedded echelon crack model F5-60_D0.04_X18_A-0.5.	330
Figure E.19. ERR distributions for mixed mode loading of embedded echelon crack model F20-60_D0.01_X18_A-0.5.	330

Figure E.20. ERR distributions for mixed mode loading of embedded echelon crack model F20-60_D0.01_X18B. (left) G_I , G_{II} , and G_{III} . (right) G_{II} and G_{III}	331
Figure E.21. Description of edges used to define meshing.	338
Figure E.22. Views of mesh for t/5 echelon crack oriented at 45° with code F5_CT6_W03-6_L08_45. (a) full view of model, (b) edge-view of refined region, (c) edge-view of near-tip region, (d) diagonal partition-view of echelon crack, (e) width-wise refinement view.	339
Figure E.23. Mode I ERR distributions for echelon cracks oriented at 90° (left) t/20 crack F20-CT6_W012-6_L04_90, (right) t/5 crack F5_CT4_W03-5_L08_90.	340
Figure E.24. ERR distributions for t/20 echelon crack oriented at 45° with code F20_CT6_W012-6_L04_45.	340
Figure E.25. ERR distributions for t/5 echelon crack oriented at 45° with code F5_CT6_W012-6_L08_45.	341
Figure E.26. Views of mesh for delamination-only model with partitions for a t/5 echelon crack oriented at 45° with code F5_CT6_W03-6_L08_45. (a) full view of model, (b) edge-view of refined region, (c) edge-view of near-tip region, (d) diagonal partition-view of refined region, (e) diagonal partition-view of near-tip region, (f) width-wise refinement view.	346
Figure E.27. Plot of ERRs for t/20 echelon crack.	347
Figure E.28. Plot of ERRs for t/5 echelon crack.	348
Figure E.29. Views of mesh for ellipsoidal crack model. (a) Full view of model, (b) planar view of model, (c) planar view of near-tip region.	352
Figure E.30. Mode I ERR distribution for ellipsoidal model.	353
Figure E.31. Views of mesh for multiple echelon crack model. (a) Full view of model, (b) echelon crack plane-view, (c) width-wise refinement full view, (d) width-wise refinement at echelon crack planes.	357
Figure E.32. ERR distributions for delamination model with multiple echelon cracks.	358
Figure E.33. ERR distributions for middle echelon crack in multiple crack model.	360
Figure E.34. ERR distributions for outside echelon crack in multiple crack model.	361

List of Tables

Table 4.1. Material properties (moduli in GPa).	80
Table 4.2. Correction factors for baseline configurations with delamination lengths $a = 32$ mm.	97
Table 4.3. Correction factors as a function of delamination length for SST NE.	101
Table 5.1. Delamination toughness data for IM7/977-3.	123
Table 5.2. Damage progression test stopping points for IM7/977-3.	126
Table 6.1. Geometries tested and associated correction factors for ERR determination.	158
Table 6.2. IM7/8552 material properties (O'Brien and Krueger, 2003).	165
Table 8.1. Percent difference in average G_{III} on delamination front for multiple echelon cracks.	253
Table A.1. Recommended channel settings for E_{11} Testing.	274
Table B.1. Recommended channel settings for G_{12} Testing.	281
Table E.1. Average values of ERR components for benchmark STB model.	300
Table E.2. Comparative results between benchmark STB model and experimental models for delamination validation without diagonal partition.	300
Table E.3. Values of ERR components at select locations along the delamination front for benchmark STB model.	304
Table E.4. Comparative results between benchmark STB model and experimental model ERRs at select locations along the delamination fronts for Linear-30 mesh.	304
Table E.5. Comparative results between benchmark STB model and experimental model ERRs at select locations along the delamination fronts for FineMesh-30.	304
Table E.6. Comparative results between benchmark STB model and experimental model ERRs at select locations along the delamination fronts for FineMeshA-60.	304
Table E.7. Comparative results between benchmark STB model and experimental model ERRs at select locations along the delamination fronts for RefinedMesh3X.	304
Table E.8. Comparative results between benchmark STB model and experimental model ERRs at select locations along the delamination fronts for FineMeshA-150.	305
Table E.9. Comparative results between average values of benchmark STB model and experimental models for delamination validation without diagonal partition.	311
Table E.10. Values of ERR components at select locations along the delamination front for B82 F20-32, which is a model with FineMeshB in the refined region, 82 elements across the width, and a $t/20$ echelon crack with 32 elements around it.	314
Table E.11. Values of ERR components at select locations along the delamination front for B82 DiagOnly, which is a model with FineMeshB in the refined region, 82 elements across the width, and a diagonal partition but no echelon crack.	314

Table E.12. Values of ERR components at select locations along the delamination front for A66 F5-60, which is a model with FineMeshA in the refined region, 66 elements across the width, and a t/5 echelon crack with 60 elements around it.	314
Table E.13. Values of ERR components at select locations along the delamination front for A66 F10-32, which is a model with FineMeshA in the refined region, 66 elements across the width, and a t/10 echelon crack with 32 elements around it.	315
Table E.14. ERR results for echelon crack subjected to mode I loading for different models. ...	323
Table E.15. ERR results for echelon crack subjected to mixed mode I-II/III loading for different models.	332
Table E.16. ERR results for combined model with t/20 and t/5 echelon cracks at 45° and 90°. ...	342
Table E.17. Values of ERR components at select locations along the delamination front for a t/20 echelon crack in the combined model.	349
Table E.18. Values of ERR components at select locations along the delamination front for a t/5 echelon crack in the combined model.	349
Table E.19. Comparative results between benchmark STB model and experimental model ERRs at select locations along the delamination fronts for the multiple echelon crack delamination only model.	349
Table E.20. ERR results for echelon cracks in multiple crack model	359

Chapter 1. Introduction

When structures are designed using continuous fiber laminated polymer matrix composites, they are traditionally optimized to prevent failure from applied static loads such as tension and bending. However, composite laminates are also susceptible to failure by delamination of the laminate plies. Delaminations may initiate at free edges, from inherent defects, or from impacts, and growth of these delaminations can be a significant issue. Growth from a delamination or defect can result in interlaminar, between plies, or intralaminar, within a ply, fracture. The type of fracture that occurs can be categorized into three modes based on the loading that causes growth: a tensile or opening mode, an in-plane shear or sliding mode, and an anti-plane shear or tearing mode. This dissertation studies the mechanisms that lead to crack growth in composite laminates subjected to anti-plane shear loading.

For unidirectional composite laminates, test methods have been developed and standardized for the determination of (opening) mode I toughness (ASTM D5528, 2013), (in-plane shear) mode II toughness (ASTM D7905, 2014), and mixed-mode I-II toughness (ASTM D6671, 2013). However, there is not currently a (anti-plane shear) mode III toughness test. Here, toughness is defined in terms of the strain energy released when a crack grows, thereby creating a new unit of surface area. The above toughness tests are used to determine the critical energy release rate, per unit of area created, for interlaminar delamination growth of continuous fiber laminated polymer matrix composites.

The initial motivation for the research conducted in this dissertation was to develop a mode III delamination toughness test. However, it was soon determined that delamination growth under mode III loading was fundamentally different from growth under modes I and II. It

was found that, under mode III loading, delamination growth is coupled to the initiation of transverse cracks in the matrix material along the delamination front, and that pure interlaminar delamination growth cannot be achieved. Because of this, it is likely that a critical energy release rate for planar delamination growth cannot be found for traditional composite laminates subjected to mode III loading, and therefore a test method cannot be developed to determine a mode III toughness for these laminates. In light of these determinations, the focus of this dissertation shifted from the search for a mode III toughness test to the more fundamental exploration of the mechanisms leading to crack growth in composite laminates subjected to anti-plane shear loading. The study of how complex fracture surfaces develop, evolve, and ultimately lead to growth of the planar delamination became an emphasis of this research. Experiments were conducted to obtain an understanding of the mechanisms driving fracture surface evolution. Subsequent to this, numerical modeling of the initial stages of crack growth was conducted in order to support the experimental results and add to the mechanistic understanding of anti-plane shear fracture.

In what follows, Chapter 2 presents a detailed literature review of the topics necessary to frame the research conducted for this dissertation. The history of mode III test method development attempts are first presented. As noted above, this dissertation studies the mechanisms for crack growth under anti-plane shear loading. Thus, the available literature on mode III and mixed-mode I-III testing in homogenous materials is also presented. To direct the subsequently performed numerical modeling, the different approaches available to model the initial stages of fracture under anti-plane shear are presented in the final section of Chapter 2. Chapter 3 will first present the overall objectives addressed in this research. The chapter will then provide a full overview of the rest of the dissertation as well as the experimental and

numerical approaches used to achieve the objectives. Chapters 4 covers the experimental investigations into mode III test method development, and the initial finding that pure interlaminar delamination growth does not occur is presented. Chapters 5-6 then cover the study of crack growth mechanisms under anti-plane shear loading. Chapters 7-8 cover the validation of a numerical model and its subsequent use in modeling the initial stages of crack growth under anti-plane shear. Finally, Chapter 9 presents a summary of the work performed for this dissertation, key conclusions, and recommendations for future work.

Chapter 2. Literature Review

2.1. Introduction

2.1.1. Delamination in Composites

When an elastic material is loaded, it stores potential energy. A crack, or even microscopic flaw, in a material will grow if the energy available to propagate the crack reaches a critical value. When this occurs, the release of energy per unit of surface area created is described by the energy release rate (ERR), and can be determined using the theories of linear elastic fracture mechanics (LEFM). Using classical LEFM (i.e., assuming small-scale damage), the energy release rate can be decomposed into three modes based on the near-tip stress field. There is an opening mode (mode I), an in-plane shear mode (mode II), and an out-of-plane or anti-plane shear mode (mode III).

Composites are strong, lightweight, elastic materials which are typically composed of a combination of a fiber and a matrix material. Carbon/epoxy and glass/epoxy are two common structural composite materials that have numerous engineering applications. Composite laminates are fabricated by stacking lamina, or plies, of material and forming them to produce a monolithic structure.

In composite laminates, it is often energetically preferential for failure to occur by crack propagation through relatively weak matrix material, rather than through fiber breakage or other failure mechanisms. Cracks propagating through laminates can arrest or become constrained by fibers. The method of fabricating composites by stacking plies of material often results in a plane between plies with little or no fiber content. Thus, crack growth at an interlaminar interface is

often an energetically “weak link” for crack growth, and the failure of composite laminates by interlaminar delamination is therefore a major concern.

2.1.2. Delamination Toughness

According to LEFM, a delamination will grow when the energy release rate equals or exceeds the critical value required for growth, i.e., when $G \geq G_c$, where (for the purposes of this work) G_c is the delamination toughness. In order for this equation to have predictive accuracy, (1) the material needs to be an elastic body, except for a small, inelastic zone in the vicinity of the crack tip, (2) the inelastic damage zone needs to be sufficiently small that the work input into this zone is an appropriate parameter on which to base the condition for crack advance, and (3) G_c must be a true material property, independent of the global loading, geometry, and boundary conditions. For small-scale damage and linear elastic conditions, where the assumption of a singular zone applies, G may be broken up into its mode I, II, and III components ($G = G_I + G_{II} + G_{III}$) using classical mode decomposition techniques. When this is true, condition (3) above is generally expanded such that G_c may be a function of the relative amounts of G_I , G_{II} , and G_{III} , i.e. $G_c = G_c(G_I/G, G_{II}/G, G_{III}/G)$, where this functional relationship is obtained by experiment.

2.1.3. Mode III Delamination Toughness

In view of the above, the generally accepted criterion for delamination growth under mode III loading is $G_{III} = G_{IIIc}$, where G_{IIIc} is the mode III delamination toughness. While delamination toughness for unidirectional 0/0 laminates loaded in modes I, II, or I-II are fairly well understood, and standardized test methods have been adopted (ASTM D5528, 2013; ASTM

D6671, 2013; ASTM D7905, 2014), this is not the case for mode III delamination toughness testing. Determining the mode III toughness for composite laminates remains an open question.

2.1.4. Reviewed Topics

This review examines the theories, experimental results, and numerical modeling efforts associated with growth due to anti-plane shear, or mode III, loading. One primary focus of this work is the determination of the mode III delamination toughness of composite laminates. Therefore, Section 2.2 provides a review of the relevant mode III composites literature. Several early tests are first briefly reviewed, and it is shown why these are no longer used for mode III toughness testing. The two most promising test methods, as well as their associated data reduction techniques and experimental results, are then reviewed in depth. Delamination toughness is a material property, which implies that it must be independent of geometry for any given mode mixity, including pure mode III. Therefore, one of the primary criterion for assessing potential toughness tests will be geometry independence; here it is shown that even the two most promising mode III tests have issues. It is not clear from these results whether the difficulty in obtaining G_{IIIc} is due to unresolved issues with the tests themselves, or with an intrinsic issue that is not yet understood. Thus, several recently introduced test methods are also presented, one of which appears quite promising for use in mode III toughness testing. This new test is used herein to help resolve this issue.

Subsequent research performed as part of this dissertation will show that there is an intrinsic issue with mode III testing that is not understood in composite laminates. While a review of the mode III composites literature presents a detailed picture of mode III toughness testing, it does not provide any information on the fundamental mechanisms causing

delamination growth, and therefore does not shed light on what this issue might be. For this reason, Section 2.3 of this dissertation reviews research conducted on homogenous materials under mode III, or anti-plane shear, loading. Here, emphasis is on details of crack initiation and fracture surface evolution during mode III loading, and experimental observations are presented for both pure mode III torsion tests and “almost-pure mode III” shear tests.

A review of the relevant literature indicates that pure anti-plane shear loading in homogenous materials is often considered as a special case of mixed-mode I-III loading. Perhaps for this reason, mode I-III has received much more attention than mode III, and in addition to experimental observations, there are numerous mechanistic theories proposed to describe crack growth. These data are potentially valuable to better understanding the mechanisms of growth in composite materials. First, the proposed theories governing different aspects of fracture are introduced. Then, the available experimental results are compared with predictions based on these theories. These results are presented in Section 2.4.

The final portion of this dissertation will be focused on the numerical modeling of the mechanisms leading up to planar delamination growth in composite laminates. Therefore, Section 2.5 will review the current state of analytical and computational modeling in mode III. To date, there is no literature on the modeling of the fundamental damage mechanisms leading to planar delamination growth in laminated composite materials subjected to anti-plane shear, and so this review will be with respect to homogenous materials.

2.2. Mode III Testing of Composite Materials

2.2.1. Introduction

This section reviews mode III testing of composite materials. Many different tests have been proposed to determine the mode III delamination toughness of laminated composite materials. Some of the proposed tests are the subjects of active research efforts, while others are not. The specimen geometries are generally either plate or beam geometries, and contain either one or two crack tips. Loads may be applied by an arrangement of pins, by bonded metal tabs or clamps, or by a combination of both.

Both unidirectional and multidirectional laminates have been used to fabricate mode III delamination toughness test specimens. However, the vast majority of tests that employ multidirectional laminates use stacking sequences where the plies bounding the delamination are oriented in the same direction, and are parallel to the direction of delamination growth. Therefore, at a level local to the delamination, the multidirectional laminates are identical to the unidirectional laminates. Those few studies where this is not the case (e.g. Donaldson, 1988; Laio and Sun, 1996) are not reviewed here. Therefore, all of the reviewed test techniques aim to determine the delamination toughness for laminates where the direction of growth is parallel to the direction of the surrounding fibers.

In order to extract G_{IIIc} from any set of test data, it is necessary to know (1) the point of delamination growth onset, and (2) the ERR when delamination growth occurs. In theory, if (1) and (2) are determined correctly, and if planar delamination advance is the only type of damage that occurs (outside of a small inelastic zone), then the extracted G_{IIIc} will be correct, and must be a material property. However, it is not definitively clear which point in a test corresponds to the delamination onset and which data reduction techniques are appropriate for various tests.

Therefore, in the subsequent sections, several techniques will be reviewed, and only the techniques deemed appropriate will be considered when evaluating the test methods.

Because the mode III delamination toughness is a material property, it must be independent of test specimen geometry. Therefore, the mode III toughness testing results presented herein consider the dependence or independence of toughness measurements on geometry. The most common geometrical variable to examine is crack length, although specimen thickness, width, and the amount of specimen overhanging the fixture, have also been examined. Additionally, only “initiation” results, those obtained from specimens with an insert pre-implanted in the laminate during manufacture to simulate an initial crack, are considered in this review.

Propagation results are not considered so as to avoid issues associated with crack propagation such as fiber bridging, multi-planar advance, or changing delamination shape.

2.2.2. Early Mode III Tests

The crack rail shear (CRS) test was apparently the first proposed mode III toughness test for composite laminates (Becht and Gillespie, 1988). It is conceptually similar to the two-rail shear test that was standardized as ASTM D4255 (2015), although the geometry is slightly modified to better apply to a thin composite laminate. As shown in Figure 2.1, the CRS geometry is composed of a plate with a pair of delaminations spanning one edge and creating three cracked regions on one side. The specimen is clamped by rails, and anti-plane shear loading is applied to the crack tips by translation of these rails. The onset of delamination advance was determined by looking for a discontinuity in the reading of strain gages placed above the delamination tips (Becht and Gillespie, 1989). G_{IIIc} was determined using a strength of materials-based closed form expression which depended on an experimental measurement of the shear modulus using those

same strain gages (Becht and Gillespie, 1989). However, there are a number of significant issues with the CRS test. During experimental studies it was found that accurate measurement of the shear modulus was difficult, there were significant issues with slippage between the rails and the specimens, and it was difficult to achieve uniform crack growth (Becht and Gillespie, 1989). Most importantly, the test resulted in the initiation of multiple cracks as well as crack growth through plies to neighboring interfaces, invalidating the assumptions of LFM (Becht and Gillespie, 1988; 1989). For these reasons, the CRS is no longer considered as a possible mode III delamination toughness test.

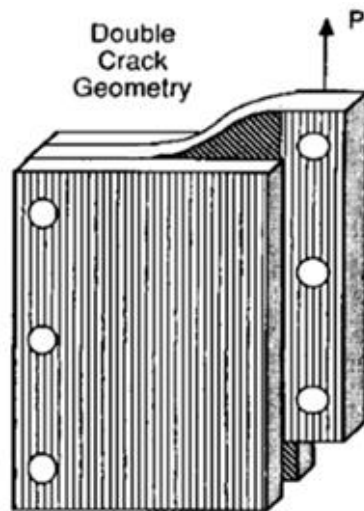


Figure 2.1. Crack rail shear (CRS) geometry (Becht and Gillespie, 1988).

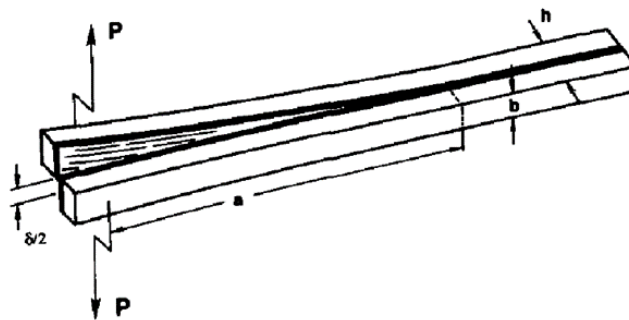


Figure 2.2. Split cantilever beam (SCB) geometry (Donaldson, 1988).

Another early mode III test was Donaldson (1988)'s split cantilever beam (SCB) test. The SCB consists of a laminate beam with a long mid-plane delamination on one end with a mode III shear loading applied to each cracked leg using pins (Figure 2.2). Toughness was calculated using three different methods: the area method, Euler beam theory, and single-specimen compliance calibration. These data reduction techniques will be discussed subsequently with respect to other tests, and so will not be discussed here. Importantly, Donaldson (1988) studied the dependence of toughness on geometry, and found toughness to depend on specimen thickness and width. However, Martin (1991) later conducted a finite element (FE) analysis on the SCB and showed that a significant mode II component arises along the delamination front due to the load application, and that the mode II component is greater than the mode III component over almost half the specimen width. As the SCB is therefore a non-uniform mixed-mode II-III test, it is not appropriate for mode III toughness testing, and is no longer actively studied for this purpose.

2.2.3. Edge Crack Torsion Test

2.2.3.1. Test Description

The edge crack torsion (ECT) test is a commonly considered mode III toughness test. Introduced by Lee (1993), the ECT specimen consists of a laminated plate which contains a pre-implanted Teflon sheet inserted at the mid-plane during lay-up to create an edge delamination on one side (Figure 2.3). While different specimen layups have been considered, almost all contain plies bounding the mid-plane with a fiber direction that is parallel to the direction of planar delamination growth. An arrangement of pins applies a torsional load to the specimen. In the original test design by Lee (1993), the specimen was constrained near three corners by stationary

hemispherical-tipped pins. An additional hemispherical-tipped pin was translated to load the specimen near the fourth corner. The loading arrangement resulted in a twisting of the ECT specimen about an axis perpendicular to the direction of planar crack advance. This geometry was used for a number of early ECT studies (e.g. Li et al., 1996; Li et al., 2004).

In the work of Li et al. (1996) it was found that the original ECT configuration resulted in a large amount of experimental scatter. They proposed to alter the test fixture such that only two opposite-edged pins would remain stationary, while the other two would apply load to the specimen. While this resulted in a slightly less uniform mode III distribution across the specimen width, it greatly improved the precision of the data Li et al. (1996). This latter geometry is now the preferred method of ECT testing, and has been used by Ratcliffe (2004), Pennas et al. (2007), de Morais et al. (2009A), Marat-Mendes and de Freitas (2012), and Browning et al. (2011). Browning et al. (2011) also made small modifications to the ECT fixture such that specimens of different geometries could be tested.

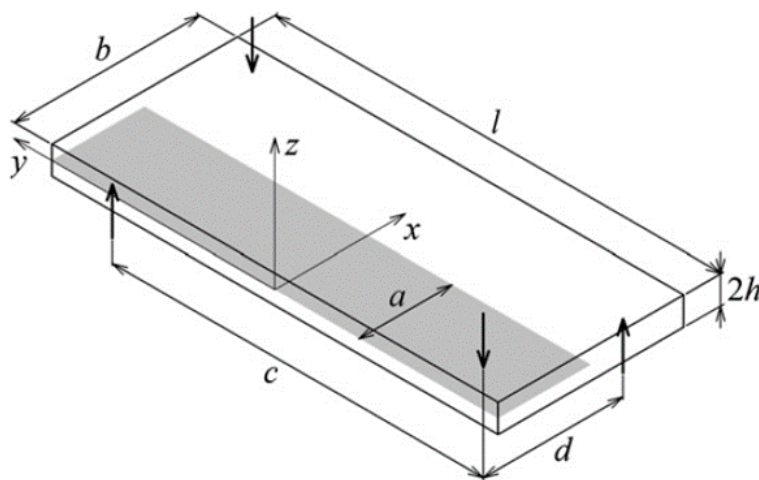


Figure 2.3. Edge crack torsion (ECT) geometry (de Morais et al., 2011).

A modified edge crack torsion (herein called the MECT) test has also been proposed, and was used by Suemasu (1999). Here, instead of two sets of pin-loads on opposite sides of the specimen, opposite sides were fixed by clamps. Then uniform torsion was applied to each edge. Laio and Sun (1996) apparently also used this geometry, although their emphasis was not necessarily to introduce or study a proposed mode III toughness test. Suemasu (1999) was able to achieve a more uniform mode III ERR distribution over the width with his MECT test. However, it was not possible to develop a specimen geometry where delamination growth initiated before failure of the specimen. Therefore, this modified test method has not been pursued.

2.2.3.2. Critical Load for Delamination Growth Determination

Delamination growth initiation is most commonly described in terms of a critical load (P_c) that is associated with the onset of growth. For mode III loading, this means that $G_{III} = G_{IIIc}$ when $P = P_c$. Several different points on a load-displacement plot have been proposed or used for this purpose (Figure 2.4), and they will be described subsequently.

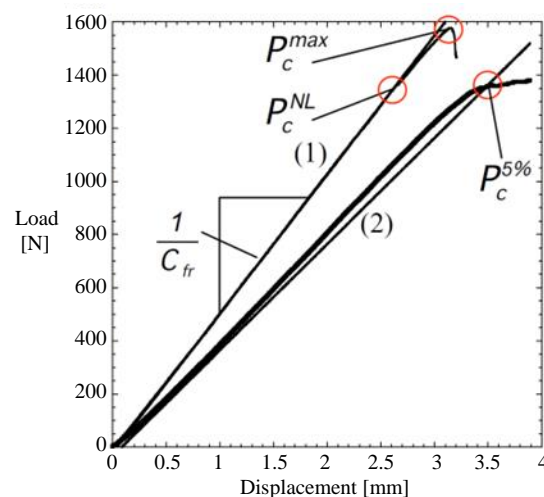


Figure 2.4. Examples of ECT load-displacement plots with several possible “critical loads” noted (Ratcliffe, 2004)

Many authors assume that delamination growth will initiate at the peak load, P_{\max} , achieved during testing, and therefore set $P_{\max} = P_c$. The use of the peak load as the critical load for growth implies that there is no sub-peak local delamination growth present in the test, which is not always straightforward to show. Some authors have tried to address the uncertainty in using P_{\max} as the critical load by considering additional possibilities as well (Ratcliffe, 2004; Pennas et al., 2007; Marat-Mendes and de Freitas, 2012). Other authors have hypothesized that if the load-deflection response remains linear up to P_{\max} , then no sub-peak delamination growth has occurred, as non-linearity near P_{\max} may be caused by localized delamination growth (Lee, 1993). Li et al. (1996) used P_{\max} even when non-linearity was observed.

Another considered critical load is the load at the onset of non-linearity, P_{NL} , in a load versus deflection response. This non-linear load can correspond to the initiation of localized delamination growth, although it is also possible that non-linearity can arise from other sources. However, many authors choose to use P_{NL} as the critical load for delamination growth initiation (Marat-Mendes and de Freitas, 2012; Li et al., 2004; Pennas et al., 2007; Carlsson et al., 2014) because it is more conservative than P_{\max} . Determining the onset of non-linearity is often done qualitatively, and so P_{NL} is often associated with a large amount of scatter. In de Moraes et al. (2009A)'s work they dealt with the uncertainty in finding P_{NL} by considering two different points. The first was at an initial, small deviation from linearity, while the second was at a more significant deviation from non-linearity.

Two different methods have been used to determine a critical load based on a quantification of non-linear specimen behavior. Both are considered “5% offset” methods. The first method superimposes a line with a slope of 5% less than the experimental load-deflection slope (determined in a linear region) on the load-deflection plot (shown in Figure 2.4). As the

test becomes non-linear, the load-deflection response and the offset line will intersect. This is considered to be the 5% offset non-linearity by Ratcliffe (2004) and Li et al. (2004). The second 5% offset method uses a localized measure of compliance, and considers the point where the compliance increases by 5% to be the initiation of delamination growth (Browning et al., 2011; Marat-Mendes and de Freitas, 2012) (not shown in Figure 2.4). The two 5% offset methods result in slightly different determination of the critical load. However, the value of 5% is somewhat arbitrary, and it has not been shown that delamination growth initiates at this point. The benefit of the 5% offset methods is that, in contrast with the P_{NL} method, the critical load is determined unambiguously and does not depend on an observer to qualitatively select it.

In determining the critical load for delamination growth in ECT specimens, there are basically two categories. The critical load has been considered to be either the peak load or some form of the load at, or offset from, the onset of non-linearity. However, Ratcliffe (2004) used X-radiography to show that damage, possibly delamination or intralaminar ply splitting, occurs prior to P_{max} , and he hypothesizes that this damage initiates at P_{NL} . Apparently all ECT studies have observed at least some non-linearity in the load-deflection response prior to delamination growth (Lee, 1993; Li et al., 1996; Ratcliffe, 2004; Li et al., 2004; Pennas et al., 2007; de Moraes et al., 2009; Browning et al., 2011; Marat-Mendes and de Freitas, 2012). However, it is unknown whether this may be due to pre-peak delamination growth, localized damage, or some other process.

2.2.3.3. G_{IIIc} Determination

A number of different methods have been used to calculate G_{IIIc} for ECT tests. G_{IIIc} may be calculated by (1) a theoretical approach that uses laminated plate theory (LPT), (2) a

numerical approach that uses FE results along with a critical load and/or displacement from experiments, or (3) compliance calibration. These techniques will be discussed subsequently.

G_{IIIc} can be calculated for ECT specimens using equations for G_{III} derived from LPT. An “equation for G_{IIIc} ” is obtained by evaluating G_{III} at the critical load and/or displacement for growth (as discussed in Section 2.2.3.2). Li and O’Brien (1996) also formulate an equation for G_{IIIc} based on LPT, but they leave it in terms of material properties that must be measured separately. Lee (1993) uses the theory of torsion of laminated plates to formulate an equation for G_{IIIc} that depends on specimen geometry, and then uses an experimentally measured compliance substituted into the equation to avoid the dependence on material properties and improve its accuracy. Ratcliffe (2004) uses a similar method, although here the compliance of the system is subtracted from the overall measured compliance of the specimen. Although these latter two techniques avoid the use of material properties, they still rely on basic assumptions of LPT. de Morais et al. (2009A) note that the compliance of ECT specimens as derived from Li and O’Brien (1996) ‘s work is significantly underestimated when compared to experimental values. Therefore, they chooses to use LPT equations formulated for MECT specimens by Suemasu (1999) as one method of calculating G_{IIIc} of ECT specimens. While the theoretical specimen compliance for MECT specimens more closely matches the experimental ECT results (de Morais et al., 2009A), the boundary conditions of ECT and MECT specimens are very different, and there is no reason an MECT expression for G_{IIIc} should work with an ECT specimen. Further, Suemasu (1999)‘s equation for G_{IIIc} depends on accurate knowledge of material properties as well as the assumption of a long, narrow specimen, which is not accurate for the ECT. Despite the many formulations for G_{IIIc} based on LPT, they are still significant issues with this basic method. Those formulations that depend on knowledge of material properties are clearly not

ideal. However, even those methods which use an experimentally measured compliance are still formulated based on elementary theories of LPT, and may not accurately reflect specimen behavior.

Another approach to determining G_{IIIc} for ECT specimens is the virtual crack closure technique (VCCT). The VCCT was introduced by Rybicki and Kanninen (1977) and is fundamentally based on Irwin's crack closure integral. This technique relies on the theory that the energy released when a crack of area A is extended to $A + \Delta A$ is equal to the energy required to close a crack of area $A + \Delta A$ by an amount ΔA (Krueger, 2004). The VCCT uses the nodal forces at the crack tip and nodal displacements just ahead of the crack tip, both of which are determined by FE analysis, to determine the ERR distribution across the width. G_{IIIc} can then be determined using either a local criterion (at P_c , G_{IIIc} is equal to the peak value of the G_{III} distribution) or a global criterion (at P_c , G_{IIIc} is equal to the average value of the G_{III} distribution). Marat-Mendes and de Freitas (2012), for example, used a local criterion. However, there are several issues with the VCCT technique. Accuracy of the method can depend on the quality of the FE model mesh, the results can be very sensitive to the applied boundary conditions, and it requires detailed knowledge of material properties. Additionally, a new analysis must be conducted for each geometry and material that is tested. While the VCCT is the only technique capable of determining the distributions of ERR components across the specimen width, it is not an ideal technique due to these drawbacks.

The third method by which G_{IIIc} may be obtained is the compliance calibration (CC) technique. G_{IIIc} is obtained by experimentally determining the specimen compliance as a function of crack length, $C(a)$, and inputting it into a form of the equation for G_{IIIc} based on a global

energy balance: $G_{IIIc} = \frac{P_c^2}{2B} \frac{dC(a)}{da}$, where B is the specimen width. In general, and if the specimen

geometry allows, either a single-specimen or multi-specimen compliance calibration technique can be performed. That is, the $C(a)$ relationship can either be obtained using a single specimen (where crack length is varied either by shifting the specimen in the fixture or by growing the crack) or multiple specimens (cut to have different initial pre-implanted insert lengths). For each specimen, the compliance is determined experimentally using the linear portion of the load-deflection response (see Figure 2.4), and a data set of compliance versus crack length is compiled. A trend line, the form of which is often based on strength of materials equations, is fit to the experimental compliance versus crack length data, and the derivative of the trend line is input into the equation for G_{IIIc} (Lee, 1993; Ratcliffe, 2004). The single-specimen compliance calibration technique is generally considered the preferred method for G_{IIIc} determination, as it requires few assumptions (e.g., linear elastic material, all energy goes into crack advance) that can be checked qualitatively and quantitatively. However, due to the ECT fixture and specimen geometry, a single-specimen CC is not possible. Because a single-specimen CC cannot be used with the ECT test, a multi-specimen CC is commonly used (Lee, 1993; Li et al., 1996; Ratcliffe, 2004; Li et al., 2004; Pennas et al., 2007; Browning et al., 2011; Marat-Mendes and de Freitas, 2012). However, there are additional uncertainties introduced with the multi-specimen CC. Specimen-to-specimen variations in geometry and material properties are the main concerns in using multi-specimen CC. However, even though there are still issues that have not been resolved, multi-specimen CC is likely the best method available for obtaining G_{IIIc} from ECT test data.

2.2.3.4. Mode III Toughness Testing

The mode III toughness test results for ECT specimens will be evaluated by examining those experiments which include studies of geometry dependence. If G_{IIIc} is being truly and accurately measured, then it will be independent of specimen geometry. However, if G_{IIIc} is shown to depend on geometry, then this indicates that there is an issue with either the specific test method or more generally with mode III testing that is not understood.

Li et al. (2004) used the ECT geometry with three stationary pins and one moving pin, and showed that G_{IIIc} is larger in specimens with longer delamination lengths. Studies using the more recent ECT design, with two stationary pins and two moving pins, by Ratcliffe (2004), de Morais et al. (2009A), Pennas et al. (2007), and Browning et al. (2011) all show higher toughnesses from specimens with longer delamination lengths, although the trends are all slightly different. Browning et al. (2011) also shows higher G_{IIIc} when the amount of specimen overhanging the load pins is large.

The above results are based on data acquired from ECT tests using several definitions of the critical load (P_{NL} , 5% offset), as well as data reduction methods that do not rely on material properties (material property-independent LPT, CC). Even with the variety of techniques utilized, all of these studies find that mode III toughness depends on geometry. Thus, it seems likely that the observed trends are not simply artifacts of the particular techniques.

2.2.4. Modified Split Cantilever Beam Test

2.2.4.1. Test Description

As discussed in Section 2.2.2, the SCB specimen could not be used for mode III testing due to a significant mode II component across the delamination front (Martin, 1991). Robinson

and Song (1994) proposed a solution to the mode II issue in the SCB. They presented an “improved” SCB test which was different from that originally introduced by Donaldson (1988) in two ways. First, they bonded and inset the composite specimen into thick steel bars. Loads were applied to the thick bars rather than the specimen itself in order to reduce the undesirable deformation associated with mode II loading. Second, rather than a single pin load in each cracked leg, they applied two sets of pins. The first set, identical to those of Donaldson (1988), applies the anti-plane shear load. The second set, which is oppositely oriented, applies a restoring moment to the crack tip that significantly reduces the mode II component. This geometry has not been used beyond the work of Robinson and Song (1994) due to issues with accurately bonding the steel bars to the specimens and difficulties aligning the specimen in the fixture (Sharif et al., 1995).

At around the same time as the improved SCB was introduced, the more commonly used modified split cantilever beam (MSCB) test (Figure 2.5) was also introduced (Sharif et al., 1995). The MSCB does not include the thick steel bars of the improved SCB, as it was found that the bars have only a small benefit, but a number of drawbacks. The MSCB, however, does take advantage of the shear load and restoring moment configuration created by two sets of pin loads applied to each cracked leg (Robinson and Song, 1994). Extensive three dimensional FE analysis have showed that the MSCB is also essentially a pure mode III test (Sharif et al., 1995). The MSCB fixture is generally configured with a number of different holes through which pins can be set, in order that specimens of different geometries can be tested with the same fixture. This setup has been used extensively for mode III toughness testing (Cicci et al., 1995; Sharif et al., 1995; Trakas and Kortschot, 1997; Rizov et al., 2006; Szekrényes, 2009; Szekrényes, 2011; Khoshravan and Moslemi, 2014).

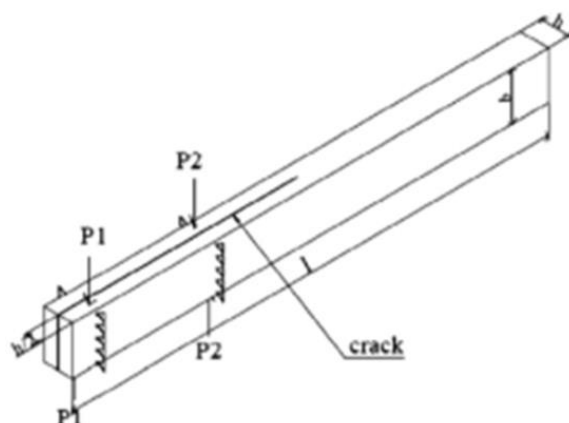


Figure 2.5. Modified split cantilever beam (MSCB) geometry (Khoshravan and Moslemi, 2014).

2.2.4.2. Critical Load for Delamination Growth Determination

In MSCB specimens, a visual observation can sometimes be used to determine the load corresponding to delamination growth, which is typically called P_{vis} . For transparent specimens, such as the MSCB specimens used by Szekrényes (2009; 2011) and Rizov et al. (2006), this technique is relatively straight forward. The entire crack front can be seen, and the accuracy of determining P_{vis} is only limited by the resolution of the imaging technique. Typically, a magnifying glass is used to achieve high accuracy. For opaque specimens, the delamination is only visible at the specimen edges, and visual observation of delamination growth initiation is not as straight forward. If delamination growth initiates locally at the specimen center, an edge observation will over-estimate the critical load. Szekrényes (2009) and Martin (1991) used FE ERR distributions to conclude that the delamination front would advance relatively uniformly across the specimen width, with only a slight amount of growth in the center of the specimen before growth reached the edges. From this, they rationalize that P_{vis} obtained from an edge-observation of delamination growth would be acceptably close to the load at which localized delamination advance actually took place. However, Szekrényes (2011) observed crack initiation in the center of transparent specimens and used the associated load as the critical values. This

work did not comment on how close an edge-observation of P_{vis} was to a center-observation of P_{vis} .

As in the ECT, P_{max} is sometimes used as the critical load for MSCB specimens. Robinson and Song (1994)'s improved SCB work show linear load-deflection plots up to the peak load, and concludes that the peak load corresponds to the critical load for delamination growth. However, the high-stiffness steel blocks adhered to the specimen make it impossible to tell whether there truly is no nonlinearity in the specimen response, or whether it is being masked by the blocks. Trakas and Kortschot (1997) used P_{max} as the critical load from their MSCB tests even though there was clear non-linearity, implying there may have been sub-peak load localized delamination growth.

Also similar to that used with the ECT, the critical load in MSCB tests may be based off of specimen non-linearity. Sharif et al. (1995) qualitatively selected a P_{NL} on the load-deflection plot to use as the critical load. Khoshravan and Moslemi (2014) used a 5% offset-type method where a line with a slope of 5% less than the experimental load-deflection slope (determined in a linear region) is superimposed on the load-deflection plot to determine the critical load (shown in Figure 2.4).

Four different determinations of critical load have been used with MSCB specimens. There are three general categories of critical load used for the onset of delamination growth in MSCB specimens. As with ECT specimens, P_{max} , P_{NL} , and 5% offset techniques have been used. Additionally, the P_{vis} technique has been used for MSCB specimens. For transparent specimens, P_{vis} is certainly the most accurate technique, as determination of delamination growth is unambiguous. For opaque specimens, however, it is not clear whether P_{vis} can be accurately used as a critical load for delamination growth initiation. As with the ECT, there is concern that P_{max}

is not appropriate for MSCB specimens due to the likelihood of pre-peak load crack growth. P_{NL} and the 5% offset technique are both likely appropriate for use as critical loads.

2.2.4.3. G_{IIIc} Determination

As described when discussing the ECT geometry, a number of different methods have been used to calculate G_{IIIc} . Compliance calibration, a theoretical approach that uses LPT, or a numerical approach that uses FE results may be used. Note that for MSCB specimen geometries, LPT can be reduced to Euler beam theory.

Beam theory is often used to calculate G_{IIIc} for MSCB specimens. Trakas and Kortschot (1997) used Euler Beam Theory (EBT) for their MSCB specimens, which considers contributions to ERR due to bending, but nothing else. As split-beam specimens are usually composed of relatively short, thick “beams,” and because shear deformation can be a significant form of deformation in composite laminates, it is not appropriate to use solely EBT to analyze the MSCB. Cicci et al. (1995) used a Timoshenko Beam Theory (TBT) formulation, which also considers the contribution due to transverse shear. Szekrényes (2009) used an “improved” beam theory (IBT) which considered TBT, Saint-Venant effects, and effects from the free torsion of orthotropic beam. Szekrényes (2011) and Khoshravan and Moslemi (2014) use these same equations. However, although the formulations of Cicci et al. (1995) or Szekrényes (2009) achieve improved accuracy, the results are still heavily dependent on knowledge of material properties.

G_{IIIc} determined via VCCT has been used by a few authors (Sharif et al., 1995; Rizov et al., 2006). However, this technique has many already-discussed drawbacks, and has not been used with any regularity for MSCB specimens.

Compliance calibration techniques can also be used to determine G_{IIIc} for MSCB specimens. A multi-specimen compliance calibration, like that for the ECT, can be used with MSCB specimens, whereby specimens with several different crack lengths are tested (Szekrényes, 2009). Additionally, a single-specimen compliance calibration can be used, where one specimen is shifted around in the fixture several times and sub-critically loaded in order to experimentally calculate a relationship between compliance and crack length (Cicci et al., 1995; Trakas and Kortschot, 1997). This eliminates the specimen-to-specimen variation concerns that exist with a multi-specimen CC. While a single specimen compliance calibration method is the preferred technique for obtaining G_{IIIc} , as it contains the fewest assumptions, there are still unresolved issues associated with MSCB testing. MSCB specimens fabricated from carbon/epoxy have very low compliance, and because of this it can be difficult to develop a $C(a)$ trend for both single-specimen CC (Cicci et al., 1995; Trakas and Kortschot, 1997) and multi-specimen CC (Szekrényes, 2009). There is also issue with determining the appropriately linear region over which to conduct the compliance calibration (see Figure 2.4), especially when specimens with large crack lengths are used.

In summary, beam theory, FE, and compliance calibration techniques have been used to determine G_{IIIc} for MSCB specimens. The beam theory and FE formulations suffer from dependence on material properties. The single-specimen CC would be the preferred technique for G_{IIIc} measurement, although there are known issues with extracting $C(a)$ for MSCB specimens. The multi-specimen compliance calibration technique has this same issue with $C(a)$ determination, but also has added uncertainty from specimen-to-specimen variation. Issues with all of these techniques has contributed to MSCB not moving forward as a generally accepted test (especially for carbon/epoxy). Nevertheless, it is likely the next best existing approach (after

ECT) for determining G_{IIIc} , and may be used to assess possible geometry dependence of the apparent toughness.

2.2.4.4. Mode III Toughness Testing

Several studies of geometry dependence have been presented using MSCB geometries. However, the results for the dependence of toughness on crack length for MSCB are not all in agreement. For glass/epoxy composites, it has been found that toughness is higher for specimens with larger delamination lengths (Szekrényes, 2009; Khoshravan and Moslemi, 2014). Conversely, for carbon/epoxy composites, toughness has been found to be lower for specimens with larger delamination lengths (Szekrényes, 2007; Szekrényes, 2009; Szekrényes, 2011). It is not clear why the trends are different for the two different materials.

The above results are based on data acquired from MSCB tests using several definitions of the critical load (P_{vis} , P_{NL} , 5% offset), as well as data reduction methods that do not rely on material properties (IBT, multi-specimen CC). Even with the variety of techniques utilized, all of these studies find that mode III toughness depends on geometry. Thus, it seems likely that the observed trends are not simply artifacts of the particular techniques.

2.2.5. Recently Introduced Mode III Tests

While the ECT and MSCB represent the tests which have been most studied to determine the mode III delamination toughness, each has significant drawbacks. In an attempt to obtain a “better” mode III test, additional toughness test methods have been proposed to determine G_{IIIc} . The four-point bending plate (4PBP) test was proposed by de Moraes and Pereira (2009B) as a simpler alternative to the ECT. The 4PBP consists of a cross-ply composite plate with a mid-

plane delamination at two opposite edges that is loaded in four point bending such that mode III conditions are transmitted to each of the crack tips (Figure 2.6). There has been a limited amount of research conducted on the 4PBP, but significant issues have already been noted. Current data reduction is based solely on finite element (FE) analysis, it is not known precisely when crack growth initiates, and there is considerable non-linearity in the load-deflection plot (de Morais and Pereira, 2009B). While it is possible that further studies could resolve these issues, such studies have not been conducted.

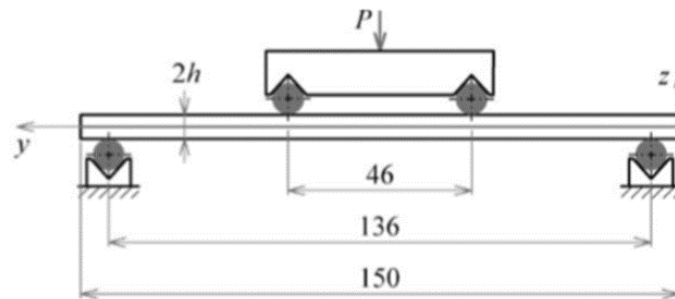


Figure 2.6. Four point bending plate (4PBP) geometry (de Morais and Pereira, 2009B).

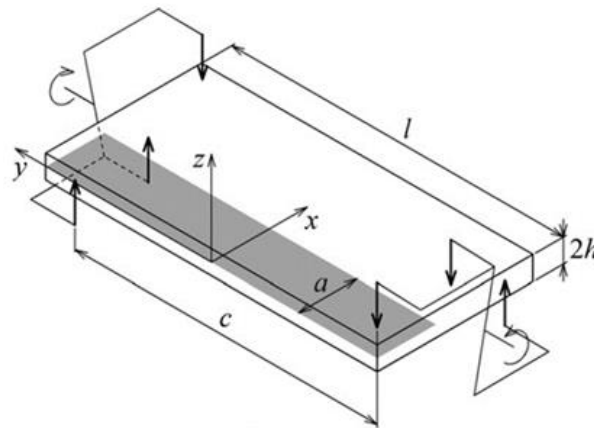


Figure 2.7. Six point edge crack torsion (6ECT) geometry (de Morais et al., 2011).

Pereira et al. (2011) proposed a modification to the ECT test which has been called the six-point edge crack torsion (6ECT) test. To produce the 6ECT, an additional set of load points was introduced to opposite sides of the specimen, resulting in three load points per side rather than the more traditional two (Figure 2.7). de Morais et al. (2011) performed initial experiments on the 6ECT. However, it was found that in order to maintain the relatively complex boundary conditions during testing, both large, expensive specimens, and a large, expensive fixture are required. Further, the only presently available data reduction technique requires FE computed parameters, and there were issues reported with migration to a different interface (de Morais et al., 2011). For these reasons, study of the 6ECT has not continued.

A newly proposed split-beam type test which can be used for mode III testing is the shear-torsion bending (STB) test (Davidson and Sediles, 2011). The STB test was originally introduced as a mixed-mode I-II-III test, as the fixture is designed to apply all three modes, either separately or coupled, to a split-beam type specimen (Figure 2.8). A mode III test is possible by holding the mode I and mode II loading components of the fixture stationary. The mode III STB is conceptually similar to the MSCB, in that both an anti-plane shear load and a restoring moment are applied to the specimen crack tip. In the STB, however, this is achieved by a zero-rotation constraint at the cracked end, and the loads are applied through bonded steel tabs rather than an arrangement of pins. The STB has not been the subject of a large amount of research, as it has been only recently introduced, but has potential as a mode III toughness test.

The 6ECT and 4PBP are relatively newer proposed tests, but both have significant issues with test fixturing that need to be solved before experimental results would be meaningful. The STB, which is also a relatively newly proposed test, has the potential to be useful for future mode III testing.

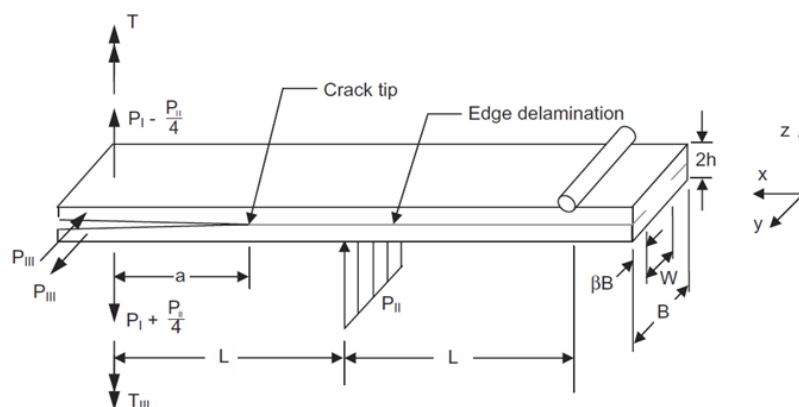


Figure 2.8. Shear torsion bending (STB) geometry (Davidson and Sediles, 2011).

2.2.6. Conclusions from Mode III Toughness Testing

The ECT and MSCB tests are the most advanced in terms of determining the validity of mode III delamination toughness measurements. Considering these two tests as well as the range of critical load possibilities and data reduction techniques, the available data indicate that toughness is dependent on geometry, which is not possible if G_{IIIc} is a material property. A significant amount of very careful research has been conducted on these tests, but it is not clear if the difficulty in obtaining G_{IIIc} is due to (1) unresolved issues with the tests or data reduction methods themselves, or (2) an intrinsic issue with mode III loading or growth mechanisms in composite materials that is not yet understood.

In this research, item (1) was first addressed. To this end, the mode III STB as well as a new, but related, mode III test method were used. As will be shown, it was found that there were intrinsic issues (item 2). These were better understood by first understanding the nature of growth under anti-plane shear loading in homogenous materials and, for this reason, a review of the associated literature is presented in what follows.

2.3. Mode III Testing of Homogenous Materials

2.3.1. Introduction

In mode III (and subsequently discussed mode I-III) testing of homogenous materials, stress intensity factors (SIFs) are traditionally used instead of ERRs to describe the state of stress at the crack tip. The three stress intensity factors (K_I , K_{II} , K_{III}) scale the stresses acting on the crack tip, and can be equated to the three components of ERR (G_I , G_{II} , G_{III}) using appropriate K-G relations.

The tests used in homogenous material mode III experiments can be separated into two categories. There are pure mode III tests, and there are tests that are “almost pure mode III.” One of the only ways to achieve a pure mode III test is to use a cylindrical rod with a circumferential notch in torsion. Almost any other geometry will result in some mode I or mode II component along the crack front. However, as was true in composite materials, it is possible to conduct a test that is “sufficiently” mode III for consideration as a mode III test. Experimental results from both of these categories of test will be discussed below.

The emphasis in mode III testing of homogenous materials has historically been less focused on measuring a G_{IIIc} (or K_{IIIc} value), and more focused on determining how a crack will advance. This most typically consists of determining the orientation and direction of crack growth. There has been a fair amount of observations on fracture path in pure mode III (and almost pure mode III) testing, yet very little theoretical prediction has been put forward. This is in contrast to mode I-III testing where, as will be discussed subsequently, there are a significant number of theories presented to determine the details of crack growth.

2.3.2. *Pure Mode III Tests*

The first experiments looking at mode III loading were carried out by Smekel (1953) on glass rods. Notched, round bar geometries have also been used by Lai (2002), Makabe et al. (2006), Berto et al. (2012A; 2012B), and Zehnder and Zella (2015). Shah (1974) also used a notched, round geometry, but with hollow tubes. Davenport and Smith (1993) used an hourglass-shaped geometry with a center notch. Cox and Scholz (1988) used round bars, but cut a narrow slot to form the starter crack. These geometries are all similar with respect to having a single, circumferential crack, which grows under pure mode III loading.

Smekel (1953) was the first to present a fractographic study on mode III. He observed that, rather than planar crack growth, the crack broke down into a large number of small “facet breaks” (also described as “echelon cracks” by other authors) that are rotated from the original crack plane to create a complex fracture surface. Similar small, echelon cracks are seen by many other authors (Cox and Scholz, 1988; Lai, 2002; Makabe et al., 2006; Berto et al., 2012A; Zehnder and Zella, 2015), and are often assumed to be oriented perpendicular to the direction of maximum principal tensile stress (MPTS) (Cox and Scholz, 1988; Lai, 2002; Makabe et al., 2006), although Zehnder and Zella (2015) note that their echelon cracks are somewhat shallower than the MPTS direction. It has also been noted that the cracks are quite small and closely spaced near the machine-cut notch (Lai, 2002). However, as the fracture propagates, the echelon cracks generally increase in length and decrease in number. This type of change in fracture surface characteristic with propagation is known as coarsening (Smekel, 1953; Lai, 2002; Makabe et al., 2006; Zehnder and Zella, 2015).

2.3.3. *Almost Pure Mode III Tests*

Almost pure mode III tests have been conducted under both bending and shearing loads. Unfortunately, there has not been FE analysis conducted on most of these geometries to determine the exact mode mixity or distribution across the crack front. Thus, while it is clear that these tests are mostly mode III tests, the true mode mixity is unknown. Some minor work has been conducted using a three point out-of-plane shear specimen (Ueda et al., 1983), four point out-of-plane shear specimen (Buchholz et al., 2004), and anti-clastic plate bending specimen (Farshad and Flüeler, 1998). Knauss (1970) used an edge-cracked glass plate and applied anti-plane shear loading through bonded rectangular brass stock. Goldstein and Osipenko (2012A; 2012B; 2014) also apply anti-plane shear loads to an edge-cracked geometry. However, their specimen contains two cracks, and the global specimen loading is achieved by a four point bend configuration.

Knauss (1970) showed that growth in his edge-cracked plate initiated as a series of discrete, parahelical cracks evenly spaced along the initial crack front. He, like those authors who studied mode III with the torsion of cylinders, also noted that the cracks were oriented at approximately 45° and were perpendicular to the MPTS direction. These small echelon cracks were similarly described by Farshad and Flüeler (1998), and Goldstein and Osipenko (2012A; 2012B).

In addition to echelon crack orientation, the crack length and the spacing between cracks is also of interest, and is much easier to discuss with respect to the almost pure mode III tests, as they typically had straight initial crack fronts. The crack spacing in Knauss (1970)'s work is relatively large, and only a few, big echelon cracks were observed. Conversely, Goldstein and Osipenko (2012B) saw the initiation of many small cracks. Although there has not been a

mechanistic theory proposed in mode III, Goldstein and Osipenko (2012B) suggest that echelon crack spacing and crack length are interconnected. They predict that echelon cracks will initiate unstably, but that they will be arrested once the crack size exceeds the spacing between the cracks. This agrees with the observations of both many small echelon cracks (Goldstein and Osipenko, 2012B), as well as a few large ones (Knauss, 1970).

The characteristics of echelon cracks are of interest during crack propagation as well as during initiation. Goldstein and Osipenko (2012A; 2012B; 2014) have extensively studied the propagation tendencies of echelon cracks in mode III specimens. They show that while crack growth initiates as many small, frequently spaced cracks, the fracture surface changes with progression. As the fracture propagates, the echelon array begins to coarsen, analogously to that seen in the torsion of cylinders. This coarsening is different from, though likely related to, the trends discussed previously for initial echelon crack length and spacing. Goldstein and Osipenko (2012B) explain the mechanisms for coarsening by noting that “only the crack located through the intervals multiple to the distances between cracks in the formed echelon obtain further development.” That is, cracks which are located in a favorable position in terms of high stress will extend and grow, while cracks which are located in regions of low stress will arrest. In this way, the echelon cracks are ordered based on the propagating stress state, and gradual coarsening occurs.

2.3.4. Conclusions of Homogenous Mode III Testing

Homogenous materials are known to show a preference for mode I crack growth. For example, in mixed-mode I-II loading, it is well known that an incipient crack will kink to align perpendicular to the direction of maximum tensile stress. The same general theory is applicable

to mode III loading of homogenous materials, although the inherent three dimensionality of anti-plane shear loading complicates matters and results in crack surface fragmentation. Crack growth in homogenous materials under mode III loading consists of an array of echelon cracks, which are rotated with respect to the incipient crack front, and which increase in size and decrease in number as they advance. The features of crack growth can be separated out into echelon crack orientation, crack length, crack spacing, and the behavior during coarsening. These features of crack growth in homogenous materials are very different from what is assumed to occur during mode III delamination growth in composite laminates.

2.4. Mode I-III Testing of Homogenous Materials

2.4.1. Introduction

In the homogenous materials literature, mode III loading is often considered as a special case of mixed-mode I-III loading. Perhaps for this reason, mode I-III has received much more attention than mode III, and the field is much more advanced. In addition to experimental descriptions of echelon cracking, there are a number of proposed theories to describe how cracks grow under mode I-III loading. These fracture theories will first be presented herein. Subsequently, the experimental results, and comparison to theoretical predictions, will be presented.

2.4.2. Fracture Theories

There are three aspects of mode I-III crack growth that have been defined to describe the path of a propagating crack. According to Cambonie and Lazarus (2014), the fracture surface of a crack extending under anti-plane shear can be defined in terms of a local twisting of small

echelon cracks, also referred to as facets. These separate from and therefore segment the incipient crack front (segmentation) leaving a measurable distance between facets (spacing), and producing a global twisting of the entire crack front (rotation). The available theories for the development of segmentation, spacing, and rotation, as well as others such as crack length or coarsening during crack propagation, are discussed.

2.4.2.1. Echelon Crack Orientation

In the mode III literature, it is generally assumed that facets grow out of the incipient crack at an angle perpendicular to the MPTS direction (Smekel, 1953; Knauss, 1970; Cox and Scholz, 1988; Lai, 2002; Makabe et al., 2006; Goldstein and Osipenko, 2012A). However, in the more broadly studied mode I-III field, there have been a number of theories proposed to predict the angle echelon cracks will make with respect to the initial crack plane.

The MPTS theory is often used to predict echelon crack orientation in mode I-III loading. However, even within this single theory there are many variations that have been utilized. MPTS predicts that crack growth will occur in the direction perpendicular to the maximum principal tensile stress. This is equivalent to a $K_{I-\max}$ or $K_{III} = 0$ (minimum circumferential stress) criterion. Sommer (1969) was the first to apply the MPTS criterion to mixed mode I-III loading. Pollard et al. (1982) was the first to present the MPTS criterion for plane strain conditions in the form of an equation that relied on the ratio K_{III}/K_I and the Poisson's ratio. This equation has been applied extensively to predict echelon crack orientation under mode I-III loading (Pook, 1985A; Hull, 1993; Cooke and Pollard, 1996; Lazarus et al., 2001B; Lai, 2002; Li et al., 2011; Goldstein and Osipenko, 2012A). The MPTS criterion has also been used with the assumption of plane stress conditions (Yates and Miller, 1989; Liu et al., 2004), but it is not clear that this was appropriate

based on the specimen geometries. Pook (1980; 1985B) developed a modified MPTS criterion that could be applied to applied to mode I-II-III loading, which reduces to Pollard et al. (1982)'s equation in the absence of mode II. Lazarus et al. (2001B) modified Pollard et al. (1982)'s equation by multiplying by a factor of one-half to better correspond to experimental results (discussed subsequently), although they were unable to provide a theory-based justification. Schollmann et al., (2002) derived a criterion based on principal stresses on a virtual cylindrical surface, for which the predictions are equivalent to those of MPTS.

The minimum strain energy density (SED) criterion, proposed for the planar case by Sih et al. (1962), predicts that a crack will grow in the direction of the minimum SED. Sih (1974) later extended the theory to the three dimensional case. However, Sih (1974) also determined that the SED was always predicted to be minimum at an angle of zero for mode III loading. Because of this, the criterion is regarded as insensitive to mode III loading, and is not applicable to predicting echelon crack angles.

The maximum energy release rate criterion predicts that crack growth will occur in the direction where the ERR is maximized. This criterion was proposed based on the fundamentals of Griffith theory by Erdogan and Sih (1963), and was further refined by Nuismer (1975) for a two-dimensional (K_I , K_{II} only) situation. Most recently, a standard equation has been developed for three dimensional loading which uses all three SIF's and material properties to predict echelon crack orientation (Ueda et al., 1983; Yates and Miller, 1989; Lawn, 1993). Cooke and Pollard (1996) studied the predictions produced by this theory using a Poisson's Ratio of $\nu = 0.38$. They found that the prediction is singled-valued below a mode mixity of $K_{III}/K_I = 1.4$, but that there are two solutions above $K_{III}/K_I = 1.4$.

The principal of local symmetry (PLS) has been cited as another theory to predict facet orientation. This method considers expansions of the equations which describe the relationship between remotely applied loads and the stress field near a crack tip. SIF's are used to match inner and outer expansions to find the main term of the asymptotic solution of the complete problem. The solution imposes constraints on the SIF's and the energy balance for the growing crack which can be used to generate a crack orientation criterion (Goldstein and Salganik, 1974). Cotterell and Rice (1980) and Hodgdon and Sethna (1993) both generalized the theory and provided two constraints to determine the angle of crack growth: $K_{II} = 0$ and some function of K_I and K_{III} equals zero. The prediction of the function of K_I and K_{III} determines the form that the PLS criterion takes. Lawn (1993) uses a plane strain MPTS-type condition to solve for the angle at which $K_{III} = 0$. Similarly, Lin et al. (2010) and Pham and Ravi-Chandar (2014) assume a form of the solution that is equivalent to MPTS. Leblond (1999) assumes a form of the PLS equation that is similar to the minimum SED criterion, and, identically to the minimum SED criterion, he finds his solution to have no dependence on the K_{III} field. Cooke and Pollard (1996) formulate the PLS function of K_I and K_{III} such that it becomes identical to the maximum ERR criterion. Amestoy and Leblond (1992) develop a form of the PLS criterion which is equivalent to the MPTS criterion plus a higher order term that is $O((\varphi/\pi)^6)$, where φ is the predicted angle (Lazarus et al., 2008). Thus, it can be seen that the PLS does not represent a criterion in itself, but is a set of constraints that can be used as a theoretical basis for the development of several criteria.

A few other minor criteria have been proposed for the determination of facet crack orientation, but none have been used as extensively as those already discussed. The equivalent stress intensity factor (ESIF) criterion was developed by Richard (1987) and Richard et al.

(2001), as a method to predict crack echelon crack angles. In the ESIF criterion an equivalent SIF is first defined, in a manner reminiscent of the Von Mises equivalent stress. An approximation function is used to determine the ESIF analytically, and this function is then used to predict crack angle orientation. Leblond and Frelat (2014) propose a tentative relationship between remote stresses and facet angle for “well-developed facets no longer ‘feeling’ the influence of the initial crack,” but they point out that the prediction is only tentative, and hasn’t been compared to any experiments. Pons and Karma (2010) have used a continuum phase field model with an applied helical crack tip perturbation (Hakim and Karma, 2009; Leblond et al., 2011) to predict crack twist angles, which appears able to predict facet orientation at any stage of fracture surface evolution.

The preceding crack orientation criteria are clearly interrelated. As discussed previously, the PLS criterion can be formulated to be equivalent with the MPTS, minimum SED, or maximum ERR criteria. The MPTS and ERR criteria predictions are identical before the solution bifurcation (Cooke and Pollard, 1996), and after the bifurcation, the average of the two solutions predicted by the ERR criterion is equal to the MPTS solution. The equivalent SIF criterion is an approximation, but correlates closely with MPTS predictions (Richard et al., 2005). Pons and Karma (2010) have shown that their phase field approach predicts somewhat smaller angles for a given mode mixity than the MPTS or maximum ERR criteria. Leblond and Frelat (2014) have not presented the relationship between their technique and other proposed techniques. At present, any of the criteria, except the minimum SED criterion which will always predict a zero twist angle, could be used to predict crack orientation. That is, it is not clear from the derivations alone whether one theory is more accurate than another.

2.4.2.2. Crack Length and Segmentation Spacing

There are very few proposed theories available to predict echelon crack length or the length of segments (segmentation spacing, or echelon crack spacing) the incipient crack front breaks into. Many authors offer conjecture of what they expect to happen, but without significant theoretical substantiation. Still, these suppositions can help frame how echelon cracks will be expected to grow.

The first basic set of conjectures concerns the conditions under which echelon crack initiation, and therefore crack front segmentation, will or will not occur. Cooke and Pollard (1996) use an energy argument formulated by Pollard et al. (1982) and Lawn (1993) to reason that crack front segmentation is the preferred mechanism for crack advance under mode I-III loading because the surface area produced is less than if the entire crack front were to rotate to align to mode I conditions, e.g., perpendicular to the MPTS direction. Authors have predicted that segmentation will occur under any mode I-III mixity, no matter the specimen geometry or how small the mode III component (Lazarus et al., 2001B; Pons and Karma, 2010; Pham and Ravi-Chandar, 2014).

Speculation concerning segmentation spacing is typically based on a stress argument (Pollard et al., 1982; Goldstein and Osipenko, 2012B). Pollard et al. (1982) was the first to propose that the finite number of echelon cracks, and the associated segmentation spacing, was due to differences in crack initiation and propagation rates in conjunction with local stress relief by dominant cracks. They propose that as echelon cracks initiate at the crack front, each crack is surrounded by a region of decreased local stress, and that a neighboring echelon crack will not initiate inside that region. Pham and Ravi-Chandar (2014) conducted a numerical analysis and found that the region of decreased local stress was approximately one echelon crack length away

from the initiated echelon crack, and theorized that echelon crack length would therefore dictate segmentation spacing.

Lin et al. (2010) formulate an energy equation to determine segmentation spacing and echelon crack length. They balance the global fracture energy available with the energy dissipated through facet formation plus the energy dissipated through formation of bridging structures that connect facets. They are able to solve for echelon crack length and segmentation spacing in terms of material properties, mode mixity, and a term representing the energy penalty associated with the formation of bridging structures. This represents the only theory available to predict echelon crack length or segmentation spacing. However, the global fracture energy term and the energy penalty term must both be extracted from a regression analysis of experimental data, and there has been no work presented showing the validity of this theory. Therefore, echelon crack length and segmentation spacing predictions are still in the early stages of development, and nothing is yet available that can be readily applied to experimental data.

2.4.2.3. Crack Front Rotation

Crack front rotation considers global orientation changes of the entire crack front, as opposed to segmentation, which considers local rotations of echelon cracks on the crack front. Crack front rotation and echelon cracking are interconnected, however. Global crack front rotation will change the apparent facet angle with respect to the crack front, while the facet angles will remain constant with respect to the direction of the applied loads. Hull (1993) theorizes that twisting along a continuous crack front cannot occur in real materials without crack front segmentation. Thus, segmentation is the first fracture step, and the global crack front

will gradually tilt and rotate until the global crack front orientation is aligned with respect to some criterion.

It is often presumed that the mechanisms causing segmentation are the same as those causing crack front rotation (Buchholz et al., 2004), but on a different scale. Lazarus et al. (2008) present three “local” and two “global” criteria to predict crack front rotation angles. For the local criteria, they assume there may be some curviness in the crack front, and suggest that it will rotate to align with some component of the local K field. The three criterion they present consist of a certain PLS formulation, MPTS (i.e., MPTS for plane stress), and “three dimensional MPTS” (i.e., MPTS for plane strain). For the global criteria, they take the criteria from Lazarus and Leblond (1998) and Lazarus et al. (2001B), and assume the crack front will rotate to a straight final position. The first global criterion says that the crack front will rotate to an angle which maximizes the mean value of K_I along the crack front. The second global criterion says that the crack front will rotate to an angle which maximizes the value of G along the crack front. According to Lazarus et al. (2008), this second criterion requires an a priori knowledge of the propagation distance at which facet behavior ceases to be “individual” and becomes “collective,” which makes implementation of this criterion difficult.

Seifi and Omdivar (2013) and Xu et al. (1994) both conduct FE simulations and look at crack front rotation. They both use width-averaged MPTS as a criterion for crack propagation direction. While their predictions for crack rotation angles appear theoretically appropriate, the fundamentals of their modeling techniques leave out important details. Seifi and Omdivar (2013) ignore initial segmentation, and in contradiction to the statements of Hull (1993), assume a continuous surface twisting. Xu et al. (1994) do include segmentation in their analysis, but they

treat the facets and the structures that connect adjacent facets identically, which Lazarus et al. (2001B) suggests invalidates their results.

The crack rotation predictions by Seifi and Omdivar (2013) and Xu et al. (1994) both ignore key physical details of fracture development, and therefore will not be considered further in this review. Although prediction of crack front rotation angles is difficult with Lazarus et al. (2008)'s maximum G criterion, there is no fundamental reason it could not be used. Therefore, all five of Lazarus et al. (2008)'s proposed criterion for crack front rotation could be applied. At this time, it is not clear from the derivations alone whether one criterion is more accurate than another.

2.4.2.4. Fracture Surface Evolution

While defining facet orientation, segmentation spacing, and crack front rotation is sufficient for describing the instantaneous state of fracture, it is not adequate to describe a changing or growing crack. During crack propagation, the fracture surface, herein used to describe the collection of cracks and branching structures, changes or evolves. It is necessary to describe this fracture surface evolution to understand how cracks propagate.

In an analysis conducted by de Freminville (1914), it was apparently determined that echelon cracks are “attracted” to each other, and that they will tend to “join up” to produce isolated prismatic shaped strips of material (Hull, 1993). This description of joining up is the earliest analytical rationale for fracture surface coarsening, which was initially introduced in Section 2.3.2. Here, as the fracture surface evolves, the number of cracks decreases as the size of crack increases. This coarsening is coupled with crack front rotation, and the combination of the two result in a final, single macro-crack. It is theorized that this final macro-crack will be

oriented perpendicular to the MPTS direction (Cooke and Pollard, 1996; Lai, 2002), and that the rate at which coarsening occurs will depend on the ratio K_{III}/K_I (Cambonie and Lazarus, 2014). However, there are no other proposed theories to describe the evolution of fracture surfaces during crack propagation.

2.4.3. Experimental Results

A number of test geometries have been used for mixed mode I-III testing of homogenous materials. Similar to those used for mode III testing, the mode I-III test specimens are typically either cylinder or plate geometries. They may be designed to produce a constant mode mixity across the crack front, or one that varies, based on the experiments required. As will be seen in Section 2.4.3.1, there is very little data available for mode I-III tests of cylinders. However, these represent some of the earliest efforts to understand the behavior of materials under mode I-III loading. Mode I-III test geometries consisting of edge-cracked specimens are much more prevalent, and their experimental results will be discussed in Section 2.4.3.2. Finally, a set of studies using specimens based on the geometry of Goldstein and Osipenko (2012A; 2012B), which yield some unique results, will be discussed in Section 2.4.3.3.

2.4.3.1. Tension (Compression) - Torsion of Cylinder Tests

The earliest mode I-III experiments were conducted on edge-cracked glass rods by Smekel (1953). However, the mode mixity was not controlled. The first controlled mode I-III experiments were carried out on glass rods with circumferential notches which were loaded in tension-torsion by Sommer (1969). The torsion was applied by a load fixture, while tension was applied to the crack faces with a pressurized fluid. More commonly, tension-torsion tests are

achieved by with a load frame that can apply both loading modes independently (Shah, 1974; Hourlier and Pineau, 1982; Petrovic, 1985; Suresh and Tschegg, 1987; Davenport and Smith, 1993; Makabe et al., 2006). Ren et al., (2012) achieved mode I-III loading with a cylinder by using a 36° spiral notch and applying pure torsion to the cylinder ends to produce a test with approximately $K_{III}/K_I = 0.33$. Conversely, Cox and Scholz (1988) used cylinders with thick machined slots, and used compression-torsion to achieve mode I-III loading.

Only a limited number of fracture surface observations have been made on cylindrical specimens subjected to mode I-III loading. Smekel (1953) and Sommer (1969) observed facets that they claimed were aligned perpendicular to the MPTS direction, although neither verify this, as the exact mode mixity was unknown in both these works. Petrovic (1985) observed that crack growth aligned with the MPTS direction in their circumferentially notched Si₃N₄ rods, although they did not present fracture surfaces or discuss segmentation. Hourlier and Pineau (1982) described “factory roof” shaped fracture surfaces which he separated in to “Type A” and “Type B” zones or cracks. Type A cracks are theoretically energetically favored and evolve due to opening mode loadings while Type B cracks are primarily predicted to occur in order to connect the Type A cracks into a uniform front (Hourlier and Pineau, 1982, Lazarus et al., 2001B, Lin et al., 2010). Hourlier and Pineau (1982) found that the angle of the Type A cracks was larger for larger K_{III}/K_I ratios. Cox and Scholz (1988) show that superposing compression and torsion results in steeper facet angles than pure torsion. Accordingly, they measure facet angles higher than 45° that are in fairly good agreement with an MPTS criterion. It is not clear how these measured angles would compare with predictions from, for example, a maximum ERR criterion.

As discussed in Section 2.4.2.2, it is predicted that segmentation will always occur if there is a component of mode III loading. Sommer (1969) presented the first experiments

looking for the presence or absence of segmentation. He conducted tests with a range of torsion-to-tensile-fluid- pressure ratios, but did not calculate mode mixities. He extrapolated his experimental data to predict a critical ratio of torsion to pressure loading where the fracture surfaces would transition from smooth to faceted. Along with this, he predicted that the minimum achievable facet angle is a material property, and for his glass material, predicted that the shallowest facet orientation achievable was 3.3° . Note that (assuming $\nu = 0.3$, and using the plane strain MPTS criterion) this corresponds to a mode mixity of $K_{III}/K_I = 0.023$. Sommer (1969) would therefore predict that, for his material, crack front segmentation would not occur below $K_{III}/K_I = 0.023$. It cannot be known for certain whether there is truly a loss of segmentation at this mode mixity, or whether perhaps facets develop that are very small and coarsen to a macro-crack very quickly, but this issue will be revisited in Section 2.4.3.3.

There is little available data on crack front rotation in cylinders under tension-torsion. Often there is a significant amount of segmentation and facet formation, but crack front rotation is not observed (e.g., see Shah, 1974; Suresh and Tschegg, 1987). This may be due to the circumferential crack front geometry, or the limited amount of growth that usually occurs in these specimens. Ren et al. (2012), who's specimens contained a 36° spiral notch, did not have these problems with crack geometry, and does show crack front rotation. They do not provide any measurements, but provide figures that show the crack front rotating to align with the principal tensile direction.

Similarly, there is no data available to discuss fracture surface evolution under tension-torsion, but Ren et al. (2012) do provide some data using their spiral-notch specimen. They show fracture initiation from a series of very small, closely spaced facets. Shortly thereafter, the fracture surface of their mode I-III specimen shows distinct coarsening as the crack grows.

2.4.3.2. Edge-Cracked Plates

Edge-cracked plates of several geometries have been used for mode I-III testing. Cooke and Pollard (1996) used a common compact tension (C(T)) specimen, and applied both anti-plane shear and tension loading to achieve mixed mode I-III conditions. Other authors have achieved mode I-III conditions by applying pure tension to a C(T) specimen for which the machined notch was angled out-of-plane (Schroth, 1986; Seifi and Omdivar, 2013). The specific mode mixity in these tests depends on the angle of cut. Mode I-III conditions using three point bend specimens have also been achieved using out-of-plane angled cracks (Pook, 1985A; 1985B; Yates and Miller, 1989; Lazarus et al., 2001B; Lai, 2002; Buchholz et al., 2004; Lazarus et al., 2008; Lin et al., 2010; Cambonie and Lazarus, 2014). This has been the most popular mode I-III test method.

Facets in edge-cracked plate specimens are reported by many authors (e.g. Cooke and Pollard, 1996; Lazarus et al., 2001B; Lai, 2002; Buchholz et al., 2004; Lin et al., 2010). Additionally, Cooke and Pollard (1996), Buchholz et al. (2004), and Lin et al. (2010) report that the echelon cracks they see are oriented in agreement with the MPTS criterion. However, although there is a fair amount of scatter, it appears that the MPTS criterion may be somewhat over-predicting facet orientation angles in these works. Yates and Miller (1989) take the additional step of assuming an uncertainty in their mode mixity measurement to account for variability in the crack front shape and smoothness, and find very good agreement between their facet orientations and the MPTS criterion, although as noted previously, they used a plane stress formulation of MPTS. Interestingly, Liu et al. (2004) also see good agreement between their facet orientations and the plane stress formulation of MPTS, while they show that the more common plane strain formulation of MPTS slightly over-predicts facet orientation angles. Pons

and Karma (2010) show that their continuum phase field simulations predict facet orientations closer to the experimental results of Cooke and Pollard (1996) and Yates and Miller (1989) than does the MPTS criterion. However, their methodology requires the assumption of both a specific “instability wavelength” and a specific $G/G_c > 1$ in order to predict facet angles, so there is some uncertainty in application of this method.

As described previously, Lin et al. (2010) formulated an energy equation to predict segmentation spacing based on facet orientation angle and measured echelon crack lengths. They measure the length and orientation of a large number of echelon cracks, and apply a best-fit line based on the form of their equation. From this analysis they extract the segmentation spacing and “energy penalty” associated with structures that bridge the echelon cracks. They find the segmentation spacing to be about 200 μm , which they note is on the order of the size of the fracture process zone for their material. However, they neglect to experimentally measure segmentation spacing, and so it is not possible to know how good their prediction is. It is important to note that this technique, in its current form, cannot be used to predict segmentation spacing based on loading and geometry alone. That is, it depends on post-experiment measurements of fracture surface features. Still, this represents the first attempt to predict segmentation spacing from a theoretical basis, and so is significant in that respect.

In experiments, crack front rotation is usually observed until the front is perpendicular to the MPTS direction (Pook, 1985A; Buchholz et al., 2004; Lazarus et al., 2008; Cambonie and Lazarus, 2014), that is, until it is oriented to eliminate the mode III component of loading. Further, Cambonie and Lazarus (2014) find the rate of rotation ($d\theta/dx$) from the initial crack configuration to the final MPTS configuration to be constant. Lazarus et al. (2008) conducted a set of experiments studying crack front rotation. They find that both their local plane stress and

plane strain MPTS criteria are fairly good at predicting crack front rotation when the rotation angle is measured from the free surface, but are poor at predicting crack front rotation angle when it is measured in the interior of the specimen. That is, they found that the amount of crack front rotation was not uniform across the width, and was larger at the specimen edges. Their global maximum G and maximum K criteria were much better at predicting the crack front rotation. They reported errors of less than 5% for specimens with initial edge-cracks oriented at 75° and 60°, and 20% error for specimens with initial edge-cracks oriented at 45° (this larger error is attributed to ignoring an increasingly significant K_{II} component).

Lai (2002) studied fracture surface evolution. He found that fractures initiated as a series of needle-like crazes visible immediately ahead of the crack front. These evolved and transformed into microcracks which bisected the main crack at a certain angle. As these microcracks grew into an array of echelon cracks and propagated along the specimen axis, the fracture surfaces were seen to coarsen until a single mode I macro-crack was present. Coarsening with crack propagation is seen by a number of authors (Cooke and Pollard, 1996; Lai, 2002; Lazarus et al., 2008; Lin et al., 2010; Cambonie and Lazarus, 2014), and is a common feature of fracture surface evolution. The only theory proposed with respect to fracture surface evolution was that the rate of coarsening would depend on the mode ratio, and Cambonie and Lazarus (2014) observed that the rate of coarsening increased with increasing K_{III}/K_I .

2.4.3.3. Geometry of Goldstein and Osipenko

Goldstein and Osipenko (2012A; 2012B) developed a mode I-III geometry that was similar to their mode III geometry, although instead of a pair of straight cracks, the cracks are canted 10-15° to achieve either superposed anti-plane shear-tension or anti-plane shear-

compression. Goldstein and Osipenko (2012A; 2012B) have conducted only a limited amount of work with their geometry. However, Pham and Ravi-Chandar (2014) developed a test that was a variation of Goldstein and Osipenko (2012A)'s. Here, rather than a canted crack of uniform depth which spanned the entire specimen width, Pham and Ravi-Chandar (2014) used parabolic cracks which did not extend to the specimen edges. This geometry was specifically designed to result in a variable mode ratio across the crack width, and they conducted extensive FE analysis to determine their local mode mixity.

In addition to studying the general behaviors of crack growth under mode I-III loading, Pham and Ravi-Chandar (2014) specifically developed their test to investigate the claim by Sommer (1969) that crack front segmentation would not occur below a critical K_{III}/K_I threshold. The crack front of their test geometry had a variable mode mixity, and at one location was $K_{III}/K_I = 0$. Upon fractographic examination, they found that crack front segmentation occurred across the entire width as soon as $K_{III}/K_I > 0$. From this they conclude, in agreement with many author's predictions, that segmentation occurs when any amount of mode III is present.

In addition to determining that crack front segmentation will occur with any amount of mode III component, Pham and Ravi-Chandar (2014) also studied fracture surface evolution in their specimen. They found that segmentation spacing occurred at several different length scales. Using an optical microscope, the visible echelon cracks were observed to initiate at the crack front with both a length and spacing on the order of two thicknesses of the machined notch ($\sim 200 \mu\text{m}$). From there, of course, they grew and coarsened as the crack propagated. However, using higher power magnification, it was shown that there was a series of even smaller and more closely spaced echelon cracks at the crack front which were on the scale of the groove lines created from the cutting particles bonded to the saw that cut the notch ($\sim 10 \mu\text{m}$). A third order,

smaller and more closely spaced still, of facets were seen at the crack front using a scanning electron microscope, and these were on the order of the “natural crack front” size ($\sim 0.5 \mu\text{m}$). From these observations, Pham and Ravi-Chandar (2014) suggest that an intrinsic length scale for crack front segmentation does not exist, but rather is to be dictated by the material microstructure. This complicates our understanding of coarsening, as it shows that in real test specimens, several orders of echelon crack spacing can exist concurrently, and this type of interaction has not been theorized or dealt with before.

2.4.4. Summary

From this review of homogenous materials subjected to mode I-III loading, it is seen that the fracture process is a complex series of interacting events. As was seen in the review of homogenous materials subjected to mode III loading, fracture occurs through crack front segmentation. Under mode I-III loading it is also seen that crack front rotation also occurs during fracture surface.

Notable progress has been made towards developing predictive techniques for facet orientation and crack front rotation, although there are still a number of uncertainties. Theories for predicting segmentation spacing and echelon crack length are still relatively new, and a robust method that does not rely on experimentally measured fracture surface features has yet to be proposed. Further, the work of Pham and Ravi-Chandar (2014) has shown that segmentation will occur on multiple length scales, and that coarsening and the interaction between growing facets is not as simple as has previously been supposed.

2.5. Modeling of Anti-Plane Shear Fracture

2.5.1. Introduction

It will be found in this dissertation that the initial fracture events in laminated composite materials subjected to anti-plane shear loading are analogous to those described for homogenous materials in Section 2.3 and Section 2.4, although after the onset of planar delamination growth in composite laminates, the behavior differs. The final portion of this dissertation will be focused on the numerical modeling of the mechanisms leading up to planar delamination growth in composite laminates. Therefore, this section reviews the current state of analytical and computational modeling of homogenous materials subjected to mode III or mixed mode I-III loading. Historically, it has been assumed that pure planar delamination advance occurs in composite laminates subjected to mode III loading, and so there is no literature available studying the development of damage leading up to planar delamination growth. This review will therefore reflect modeling efforts in homogenous materials.

As discussed on Section 2.3 and Section 2.4, the first fracture events in homogenous laminates subjected to loading containing an anti-plane shear component is the segmentation of the original macro-crack front and the development of an array of echelon cracks. Efforts to model this behavior generally fall into one of two categories. The first category will be referred to as “perturbation methods.” Here, an arbitrary perturbation is applied to the crack front, and the resulting instability is used to characterize the echelon array development. The second category will be referred to as “discrete echelon crack models.” These models include a discrete echelon crack or cracks and examine the energetics of the system to draw inferences about echelon array development.

2.5.2. Perturbation Models

In perturbations models, a small displacement or rotational instability is used to represent inherent defects or deviations in the crack front shape, such that an echelon array can be predicted to grow. Investigations into perturbation analyses have been conducted with both analytical (e.g., Gao and Rice, 1986; Lazarus et al., 2001A; Leblond et al., 2011, Leblond and Lazarus, 2015) and numerical (e.g., Xu et al., 1994; Pons and Karma, 2010) models.

2.5.2.1. Analytical Instability Investigations

Gao and Rice (1986) performed possibly the first analyses of the effect of a perturbed crack front on shear stress intensity factors by considering the variation caused by a crack front which was slightly curved. From their analysis, Gao and Rice (1986) concluded that small deviations in crack front straightness could be the cause of segmentation in mixed mode I-III loading. Gao (1992), Amestoy and Leblond (1992), and Movchan et al. (1998) all expanded on the original work of Gao and Rice (1986) by performing more detailed calculations of the stress intensity factors for a perturbed crack front, and these papers have been used collectively as a basis for instability investigations.

The works of Lazarus et al. (2001A; 2001B) present a notable instability analysis for a locally perturbed crack front under arbitrary loading. The main focus of these works were the calculation of stress intensity factors on an infinitesimally rotated crack front, and the extraction of a predicted rate of global crack front rotation under mixed mode I-III loading. They are able to show reasonable agreement between their analytical predictions and experimental rates of crack front rotation (Lazarus et al., 2001B). However, their analysis is limited to thin plates, where only crack front rotation, and not segmentation, occurs. Thus, the analysis is not appropriate for modeling the general case of anti-plane shear fracture.

Leblond et al. (2011) conducted a linear stability analysis on a crack subjected to global mode I+III loading in order to predict when instability leading to crack front segmentation might occur. They used the findings of Gao and Rice (1986) as rationale to apply a small perturbation to the straightness and flatness of an initially planar crack front and derive the variations in stress intensity factor for the perturbed crack front. Perhaps unsurprisingly, Leblond et al. (2011) apply an elliptic helix perturbation to the crack front, and find that unstable crack growth occurs in an elliptic helix shape. While this result fairly well captures a factory roof crack front segmentation shape (Hourlier and Pineau, 1982), it seems most likely to be a result based on the assumed input perturbation. Additionally, Leblond et al. (2011) note that their analysis requires a “regularization” of the crack propagation criterion at short scales in order to predict initial segmentation spacing, as their results currently require an initial, finite instability wavelength to be input into the model representing initial segmentation spacing. Importantly, one of the main findings in Leblond et al. (2011) is that an instability leading to echelon crack formation occurs above some threshold of global K_{III}/K_I , although it is noted by Leblond and Lazarus (2015) that this threshold is not supported by experiments (Sommer, 1969; Pham and Ravi-Chandar, 2014). Leblond et al. (2011) theorizes that the discrepancy between their model and the experimental results may be due to a strong influence of initial imperfections at the crack front that are not accounted for in their perturbation model.

The recent work by Leblond and Lazarus (2015) also presents an analysis based on a perturbed crack front subjected to mode I-III, but considers the theorization of Leblond et al. (2011) that local imperfections may be causing the instability that results in crack front segmentation. To this end, Leblond and Lazarus (2015) represent local changes to the material's fracture toughness due to imperfections as a crack front displacement perturbation and calculate

the variation in stress intensity factors, as well as the directional stability of crack growth (Cotterell and Rice, 1988). Leblond and Lazarus (2015) find that for a local protrusion ahead of the crack front, the local mode II loading predicts a kink angle which would result in a typical Type A crack, while for a protrusion behind the crack front, the predicted kink angle would result in a typical Type B crack. Based on this, it can be concluded that initial echelon crack spacing would be based on local material imperfections and microstructure. These findings hold for any value of K_{III}/K_I , and thus better align with the experimental results of Sommer (1969) and Pham and Ravi-Chandar (2014) than any of the previous perturbation studies. This work represents perhaps the most promising perturbation model, as it is based on a minimal number of assumptions, and in particular, the conclusions are not dependent on the form of the assumed perturbation.

2.5.2.2. Numerical Instability Investigations

Numerical investigations have been conducted with both FE analysis (Xu et al., 1994) and a continuum phase field model (Pons and Karma, 2010). As in the analytical models, the numerical models assume an initial perturbation of the crack front, and develop the criteria for which crack growth becomes unstable.

Xu et al., (1994) develops an FE model with a finitely wavy three-dimensional crack front, representing a periodic perturbation. They show that the magnitude of crack waviness increases with each increment of growth, which represents some coarsening, for several ratios of K_{III}/K_I . However, the coarsening result is based on the initial assumed perturbation wavelength. Additionally, the echelon array (Type A) and its connecting structures (Type B) are treated

identically, which Lazarus et al. (2001A, 2001B) claims invalidates the results, and Movchan et al. (1998) note that there are other errors in the analysis.

Pons and Karma (2010) develop a numerical continuum phase field model (Karma et al., 2001) to study the development and growth of an array of echelon cracks. Here, the total energy in the materials is represented as a function of displacement, a phase variable representing fracture, and the strain energy density (Pons and Karma, 2010). A helical displacement perturbation is applied to a planar crack front, and a finite difference approach is used to automatically track the shape of the crack front as it develops. This approach is beneficial because it contains a self-consistent description of both linear elastic fracture mechanics-based failure (outside the process zone) and short-scale materials-based failure (inside the process zone).

Using the above method, Pons and Karma (2010) are able to show that the instability develops with a preferred wavelength, representing segmentation spacing, which coarsens with additional growth and is in agreement with experimental results (Cooke and Pollard, 1996; Lai, 2002; Lazarus et al., 2008; Lin et al., 2010; Cambonie and Lazarus, 2014). Pons and Karma (2010) also show that the Type A and Type B zones described by Hourlier and Pineau (1982) and Lazarus et al. (2001B) will develop, with Type A zones, which are energetically favored, leading ahead of the Type B zones.

The results of Pons and Karma (2010) represent the most experimentally consistent attempts at modeling echelon crack orientation and fracture surface evolution, however, there are several issues with this approach. Most significantly, the applied perturbation is not arbitrary. Pons and Karma (2010) are able to show Type A and Type B zones because they use a helical perturbation that implicitly results in Type A and Type B zones, not because their energy

equation favors the formation of Type A zones ahead of Type B zones. While the helical instability shape is consistent with Gao and Rice's (1986) argument that the crack front will protrude out of plane, it cannot be derived from continuum fracture mechanics (Pons and Karma, 2010). Therefore, one of their most significant results is dependent on their input assumption. A second issue with this approach is that the applied loading to propagate the instability must be higher than G_{crack} , the ERR necessary to drive planar crack growth, which does not represent a physically realistic scenario. The results of Pons and Karma (2010) are based on somewhat arbitrarily defined loadings of $G/G_{\text{crack}} = 1.25$ and 1.50 . Thus, while the continuum phase field approach of Pons and Karma (2010) does present remarkable correlation with experimental observations of echelon array development and growth in homogenous materials, it is too heavily based on assumptions for use in modeling the energetics of echelon array development.

2.5.3. Discrete Echelon Crack Models

In comparison to perturbation methods, discrete echelon crack models represent a relatively newer attempt at modeling echelon array formation and development. Therefore, the research in this area is still relatively immature. Echelon cracks have been modeled discretely using two methods: as a dipole approximation in an analytical model (Lai, 2002), and as an infinitely sharp crack in numerical analysis (Ressel and Theilig, 2012; Pham and Ravi-Chandar, 2014). In these approaches, an echelon crack is assumed to already have initiated at the front of a macro-crack, and the energetics of the system can be used to predict subsequent growth of both cracks.

Lai (2002) approximated a single echelon crack as a dipole in order to determine the effect an echelon crack has on a planar macro-crack. The extracted effect is only qualitative, as

the influence of the dipole on the macro-crack approaches zero as the dipole is located increasingly close to the macro-crack front. At some distance ahead of the macro-crack, he finds that the presence of the dipole increases the local values of K_I on the macro-crack front, which agreed with his experimental analyses of echelon crack growth under mode I-III loading. However, the dipole approximation does not represent the physics of the system, as it has no effect on the macro-crack SIFs when it is coincident with the macro-crack, as a real echelon crack would. Thus, while the results are certainly interesting, the dipole approximation does not represent a physically realistic model.

Perhaps a more promising approach than using a dipole approximation is to use a numerical method where an echelon crack is explicitly modeled as a dislocation between material elements. This has been done using a boundary element method (Pham and Ravi-Chandar, 2014) for mixed-mode I-III loading, and a finite element method (Ressel and Theilig, 2012) for pure mode III loading. Both of these models look at the effect of an echelon crack on the SIFs of a macro-crack, and Ressel and Theilig (2012) go a step further to evaluate the SIFs on the boundary of the echelon crack itself. Note that the work of Ressel and Theilig (2012) is a short communication, and does not provide enough details to evaluate the validity or accuracy of their work. However, it does provide conceptual proof that discrete echelon crack modeling may be possible using a finite element method.

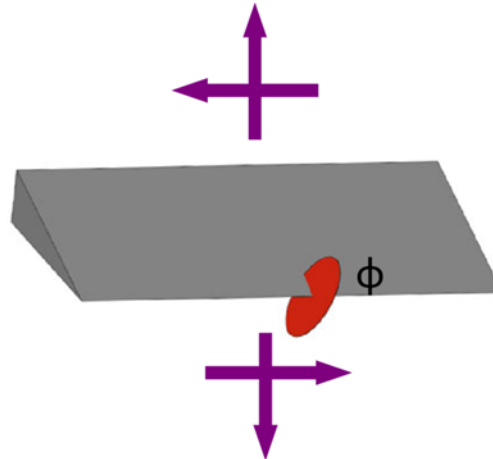


Figure 2.9. Boundary element model geometry of Pham and Ravi-Chandar (2014) showing a disk-shaped daughter crack intersecting a planar parent crack and subjected to mixed mode I-III loading.

Pham and Ravi-Chandar (2014) model an infinitesimally thick, planar “parent” macro-crack intersected by a three-dimensional disk-shaped “daughter crack” that included a semi-circular crack tip radius, as shown in Figure 2.9. They note that the shape of the daughter crack is not necessarily physically representative of an echelon crack, but was necessitated by limitations in the boundary element code. The daughter crack is canted at an angle ϕ predicted using an MPTS criterion such that its orientation is consistent with a given mode I-III ratio. The focus of their study was to determine the region over which the daughter crack “shields” the parent crack. That is, to determine the region over which the presence of the daughter crack results in elastic unloading and therefore altered SIFs on the parent crack front. It was found that, for global $K_{III}/K_I = 0.42$ and therefore $\phi = 35^\circ$, the parent crack is shielded over a distance of one to two daughter crack radii (Pham and Ravi-Chandar, 2014). In this shielded region, K_I decreases significantly, and even becomes negative very near the daughter crack, which may be an artifact of the boundary element model. As K_I decreases, K_{II} peaks near the daughter crack, and K_{III}

decreases, although always remains positive. Therefore, their model shows that the effect of a daughter crack is to reduce the global mode I-III loading on the parent crack as well as give rise to a local mode II component. While there are a number of assumptions in the model of Pham and Ravi-Chandar (2014), particularly with respect to the shape and orientation of the daughter crack, it appears to be a promising approach that could be applied to further modeling of echelon array development.

2.5.4. Summary

Many of the analytical instability analyses (Lazarus et al., 2001A; 2001B; Leblond et al., 2011; Leblond and Lazarus, 2015) find the conditions under which echelon cracks will grow, or show at what orientation growth will occur, but they are not able to handle the actual growth itself. The numerical instability methods (Xu et al., 1994; Pons and Karma, 2010) are able to track the progression of an echelon array, but they have a very strong dependence on the form of the assumed initial perturbation. Thus, while these works have been very useful in understanding what mechanisms may be leading to echelon array initiation, they are not appropriate for modeling echelon array development itself.

There has been only a limited amount of work aimed at modeling the energetics of an echelon crack or echelon array intersecting a macro-crack. The dipole approximation of Lai (2002) is not representative of a crack subjected to mode III loading, but a numerical model explicitly representing a parent crack and a daughter crack appears to be able to extract the appropriate mechanisms necessary for studying echelon array development. Therefore, a numerical model based on the approach of Pham and Ravi-Chandar (2014) appears to be the most promising for further investigation into the mechanisms that drive echelon array growth.

2.6. Conclusions of Literature Review

This chapter has reviewed the literature that is, and will be, relevant for research conducted as part of this dissertation. The literature concerning mode III toughness testing in laminated composites has been reviewed, and it has been found that there are significant issues with all presently proposed mode III toughness tests, particularly in that the mode III delamination toughness appears to depend on geometry. The behavior of homogenous materials subjected to mode III and mode I-III loading was also reviewed. The theories available to predict fracture surface features are discussed and, when available, compared to experimental results. Finally, the techniques to model growth under anti-plane shear loading have been reviewed, and a proposed method for modeling of echelon array development is proposed. With this background, it is now possible to appropriately lay out the approach that will be taken to achieve the goals of this dissertation.

Chapter 3. Objectives and Approach

3.1. Introduction

This dissertation focuses on understanding the effects anti-plane shear loading has on crack initiation and propagation in composite laminates. In this chapter the objectives of this dissertation are first presented. Subsequently, the experimental and modeling approaches taken to address the objectives are discussed. Finally, overviews of the different sections of this dissertation are given that include how each objective is achieved.

3.2. Objectives

The overall goal of this dissertation is to study crack growth mechanisms in composite laminates that are subjected to anti-plane shear (mode III) loading. Four objectives have been developed to accomplish this goal. The first is to develop an experimental technique that can be used to study anti-plane shear loading in composite laminates. The second objective is to determine the mechanisms associated with delamination advance under anti-plane shear loading. The third objective is to develop a model that will contribute to crack growth prediction capabilities with emphasis on the events associated with mode III initiation. The final objective is to apply the findings from the above to issues of delamination toughness assessment and growth prediction under mixed mode loadings where mode III is present. These objectives will be accomplished using both experiments and numerical modeling. The sections that follow outline the experimental and modeling approaches used.

3.3. Experimental Approach

3.3.1. Mode III Toughness Determination

In order to study the mechanisms associated with delamination advance under mode III loading, the first step in this work is to develop an alternative test method to determine the mode III toughness. To this end, a number of different fixtures and specimen geometries are studied using three different carbon/epoxy composite materials. Additionally, different data reduction methods are studied to determine the preferred method for mode III toughness calculations.

The fixtures studied are based on the mode-III STB test (Davidson and Sedlies, 2011), which was discussed as a promising test method in Section 2.2.5. Four different “baseline” configurations, which are derived from the mode-III STB specimen and fixture geometry, are created. FE analyses are used to show that all tests are essentially pure mode III tests, and are appropriate for mode III toughness determination. A single configuration is selected for subsequent study.

Studies are carried out on the baseline configurations to determine the most appropriate data reduction technique and determination of an appropriate measure of critical load. The VCCT and multi-specimen compliance calibration techniques are considered for data reduction techniques. The appropriate critical load for delamination growth is determined using a series of interrupted tests, where the specimen is removed and examined for evidence of growth. Subsequently, only a single critical load and data reduction technique are used to calculate the mode III delamination toughness.

3.3.2. Dependence of Toughness on Geometry

Studies examining the effect of geometry on toughness measurements are conducted using two of the baseline configurations. Toughness testing is carried out on specimens with varying widths, thicknesses, and delamination lengths. As will be shown in this dissertation, for both test configurations, toughness is dependent on specimen geometry. The apparent value of toughness is lower for specimens with longer delamination lengths, narrower widths, and smaller thicknesses.

In order to understand these phenomena, the mechanisms leading to delamination growth are studied using a single configuration. Specimens of several different thickness and delamination lengths are tested, and, as will be discussed subsequently, the mechanisms leading to crack growth are studied. It will be shown that the effects of specimen geometry, the method of remote load introduction, boundary conditions, and laminate architecture all affect the details of crack growth, and therefore result in an apparent dependence of toughness on specimen geometry.

3.3.3. Growth Mechanisms in Anti-Plane Shear Loading

The mechanisms causing and affecting crack growth under mode III loading will be determined, in part, by examining the fracture surfaces that are created. The fracture surfaces in the composite laminates will be compared to fracture surfaces of homogenous materials presented in the literature to aid in understanding the processes that ultimately lead to delamination growth.

The fracture surfaces of the composite laminates will be observed both destructively and non-destructively, as necessary. The non-destructive techniques, which are subsequently

discussed, are advantageous because they allow observation of fracture surfaces without compromising the specimen. Additionally, it is possible to obtain data at many locations. The destructive techniques, also subsequently discussed, can only be used to obtain data at a limited number of locations, but this data is of much higher resolution than can be obtained from the non-destructive techniques. Additionally, the destructive techniques are used to validate the non-destructive methods and results. The different techniques discussed are used to obtain either planar (i.e., x-y plane in Figure 2.8) or transverse (i.e., y-z plane in Figure 2.8) views of the fracture surfaces. In this way, a much fuller view of the fracture surfaces can be obtained than is possible using a single technique.

Non-destructive examinations will be conducted using two different techniques.

Ultrasonic scanning with time-of-flight data analysis will be used to view the shape and extent of planar delaminations. Conversely, transverse views of fracture surfaces will be generated using X-ray computed tomography (CT). While ultrasonic scanning is commonly used to observe delamination growth in composite laminates, X-ray CT is a much newer technique, and, in conjunction with collaborators, have been newly applied in this work.

Destructive examinations will also be conducted to obtain both planar and transverse views. Planar sectioning is a standard practice in the composites community. However, for mode III specimens, transverse sectioning practices have been newly developed, in conjunction with collaborators, as part of this work. Planar sectioning is achieved by fully delaminating a specimen along the plane of delamination growth and viewing the fractured surfaces under an optical microscope. For transverse views, cross sections are cut from the specimen, potted in epoxy, and polished to a high surface finish. These are also viewed using an optical microscope.

In this work, it is found that transverse sectioning is much more valuable of a tool for understanding crack growth mechanisms due to anti-plane shear loading.

In order to understand the mechanisms leading to growth under mode III loading, it is necessary to obtain data at multiple stages of crack growth. Thus, fracture surfaces will be evaluated using the above techniques at several different stages. These stages will consist of (1) tests stopped before the onset of planar delamination growth, (2) tests stopped shortly after the onset of planar delamination growth, and (3) tests stopped after the delamination has been allowed to grow an extended amount. Studying these three stages allows for the observation of crack growth from initiation through extended propagation.

3.4. Modeling Approach

In order to understand and predict crack growth in composite laminates subjected to mode III loading it is necessary to be able to accurately model the development of fracture surfaces. Once crack growth under mode III loading is understood, it can be applied to growth predictions for general loadings, which is in line with the last two objectives of this dissertation. Thus, this section first lays out general delamination growth prediction methodologies. Once the overall modeling need has been framed, the specific modeling approach taken in this dissertation can be seen in its proper context, and is subsequently discussed.

3.4.1. Delamination Growth Prediction Methodology

As will be shown in this dissertation, crack growth under loadings that include a mode III component is a very complex phenomenon. The fracture surface evolution under mode III loading is significantly more complicated than for mode I-II loading. Crack growth under modes

I-II is relatively straightforward, and the crack tends to grow along a single, primary path. There are several proposed techniques for predicting how mode I-II cracks grow along a primary path, where both interlaminar and intralaminar delamination may occur. Pernice et al. (2015) use a maximum principal tensile stress criterion and an additional criterion that accounts for constraints due to fiber architecture. Canturri et al. (2014) uses a criterion which determines the energy release rate parallel and perpendicular to the fibers. Both these techniques use a classical energy release rate criterion to determine growth. While these techniques are still in development, they appear to be able to predict delamination growth under mode I-II loadings.

This dissertation will show that crack growth under mode III loading will almost always result in crack front segmentation and breakdown of the primary path. This is conceptually similar to the behavior of homogenous materials under mode III or mode I-III loading discussed in Sections 2.3 – 2.4, where an array of echelon cracks initiates at the original crack front. A delamination growth prediction methodology for mode III loading, then, requires the ability to predict both the initiation of echelon cracking as well as subsequent fracture surface development and evolution. Echelon initiation prediction would include criteria for initiation, echelon orientation, the spacing between echelon cracks, and the length of echelon cracks. Fracture surface evolution prediction would require criteria for the interaction between echelon cracks, growth of bridging structures, effects of the weak interlaminar interface in composite laminates, and constraint due to fiber architecture.

In order to develop a rigorous delamination growth prediction methodology for composite laminates subjected to general mode I-II-III loading, all of the above must be understood. The work in this dissertation will contribute to the above by studying the initial development of an echelon array under mode III loading. Understanding the initial echelon crack

development is a necessary first step that must be carried out before crack propagation and evolution under loadings that contain a mode III component may be studied.

3.4.2. Discrete Modeling of Echelon Cracks

In order to understand echelon array development under mode III loading, numerical modeling will be conducted using discretely modeled echelon cracks at the delamination front of a plate-like, homogenous, orthotropic material. This technique was discussed in Section 2.5.3, and was found to be a promising method to capture the energetics behind echelon array development.

First, a FE model is developed with the necessary loading and geometry to impose essentially pure mode III conditions along a planar delamination front. The behavior of a single echelon crack at the front of a planar delamination is initially considered. The virtual crack closure technique is used to extract the energy release rates on the echelon crack and the planar delamination in order to determine the energetics that drive crack growth. Different size and geometry echelon cracks are modeled to understand how a single echelon crack develops. Rather than modeling the actual crack growth, quasi-static analyses will be conducted and the ERRs will be used to predict the next stage of growth, which will then be modeled. In this way, the development of an echelon crack will be modeled by a series of “snapshots” at different stages of growth.

Subsequent to the modeling of a single echelon crack, multiple echelon cracks representing an array will be modeled. The same technique of ERR extraction via VCCT and predictions for the next stages of growth as discussed above will be use with multiple echelon cracks. A select number of cases will be modeled to understand how multiple echelon cracks

may interact with each other. Finally, the combined results from the single echelon crack and multiple echelon cracks will be used to determine how an echelon array develops before the onset of planar delamination advance.

3.5. Dissertation Overview

The chapters in this dissertation can be grouped into four sections. The first section is comprised of the first three chapters and serves to set up the background and purpose of this dissertation. Chapter 1 provides an introduction. The current state of knowledge on mode III testing, in both composite and homogenous materials, and techniques to model growth under anti-plane shear loading are presented in Chapter 2. The objectives of this dissertation and an overview of what will be accomplished are discussed in Chapter 3.

The second section comprises Chapters 4-6, and covers the experimental work conducted for this dissertation. Chapter 4 covers the first objective of this dissertation: to develop an experimental technique that can be used to study anti-plane shear loading in composite laminates. In Chapter 4, several proposed methods for mode III delamination toughness testing are introduced and studied both computationally and experimentally. From this, a preferred test method is determined. This preferred method is then used in an investigation of the dependence of the apparent mode III toughness on geometry. It is found that the apparent toughness does depend on geometry, and that transverse matrix cracks initiate at the planar delamination front during the test. Chapter 5 studies how transverse matrix cracks grow, both prior to and subsequent to the onset of planar delamination advance. This provides detailed information on the evolution of fracture surfaces during mode III testing. Chapter 6 reconsiders the experiments presented in Chapters 4-5, and conducts additional tests where specimen twisting is measured.

From these tests, it is determined that the details of the fracture surface evolution and resultant apparent toughness dependency are highly dependent on the specimen geometry and boundary conditions. The second objective is therefore achieved in Chapters 5-6, i.e., the mechanisms associated with delamination advance under anti-plane shear loading are determined.

The third section comprises Chapters 7-8, and covers the third objective of this dissertation; the development of a model that will contribute to crack growth prediction capabilities by capturing initial mode III fracture events. As noted previously, this will be accomplished by developing a discrete echelon crack FE model. As discrete echelon crack models have not received extensive use in the literature, Chapter 7 presents the model formulation as well as a detailed series of model validation steps. This validation ensures that the actual modeling conducted subsequently is accurate. The modeling of echelon array development is then conducted in Chapter 8.

The final section consists of Chapter 9. A summary and conclusions from the experimental and numerical work conducted for this dissertation are first presented. Then, recommendations for further studies, considering both experiments and modeling, are discussed. In the final discussions of Chapters 9, as well as in the discussion sections of Chapters 5-8, the final objective of this dissertation is accomplished: both the experimental and computational findings are applied to issues of delamination toughness assessment and growth prediction under mixed-mode loading.

3.6. Conclusions

This chapter lays out the dissertation objectives, the approaches taken to achieve these objectives, and presents an overview of the rest of this dissertation. The overall goal of this

dissertation is to study the crack growth mechanisms in composite laminates subjected to anti-plane shear (mode III) loading. Experiments will be conducted to develop a technique to study anti-plane shear loading in composites and to determine the mechanisms associated with delamination advance. Numerical modeling will be used to capture initial mode III fracture events in order to contribute to crack growth prediction capabilities. Finally, the combination of experimental and numerical results will be applied to issues of delamination toughness assessment and growth prediction under mixed-mode loading.

Chapter 4. Delamination Toughness Testing: Experiments and Analysis

4.1. Introduction

As described in Section 3.3.1, developing a mode III toughness test method is the first step towards understanding the apparent dependency of toughness on geometry. This work introduces a simplified test fixture and loading that is based on the mode III shear-torsion-bending (STB) test. The STB was introduced for the determination of mixed-mode I-II-III delamination toughnesses (Davidson and Sediles, 2011). Figure 4.1a presents a schematic of this test when only mode III loading is applied. As described in Section 2.2.5, the STB utilizes a similar idea as the modified split cantilever beam (MSCB) test, but applies both the shear load and restoring torque using load tabs that are bonded to the specimen and which are constrained to enforce a zero slope condition at the specimen's cracked ends. The restoring torque is found to be less than that which is applied in the MSCB, but the energy release rate (ERR) distribution is still observed to be nearly pure mode III. The difficulty with using the STB, however, is that it requires a relatively complex fixture and loading arrangement.

A schematic of the simplified test fixture used herein is shown in Figure 4.1b, where the fixture has been modified for use in a uniaxial load frame by rotating the STB arrangement about its longitudinal axis. Further, as will be described subsequently, relatively minor modifications to the fixture and/or test specimen will produce three alternative mode III test configurations. Thus, a total of four split beam-type tests can be performed, and in that sense this new idea is well-

suited to investigate the potential geometry-dependence of the apparent mode III delamination toughness in laminated polymeric composites.

In this chapter, the four variations of new mode III tests are first introduced and then evaluated as possible test methods. To this end, the ERR distribution from each test, obtained from three dimensional finite element (FE) analysis are presented. Note that this FE analysis was conducted by Mr. Kiran Simon in parallel with the experiments conducted for this dissertation. The results of the FE analysis have been published in Johnston et al. (2014), and necessary results will be presented herein. The FE results show that each of these four “baseline configurations” are viable test methods. The four configurations are then evaluated experimentally using specimens with the same delamination length. For each configuration, two different unidirectional carbon/epoxy materials are considered. Tests of these two materials in the four baseline configurations are conducted and the results compared to assess any potential geometric dependencies. The experimental results are then used in conjunction with those from the FE analysis to select a single “preferred test geometry.” Finally, this preferred geometry is used to evaluate any potential effects of delamination length on the apparent toughness.

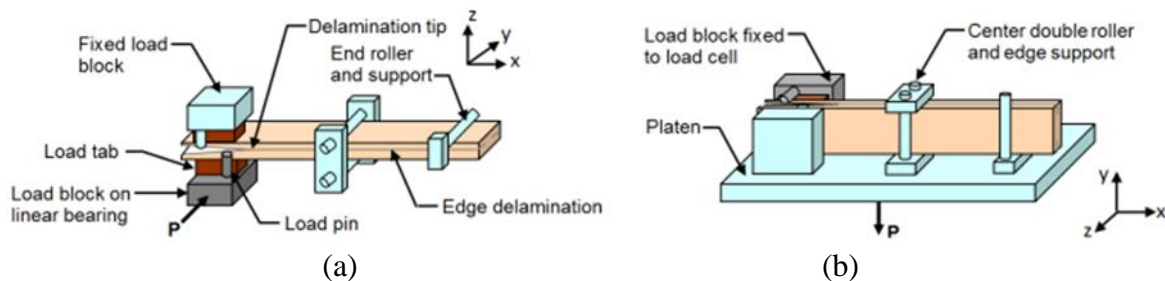


Figure 4.1. Mode III STB test. (a) Original orientation, (b) rotated 90° about x-axes.

4.2. Test and Specimen Design

Figure 4.1 presents a schematic representation of the mode III STB test shown in two orientations. As indicated in Figure 4.1, the loading on the specimen was introduced via load blocks, load pins, and load tabs at the delaminated end, along with a center double roller and edge support, and an end roller and edge support. Each load block and load pin assembly is an integral unit and contains two load pins that are arranged diagonally. One of the load pins acts on one edge of the specimen near the delamination tip (evident in the lower load block in Figure 4.1a), and the other acts on the opposite edge closer to the delaminated end (evident in the upper load block in Figure 4.1a).

Figure 4.1b represents the simplified fixture used in this work. Here, the back (negative z) load block and load pin assembly shown in Figure 4.1b is directly threaded into the load cell, which is located in the top portion of a uniaxial load frame. The front (positive z) load block and pin assembly that is shown in Figure 4.1b attaches to a platen that is threaded into the actuator. The z -direction location of this front load block is adjustable. This is achieved via a slotted connection to the platen and allows specimens of various thicknesses to be accommodated. The center and end roller and support assemblies also attach to the platen and are adjustable in both the specimen's width and thickness directions. Downward, or tensile direction movement of the actuator in Figure 4.1b corresponds to the loading shown in Figure 4.1a. Note that in the original STB (Figure 4.1a), only one load block was forced to translate and all other components were fixed, whereas in the implementation herein, that load block is fixed and all other components are forced to translate. However, it is clear that the two approaches produce the same loading on the specimen.

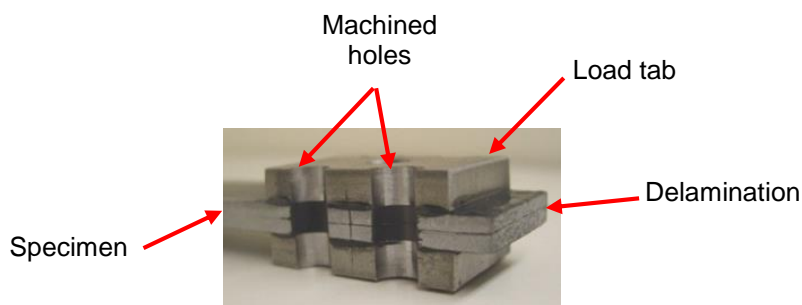


Figure 4.2. Specimen with load tabs.

Following Davidson and Sediles (2011), all specimens used in this work were 25 mm wide. The load tabs were also identical to those used in this earlier work, and appear as shown in the photograph in Figure 4.2. The load tabs are 38 mm long x 25 mm wide x 6.3 mm thick. They are bonded to the specimen using Hysol EA 9309.3 NA adhesive, which is a two-part epoxy containing 0.13 mm diameter glass beads to enforce a consistent and uniform thickness bond line. An 8 mm diameter threaded hole is in the center of the load tab. A bolt may be run through the center of the load block to attach to the load tab. This feature was instituted in the original STB specimens to accommodate the mode I loading and is retained here for possible use. The load pins mate to machined semicircular holes in the load tabs and extend through the tabs to nearly the plane of the delamination.

The nomenclature for the STB test is presented in Figure 4.3a. Here and subsequently, the term “STB” will be used to denote “mode III STB” as applied in a uniaxial load frame. The delamination in Figure 4.3a consists of a Teflon insert at the specimen’s mid-plane that spans the full width of the specimen. All specimens considered are unidirectional with their fibers oriented in the x-direction. The delamination length, a , is defined from the midpoint between load pins to the delamination tip. This datum point for delamination length is also used to define the half-span length, L , as shown. The specimen’s width is denoted by B and the thickness by $2h$.

Figure 4.3b shows a plan view of a specimen containing preimplanted edge delaminations (EDs). The EDs extend a distance βB into the specimen, such that the width of the delamination front that advances during the test is $W = B(1-2\beta)$. In the absence of EDs, the traction free boundary conditions on the edge surfaces of the specimen require that the mode III ERR, G_{III} , goes to zero. This further requires that significant mode II stresses and an accompanying mode II ERR, G_{II} , arise near the free edges to enforce equilibrium. That is, there is an intrinsic coupling of mode II and mode III at a free edge under anti-plane shear loading (Bažant and Estenssoro, 1979; Nakamura and Parks, 1989; Dhondt et al., 2001; Buchholz et al., 2004). Davidson and Sediles (2011) addressed this in the original STB by introducing EDs. They studied the effect of the non-dimensional edge delamination length, β , on the ERR distributions and showed that choosing $\beta = 1/16$ provides an essentially uniform distribution of G_{III} across the specimen's width and produces reasonably small local and average values of G_{II} . Further, mode III fracture tests resulted in simultaneous advance of the delamination across the full width for these types of specimens. For this reason, specimens containing preimplanted EDs were also considered herein. However, the EDs significantly complicate specimen fabrication, and it is unclear whether the intrinsic coupling of the mode II and III components near the free edge of a specimen without EDs affect a region that is sufficiently large to prevent obtaining accurate values of G_{IIIc} . This is one issue addressed in the study that follows. To this end, specimens with and without EDs represent the two permutations of the STB test to be evaluated. All specimens containing EDs appeared as shown in Figure 4.1a and Figure 4.3b, and used $\beta = 1/16$. This was achieved by using an appropriate template for the preimplanted Teflon insert during specimen manufacture. Specimens without EDs were similar, but there was no preimplanted Teflon insert to the right of the delamination tip, as in the specimen of Figure 4.3a.

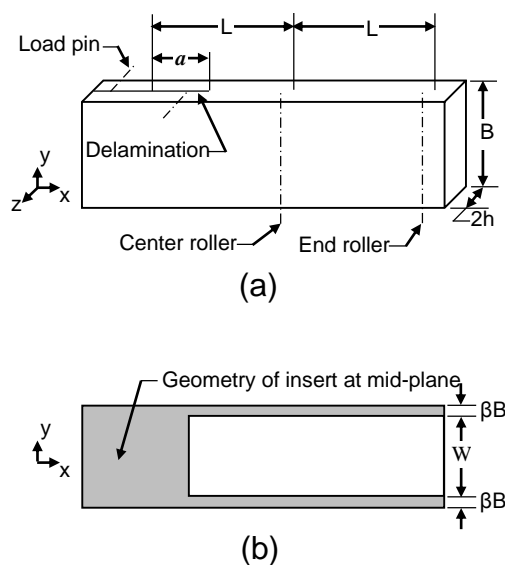


Figure 4.3. (a) Nomenclature and (b) edge delamination geometry.

The geometries described above are attractive because the work performed by Davidson and Sediles (2011) on the original STB can be directly transferred. However, a simpler test would be to eliminate the fixture mid-span and end supports. This test configuration can readily be visualized using Figure 4.1b. This results in a fixture that is similar to the MSCB test, in the sense that it consists solely of a split beam geometry with a shear load and restoring torque applied to the delaminated regions (Sharif et al., 1995; Cicci et al., 1995; Trakas and Kortschot, 1997; Szekrényes, 2009; 2011). However, the method of load introduction is different and perhaps somewhat simpler. Also, FE results indicate that the restoring torque that is produced by the load blocks in order to maintain the zero slope condition is less than the torque that is applied in the MSCB (Davidson and Sediles, 2011). In what follows, this configuration will be referred to as a split shear torsion (SST) test. In addition to its increased simplicity, the SST geometry allows thinner specimens to be tested in comparison to the MSCB, and more flexibility in the choice of delamination length, a , in comparison to the STB. As in the case of the STB, SST geometries will be considered with and without EDs. Thus, the four baseline configurations

evaluated consist of STB tests with edge delaminations (ED) and without edge delaminations (NE), subsequently referred to as STB ED and STB NE tests respectively, and SST tests with and without edge delaminations, referred to as SST ED and SST NE tests.

4.3. Finite Element Modeling

A FE model was developed for use in conjunction with this work, and is presented in Johnston et al. (2014), however the development itself was not part of this dissertation. The FE model is, however, integral to analyzing, understanding, and interpreting the experimental delamination toughness test data. For this reason, necessary results from Johnston et al. (2014) are presented herein.

4.3.1. Overview

All FE modeling in Johnston et al. (2014) was performed using Abaqus Version 6.8. All models were similar to the original three dimensional model developed and validated for analysis of the STB test (Davidson and Sediles, 2011). This earlier work described an extensive series of mesh refinement and validation studies that were performed before the model was applied to the original three dimensional STB configuration. Therefore, as a starting point, a model of the STB specimen was initially developed and constrained in accordance with the descriptions in their work. Energy release rate components were computed by the virtual crack closure technique (VCCT) (Rybicki and Kanninen, 1977; Krueger, 2004). For all cases considered, the average ERRs obtained by Johnston et al. (2014) were within 1% of those given by Davidson and Sediles (2011), and the graphical distributions of the ERR and its individual components were essentially indistinguishable.

Following the above, the appropriate changes to the boundary conditions were first made. That is, the original STB configuration included pivot points exterior to the load tabs in order to allow rotations about the y-axis (cf. Figure 4.1). This was necessary to facilitate the mode I loading, but is not present in the mode III STB studied herein and was therefore removed. Next, a new and improved mesh was developed in the vicinity of the loading tabs, and additional mesh refinement studies were performed in order to select the final model used for the evaluations discussed herein.

4.3.2. Mesh and Boundary Conditions

Figure 4.4 presents a FE mesh that is typical of all models used in Johnston et al. (2014). As in Davidson and Sediles (2011), all load tabs utilize the same isotropic material properties (Young's modulus, $E = 209$ GPa, Poisson's ratio, $\nu = 0.3$) and nominal dimensions as the steel load tabs used in the experiments. Based on measurements from physical test specimens, the epoxy bond-line thickness between the load tabs and the specimen was modeled as 0.15 mm, with isotropic material properties ($E = 2.2$ GPa, $\nu = 0.4$) as taken from the manufacturer's data sheet (Henkel, 2015). In comparison to the models of Davidson and Sediles (2011), the primary difference is the mesh in the tabbed region, which agrees with the physical geometry of the test specimens, as well as the way that the load pins are modeled. As indicated in Figure 4.4, each load pin extends through the thickness of the load tab, adhesive, and one of the cracked regions and connects to the corresponding nodes of the specimen and load tab along the inner curved surface. Each load pin is modeled as a rigid rod with a reference point, i.e., the point about which it can potentially rotate, at its own geometric center.

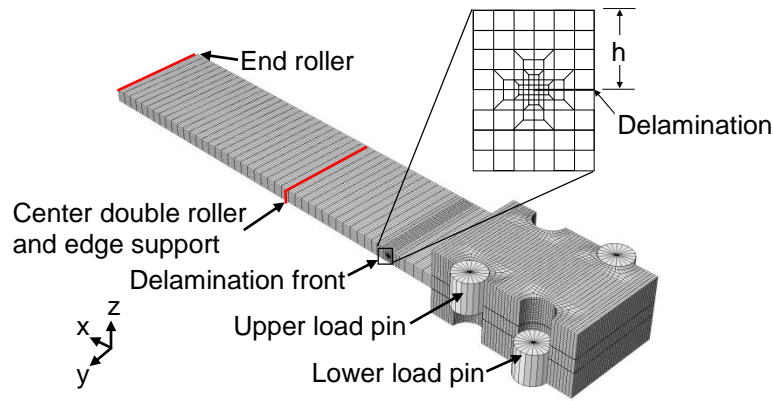


Figure 4.4. FE model of STB test with inset view of near-tip mesh.

For simplicity, the loading of Figure 4.1a is modeled. That is, one load block assembly is forced to translate in the y -direction and all other constraint locations are fixed with respect to y -direction translations. Thus, load is applied by imposing equal positive values of u_y onto the two lower load pins and by constraining $u_y = 0$ for the upper load pins. The x -direction displacements of all pins are fully constrained, and u_z and all rotations of the pins are unconstrained. In the above, u_y and u_z represent translational displacements in the y and z directions, respectively.

In addition to the above, and in order to simulate the constraints that the loading blocks impose on the load tabs, rigid surfaces are attached to all nodes that define the outer surface of each load tab. The reference point for each rigid surface is at its geometric center. The rigid surfaces impose the constraints that the outer surfaces of the load tabs cannot translate in the z -direction nor rotate about the x - or y -axes ($\theta_x = \theta_y = 0$). Translations in the x - and y -directions are coupled to those of the load pins, and rotations about the z -axis are not constrained.

When the STB configuration is modeled, as shown in Figure 4.4, the end support and the center double roller and edge support (cf. Figure 4.1) are included via rigid rods attached to the corresponding nodes. Here, the horizontal rollers impose $u_z = \theta_x = 0$, and the vertical edge

supports impose $u_y = 0$. For the SST, these constraints are not used. In all cases, the near-tip mesh appears as shown in the insert of Figure 4.4 and is based on the original mesh refinement studies conducted by Davidson and Sediles (2011).

4.3.3. Mesh Refinement Studies

In order to develop and validate the mesh described above, Johnston et al. (2014) performed mesh refinement studies using the material properties of either IM7/977-3 or T800S/3900-2B unidirectional carbon/epoxy, which are the two materials that are considered in the baseline experimental investigations. Material properties are presented in Table 4.1. Here, the values of the longitudinal modulus (E_{11}) and in-plane shear modulus (G_{12}) come from experiments performed at the Syracuse University Composite Materials Laboratory (SU-CML), as they are the two properties to which the ERR is most sensitive (Davidson and Sediles, 2011). For T800S/3900-2B, the remaining properties were obtained from Davidson et al. (2007). For IM7/977-3, the remaining properties were obtained from Gregory and Spearing (2006), the supplier's data sheet (Cytec, 2012), and the assumption of transverse isotropy.

Two separate mesh refinement studies were conducted to establish meshing across the specimen's width and along its length. To investigate the former issue, meshes were considered that contained from 48 to 92 constant-width elements across the specimen's width. A difference of approximately 1% in average ERRs was observed between these two extremes. The results of the 48-element model were also indistinguishable from those obtained from the variable-width element model that was developed to agree with the modeling approach of Davidson and Sediles (2011), described above. Thus, due to the simplicity and accuracy of the approach, all models were meshed in the y-direction with 48 constant width elements.

Table 4.1. Material properties (moduli in GPa).

Material	E_{11}	E_{22}	E_{33}	G_{12}	G_{13}	G_{23}	ν_{12}	ν_{13}	ν_{23}
IM7/977-3	163.8	8.34	8.34	4.95	4.95	2.98	0.27	0.27	0.40
T800S/3900-2B	147.6	7.58	7.58	4.31	4.31	2.87	0.32	0.32	0.32

The lengthwise, or x-direction meshing of all models was as shown in Figure 4.4. Considering the delamination plane in the cracked regions, the element length gradually transitions from $h/16$ at the delamination tip to approximately $1.4h$ at the load tab, where h is the thickness of one of the cracked regions. A similar variation in element length is used in the uncracked region. To study refinement in this direction, Johnston et al. (2014) created a new model where this x-direction mesh density was doubled. Differences in ERRs of less than 0.5% were observed, so the mesh of Figure 4.4 was retained. For SST models with delamination lengths greater than 32 mm, more of the longest elements (e.g., next to the load tab) were included, with an element length never exceeding $1.5h$.

4.4. Experimental Overview

4.4.1. Materials and Manufacturing Procedures

The experimental portion of this study primarily utilized 26-ply IM7/977-3 and 18-ply T800S/3900-2B test specimens. These were chosen based on the results in Davidson and Sediles (2011), and produced specimens of both materials that were nominally 3.3 mm thick. A limited number of 32-ply IM7/977-3 specimens were also fabricated and used for exploratory testing. All test specimens were fabricated at the SU-CML using an autoclave and the manufacturer's recommended cure cycle.

As described above, specimens were fabricated with and without EDs, and with a variety of preimplanted insert lengths. All specimens that contained EDs were tested with a delamination length of 32 mm. These were generally fabricated following the procedure described in Davidson and Sediles (2011). Here, a 12.7 μm Teflon template is cut and placed at the mid-plane of a 330 mm long (fiber direction) x 305 mm wide plate during manufacture. The template is such that it will produce 10 specimens containing starter delaminations and EDs. Following plate manufacture, a sequential c-scanning and cutting procedure is performed to obtain the specimens, each of which is nominally 25 mm wide with $\beta = 1/16$. For NE specimens, manufacture is simpler and only requires that a rectangular 12.7 μm Teflon insert of the desired length be placed at the mid-plane during plate fabrication. These plates produced 20 NE specimens with $B = 25$ mm. A Teflon template was also created such the 5 ED and 10 NE specimens could be obtained from the same plate. As described subsequently, this allowed toughness results from ED and NE specimens from the same plate to be compared, thereby eliminating any possible effect of plate-to-plate property variations.

After final cutting, all specimens are c-scanned to locate the distance from their delaminated end to the end of the Teflon insert. An alignment jig is then used to bond rectangular (non-machined) low-carbon steel load tabs to the specimen at a location that will result in the desired delamination length. Four semi-circular cut-outs are then machined through the tabs and specimen to create the configuration of Figure 4.2. Specimens are compressed through their thickness to prevent delamination growth during machining. Following the above, specimens are again c-scanned to obtain a pre-test scan that contains the tab, and therefore to which post-test c-scans can most accurately be compared.

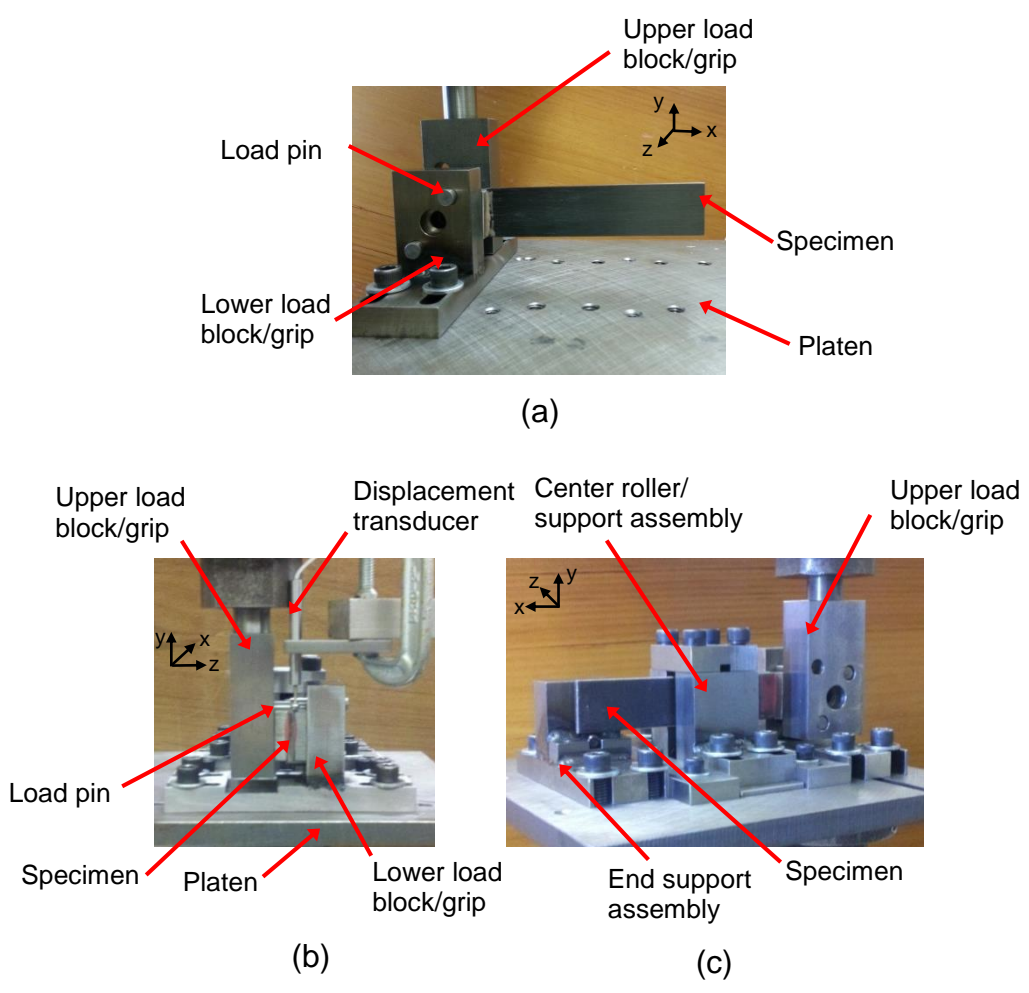


Figure 4.5. Test fixture setup. (a) SST front view, (b) side view, (c) STB back view.

4.4.2. Fixture Design

Photographs of the SST and STB fixtures are presented in Figure 4.5. Figure 4.5a presents a front view of the SST fixture containing a specimen. A small amount of the (pink) adhesive used to bond the load tabs is evident just outside of the gripping arrangement. The tabbed specimen is sandwiched in-between two load block/grip assemblies. These are integral units, each of which contains two load pins and a backing plate that presses against the outer surface of the load tab. The upper assembly connects to the load cell and remains stationary

during testing. The lower assembly is mounted to a platen that connects to the actuator and is displaced downwards during the test. As shown in the figure, this lower load block/grip assembly is bolted to the platen through slots. This allows it to slide during specimen installation and thereby to accommodate specimens of different thicknesses.

Figure 4.5b shows the view looking from the left side of Figure 4.5a, and is identical for both the SST and STB tests. A displacement transducer is evident in this figure and is utilized to measure the movement of the delaminated region outside of the grips for both tests. The displacements measured by this transducer were found to be essentially the same as those from the actuator, indicating the desired zero slope boundary conditions were maintained for all specimens tested. Thus, in what follows, all displacement measurements are as obtained from the actuator.

Figure 4.5c shows the back view of the STB fixture. The upper load block/grip assembly and its attachment to the load cell adapter are visible in the right of the figure. The lower load block/grip assembly is behind this and attaches to the platen. As is evident from a comparison of this figure to Figure 4.5a, the STB fixture is obtained by bolting a center roller/support assembly and an end support assembly to the configuration shown in Figure 4.5a. Both of these assemblies bolt to the platen through slotted holes in order to allow specimens with different thicknesses to be tested. The top of the center roller/support assembly is a separate piece that is bolted onto the two sides of the center roller support and which contains the center edge support, comprised of a captive 6.4 mm diameter steel rod. The edge support at the end of the specimen is also a 6.4 mm diameter rod and is visible in Figure 4.5c near the lower left corner of the specimen. As described previously, when the actuator is lowered, the lower block/grip assembly, the center roller/support assembly and the end support assembly all displace downwards uniformly.

4.4.3. Test Procedures

The procedures to install tabbed specimens into the grips are similar for all configurations and were developed to maximize reproducibility. A specimen is initially placed into the upper grip. The load tabs are aligned with the tab cut-outs and the tab is lightly pressed against the backing plate. The lower (platen-mounted) grip is then slid into place until its load pins mate with the cut-outs and the backing plate contacts the tab. Here, we endeavor to ensure that no gaps are observable between either load tab and its associated backing plate and that there is little or no through-thickness compression acting on the delaminated region. For SST tests, this completes the procedure. For STB tests, the center double rollers are then adjusted to contact the specimen and are bolted into place. Next, the specimen is preloaded to approximately 1000 N, at which time the center edge support is aligned to be perpendicular to the specimen, but not yet secured. This alignment is performed under load to eliminate any movement of the specimen. The specimen is then unloaded and the support tightened into place. The height of the edge roller at the end of the specimen is then adjusted via shims to contact the lower edge, and the end roller that contacts the specimen along its width direction is slid and bolted into place such that light contact is maintained.

All tests were performed under displacement control at a loading rate of 2.0 mm/min for loading and 3.8 mm/min for unloading. After testing, c-scans were again performed to assess whether the delamination front advanced in its entirety and, in those instances where growth did not occur along the entire delamination front, to ascertain where advance occurred. Post-test destructive assessments were also conducted to measure the preimplanted Teflon insert size and therefore to validate or correct the pre-test delamination length measurement and, for specimens with edge delaminations, to measure the actual edge delamination width.

4.4.4. Material Property Determination

As discussed in Davidson and Sediles (2011), Johnston et al. (2014), and subsequently, the accuracy of the data reduction approach will be quite sensitive to the accuracy in material property determination; in particular, to the values of E_{11} and G_{12} . Therefore, similar to the approach used in Davidson and Sediles (2011), two specimens were cut from the non-delaminated portions of each plate that was manufactured. These specimens were used to determine E_{11} in accordance with ASTM D3039 (2014) and using the procedure given in Appendix A. Relatively tight distributions were obtained, with coefficients of variation (CVs) on the order of 2% for specimens taken from all plates manufactured from a given material. Testing to determine G_{12} was conducted according to ASTM D5379 (2012) and using the procedure given in Appendix B. Here, v-notched beam specimens were cut from an additional plate fabricated specifically for the purpose of determining G_{12} . Shear modulus testing produced distributions with CVs on the order of 6% for each material. The experimentally determined values for these two properties correspond to those listed in Table 4.1 for both IM7/977-3 and T800S/3900-2B, and were used in the reduction of all data.

4.5. Evaluation of Baseline Configurations

4.5.1. FE Analyses for Baseline Configurations

Total ERR distributions for the four configurations as determined by FEA (Johnston et al., 2014) are presented in Figure 4.6a for an IM7/977-3 specimen. For all plots in Figure 4.6, the NE geometries show ERR distributions from $y/B = 0$ to 1 and the ED geometries show results for $y/B = 1/16$ to $15/16$, i.e., for the region of the specimen that will delaminate (cf. Figure 4.3). Each result in Figure 4.6a is for an applied load (P) of 1500 N. To achieve this, models were run

with a small applied displacement (u_y) as described previously, and the proportionality of G to P^2 was used to scale the results appropriately. At the same load, note that the distribution of ERR in the STB ED and SST ED is essentially the same, as are the G distributions for the STB NE and SST NE. However, the magnitudes are quite a bit higher for the SST configurations. This is because approximately $1/3$ of the applied load in the STB is reacted out by the center edge support, i.e., the reaction on the constrained leg ($u_y = 0$) is approximately $2/3$ of the applied load. This does not occur in the SST, where the applied and reaction loads are identical, and therefore more load transfer across the delamination plane occurs in the vicinity of the delamination front for this test. This implies that for any given specimen, i.e., for a specific specimen geometry and choice of β , delamination advance will occur at a lower load in the SST than in the STB configuration.

Figure 4.6b and Figure 4.6c present the normalized G_{III} and G_{II} distributions, respectively, where normalization is with respect to G_{avg} for that particular specimen. Here and subsequently, the term “average” applied to G or to any ERR component is used to denote results for the specimen’s full width (Davidson and Sediles, 2011). From this normalization, it may be observed that the ERR mode distributions in the STB and SST are essentially identical for the same specimen geometry (ED or NE). Further, Figure 4.6b indicates that, for either fixture geometry (STB and SST), the mode III ERR distribution for a specimen with $\beta = 1/16$ is more uniform over the majority of the specimen’s width than it is for one with $\beta = 0$. Rather than going to zero at the free edges as occurs for $\beta = 0$, in the $\beta = 1/16$ geometry there are only small localized peaks in G_{III} at the internal edges of the delamination front, i.e., at $y/B = 1/16$ and $y/B = 15/16$. In view of the coupled mode II-III response at the free edge for an NE specimen, it is consistent that Figure 4.6c shows peaks in the mode II ERR at the free edges for the NE geometry, whereas no

peaks occur at the internal edges of the delamination front for the ED geometries. Although Figure 4.6a-c are for IM7/977-3, other than a slight change in the scale of the y-axis in Figure 4.6a, the results for T800S/3900-2B are essentially indistinguishable.

The combined results of Figure 4.6 indicate that, for both fixture geometries, delamination advance will likely initiate essentially across the full width of a specimen containing EDs, albeit perhaps with a bit of highly localized advance near the inner edge of the EDs where the G_{III} peaks occur. This agrees with the findings of Davidson and Sediles (2011) for the original STB ED test, who reported that delamination advance occurred essentially simultaneously across the full width of their specimens. Conversely, assuming that the mode II peaks at the free surfaces do not dominate or that there is only limited growth near the free edges, it is likely that macroscopic mode III delamination advance will initiate in the center of the specimen for NE geometries. This is consistent with what has been observed in the MSCB test (Szekrényes, 2009; 2011).

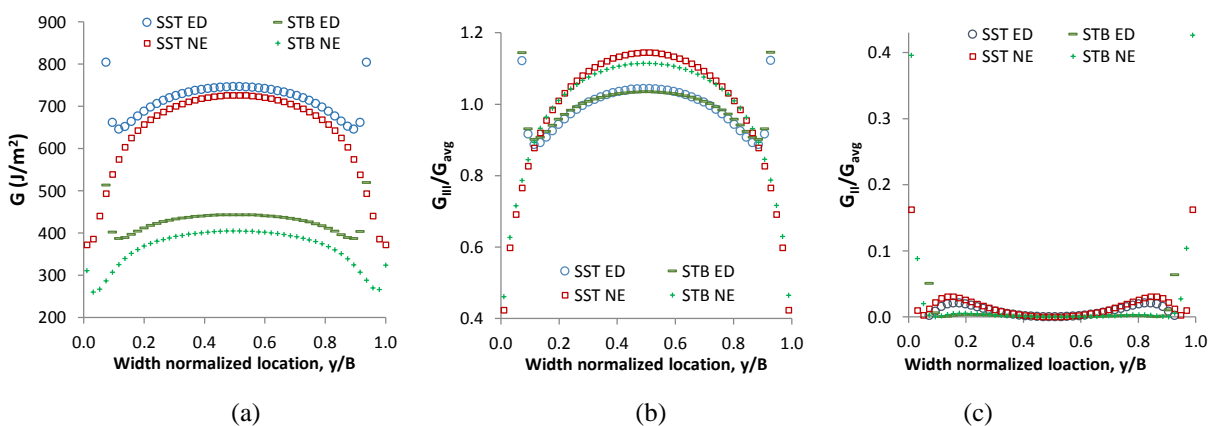


Figure 4.6. ERR distributions for IM7/977-3. (a) G for $P = 1500N$. (b) G_{III}/G_{avg} . (c) G_{II}/G_{avg} .

Finally, for both fixture geometries (STB and SST), the $\beta = 1/16$ configurations are over 99% mode III and for $\beta = 0$ they are both approximately 98% mode III. Thus, the FE results indicate that all four configurations appear viable. Specimens with and without EDs were therefore fabricated of both materials for experimental evaluation. This is described in what follows.

4.5.2. Load versus Deflection Response

Typical load versus deflection plots from STB and SST tests are shown in Figure 4.7. The STB geometry exhibits a stiffer response than SST due to the mid-span and end supports. For either fixture geometry, these results are essentially independent of the value of β and also look essentially the same for either material tested. The overall behavior is similar to that described for the original STB test (Davidson and Sediles, 2011). For both test geometries, the load versus deflection plots exhibit some nonlinearity. Preliminary investigations indicate that the nonlinearity is due to a combination of localized effects in the load pin region at lower loads, i.e., as the pins “settle in” to the machined cut-outs and, at higher loads, due to a limited amount of localized yielding of the epoxy in the highly stressed region close to the end of the load tab. Thus, the amount of nonlinearity increases with increasing load up to a “load plateau” where delamination advance initiates. Sufficient growth will then cause a load drop. This behavior was first described for the original STB (Davidson and Sediles, 2011).

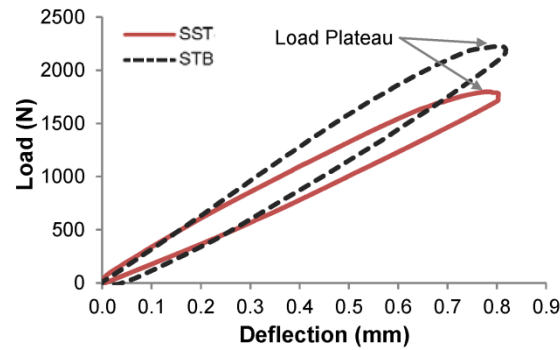


Figure 4.7. Typical load-deflection plots for STB and SST test specimen.

4.5.3. Onset of Delamination Growth

In order to ensure that none of the nonlinearity prior to the plateau region was associated with delamination growth, a study was conducted using the SST NE geometry. The methodology was essentially the same as that described for the ED STB by Davidson and Sediles (2011). Here, a series of specimens were loaded to values below the plateau, unloaded, and then c-scanned to evaluate potential growth. If no growth was observed, specimens were returned to the fixture and the process was repeated up to a higher load. This “load-unload-scan” process continued in very small load increments up until the plateau region was reached. Planar delamination growth prior to the plateau region was never observed in these specimens, nor has it been observed in any of the other STB or SST specimens tested in this work. Conversely, planar delamination growth has always been observed during the plateau region in all test configurations.

As previously described in Section 4.5.1, the ERR distributions for the baseline configurations suggests that growth will initiate along essentially the entire delamination front for ED specimens and near the center region for NE specimens. The former behaviors have been

observed in STB ED specimens (Davidson and Sediles, 2011). The latter behavior was therefore investigated as part of the “load-unload-scan” study for the SST NE described above. Once the load plateau was reached, tests were immediately stopped. For those tests that were stopped quickly enough, i.e., before delamination advance occurred across the specimen’s full width, the c-scan showed a “thumbnail-shaped” delamination front, where advance had occurred only along the central portion of the delamination front. In general, a fracture test needs to be stopped exactly when the plateau begins in order to observe this initiation. However, the crucial point is that the peak load in the test, which also corresponds to the plateau load and therefore to the critical load, is not affected by whether or not the test is stopped in time to catch this initiation. Thus, the peak load from a test on a NE specimen will always equal the critical load corresponding to initiation in the center of the specimen. Similarly, as first shown in Davidson and Sediles (2011), the critical load from tests on ED specimens also corresponds to the peak load in the test, and will always represent initiation across the full width of the specimen. This also does not depend on when the test is stopped.

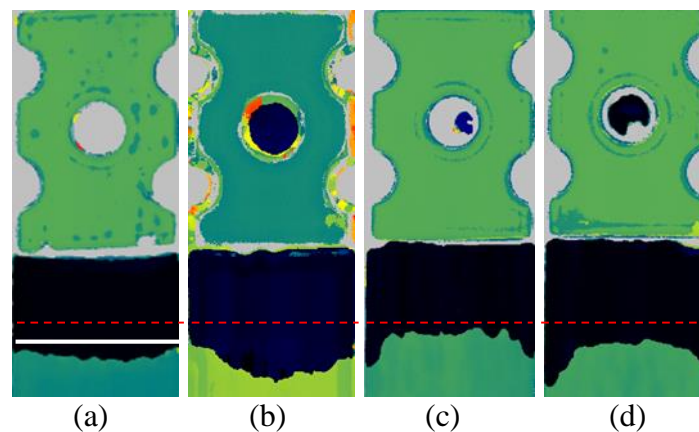


Figure 4.8. Typical post-test delamination front shapes from SST NE (a, b) and STB NE (c, d) specimens.

4.5.4. Post-Test C-Scan Results

Figure 4.8 shows typical post-test c-scans from SST NE and STB NE specimens. The dashed line in these images is used to indicate the end of the Teflon insert, i.e., the initial delamination front. The solid line in Figure 4.8a is referred to subsequently and represents the location where SST specimens were typically cut for microscopic inspection. For the SST geometries, shown in Figure 4.8a and b, more (longer) delamination advance was generally observed in the center region as compared to the regions near the specimen's edges, producing "thumbnail shaped" growth. Delamination growth shapes in SST ED specimens looked similar. A few SST specimens showed thumbnail shaped growth only in the center region, where the delamination front had not yet advanced across the entire specimen width. C-scans of typical STB NE specimens are shown in Figure 4.8c and d, and post-test delamination growth shapes in STB ED specimens were similar. Thus, STB specimens generally showed an inverse trend in comparison to SST, with STB specimens displaying more delamination advance near their edges than in their centers. It is interesting to observe from the delamination initiation studies described herein and in Davidson and Sediles (2011) that delamination advance *initiates* in the center of the specimen for NE specimens and essentially across the full width for ED specimens in both test geometries. That is, the onset location is controlled by specimen geometry, i.e., whether or not edge delaminations are preimplanted during manufacture, regardless of the test fixture that is used. In contrast, the c-scans of Figure 4.8 indicate that delamination *arrest* is apparently controlled by the test fixture, regardless of whether or not edge delaminations are present. It is possible that when the STB fixture is used, and therefore when the constraint of the center double roller is present, that the local peaks that occur near the edges of the delamination front in G_{II} and G_{III} , for the STB NE and STB ED geometries, respectively (cf. Figure 4.6), play more of

role in continuing to advance the delamination front than they do in the two SST specimen geometries.

The majority of specimens tested showed delamination growth along their entire front that was essentially symmetric about their width-centerlines, similar to the growth behaviors displayed in Figure 4.8. Toughnesses for all of these specimens were determined from each specimen's critical load, geometric parameters, and material properties using the data reduction approach described subsequently. However, the post-test c-scans of 10 specimens (from a total of over 60) indicated that no growth had occurred. Here, the fracture tests may have been stopped too early. These specimens were placed back into the fixture and reloaded to fracture. In all cases, this occurred at essentially the same load or a slightly higher value than the maximum load in the first test. These specimens were c-scanned after this retest and, if symmetric partial width growth occurred, toughnesses were determined as above. Three specimens (two T800S/3900-2B and one IM7/8552) displayed non-symmetric partial width growth, i.e., only one side of the delamination front advanced. This was always traced to some issue in aligning the fixture or placing the specimen in the fixture. These specimens were not appropriate for toughness determination and were excluded from further consideration.

4.6. Data Reduction Techniques

As discussed in Section 2.2, a number of different methods that have been used to calculate G_{IIIc} for mode III toughness tests. Due to its complex fixture and load application, data reduction in the original STB (Davidson and Sediles, 2011) was determined via a FE based method with a critical load determined by experiments. However, it is possible that a compliance calibration based method may be possible herein. Thus, both FE based and compliance

calibration based methods were investigated for STB and SST data reduction as part of these initial studies.

4.6.1. Compliance Calibration

4.6.1.1. Compliance Calibration Technique

The compliance calibration (CC) technique was explored as a potential data reduction technique due to the minimal assumptions required, in comparison to other techniques, to calculate G_{IIIc} . Due to the tabs on SST and STB specimens which preclude shifting the specimen in the fixture to obtain multiple delamination lengths, a multi-specimen compliance calibration similar to the method of Szekrényes (2009) discussed in Section 2.2.4.3 is considered.

4.6.1.2. Compliance Calibration of Tabbed Specimens

Due to its simplicity, the SST test was used for the initial evaluation of the potential accuracy of a multi-specimen compliance calibration data reduction method. Only NE specimens were considered in order to ensure similarity from specimen to specimen. In view of the above, both 24-ply and 32-ply IM7/977-3 test specimens with 150 mm long Teflon inserts were fabricated to determine the viability of the CC approach. Specimens with end tabs were prepared with delamination lengths of 91.5 – 106.5 mm in 5 mm increments. Compliance tests were performed to various percentages of the predicted critical load. Although different specimen responses were clearly obtained at the different delamination lengths (for each given specimen thickness), there was never a long, highly linear region within the load versus displacement plots where compliance could uniquely and unambiguously be defined. The reasons for this behavior are discussed subsequently. That is, all load versus displacement responses were similar to, or

more severe than, Figure 4.7, as significant nonlinearities were present in the tests. This behavior precluded the possibility of using CC with these test geometries.

4.6.1.3. Untabbed Specimen Assessments

Although the above work showed that compliance calibration was not viable with tabbed specimens, exploratory SST tests on untabbed specimens were conducted to examine whether a more linear load versus displacement plot might be obtained, and therefore a compliance calibration method of data reduction might be viable. Because of the specific geometry of the test fixture, it was found that untabbed specimens could only be tested if tab blanks were used as spacers between the specimen and load blocks. Rather than modify the fixture, a decision was made to initially consider this approach and, if promising, subsequently modify the fixture as necessary. Thus, a limited number of 18 ply T800S/3900-2B and 26 ply IM7/977-3 specimens without load tabs were tested for this purpose. In comparison to tabbed specimens, the undelaminated regions of all of these specimens showed a significant amount of rotation about the x-axis (cf. Figure 4.1) during loading. Further, as there is less contact area for load introduction, variations in the load pin length had a strong influence on the load versus displacement results and on the observed rotations. It was difficult or impossible to get the load pin to have full contact over the edge of one delamination leg while not contacting the surface of the other leg, and there were slight variations in contact from specimen to specimen. It was therefore concluded that the above problems were significant and that the accuracy and repeatability required to make a multi-specimen compliance calibration viable could not be achieved with untabbed specimens, regardless of whether or not fixture modifications were performed to eliminate the load tab blanks. For these reasons, untabbed specimens were not

pursued further in this study, and the compliance calibration was no longer considered as a possible data reduction technique.

4.6.2. FE Based Method

As CC was found to be non-viable for the desired test and specimen geometries, focus shifted to a FE based method of data reduction. Here, the VCCT (Rybicki and Kanninen, 1977; Krueger, 2004) is used to calculate ERRs along the delamination front, as in Figure 4.6. These ERRs are used in conjunction with the critical load for delamination advance to determine the toughness.

4.6.2.1. G_{IIIc} Basis for Baseline Configurations

The experimental results discussed in Section 4.5.3 indicate that the critical load in tests of both STB ED and SST ED specimens corresponds to delamination advance across the full width of the specimen. Thus, if this critical load (P_c) were used in a FE analysis of that particular specimen, the critical ERR (G_c) may be obtained. Due to full-width advance, G_c should be based on G_{avg} , i.e., one should evaluate G_c as G_{avg} at $P = P_c$. Alternatively, as the test is essentially pure mode III, the approach of Davidson and Sediles (2011) may be adopted, where one ignores the small mode II component and defines G_{IIIc} as $G_{III-avg}$ at $P = P_c$. This latter approach is adopted herein. Note that this approach also ignores the peak ERRs that occur at the delamination's edges (cf. Figure 4.6b). However, considering the peak ERRs that occur near the EDs, i.e., near $y/B = 1/16$ and $y/B = 15/16$, the regions where the magnitude of the peak exceeds the center value is confined to the single element at each of these edge locations. Thus, the most refined model considered (92 elements across the width) indicates that the peak is confined to a region that is

on the order of 0.5-1% of the specimen's width. This is not dramatically different from the small mode III component that occurs at the edges of mode II end-notched flexure specimens (Davidson et al., 1995), and experience has shown that this has no observable effect on toughness.

In contrast to the above, the experimental results indicate that, in NE specimens, G_{IIIc} must be based on the ERR in the center of the specimen, which represents the peak value in these geometries, G_{III-pk} . This agrees with the conclusions from the baseline FE analysis. Thus, in the case of NE geometries, $G_{IIIc} = G_{III-pk}$ at $P=P_c$.

4.6.2.2. Determinations of G_{IIIc} of Baseline Configurations

To facilitate data reduction, the equation for average mode III ERR for an STB specimen with $a=32$ mm is introduced (Davidson and Sediles, 2011):

$$G_{III-avg}^{STB} = \frac{P^2}{B^2 h G_{12} (1-2\beta)} \left(0.66 + 1.15 \sqrt{\frac{G_{12}}{E_{11}}} \right) \quad (4.1)$$

In Equation (4.1), B is the specimen width, β is the normalized edge delamination length, E_{11} and G_{12} are experimentally determined material properties, and P is the applied load. For convenience, Equation (4.1) is used as a scaling factor to express all key FE results for the different baseline configurations, and therefore to have a simple expression for data reduction. Correction factors were used to scale the FE results from the four baseline configurations to Equation (4.1) such that

$$G_{III-avg} = C_{fa} G_{III-avg}^{STB} \quad G_{III-pk} = C_{fp} G_{III-avg}^{STB} \quad (4.2)$$

where C_{fa} is a correction factor for the average ERR and C_{fp} is a correction factor for the peak ERR. Values of C_{fa} and C_{fp} are extracted from a comparison of Equation (4.2) to the FE results and are presented in Table 4.2 for the baseline geometries. The first row presents the test configuration, the second is the basis on which G_{IIIc} is to be determined, and the final two rows provide the appropriate correction factor. Note that C_{fa} and C_{fp} do not depend on the material used.

In the tests that follow, all data reduction was performed using Equation (4.1), Equation (4.2) and the appropriate correction factor from Table 4.2. Note that Equation (4.1) and Equation (4.2) simply provide a convenient expression to obtain G_{IIIc} from the measured P_c in the test. Fundamentally, data reduction is being performed via FE analysis.

4.7. Baseline Delamination Toughness Test Results

Delamination toughness tests were performed on the four baseline configurations following the approaches described previously. Unless otherwise specified, bolts through the grips that attach to the load tabs were not used. Loading was stopped and the specimen was unloaded as soon as there was a reasonable indication that the plateau was reached. In order to facilitate the types of evaluations derived with respect to Figure 4.8, all specimens were c-scanned subsequent to testing.

Table 4.2. Correction factors for baseline configurations with delamination lengths $a = 32$ mm.

Configuration	STB	STB	SST	SST
	ED	NE	ED	NE
G_{IIIc} basis	Avg.	Peak	Avg.	Peak
C_{fa}	1.00	-	1.70	-
C_{fp}	-	1.10	-	1.96

Figure 4.9a and Figure 4.9b present the toughness data for the four baseline configurations for IM7/977-3 and T800S/3900-2B, respectively. Each figure presents the toughness of all specimens tested in each configuration and, within each configuration, separated by the plate from which they were cut. As described previously, the toughness for all ED specimens is based on $G_{III-avg}$, and for all NE specimens it is based on G_{III-pk} . Initially, consider Figure 4.9a, which presents results for specimens from plate I9. This provides a means to eliminate plate-to-plate variation from consideration while retaining reasonable sample sizes (5 specimens in each of 3 configurations). These data provide strong indication that the SST NE, STB NE and SST ED configurations all yield the same result. Although the sample sizes are much smaller, comparisons between STB ED and SST ED for specimens from plate I7 and, referring to Figure 4.9b, from plate T17, provide indications that essentially the same results are obtained by these two configurations. Combined with the above, these “single-plate comparisons” indicate that essentially the same toughness values are obtained from each test. However, it appears that examining the data on a plate-by-plate basis is not necessary. Considering the data for either material within any single configuration, there are no differences in toughness obtained from specimens from different plates. This observation indicates that the data from the different plates can be grouped. Comparing the grouped data across configurations provides larger sample sizes, and leads to a relatively strong conclusion that all test configurations will yield the same mean toughness within normal scatter. Pooling all data from all test methods for each material, the apparent mode III toughness of IM7/977-3, based on 30 specimens, is found to be 1036 J/m^2 with a CV of 10.2%. The mode III toughness of T800S/3900-2B, based on 23 specimens, is found to be 1225 J/m^2 with a CV of 10.3%.

4.8. Dependence of Toughness on Delamination Length

As described above, all four baseline configurations (SST ED, STB ED, SST NE, and STB NE) produced consistent values of apparent toughness. Thus, any of these configurations could be used to investigate whether the observed toughness is independent of delamination length, and therefore whether a true material property is being measured. To this end, the SST NE configuration was chosen, and is used here and for all experimental work described in subsequent chapters. Non-edge delaminated specimens were selected because specimen manufacture is considerably easier than for ED specimens, and twice the number of specimens can be made per plate. The SST was chosen over the STB because of the larger range of potential delamination lengths. That is, the insert length in the STB is limited by the position of the mid-span support; inserts that end close to, or beyond, this would subject the specimen to delamination face compression by the support rollers and invalidate the test.

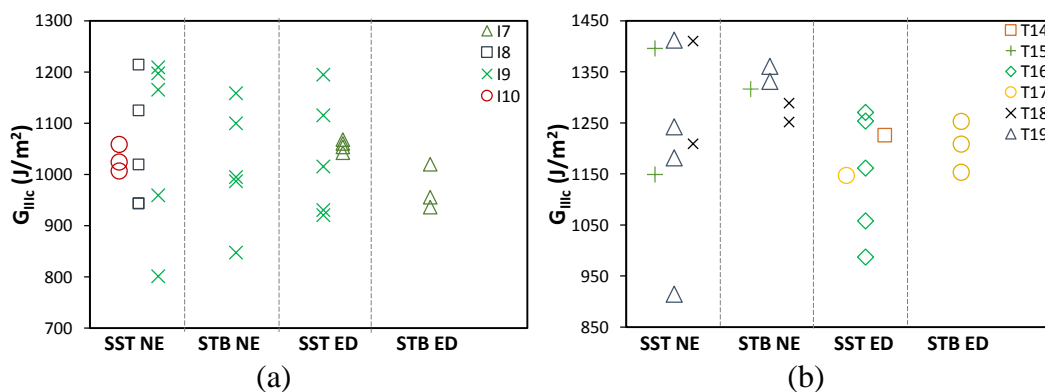


Figure 4.9. Toughness data for (a) IM7/977-3 and (b) T800S/3900-2B specimens.

4.8.1. FE Analysis

To support the study of the effects of delamination length on the apparent toughness, Johnston et al. (2014) conducted FE analyses conducted on SST NE specimens with delamination lengths from 25 mm to 127 mm. Models of specimens with delamination lengths equal to or greater than 32 mm used the meshing approach described previously. The model with $a = 25$ mm was essentially the same as that used for $a = 32$ mm, except that some of the longest elements in the cracked regions adjacent to the load tab were removed, and the maximum element length did not exceed 1.1h.

Figure 4.10 presents the predicted mode II and mode III ERR distributions. Here, normalized values of G_{III}/G_{avg} are plotted using the left side vertical axis, and normalized values of G_{II}/G_{avg} are plotted using the right side vertical axis. Note that the G_{III}/G_{avg} distributions are similar for all delamination lengths. All geometries are predominantly in mode III with a slight decrease in the global mode ratio as the delamination length increases, from 99.1% mode III at $a = 25.4$ mm to 95.3% mode III at $a = 127$ mm. As G_{III} decreases with delamination length, an increasing mode II component arises at the specimens' edges. However, as discussed previously, delamination growth in the SST NE configuration will initiate in the center of the specimen at $G_{IIIc} = G_{III-pk}$. From Figure 4.10, it can be observed that this region is essentially pure mode III for all geometries. Thus, the mode II component near the edges will not affect the observed toughness and the same value of G_{IIIc} should be obtained by testing specimens with any of the insert lengths considered.

4.8.2. Experimental Investigation

In anticipation of this study, one of the previously fabricated IM7/977-3 plates (plate I10) had a longer Teflon insert length, allowing test specimens with delamination lengths up to 76 mm to be tested. An additional 26-ply IM7/977-3 plate (I11) was also fabricated with a similar insert length. A series of tests were then conducted on specimens with delamination lengths between 32 mm and 76 mm. Test procedures were identical to those described previously. Growth will initiate in the center of the specimen at the peak value of G_{III} for all SSE NE geometries. Therefore, only C_{fp} , which will vary with delamination length, is required. Therefore, additional FE runs were performed to obtain C_{fp} for all delamination lengths considered. The values obtained and used for data reduction are presented in Table 4.3.

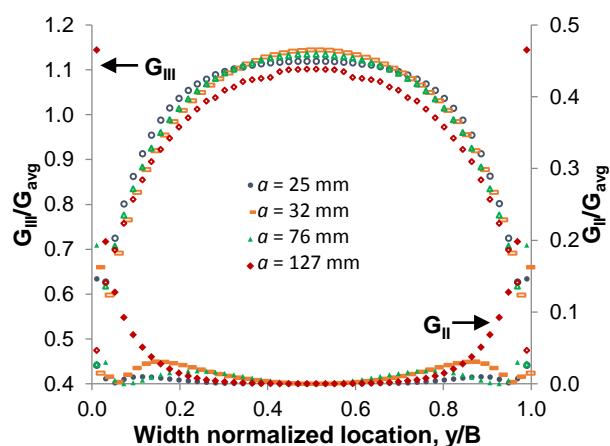


Figure 4.10. ERR distributions as a function of delamination length for IM7/977-3 SST NE.

Table 4.3. Correction factors as a function of delamination length for SST NE.

Crack Length a (mm)	30	32	34	38	44	54	76
C_{fp}	1.89	1.96	2.07	2.25	2.52	2.92	3.81

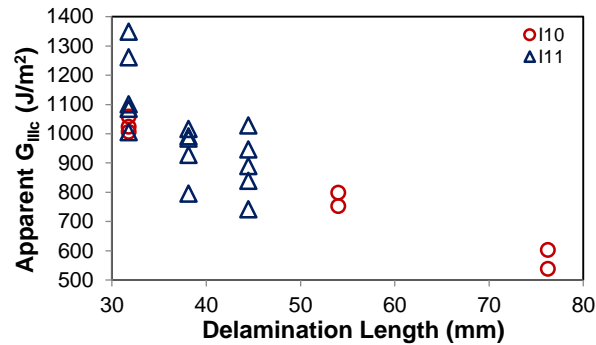


Figure 4.11. Apparent G_{IIIc} versus delamination length for IM7/977-3 SST NE specimens.

Figure 4.11 plots the experimental results for apparent toughness versus delamination length. The three results from plate I10 at $a = 32$ mm are the same as those appearing in Figure 4.9. Similar to that observed in the MSCB test (Szekrényes, 2011), there is a significant drop in apparent toughness as delamination length increases.

Since variations in apparent G_{IIIc} with test geometry have also been observed in both the MSCB and ECT tests, as discussed on Section 2.2, it is useful to consider mechanisms that may be common to all test methods. To this end, an examination of the literature for mode III experiments using homogenous materials is beneficial. Recall from Section 2.3.3 that specimens containing planar cracks and subjected to anti-plane shear loads developed a series of “penny shaped” (Knauss, 1970) or “parahelical” (Palaniswamy and Knauss, 1978; Li et al., 2011) cracks, rather than planar mode III growth (as assumed herein for the composite laminates). These cracks were observed to initiate and grow at a 45° angle to the original crack plane, with the angle of inclination such that they were oriented perpendicular to the direction of maximum tensile stress. As described by both Knauss (1970) and Palaniswamy and Knauss (1978), and more recently by Goldstein and Osipenko (2012), fracture occurs through the development,

extension, and ultimately coalescence of a series (or echelon) of parallel cracks that initiate along the original crack front.

In view of the above, it seems quite possible that the same mechanisms identified for homogeneous materials will occur under mode III loadings of laminated polymeric composites when the plies bounding the delaminated interface have their fibers aligned with the intended direction of growth, a feature common to SST, STB, MSCB and ECT specimens. That is, in these cases, the fiber architecture would not constrain the types of cracks that are observed in homogeneous materials from initiation and local growth within the composite. This was first hypothesized by Sharif et al. (1995) who referred to these as “shear crevices,” and who observed these cracks in fractured MSCB specimens via post-test fractographic examinations of the delamination plane. The same approach showed similar types of cracks in fractured glass/epoxy ECT specimens (Li et al., 2004). Ratcliffe (2004) made similar observations in carbon/epoxy ECT specimens via x-radiographic imaging and, analogously to both Sharif et al. (1995) and Trakas and Kotschot (1997), also hypothesized that this occurred prior to macroscopic mode III delamination advance. Other researchers who performed post-test fractographic examinations of the delamination plane of fractured mode III specimens reported no such cracks (Lee, 1993; Robinson and Song, 1994; Pennas et al., 2007; de Moraes et al., 2009; Browning et al., 2011; Davidson and Sediles, 2011, Marat-Mendes and de Freitas, 2013). However, as a result of the crack size, the plane of delamination growth, and/or the process of splitting the specimens along the plane of the delamination for post-test fractography, it may be that these cracks are not readily observable by this approach. For this reason, examinations of fractured specimens for matrix cracks were conducted via transverse sectioning. This (apparently new) approach to

assessing damage in laminated composite mode III delamination toughness test specimens was developed in conjunction with Czabaj et al. (2014) and is described in what follows.

4.8.3. Photomicroscopy

Six specimens from plate I10 were selected for photomicroscopic evaluation: two from each of the three delamination lengths tested. A diamond wheel saw was used to cut each specimen in the transverse direction, such that a cross section in the y - z plane was exposed. The x -direction location was chosen using the post-test c-scan of that specimen such that it was just ahead of the original Teflon insert and in the newly delaminated region. This is depicted by the solid white line in Figure 4.8. Each section was potted in epoxy, then ground and polished using standard techniques (Geels, 2007). Reflected light differential interference contrast (DIC) microscopy was used to examine the cross sections, and photomicrographs were taken at various magnifications across the entire width of each specimen.

A photomicrograph of the delamination front of specimen I10-8 is presented in Figure 4.12. This specimen was tested with a delamination length of $a = 54$ mm. The mid-plane delamination front is the jagged path running horizontally at the center of the photomicrograph. At this scale the individual plies are just discernible, and approximately 11 plies are visible in the image. As indicated by the smaller arrows, it is evident that there are large matrix cracks oriented at approximately 45° from the horizontal that extend both above and below the plane of the delamination. The direction of applied loading, P , is shown using large horizontal arrows. In view of the direction of the loading, it is evident that the planes of extension of these cracks are all oriented essentially perpendicular to the direction of maximum tensile stress associated with the K_{III} field (Li et al., 2011; Palaniswamy and Knauss, 1978), where K_{III} is the mode III stress

intensity factor. This is consistent with the original observations by Knauss (1970) of crack advance in cracked homogeneous materials, as well as with the schematic representation of Trakas and Kortschot (1997) showing the expected formation of shear crevices in laminated composites, for anti-plane shear loadings.

Also evident in the image of Figure 4.12 are a number of intralaminar voids, i.e., voids within individual plies, indicating a possible compaction issue during fabrication. However, considering this image, those that follow, and the many that have not been presented, there was no clear preference observed for the initiation of the matrix cracks from the intralaminar voids. Thus, it does not appear that these voids have any significant effect on the initiation or growth of the matrix cracks. Figure 4.13 and Figure 4.14 show cross sectional views near the delamination front for specimens of delamination length $a = 32$ mm and $a = 76$ mm respectively. Note that these two figures are at a magnification that is 2.5 times greater than that of Figure 4.12. Small arrows are again used to indicate the matrix cracks.

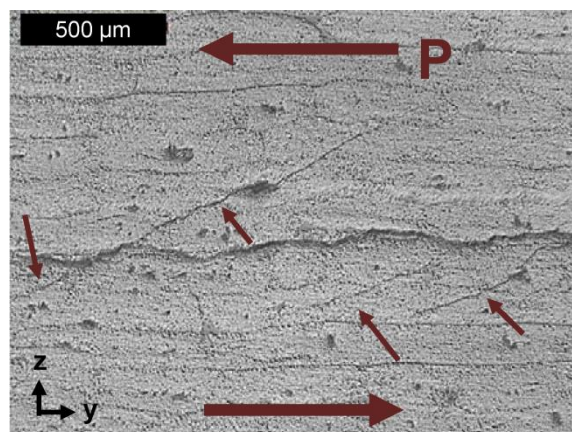


Figure 4.12. Photomicrograph at the delamination front of specimen I10-8 with delamination length $a = 54$ mm.

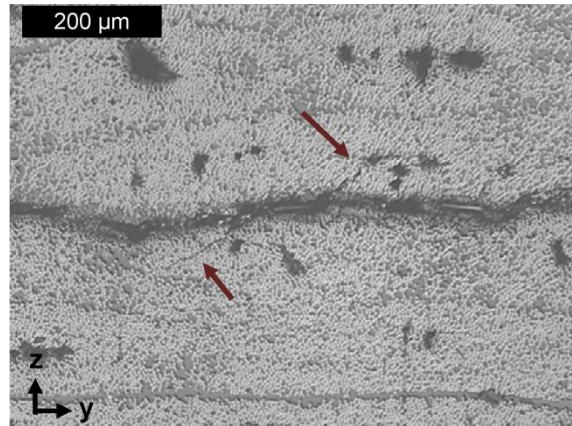


Figure 4.13. Photomicrograph at the delamination front of specimen I10-10 with delamination length $a = 32$ mm.

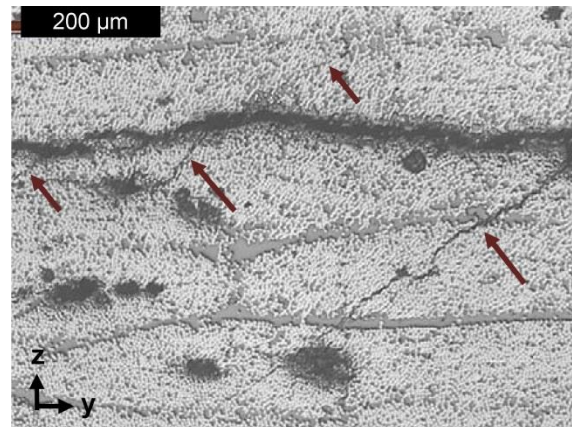


Figure 4.14. Photomicrograph at the delamination front of specimen I10-4 with delamination length $a = 76$ mm.

Note that the images presented here represent only a small percentage of each specimen's width. The complete photomicroscopic evaluation indicates that matrix cracks are present across the entire width of each specimen and vary in size and spacing. When comparing Figure 4.12, Figure 4.13, and Figure 4.14, it is evident that these cracks vary in length and spacing from specimen to specimen; this was also true from location to location within a specimen. To determine whether there was any correlation between observed matrix cracking and apparent toughness, the photomicrographs taken from the six specimens were evaluated using graphical

analysis software to measure the length and the spacing between all visible cracks. No correlations were found between the delamination length of the specimen and the number of matrix cracks, their length, or their spacing. That is, there is essentially the same variation in these parameters within and between specimens that were tested at a given delamination length as there is between groups of specimens tested at different delamination lengths. In the specimens studied herein of width $B = 25.4$ mm and thickness $2h = 3.3$ mm, there may be anywhere from 30 – 80 matrix cracks visible with lengths ranging from 0.5 mm to 2.3 mm. Smaller cracks are likely present, but are not easily measureable.

The above observations indicate that matrix cracks are present at the delamination front subsequent to growth. These cracks are similar to those that form prior to anti-plane shear fracture in homogeneous materials. Interestingly, matrix cracks have also been observed in post-fracture examinations of ECT delamination toughness test specimens (Czabaj et al., 2014), indicating that this is not a phenomenon in only the SST. It seems likely that the matrix cracks seen in this work and in Czabaj et al. (2014) occur due to the same crack front instability that has been widely discussed for homogenous materials under mixed-mode I–III loadings (Lin et al., 2010; Pons and Karma, 2010; Leblond et al., 2011). However, it is not clear from the current study or from previous studies on laminated composites whether the observed matrix cracks are formed before, coincident with, or subsequent to, delamination advance. Data reduction techniques for all current mode III delamination toughness tests assume the growth of a single interlaminar delamination in an uncracked matrix. Thus, if the matrix cracks initiate after delamination growth, then the delamination toughness measured by current mode III tests would be expected to be accurate. This would indicate that there may be some other issue responsible for the observed dependence of apparent toughness on test geometry. However, if the matrix

cracks initiate before or concurrently with delamination advance, then they may be the cause behind these observations. Although further work is required to resolve this issue, it seems likely based on observations in homogeneous materials, and therefore will be studied in Chapter 5.

4.9. Conclusions

Four split beam-type tests were introduced and used to investigate issues related to the geometry-dependence of the apparent mode III delamination toughness of laminated polymeric composites. When specimens with the same delamination length were tested, a constant apparent mode III toughness was obtained using all four test methods. This provided strong validation of the accuracy of the test methodologies and associated data reduction procedures. A single configuration, the split shear torsion non-edge delaminated test, was then used to study toughness as a function of delamination length. It was found that as delamination length increased, apparent toughness decreased. In an effort to understand this trend, specimens were sectioned at the delamination front and examined microscopically. Similar to what is seen in the mode III testing of homogenous materials, it was found that the specimens contained matrix cracks at the delamination front that were oriented at 45° to the plane of the delamination. If these matrix cracks initiate before or concurrently with planar delamination advance, then this may explain the observed dependence of apparent G_{IIIc} on delamination length in mode III tests. This issue is studied in Chapter 5.

Chapter 5. Fracture Surface Evolution

5.1. Introduction

It was shown in Chapter 4 that both matrix cracks and a planar delamination advance in the SST test. However, it is not clear whether the matrix cracks form before, concurrently with, or subsequent to planar delamination growth. As discussed previously, if matrix cracks initiate after delamination growth, then the delamination toughness measured by current mode III tests would be expected to be accurate. This would indicate that there may be some other issue responsible for the observed dependence of apparent toughness on test geometry. However, if the matrix cracks initiate before or concurrently with delamination advance, they may be the cause of these observations. In view of the above, the first goal of the investigations undertaken in this chapter is to assess whether the matrix cracks that have been observed at the delamination front in delaminated SST specimens are already present when delamination advance initiates. The second, related goal is to assess the specific progression of “damage,” used here to denote the accumulation and growth of matrix cracks and their interaction with the original delamination front that is associated with what has heretofore been considered mode III growth. Testing to achieve these two goals will be known as “damage progression testing,” as it is aimed at determining the progression and accumulation of damage prior to the onset of planar delamination growth, and is different from the delamination toughness testing introduced in Chapter 4.

It is also clear from the results of Chapter 4 that as growth occurs in SST specimens, the fracture surfaces that develop will be very complex. In order to understand what is driving the

development of these complex fracture surfaces, it is important that the mechanics of both initiation and propagation of delamination growth be understood. Thus, subsequent to determining the progression of damage leading up to delamination advance, growth after the onset of planar delamination advance will be studied. In line with this, the third goal of the investigations undertaken in this chapter is to determine the manner in which the coupled system of a delamination and multiple transverse cracks develops and advances after the onset of planar delamination growth. These tests will be known as “extended growth tests,” as they will examine how the fracture surfaces, comprised of a planar delamination and multiple transverse cracks, grow and evolve as the delamination grows an extended amount.

To achieve the above goals, a series of SST specimens were manufactured and tested. Ultrasonic inspection, X-ray computed tomography (CT) and optical microscopy were utilized to observe the development and evolution of cracking both before and after the onset of planar delamination growth. In what follows, the three-dimensional fracture surfaces from several SST test geometries are compared to each other and to analogous results from homogeneous materials, and the effects of specimen geometry on damage progression and fracture surface evolution are assessed. The results are then used to draw inferences on the application of conventional toughness test and delamination prediction methodologies to laminated composites.

5.2. Test Design

5.2.1. Specimen Design

In Chapter 4 it was found that delamination growth in SST NE specimens initiated in the center of the specimens, and EDs were not required for predominantly mode III delamination

advance. Thus, the studies conducted in this chapter use only the SST NE configuration, which will subsequently be referred to as simply the SST.

The method of load introduction to the specimen used herein is slightly different from that used in Chapter 4 (cf. Figure 4.2), where load transfer was achieved via load pins that were press-fit into the load blocks and were mated to semi-circular machined cut-outs in the load tabs. However, it was found that, due to small specimen-to-specimen variations in load tab machining, each specimen underwent small rotations while the load pins “seated,” i.e., while they achieved full contact within each semi-circular load tab cut-out with increasing load. This resulted in a somewhat nonlinear load versus deflection response at low loads and is what motivated a load tab and load block redesign which will result in the desired zero slope boundary condition within the tabbed region.

Figure 5.1 presents schematic representations of the SST test and the associated method of load introduction used in this chapter and in Chapter 6. As shown in Figure 5.1a, both a shear load and a restoring torque are applied to the specimen remote from the delamination tip. These loads are applied via load tabs that are bonded to the specimen and which are constrained to enforce a zero slope condition at the specimen’s cracked ends. As indicated in Figure 5.1b, the SST loading in this study is introduced via load blocks, bolts and load tabs. The load tabs can be seen in the photograph presented in Figure 5.2.

5.2.2. Materials and Manufacturing Process

This study first used unidirectional 26-ply IM7/977-3 test specimens with nominal thicknesses of $2h = 3.3$ mm, which are identical to those used in Chapter 4. However, the high specimen porosity (voids evident in Figures 4.12 – 4.14) described in Section 4.8.3 complicated

the investigations therein. Thus, a number of tests were conducted using unidirectional IM7/8552, which produced specimens with far fewer voids. Both 24-ply and 48-ply IM7/8552 test specimens were fabricated, which produced specimens that had a thickness of $2h = 3.0$ mm and 6.0 mm respectively. All specimens used in this study were nominally sized to have widths, B , of 25 mm and delamination lengths, a , from 32–76 mm.

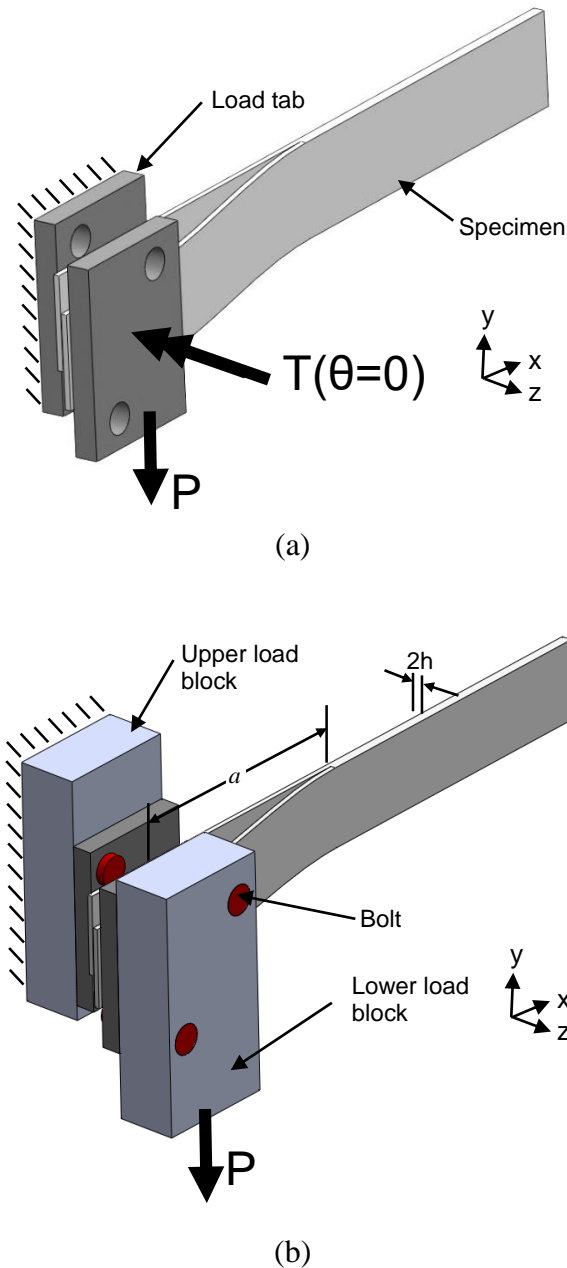


Figure 5.1. SST test (a) loading, (b) method of load introduction.

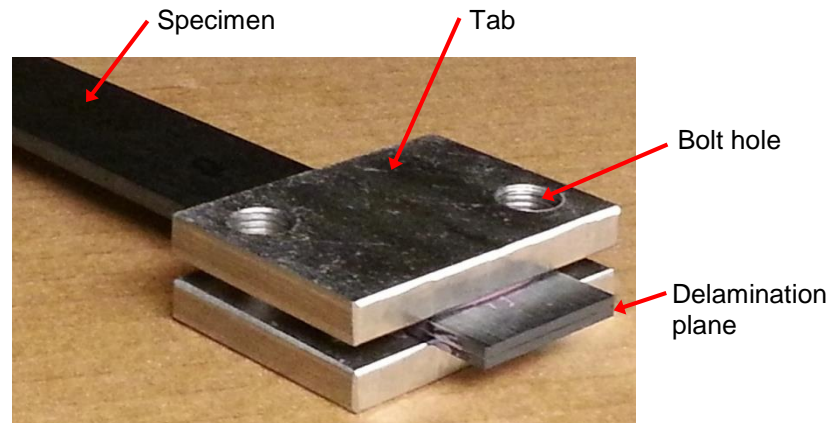


Figure 5.2. SST specimen with load tabs.

All IM7/977-3 test specimens were fabricated at the Syracuse University Composite Materials Laboratory (SU-CML) using an autoclave and the manufacturer's recommended cure cycle. The fabrication procedure generally followed that described in Section 4.4.1. An additional step was added during layup, however. The 24-ply plates were debulked after the 8th and 16th plies in an attempt to minimize porosity. In another attempt to minimize porosity, and to avoid bias due to the potential effects of manufacturing procedure, one 24-ply IM7/8552 plate was fabricated at NASA Langley Research Center (NASA LaRC) in a hot press following essentially the same procedure as was used for the plates fabricated at SU-CML. An additional 24-ply plate and a 48-ply plate of IM7/8552 were fabricated at SU-CML using an autoclave, and a similar debulking process to that undertaken for IM7/977-3 was used approximately every eight plies.

After cutting, an alignment jig was used to bond the specimens to rectangular, machined low-carbon steel load tabs. To this end, the threaded bolt holes in the tabs were secured to two

sides of the jig, and a specimen was sandwiched between them. Alignment rails were used to orient the specimen correctly with respect to the load tabs. After tabbing, specimens were c-scanned to obtain a pre-test scan of the delamination front. All specimens were scanned a second time after testing. Both of these scans included the tabbed region, which acted as a common datum to compare images. This provided a determination of whether or not the crack front advanced and, in those instances where growth did occur, to ascertain the shape of the new delamination front. Post-test destructive assessments were also conducted on a number of specimens, the details of which are described subsequently.

As was discussed in Section 4.3.3, the data reduction method used for the SST test is sensitive to the values of the axial and shear moduli. Thus, in addition to obtaining SST specimens, two specimens were cut from the non-delaminated portion of each plate manufactured and were used to determine the axial modulus (E_{11}) following ASTM Standard D3039 (2014) and the procedure described in Appendix A. Relatively little variation was observed within or, between plates. Considering the data from the IM7/977-3 plates fabricated for this study and previous data for this material from SU-CML, coefficients of variation (CVs) were on the order of 2%. Because of the extremely small variation, the value of E_{11} used in Chapter 4 was retained for consistency. Testing to determine the shear modulus (G_{12}) followed ASTM Standard D5379 (2012) and the procedure described in Appendix B and also produced relatively tight distributions, with CVs on the order of 6% for both materials. For IM7/977-3, $E_{11}=163.8$ GPa and $G_{12}=4.95$ GPa, where G_{12} has also been retained from Chapter 4 for consistency. No previous data for IM7/8552 was available, and so E_{11} and G_{12} used in this chapter came from the plates fabricated for this study. For IM7/8552, $E_{11}=187.2$ GPa and $G_{12}=7.33$ GPa.

5.2.3. Fixture Design

Figure 5.3a presents a photograph of the front view of the SST fixture containing a specimen. With the improved load tab design, the load block/grips also had to be redesigned. The bolts and machined slots which connect the lower load block/grip to the platen to accommodate specimens of different thicknesses are the same as in the original design shown in Figure 4.5a. As in the original design, the lower load block/grip assembly is mounted to a platen that connects to the actuator and is displaced downwards during the test. The upper assembly still connects to the load cell and remains stationary during testing. However, rather than the load pins used with the original load block/grips, the new design contains through holes sized for bolts. These bolts are bolted through the load block/grip assemblies directly into the specimen's load tabs.

Figure 5.3b shows the view looking from the left side of Figure 5.3a. The upper load block/grip assembly and its attachment to the load cell adapter are visible in the left of the figure. The lower load block/grip assembly is to the right and attaches to the platen. The procedures to install specimens into the grips were developed to maximize reproducibility. A specimen is initially bolted loosely into the upper grip. The lower (platen-mounted) grip is then slid into place until its bolt holes mate with the threaded holes in the tabs, and the lower backing plate contacts the tab. The location of the lower grip is then fixed such that no gaps are observable between each load tab and its associated backing plate and that there is little or no through-thickness compression acting on the cracked region. The specimen is then bolted tightly into the lower grip, after which the bolts attaching the upper grip to the tabs are tightened.

All tests were performed under displacement control at a rate of 1.0 - 2.0 mm/min for loading and 3.8 mm/min for unloading. During testing, load was measured using the load cell

attached to the upper grip, while displacement was measured using the actuator. These test methods were identical to the methods used in Chapter 4.

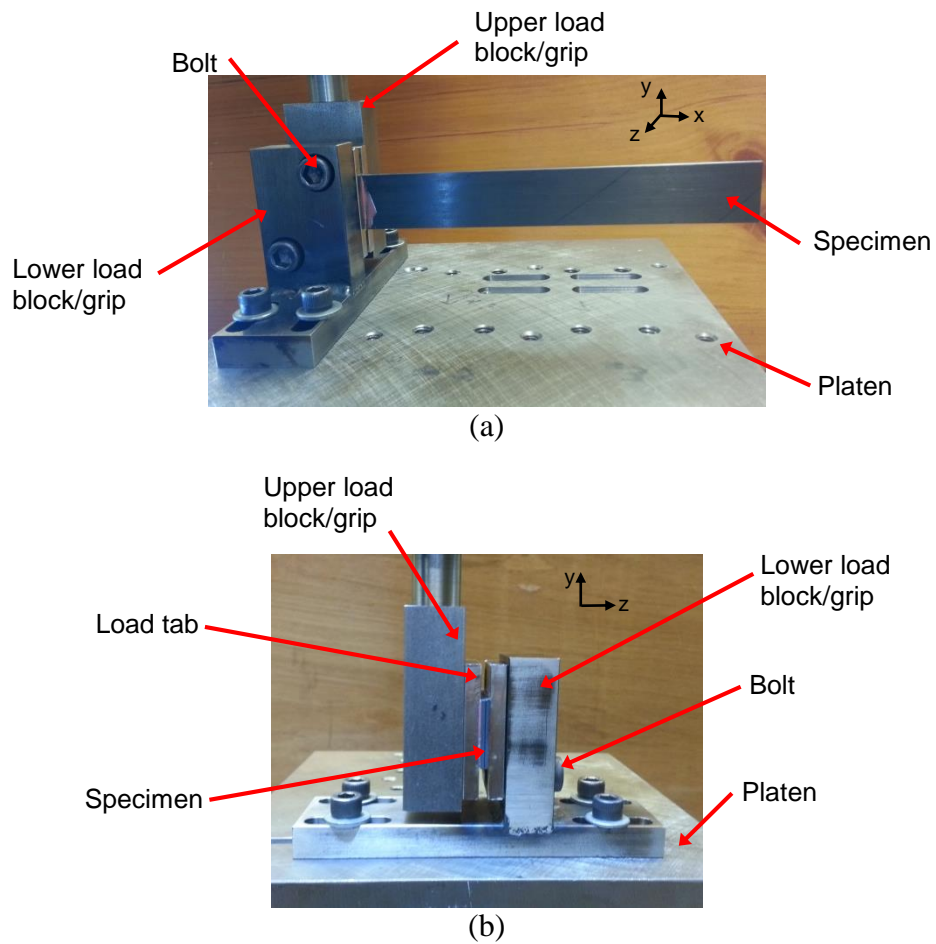


Figure 5.3. SST test fixture setup (a) front view, (b) side view.

5.2.4. Test and Evaluation Procedures

5.2.4.1. ERR Determination

As discussed in Section 4.6.1, compliance calibration was initially considered for data reduction. However, this approach could not be implemented due to the small deflections in the test, the need to use load tabs to avoid significant local deformations in the composite specimen, and a small amount of nonlinearity that occurs in the load versus displacement response. This latter issue was mitigated by the redesign of the load blocks and load tabs described previously. Even with these modifications, however, it is unclear whether a multi-specimen compliance calibration technique, as used for the edge crack torsion test (ECT) (Browning et al., 2011; de Morais et al., 2009; Pennas et al., 2007; Ratcliffe, 2004), would be accurate. Therefore, in this work the original, finite element-based approach to data reduction for the SST test, as described in Section 4.6.2, is utilized.

The finite element (FE) analyses used in this chapter were conducted by Mr. Kiran Simon and published in Johnston and Davidson (2014). The analyses utilized essentially the same model and mesh as that used in Chapter 4; only the mesh in the region of the load tabs was modified to reflect the new design presented herein. The mesh still uses 20 noded quadratic brick elements, and builds on the original FE work performed for the STB (Davidson and Sediles, 2011). Energy release rates (ERRs) were computed along the delamination front using the virtual crack closure technique. As described in Section 4.3.3, a series of mesh refinement studies showed that the FE predictions were insensitive to the mesh used, and that this mesh was sufficiently refined to capture the variation in ERR across the specimen's width. The ERR results for the geometries used in this work are analogous to those shown in Figure 4.6 and discussed in Section 4.5.1.

As described in Section 4.5.1 and experimentally verified in Section 4.5.3, delamination advance will initiate in the center of the SST specimens, which was shown by FE analysis to have pure mode III conditions. Thus, the delamination toughness is calculated using the peak value of the local ERR (G_{III-pk}), i.e., at the center of the specimen, computed at the delamination onset load. Fundamentally, this is determined using the FE results. However, as was established in Section 4.6.2.2, rather than perform a FE analysis of each individual specimen, an approach is adopted that simplifies the data reduction process. In Section 4.6.2.2, the equation developed for the mode III ERR in an STB specimen is modified to yield:

$$G_{III-pk} = C_f(a) \frac{P^2}{B^2 h G_{12}} \left(0.66 + 1.15 \sqrt{\frac{G_{12}}{E_{11}}} \right) \quad (5.1)$$

For this work using the SST specimen without edge delaminations, $C_f(a)$ is analogous to C_{fp} as given in Equation 4.2 and Table 4.3. It is referred to here as $C_f(a)$ to indicate that the value depends on geometry. The subscript ‘p’ has been removed since all correction factors will be for G_{III-pk} .

Following the above procedure for the 24-ply specimens considered herein yielded $C_f = 1.93^1$ for $a = 32$ mm, $C_f = 2.84$ for $a = 54$ mm, and $C_f = 3.76$ for $a = 76$ mm. These values are used subsequently along with Eq. (1) to determine G_{III-pk} as a function of the applied load, P , and to determine the apparent value of G_{IIIc} . This is taken as the value of G_{III-pk} when $P=P_c$, where P_c is defined to be the “critical value,” i.e., the delamination onset load. Note that the correction factors presented above are approximately 2% different from those given in Table 4.3 due to the modified load block and load tab designs.

¹ The value of 1.98 published in Horner and Davidson (2015) was a typographical error.

5.2.4.2. Test Plan

SST tests were performed on specimens of both IM7/977-3 and IM7/8552 in three categories: delamination toughness tests, damage progression tests, and extended growth tests. Note that the main purposes of this work were to determine the progression of events leading up to planar delamination advance (*damage progression tests*), and how the coupled matrix cracks and planar delamination advance and evolve (*extended growth tests*). However, as the load tabs and fixture were redesigned for this work, and new, additional geometries were studied, it was valuable to first perform *delamination toughness tests* to verify the trends in apparent toughness based on geometry.

Delamination toughness tests were performed on SST specimens at three nominal delamination lengths: $a = 32, 54$ and 76 mm. For IM7/977-3, 26-ply specimens were used, and 24-ply specimens were used for IM7/8552. All of these specimens were tested to the critical fracture load, P_c , and Equation (5.1) was used to calculate the apparent toughness for each specimen.

Damage progression tests were conducted on SST specimens of both materials at delamination lengths of $a = 32$ mm and $a = 76$ mm. These tests were stopped at a lower load, i.e., before delamination occurred. These tests were stopped in the region between the load plateau (cf. Section 4.5.3) and the onset of high-load nonlinearity, as shown in Figure 5.4. It was believed that this region had the greatest likelihood of containing potential fracture events prior to delamination growth. These tests were quantified based on the ERR calculated at the peak load each specimen reached before the test was stopped, and normalized by the average apparent delamination toughness obtained for that geometry.

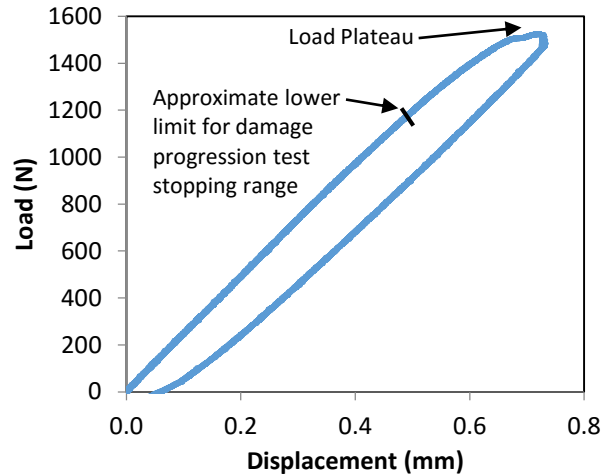


Figure 5.4. Typical load versus deflection plot.

Extended growth tests were conducted on 24-ply and 48-ply SST specimens fabricated from IM7/8552 with delamination lengths of $a = 32$ mm. These tests were continued past the onset of planar delamination advance, signified by the load plateau. Delamination growth was allowed to continue for 14-16 mm before these tests were stopped. For this study, it was of interest to test specimens with different thicknesses rather than different delamination lengths. For this work, the fracture surface evolution, and not the apparent toughness, was of interest, and so it was not necessary to produce delamination toughness tests for the additional geometry.

As described previously, a c-scan was performed subsequent to all tests. In specimens tested to fracture (delamination toughness and extended growth tests), the c-scan served to verify that delamination advance occurred over the majority of the specimen's width and to show the extent of growth. In damage progression specimens, the c-scan was used to confirm that no delamination advance had occurred.

All three specimen types were sectioned for microscopic examination after testing. Toughness test specimens were sectioned in order to compare to the previous results presented in Chapter 4, where matrix cracks were visible in the region of delamination advance in IM7/977-3

specimens. These previous specimens had somewhat large porosity, and were tested using an earlier load tab design. As these earlier observations motivated the present study, it was important to determine whether cross-sections within the specimens tested herein – which were manufactured using the debulking procedure and which used the new load tab design – appeared essentially the same. Thus, a transverse cut exposing the y-z plane (cf. Figure 5.1) was made in these specimens just ahead of the original Teflon insert in the newly delaminated region. This corresponded to the location of the section cuts made in Section 4.8.3. Damage progression specimens were also cut transversely to expose a y-z plane. This was done in order to assess whether matrix cracking occurred prior to delamination advance and, if so, its extent. To this end, damage progression specimens were sectioned in the region of the Teflon insert and fairly close to its end. Each cross section was then carefully ground until the visible plane was the same as the end of the Teflon insert. Extended growth specimens were cut transversely at several locations to expose y-z planes ahead of the Teflon insert tip.

For all specimen types, the cut sections were potted in epoxy, polished, and cleaned according to Geels (2007). These cross sections were then examined using optical microscopy and photomicrographs were taken. Here, photomicrographs of close-up sections were taken across the entire cross section, and later stitched together such that a full view of the transverse section was available for analysis. Prior to transversely sectioning the extended growth specimens for optical microscopy, Dr. Mike Czabaj conducted X-ray computed tomography (CT) scans at NASA LaRC. While the optical microscopy provides a very fine level of resolution, only at a limited number of locations can be sectioned per specimen. Conversely, X-ray CT provides a three-dimensional view of the entire cracked region, but at a somewhat lower resolution. Each X-ray CT image captures the full specimen cross section, so there is no need to

stitch multiple images together, as with photomicroscopy. Combining the information from these two techniques provides a full view of the fracture surface evolution.

5.3. Delamination Toughness Testing

5.3.1. Apparent Toughness Test Results

Figure 5.5 presents results from the apparent G_{IIIc} tests of 26-ply IM7/977-3 using the new tab design. These data were obtained from tests of 14 specimens that were cut from two different plates (I13 and I14) of IM7/977-3. A trend of decreasing apparent toughness with increasing delamination length is clearly seen and is similar to that observed in Figure 4.11. The average values for apparent G_{IIIc} along with the associated CVs are presented in Table 5.1. Note that these results are somewhat lower than those presented in Section 4.8.2 for the same material and delamination lengths. This is likely due to the change in load tab and load block design. The current design is closer to a true zero slope boundary condition within the tabbed region which, consistent with a comparison between the results herein and those reported previously, would yield a change in perceived toughness that is more pronounced at shorter delamination lengths. Alternatively, given the observed dependence of the apparent toughness on geometry illustrated in Figure 5.5, it is also possible that there are other influencing factors. This difficulty of separating out material versus structural effects is one of the key problems with current mode III testing, and is one that the present study hopes to address.

A limited number of toughness tests were conducted for 24-ply IM7/8552. Two tests were performed on specimens at delamination lengths of $a = 32$ mm and yielded an average toughness of $G_{IIIc} = 556$ J/m². One test was performed on a 24-ply specimen at a delamination length of $a = 76$ mm yielding $G_{IIIc} = 262$ J/m². Only a small number of specimens were tested for these

geometries because the main focus of using this material with these geometries was to compare the damage progression test data with that of 26-ply IM7/977-3. However, in order to interpret damage progression specimen test data, it is useful to know the approximate apparent $G_{IIIc}(a)$. Note that even with the limited set of data for this material, a distinct variation of apparent G_{IIIc} with delamination length is evident.

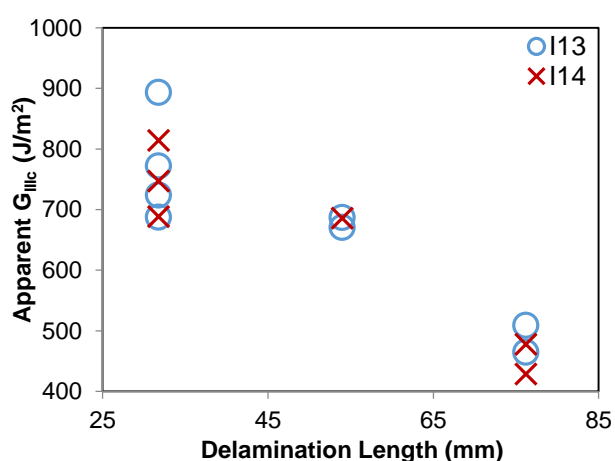


Figure 5.5. Apparent G_{IIIc} vs. delamination length for IM7/977-3.

Table 5.1. Delamination toughness data for IM7/977-3.

Delam. Length (mm)	Apparent G_{IIIc} (J/m ²)	CV (%)
32	760	9.7
54	681	1.3
76	469	7.1

5.3.2. Delamination Toughness Photomicroscopy

A photomicrograph of an IM7/977-3 specimen with delamination length $a = 32$ mm where the delamination front has advanced is shown in Figure 5.6. This photomicrograph was taken from one of the delamination toughness test specimens, and the delamination fronts of toughness test specimens with other delamination lengths look similar. The shape, size, and orientation of these matrix cracks agree with what was observed in Section 4.8.2 as well as for the IM7/8552 specimens tested in this study. This corroborates the conclusion in this earlier work that the presence of small intralaminar voids in the material, i.e., within plies, does not influence the onset or location of the matrix cracks. They also indicate that there are no apparent changes in the post-growth damage state as a result of the redesigned load tabs.

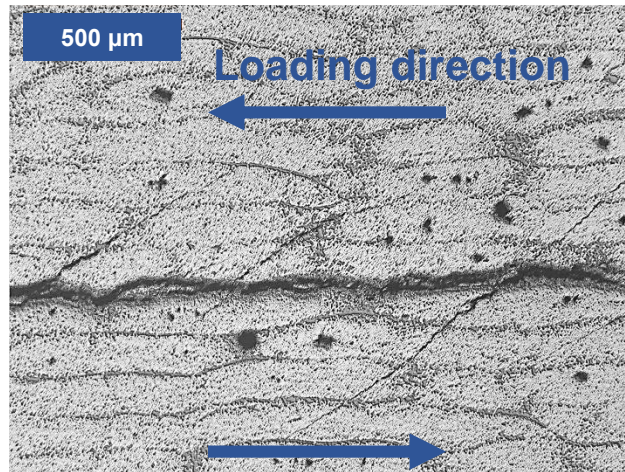


Figure 5.6. Photomicrograph of an IM7/977-3 delamination front, I13-7B, $a = 32$ mm, apparent $G_{IIIc} = 723$ J/m².

5.4. Damage Progression Testing

5.4.1. Damage Progression Test Results

Damage progression testing was performed on specimens of both materials and multiple delamination lengths. Four 26-ply IM7/977-3 specimens were tested at a delamination length of $a = 32$ mm and three specimens were tested at a delamination length of $a = 76$ mm. These tests were stopped prior to the onset of delamination growth, i.e., prior to the load plateau (cf. Figure 5.4), but otherwise were conducted identically to the delamination toughness tests. After testing, all specimens were c-scanned to verify that no growth occurred.

As described previously, the goals of the damage progression tests were to identify the onset and progression of matrix cracking and how this relates to delamination advance. To this end, damage progression tests were stopped at loads where the apparent G_{III} was less than the apparent G_{IIIc} obtained for specimens with the same delamination length. The specific points at which each test was stopped are presented in Table 5.2. As is evident from the table, the value of ERR where any test was stopped was equal to or greater than 73% of the apparent G_{IIIc} . This range was chosen to roughly coincide with the range in Figure 5.4 between the load plateau and the range of increasing in nonlinearity that was observed in the upper portion of the load versus displacement plots obtained from the apparent G_{IIIc} test specimens. It is important to note that, because of the delamination length dependency in apparent G_{IIIc} , tests on specimens with two different delamination lengths that were stopped at the same percentage of their respective G_{IIIc} were stopped at different values of apparent G_{III} .

Table 5.2. Damage progression test stopping points for IM7/977-3.

Spec.	Delam. Length (mm)	Apparent G_{III} at Test Stop (J/m^2)	Percent of Apparent G_{IIIc}
I14-10B	32	581	76
I14-9B	32	601	79
I13-11B	32	608	80
I14-12B	32	638	84
I13-9T	76	343	73
I14-3T	76	413	88
I13-10T	76	427	91

5.4.2. Damage Progression Photomicroscopy

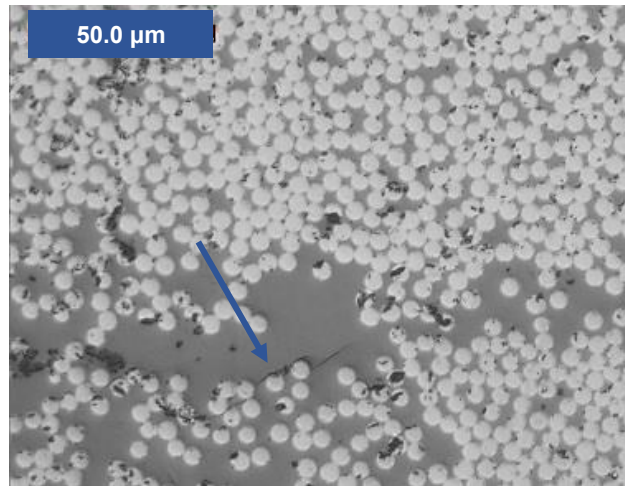
5.4.2.1. 26-ply IM7/977-3 Specimens

A series of photomicrographs obtained from IM7/977-3 damage progression specimens with delamination lengths $a = 76$ mm are presented in Figure 5.7. Note that these images are at approximately ten times higher magnification than the image in Figure 5.6. The three images in Figure 5.7 are from three different damage progression test specimens. All sections are taken just ahead of the Teflon insert, and no delamination advance occurred in any of these specimens. The images are ordered based on increasing maximum G_{III} . This is expressed in the figure caption as percentage of apparent G_{IIIc} , and the corresponding values of G_{III} are presented in Table 5.2.

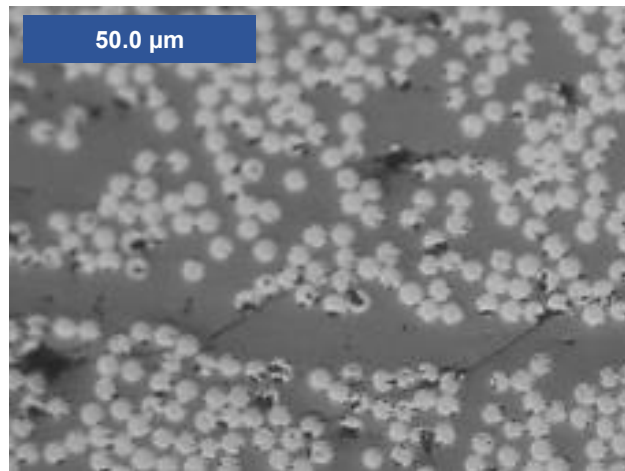
The specimen shown in Figure 5.7a, for which the maximum ERR was 73% of G_{IIIc} , primarily has matrix cracks in the resin rich interlayer ahead of the Teflon insert. In this figure, matrix cracks have just begun to initiate. Matrix cracks are present across the middle 25-75% of the specimen's width, and are concentrated in the center where the local ERR is highest. A few of the cracks extend one or two fiber diameters into one of the adjacent plies, but the majority are in the resin interlayer only. In general, the matrix cracks in this specimen, and in other

specimens loaded to similar levels, appear to initiate either at the interface between a fiber and the matrix material, or at small (fiber-diameter or less) voids within or immediately adjacent to the resin-rich region between plies. For example, the matrix crack indicated by the arrow in Figure 5.7a appears to have initiated at a small void between two fibers. The stress concentrations associated with these small local defects provide preferential initiation points for the cracks. However, the spacing of the cracks is not dictated by the void locations, and the matrix cracks initiate whether or not they are present. Thus, it is likely that their presence is not affecting the results. Additionally, while the local crack initiation may be at an angle other than 45° from the x-y plane based on the location or orientation of the defect, it may be observed in Figure 5.7a that the crack rapidly orients itself perpendicular to the direction of maximum tensile stress.

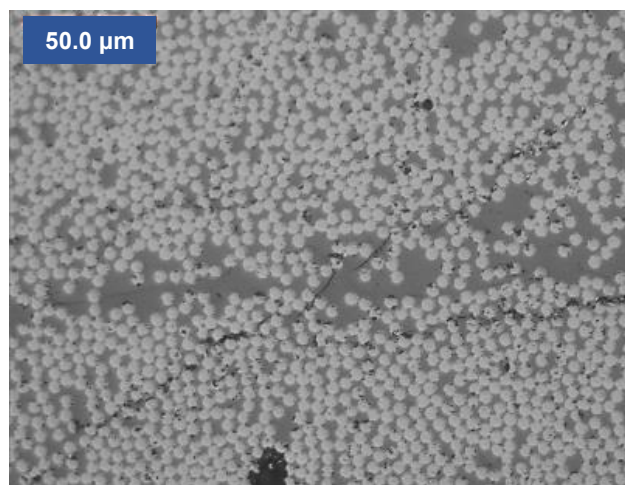
The specimen shown in Figure 5.7b was tested to 88% of G_{IIIc} . This figure shows the damage evolution that occurs with increasing load. In comparison to the specimen of Figure 5.7a, this specimen had a higher number of matrix cracks, and the distribution of cracks extended closer to the edges (middle 10-90% of width) than the specimen from Figure 5.7a. Additionally, the matrix cracks are seen to extend further into the plies, although they do not generally travel more than 10 fiber diameters.



(a)



(b)



(c)

Figure 5.7. Photomicrographs of IM7/977-3 delamination fronts, $a = 76$ mm. (a) I13-9T, 73% of apparent G_{IIIc} . (b) I14-3T, 88% of apparent G_{IIIc} . (c) I13-10T, 91% of apparent G_{IIIc} .

Figure 5.7c shows a specimen that was loaded to 91% of apparent G_{IIIc} . Matrix cracks were visible across the full width of this specimen and, as may be observed in the figure, extend through entire plies. The largest cracks were observed in the center region of the specimen where the ERR is highest (cf. Figure 4.6). Further, as can be seen on the right side of Figure 5.7c, some of the matrix cracks also have horizontal branches that extend along the mid-plane. In some instances these horizontal cracks intersect and connect two transverse (45°) cracks. However, this is not always the case, and there are many transverse cracks that have grown into the adjacent plies which do not have horizontal cracks associated with them. Those horizontal cracks that do occur, which were not observed in the specimens tested to lower loads, are the precursors to delamination advance.

The sequence of images of Figure 5.7 clearly shows how delamination advance evolves. With additional load, the entire “system of damage” of Figure 5.7c connects and advances to produce a state similar to that shown in Figure 5.6. Note, however, that the image in Figure 5.7c is prior to the conventional definition of delamination advance, i.e., as would be indicated by a plateau in the load-deflection response or as evident by c-scan. Combining this image with similar images from other damage progression specimens tested near their apparent G_{IIIc} indicates that a significant amount of matrix cracking always occurs prior to macroscopic delamination advance, and that near-tip matrix cracking and delamination advance are intrinsically coupled in this material.

5.4.2.2. 24-ply IM7/8552 Specimens

Damage progression tests for 24-ply IM7/8552 specimens were also conducted. Two specimens at delamination lengths of $a = 32$ mm and three specimens at delamination lengths of

$a = 76$ mm were tested. Photomicrographs of the resin interlayer region ahead of the Teflon insert for specimens with delamination lengths of $a = 76$ mm are shown in Figure 5.8. Figure 5.8a is at essentially the same percentage of apparent G_{IIIc} as the specimen shown in Figure 5.7a. The arrows in this figure point out four different cracks, all of which appear to initiate at a fiber/matrix interface. The crack sizes and spacings in this specimen were not significantly different from those observed in the specimen of Figure 5.7a. Combined with other images taken from the 24-ply IM7/8552 damage progression specimens, this figure indicates that the progression of damage is essentially the same for 24-ply IM7/8552 as for 26-ply IM7/977-3.

Figure 5.8b presents a photograph of a cross section that was approximately 0.25 mm ahead of the insert, i.e., within the uncracked region, and therefore further ahead of the insert than the images included previously. This specimen was loaded to 100% of apparent G_{IIIc} , i.e., the test was stopped at a value of apparent G_{III} equal to 262 J/m^2 , the same apparent ERR at which growth occurred in the delamination toughness test specimen. However, there was no evidence of delamination growth in this specimen: no load-plateau appeared, and a post-test c-scan did not show any differences from the pre-test scan. The arrows in Figure 5.8b are used to show the progression of the left-most transverse crack through its adjacent ply. Similar to Figure 5.7c, some of the cracks from the specimen in Figure 5.8b showed horizontal branches at the specimen's mid-plane, and in some instances these horizontal branches connected pairs of inclined cracks. Thus, the state of damage a short distance ahead of the insert is essentially the same as that found at the insert's end (Figure 5.7c), and clearly show that the matrix cracks grow into the uncracked region prior to delamination advance.

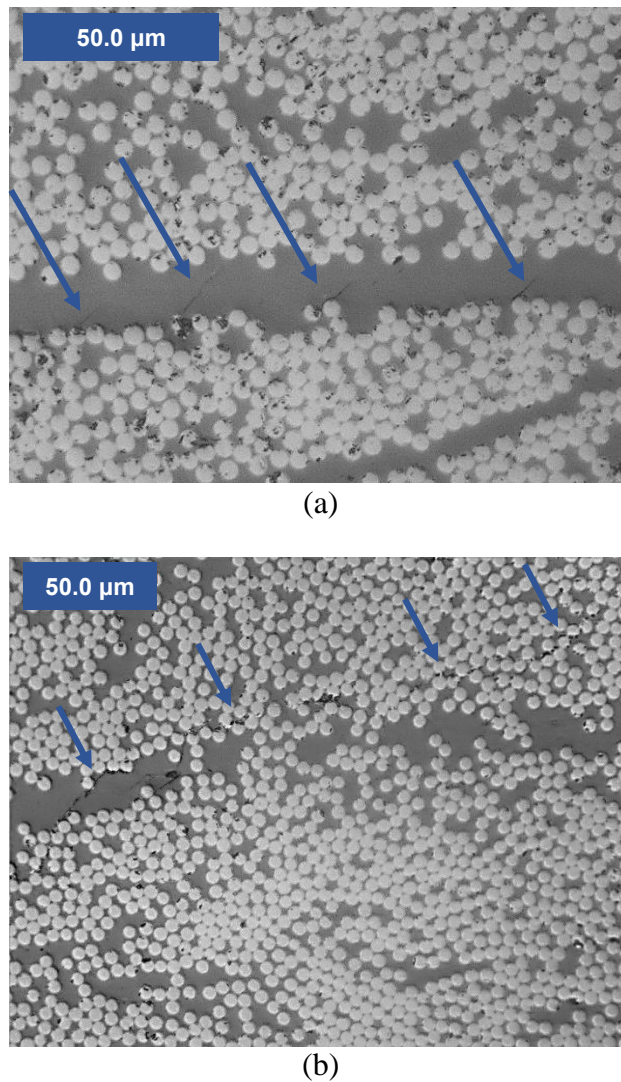


Figure 5.8. Photomicrographs of IM7/8552 delamination fronts, $a = 76$ mm. (a) J2-3, 75% of apparent G_{IIIc} . (b) J2-9, 100% of apparent G_{IIIc} .

5.4.3. Analysis of Damage Progression

The above observations indicate that matrix cracking will always precede planar delamination growth in unidirectional SST specimens in the materials tested and, as described below, it is likely that this will be true for other laminated unidirectional polymeric matrix composites. The matrix cracks form immediately ahead of the delamination front within the resin rich interlayer at a load well below that required for macroscopic delamination advance. As the

load continues to increase, these cracks grow transversely, at an inclination of approximately 45° , into their neighboring plies. Figure 5.8b shows that these cracks extend at least a small distance into the uncracked region and, although not investigated in this work, it is possible that they display the characteristic parahelical shape (Li et al., 2011; Palaniswamy and Knauss, 1978) observed in homogeneous materials. With increasing load these transverse cracks continue to grow through additional adjacent plies. Horizontal branches also initiate and grow along the laminate's mid-plane and begin to connect the transverse cracks. Initially, these do not extend into the uncracked region a sufficient amount to be detectable by c-scan, nor do they span the entire specimen width as viewed from the transverse cuts taken herein. This changes with increasing load, and these precursors to delamination advance ultimately connect and advance into the uncracked region in what is typically taken to be macroscopic delamination growth. This corresponds to the sequence of events given in Figure 5.7a, b, c, and finally Figure 5.6. It is possible that what actually occurs is mode II advance between the transverse matrix cracks in the specimen's width-wise direction Greenhalgh (2009), but this was not validated in the current study. It is clear, however, that an assumption of mode III advance of a single planar delamination does not accurately reflect the physical processes that occur.

An important observation related to the mechanistic understanding of the above behavior is that, in both materials used in this study, there is a visible similarity between the damage state in specimens with different delamination lengths that are at comparable percentages of their apparent $G_{IIIc}(a)$. For example, specimens I14-10B and I13-9T (cf. Table 5.2) are at similar values of apparent G_{III}/G_{IIIc} and are similar in terms of both length and number of matrix cracks. Note, however, that these two specimens were tested to very different values of apparent G_{III} . The same is true for a comparison of specimens I14-12B and I14-3T. This similarity could also

be expressed in terms of the percentage of average delamination onset load at any delamination length. What is interesting is that this correspondence cannot be expressed using conventional linear elastic fracture mechanics (LEFM) parameters, such as G_{III} or K_{III} , as one might expect if matrix cracking is used to explain the apparent dependence of toughness on delamination length. However, it is important to note that the predictions of ERR are based on an analysis that assumes an uncracked matrix, and these predictions are therefore only valid until matrix cracking initiates. At that point, local stress intensity factors associated with the newly formed cracks will change the near-tip field from that predicted by the original analysis.

It is possible that the true initiation of matrix cracking occurs at the same value of G_{III} for specimens with different geometries. This is what would be predicted by LEFM using an approach such as that employed by Leblond et al. (2011) for crack front instability under mixed-mode I-III loading. This could not have been deduced from the current study, however, as the lowest load for any damage progression test was 73% of the apparent $G_{IIIc}(a)$. This was done in an effort to first establish whether or not matrix cracks occurred prior to delamination onset. With this established, it appears that additional study would be required to deduce the exact onset point of matrix cracking. However, in order to mechanistically explain the observed dependence of toughness on delamination length, one would also need to perform analyses that account for the true state of damage evolution up to some critical state where macroscopic delamination advance occurs. Analysis of this type will be discussed in Chapter 7 and Chapter 8.

5.5. Extended Growth Testing

5.5.1. Extended Growth Test Results

Extended growth testing was conducted on IM7/8552 specimens with delamination lengths of $a = 32$ mm. One 24-ply specimen and one 48-ply specimen was utilized for the extended growth tests. These tests were continued past the onset of planar delamination growth, and were allowed to continue until approximately 14-16 mm of delamination advance had occurred.

5.5.2. Extended Growth X-ray CT and Photomicroscopy

5.5.2.1. 24-ply Specimens

X-ray CT and photomicroscopy results for the 24-ply extended growth specimens are presented in Figure 5.9 in the form of a sequence of images at different (x-direction) distances ahead of the insert tip, all of which are representative of the central region of the specimen's width. Figure 5.9a and b present photomicrographs from cross-sections 0.5 mm and 2 mm ahead of the insert tip, respectively. Figure 5.9c presents an X-ray CT image that is also from the cross-sectional plane 2 mm ahead of the insert tip, and the inset of Figure 5.9c shows the location at which the photomicrograph of Figure 5.9b was taken. The images in Figure 5.9c - f were obtained by X-ray CT, and all display the specimen's full 3 mm thickness. Note that the concentric arcs centered near the upper right corner of the X-ray CT images are artifacts of the X-ray CT process. In Figure 5.9a - e, the thick dark line near the specimen's centerline is the delamination, which is no longer evident in Figure 5.9f. The X-ray CT images showed no evidence of additional planar delamination growth beyond 16 mm, but the transverse matrix cracks extended an additional 2 mm ahead of the insert tip.

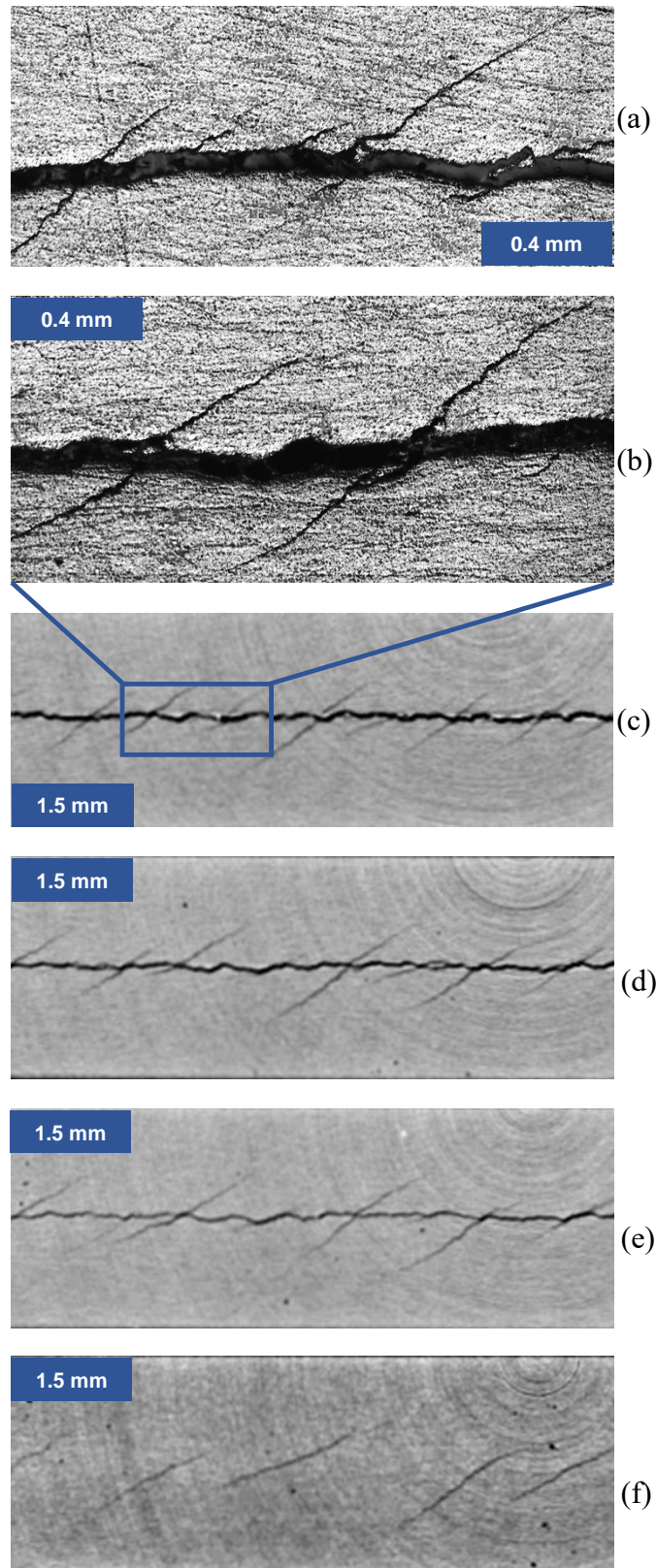


Figure 5.9. Images obtained from 24-ply SST specimen. (a) and (b) by optical microscopy, (c) – (f) by X-ray CT. Distances ahead of insert tip: (a) 0.5 mm, (b) 2 mm, (c) 2 mm, (d) 7 mm, (e) 11 mm, (f) 16 mm.

A comparison of all images in Figure 5.9 shows that the transverse matrix crack spacing increases with increasing distance ahead of the Teflon insert tip. As their spacing increases, however, so do their lengths. That is, there is a coarsening process, with, on average, many small, closely-spaced transverse cracks where planar delamination growth first initiates from the insert, and which gradually change to fewer, larger transverse cracks as the planar delamination grows. Further, as is most evident in the last few images in the sequence, the angles of the transverse cracks become increasingly shallow, and in some cases begin to develop a slight s-shape, as planar delamination growth progresses. The planar delamination remains at the mid-plane across the width of the specimen over the entire extent of growth. As noted previously from examinations of the many specimens with different delamination lengths in this work, as well as the damage progression test results such as those in Figure 5.7c, the transverse cracks always clearly precede the planar delamination in growing into the uncracked region.

In terms of the shape of the evolving structure across the specimen's width, the delamination advanced across the full width of the specimen for the first 12 mm of growth, and transverse matrix cracks covered the full width for the first 14 mm. From 12 mm – 16 mm the delamination is thumbnail-shaped, with the tip at 16 mm and the outer edges at 12 mm. The transverse crack profile, i.e., if one were to consider their lengths in x across the width y (cf. Figure 5.1a), is also thumbnail-shaped, and extends approximately 2 mm ahead of the delamination front at all width locations. Superposed onto this is the coarsening behavior described above. Quantitative assessments of coarsening, presented subsequently, utilized only the X-ray CT data. This was due to the different accuracies inherent in the microscopy versus X-ray CT evaluations. That is, a comparison of Figure 5.9b and c indicates that the X-ray CT is able to find larger transverse matrix cracks, but the smaller ones, such as near the right side of

Figure 5.9b, are not visible. Additionally, X-ray CT imaging also slightly under-estimates the length of each crack. However, quantitative comparisons made from these and similar figures indicated that the X-ray CT's accuracy was quite good for cracks above approximately 1 mm in length.

5.5.2.2. 48-ply Specimens

Figure 5.10 presents a sequence of images for the 48-ply, $a = 32\text{mm}$ IM7/8552 specimens, all of which were obtained by X-ray CT. These images show the entire 6 mm thickness, and are at similar distances ahead of the Teflon insert tip as those presented in Figure 5.9d-f. A comparison of the images shows that, particularly for the two sections furthest ahead of the Teflon insert tip, the transverse crack length is greater in the 48-ply than in the 24-ply specimens, and the spacing between cracks is also greater. Also, the “thumbnail portion” of the 48-ply specimen was somewhat smaller than in the 24-ply specimen. As in the 24-ply, the full width delamination ended 12 mm ahead of the insert tip. The region from 12 mm – 14 mm was thumbnail-shaped, i.e., the tip progressed 2 mm less into the uncracked region than in the 24-ply specimen. As in the case of the 24-ply specimen, the transverse crack profile was also thumbnail-shaped and extended approximately 2 mm ahead of the delamination front at all width locations, with similar coarsening behaviors.

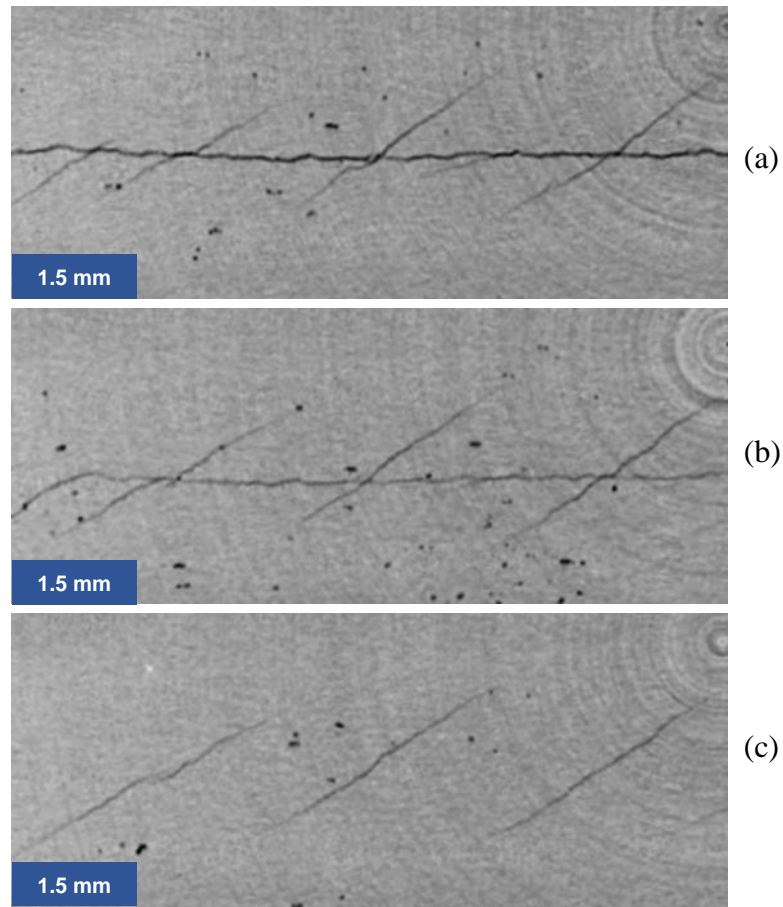


Figure 5.10. X-ray CT images from 48-ply SST specimen. Distances ahead of insert tip: (a) 6 mm, (b) 10 mm, (c) 14 mm.

5.5.3. Analysis of Extended Growth Testing

In order to compare coarsening behaviors in the different thickness SST specimens, graphical crack analysis was conducted on the X-ray CT images. Every visible crack in each image was counted and measured, and these measurements were taken in increments every 0.5 - 1.0 mm ahead of the Teflon insert tip until no transverse cracks were visible. Counting the number of cracks was straightforward, and crack measurement was conducted using a secant line approach. Here, where a straight line was superposed on each transverse crack, and the length of the matrix crack was approximated as the length of this line. Figure 5.11 presents plots of the

average transverse crack length (Figure 5.11a) and the number of transverse cracks (Figure 5.11b) versus distance ahead of the insert tip. As SST specimens are all the same width, the number of transverse cracks will be directly related to the average crack spacing. The vertical line on each plot in Figure 5.11 denotes the distance ahead of the insert after which there was no longer a full planar delamination. Beyond this point, the data are obtained only for the transverse cracks in the center region of the specimen that continued advancing.

Figure 5.11 indicates that transverse crack lengths are similar in the two specimen thicknesses for the first 5 mm ahead of the Teflon insert tip, but that there are more transverse cracks in the 24-ply specimen. Note that the transverse cracks within this region are fairly small, so the length and number results may be somewhat influenced by the resolution of the X-ray CT. Starting at a distance of 5 mm beyond the insert tip there is a divergence between the two sets of data in Figure 5.11a. The transverse cracks in the 48-ply specimens continue to grow in length at a reasonably similar rate, whereas there is only a small additional increase in length of the transverse cracks in the 24-ply specimen. The divergence occurs when the average crack length is approximately 1.5 mm, or 50% of the 24-ply specimen's thickness. It is likely that this occurs due to the proximity to the 24-ply specimen's free surface, as stresses, and therefore crack driving forces, must go to zero at the free surface. In contrast, the difference in the two data sets remains fairly constant in Figure 5.11, where more transverse matrix cracks are observed in the 24-ply specimen at any distance ahead of the insert tip. Both data sets show a gradual decrease in the number of cracks due to the coarsening process.

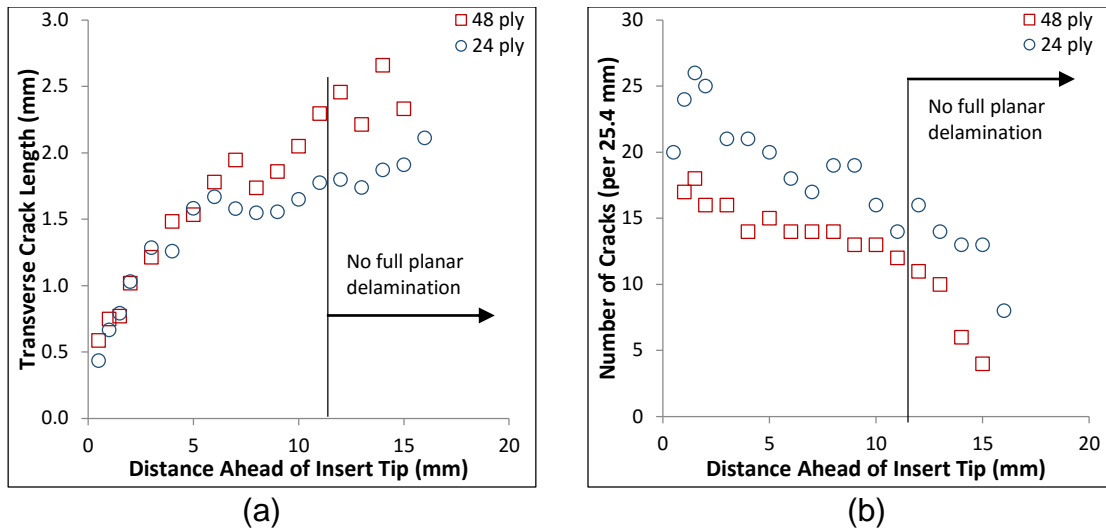


Figure 5.11. Crack surface evolution data for $a = 32$ mm SST specimens. (a) Average transverse crack length. (b) Number of transverse cracks detected.

5.6. Effect of Materials and Laminate Architecture on Fracture Surface

Development and Evolution

As described in Sections 2.3-2.4, results from the literature indicate that planar cracks in homogeneous and geologic materials subjected to anti-plane shear loading initially advance in the same manner as growth that initiates from the tip of the insert in SST specimens. That is, propagation of the planar crack initially occurs through the development of an echelon crack array oriented at approximately 45° to the original plane. The subsequent evolution of the fracture surface in homogeneous and geologic materials subjected to anti-plane shear has most commonly been studied under loadings that also produce some amount of crack opening or in which crack face compression occurs. Under these conditions, certain combinations of the spacing, length and orientation of the extending echelon array has been shown to cause some of the echelon cracks to be in regions of decreased stress and to arrest, and others to be in more

dominant stress regions and to extend (Pollard et al., 1982; Goldstein and Osipenko, 2012). This produces coarsening. Typically, this is also accompanied by an overall twisting of the crack path from its original plane to one that ultimately aligns with the echelon array (Pollard et al., 1982; Lazarus et al., 2001; Hull, 1993; Mróz and Mróz, 2010). All of these mechanisms lead towards the expected final transition to a single mode I crack. For the SST specimen, however, the crack surface evolution is different. One important reason for this is that the laminate's free surfaces bound the length of the transverse cracks. Thus, the energy-absorbing capacity of the transverse crack array is limited in comparison to homogenous materials. In addition, the longitudinal (0°) fibers constrain the original delaminated surface from gradually twisting to align itself with the transverse cracks, i.e., a significant amount of fiber breakage would have to occur in order for this to be accommodated. These observations indicate that it is unlikely that the SST will display a twisting crack path similar to that which often occurs in homogeneous materials. Rather, considering that the SST specimen contains a relatively weak interlaminar interface, the mechanism displayed – of the delamination extending along the interlaminar interface in the wake of the transverse crack array – would appear to be the most energetically favored.

5.7. Implication for Mode III SST Testing

For conventional SST laminates layups, where the orientation of the plies is aligned with the direction of “macroscopic delamination advance,” the first fracture events that occur will consist of the initiation and growth of cracks at an inclination of approximately 45° to the delaminated plane. With increasing load, these cracks will increase in number, grow, and branch along the plane of the preexisting planar delamination. What is typically taken as the macroscopic initiation event corresponds to a certain stage within the evolution and linkage of

these processes, rather than to a simple planar advance of the delamination along its original plane. Thus, similar to what has been observed in other materials, delamination advance in laminated polymeric matrix composites occurs via segmentation of the delamination front into multiple crack fronts. This produces a relatively rough surface with a “sawtooth” (Pons and Karma, 2010) profile that the geologic fracture literature refers to as echelon cracking (Pollard et al., 1982; Roering, 1968) and the literature on fracture of homogeneous materials refers to as being comprised of “lances” (Knauss, 1970; Sommer, 1969), “river lines” (Hull, 1995) and/or “facets” (Goldstein and Osipenko, 2012; Mróz and Mróz, 2010; Pons and Karma, 2010; Greenhalgh, 2009; Lazarus et al., 2001). The above growth behaviors bear some resemblance to what occurs during mode II delamination toughness testing of unidirectional specimens, where a “mode II delamination” also consists of a linking and coalescence of mode I events. The difference is that the plies bounding the delamination in a unidirectional mode II specimen constrain the microcracking to the interlaminar region (O’Brien, 1998), whereas in conventional SST specimens the bounding plies allow the microcracks to develop into intralaminar transverse cracks.

In terms of application to delamination toughness testing, the fracture surface evolution in SST specimens is clearly quite different than that assumed to occur. All current mechanistic models used to extract a mode III delamination toughness (including the assumptions used in a compliance calibration method of data reduction) are therefore invalidated, and the critical values of ERR that are obtained are inaccurate. Thus, a true delamination toughness cannot be extracted with this method or any method that assumes an uncracked matrix. In this light, the observed variations in apparent G_{IIIc} with delamination length in SST tests are perhaps not surprising, as a material property is not being measured. However, it is expected that the

calculated ERR may be reasonably accurate prior to the onset of transverse cracking, and it is possible that the apparent delamination toughness may still reflect a measure of the energy expended in the overall fracture and growth processes. The fact that it has not been possible to correlate the apparent toughness with the development of different fracture surfaces may be due to either (1) errors in extracting toughness from SST tests due to the data reduction method used, or (2) a missing piece to the understanding of fracture mechanisms in SST testing.

5.8. Conclusions

This chapter described a study to determine the manner in which the progression of damage and development of fracture surfaces occurs in the mode III split shear torsion delamination toughness test. To this end, specimens from two different carbon/epoxy materials were tested in an SST fixture using an improved test geometry compared to that introduced in Chapter 4. A series of tests examining damage progression found that the first inelastic event consists of the initiation of near-tip matrix cracks within the resin rich region between plies. These cracks were inclined to the direction of loading and were perpendicular to the direction of maximum tensile stress. With increasing load, they were observed to extend into the neighboring plies above and below the plane of the delamination as well into the uncracked region ahead of the original delamination front. A network of crack branches that were essentially parallel to the delamination front was also observed to develop. All of these processes occurred prior to any observations or indications of planar delamination advance, which helps explain the apparent delamination toughness dependency initially described in Chapter 4. Thus, what has heretofore been referred to as “mode III advance” in laminated composites actually reflects an intrinsically coupled process of near-tip matrix crack formation and growth that occurs prior to any advance

of the planar macrocrack, and is quite similar to processes previously identified in homogeneous and geologic materials.

A series of tests examining fracture surface evolution produced clear differences that caused the fracture surfaces that develop in composite laminates to differ from those in homogeneous materials. The first is that composite laminates contain energetically preferential fracture paths along interlaminar interfaces. The second is that the laminate's fibers constrain the fracture surface from twisting as the planar delamination advances. The third is that the amount by which transverse cracks can extend in a laminate is determined by the proximity of the preimplanted insert to the laminate's free surfaces.

As a direct consequence of the events determined in damage progression testing, ERR predictions that are based on any mechanistic model or set of assumptions that considers an uncracked matrix will no longer be accurate once any appreciable amount of near-tip damage has occurred. However, it has not been possible to correlate the damage observations presented in this chapter to the measured variations in $G_{IIIc}(a)$. It therefore appears the dependency of apparent toughness on geometry has not been fully explained and could be due to errors in the toughness data reduction technique or a lack of full understanding of the mechanisms of fracture in these specimens. This will be addressed in Chapter 6.

Chapter 6. Effects of Split-Beam Specimen Twisting

6.1. Introduction

It has been shown in Chapter 4 and Chapter 5 fracture in SST specimens initially occurs via the initiation of transverse matrix cracks that are inclined at an angle to the delamination plane. This initiation process is similar to that which occurs in homogeneous and geologic materials subjected to anti-plane shear loading, where an array, or echelon, of cracks initially develops along the original crack front (Roering, 1968; Knauss, 1970; Li et al., 2011; Pollard et al., 1982; Goldstein and Osipenko, 2012A; 2012B). For homogeneous materials, macroscopic advance of the system occurs via extension of this echelon array. This requires the initial crack front to fragment into a series of segments. The evolution of this system therefore produces a fracture surface that shows segmentation and macroscopic rotation towards the maximum tensile stress direction (Pollard et al., 1982; Goldstein and Osipenko, 2012A; 2012B; Cox and Scholz, 1988; Makabe et al., 2006; Mróz and Mróz, 2010). Similar behaviors occur under mixed mode I-III loadings of homogeneous materials (Roering, 1968; Pollard et al., 1982; Lin et al., 2010; Pons and Karma, 2010; Leblond et al., 2011), where it has recently been shown that any non-zero mode III component will induce this fragmentation (Pham and Ravi-Chandar, 2014). In contrast, it has been shown in Chapter 5 for the SST and by Czabaj et al. (2014) for the ECT that both the echelon array and the planar delamination advance in laminated composites, with the echelon array leading the planar delamination (Johnston and Davidson, 2014; Horner et al., 2015). The differences in fracture surface evolution between composite and homogeneous materials were shown to occur due to the composite's propensity for delamination growth along an interlaminar interface, the limitations on transverse crack size created by the relatively thin nature of the

composite fracture specimens, and the energetic restrictions on fracture path twisting due to the laminate's fibers.

While corroborating results have been presented using the ECT test (Czabaj et al., 2014; Horner et al., 2015), many of the preceding conclusions were obtained herein via the SST test, which utilizes a split beam type geometry. It has been shown in Chapter 4 and Chapter 5 that this test produces an apparent mode III delamination toughness, G_{IIIc} , which decreases with increasing delamination length. Interestingly, it was observed during these experiments that the rotation, or angle of twist, of the uncracked portion of the SST specimen also increases with increasing delamination length. This motivated an additional study, designed to understand whether specimen twisting affects the toughness and/or the way in which the fracture surface evolves. As will be shown subsequently, a reevaluation of the earlier results in Chapter 4 and Chapter 5 indicated that twisting introduces a mode I component of the energy release rate that is proportional to the angle of twist. This led to the conclusion that the SST test actually induces mixed mode I-III loading conditions, where – for a specimen of a given thickness – the percentage of mode I that is present increases with increasing delamination length.

To further study the above, SST specimens with different thicknesses and delamination lengths were manufactured and tested. These geometries were chosen to produce different amounts of specimen twisting prior to fracture. The load at the onset of delamination growth was used to obtain the apparent toughness. The associated angle of twist of the delamination front was measured using digital image correlation and used to obtain the mode mixity. Subsequent to testing, specimens were sectioned transversely, and optical microscopy was used to observe the details of transverse cracking and delamination advance. These results were used to determine the relationships between specimen twist, mode mixity, apparent toughness, and fracture surface

evolution. These relationships are used to extract an improved understanding of the mechanisms responsible for the decrease in apparent toughness with increasing delamination length that has been observed in SST testing. They also reinforce findings in Chapter 5 on the reasons for the different fracture surface evolutions that occur in homogeneous materials in comparison to unidirectional laminated composite delamination toughness test specimens. Finally, a synthesis of current and previous results is used to make recommendations regarding future mode III delamination toughness testing of laminated composites.

6.2. Test Design

6.2.1. Test Geometry and Specimen Preparation

Figure 6.1 presents exactly the same schematic representation of the SST test as that presented in Figure 5.1. As before, the specimen is unidirectional with all plies oriented in the x -direction. It contains a pre-implanted insert at its mid-plane that spans the specimen's width, B , and which creates a starter delamination of length a . As shown in the figure, load is introduced to the specimen through loading tabs and blocks. The upper load block (so-named as it attaches to the upper portion of the load frame) is fully constrained, and the lower load block is constrained such that only vertical translation may occur. Thus, both shear and torsional loadings are transmitted to the specimen. To maintain static equilibrium, the load blocks in the SST test produce a restoring torsional moment about the x -axis that is transmitted into each of the cracked regions. This produces an equal rate of twist in each cracked region, and therefore an angle of twist that increases linearly with distance from the load block. The restoring moments and torque produced by the applied load equilibrate to produce a load- and torsion-free uncracked region. Therefore, the angle of twist does not change within the uncracked region, but rather equals the

value in each of the cracked regions at the delamination tip. The direction of twist is indicated in Figure 6.1. Similar behavior occurs in the modified split cantilever beam (MSCB) specimen (Szekrényes, 2009; 20011). In both tests, this produces an angle of twist of the uncracked region that, for a given applied load, increases with increasing delamination length.

Unidirectional IM7/8552 pre-preg tape was used to make all specimens for this portion of the study. Twenty four- and 48-ply SST specimens with nominal thicknesses, $2h$, of 3.0 mm and 6.0 mm were fabricated for this study. The fabrication procedure followed that described in Section 4.4.1 and 5.2.2. Here, Teflon inserts that were 13 μm thick and with lengths varying from 70 – 150 mm were implanted at the laminate's mid-plane during layup in order to produce specimens with delamination lengths, a , of 32 – 127 mm. All SST specimens were nominally sized to have widths, B , of 25 mm. These geometries were chosen to produce different amounts of specimen twisting prior to fracture.

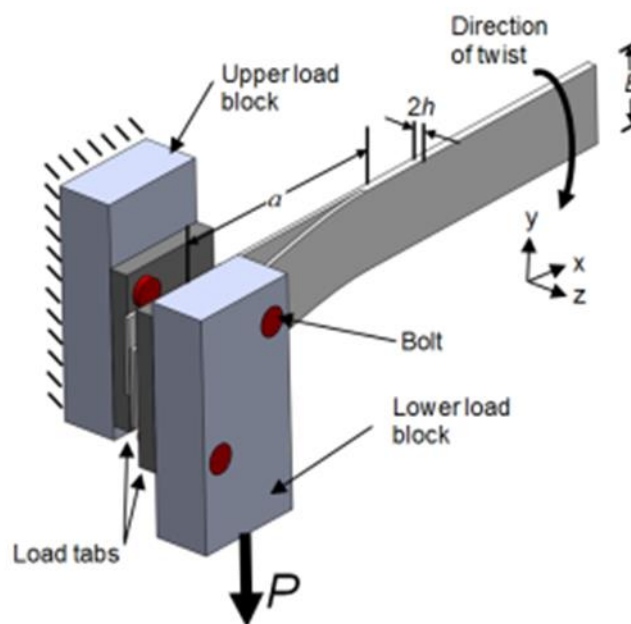


Figure 6.1. Schematic of SST test geometry and loading.

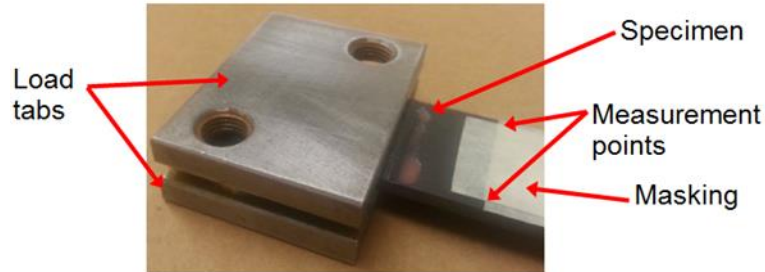


Figure 6.2. Photograph of masked, tabbed SST specimen with $a = 32$ mm.

6.2.2. Specimen Rotation Measurement

Before testing, each SST specimen was masked using opaque tape as shown in Figure 6.2. One piece of tape is aligned with the delamination front and covers the entire width of the specimen. The other is oriented perpendicularly and is aligned to cover the majority of the specimen's width while leaving the outside edges unmasked. The intersections of the masking creates two corners that are used as reference points.

In order to visually capture changes in specimen rotation during testing, a digital camera is clamped to the test fixture platen of Figure 5.3. The camera lens is oriented orthogonally to the plane of the specimen, and is focused at the two reference points created by masking the specimen. The camera remains fixed in this location throughout the test. To begin the data acquisition process, an initial reference image of the unloaded specimen is taken. Images are then taken during testing approximately every 200 N, and again when the peak load is reached. Additional images are also captured during the specimen unloading, and a final image is taken once the specimen is fully unloaded.

The images captured during testing are evaluated using graphical analysis software. First, the distance between the masked corners is measured in pixels for the pre-test reference image.

The distance between these two corners is then measured for each subsequent image. The difference between the reference distance and the distance measured for a given image is then used to determine the angle of twist of the specimen at each load.

6.2.3. Transverse Crack Measurement

In order to observe transverse cracks, SST specimens were destructively sectioned subsequent to testing using a diamond-tipped low-speed cut-off saw. Specimens were sectioned just ahead of the initial delamination tip created by the Teflon insert and/or at various specific locations ahead of the insert tip, consistent with the techniques in Section 4.8.3 and Section 5.2.4.2. These section cuts were made transverse to the direction of planar delamination growth, such that the specimens' y-z planes were exposed. Cut sections were then potted in epoxy, polished, and viewed under a differential interference contrast (DIC) reflected light microscope. Photomicrographs of close-up sections were taken across the entire cross section, and later stitched together such that a full view of the transverse section was available for analysis. These sections were used to determine the progression of the transverse matrix crack development and their interactions with the planar delamination as the entire system evolved. This evolution was subsequently correlated to an associated angle of twist.

6.3. Analyses

6.3.1. Energy Release Rate and Mode Mixity

In Chapter 4 and Chapter 5, energy release rate (ERR) distributions for various SST specimens were determined using 3D linear finite element (FE) analyses. In these works, the virtual crack closure technique (VCCT) (Rybicki and Kanninen, 1977; Krueger, 2004) was used

to partition the ERR, G , into its mode I, II, and III components in terms of the undeformed coordinate system, depicted using (y, z) in Figure 6.3. Figure 6.3b shows the cross-section at the delamination tip in its deformed state. This figure introduces a (y', z') system and the angle ϕ between the two coordinate systems. The (y', z') coordinate system defines the orientation of the delamination tip during deformation. The angle ϕ is a function of the applied load, P , and defines the angle of twist of the delamination tip and of the uncracked region.

Considering the geometry of Figure 6.3 and assuming solely planar delamination advance, Section 4.5.1 showed that growth will initiate in the center of the specimen ($y=0$) where the ERR is a maximum. It was further shown that pure mode III conditions exist at this location. Considering the VCCT calculations (Krueger, 2004), this means that in the center of the specimen, only the multiplication associated with the y -components of the near-tip forces and displacements produce non-zero contributions to G . However, these analyses were performed with respect to the undeformed coordinate system. Transforming the y -components of force and displacement into the (y', z') system yields non-zero mode I and mode III components of ERR, G_I and G_{III} , respectively, as

$$G_I^{(y',z')} = G^{(y,z)} \sin^2 \phi ; \quad G_{III}^{(y',z')} = G^{(y,z)} \cos^2 \phi \quad (6.1)$$

From Equation (6.1), the mode mixity, defined here with respect to the primed coordinate system, is given by

$$G_{III}^{(y',z')} / G_I^{(y',z')} = \cot^2 \phi \quad (6.2)$$

and is independent of the value of the total ERR. However, note that, in terms of the (y, z) coordinate system, $G_I = 0$ for all values of y , that is, $G_I^{(y, z)} = 0$ along the entire delamination front,

as discussed in Section 4.5.1 and determined by Johnston et al. (2014). Therefore, the value of $G^{(y, z)}$ in Equation (6.1) may be taken as $G_{III}^{(y, z)}$, at any value of y , as obtained from the linear FE analyses of SST specimens using the undeformed (y, z) system. $G_I^{(y', z')}$ and $G_{III}^{(y', z')}$ in Equation (6.1) then give the corresponding values in the more physically appropriate (y', z') system. In this manner, the transformation given by Equation (6.1) may be used for all elements along the delamination front. The small mode II components that arise (cf. Figure 4.6c) are unaffected by this transformation. Note that fundamentally, the ERR must be defined with respect to the (y', z') system. Thus, unless otherwise specified, all subsequent discussions of the ERR will be with respect to this system, and the superscripts “ (y', z') ” will be omitted.

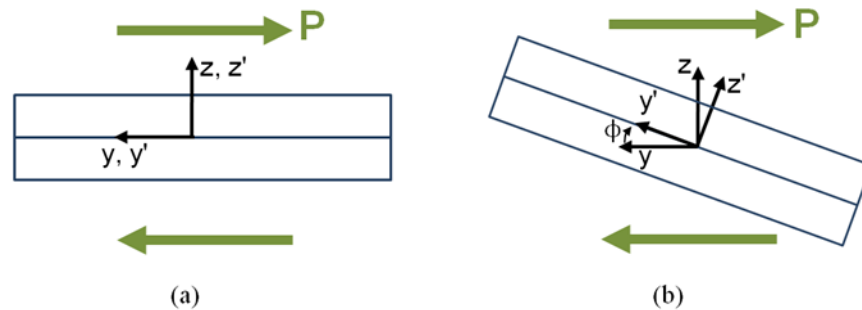


Figure 6.3. Schematic showing orientation of SST specimen cross-section (a) before and (b) after deformation.

6.3.2. Apparent Toughness

In Section 4.5.3 it was shown experimentally that planar delamination advance always initiates in the center of an SST specimen, where the ERR is a maximum, at the maximum value of load achieved during the test. Therefore, defining the delamination onset load as the maximum value of load during the test, the apparent toughness has been based on the center, or peak value, of ERR at this load. Fundamentally, this has been achieved by using the maximum load from the test along with a FE model of the test and specimen to determine the peak ERR. However, rather than perform a FE analysis of each individual specimen, an equation has been used that has been calibrated to multiple FE. This equation, which yields the ERR in the center of the specimen in terms of the (y, z) coordinate system, is given by

$$G = C_f(a, h) \frac{P^2}{B^2 h G_{12}} \left(0.66 + 1.15 \sqrt{\frac{G_{12}}{E_{11}}} \right) \quad (6.3)$$

As in Chapter 4 and Chapter 5, P is the applied anti-plane shear load, B is the specimen width, and h is the specimen half thickness. E_{11} is the modulus in the fiber direction, and G_{12} is the in-plane shear modulus, given for the IM7/8552 used in this work in Section 5.2.2. $C_f(a, h)$ is a correction factor that depends on thickness and delamination length. It is extracted from a FE analysis of a single specimen for each geometry tested. Values for $C_f(a, h)$ used in this chapter are listed in Table 6.1. Note that this is equivalent to the correction factor introduced in Section 5.2.4.1, but in this case a variety of new delamination lengths and thicknesses are included.

For a delamination toughness test, G_c is calculated from the delamination onset load using Equation (6.3), and the mode mix is computed from the measured angle at that load, ϕ , and

Equation (6.2). However, as shown in Section 5.4, the onset of matrix cracking occurs prior to the onset of planar delamination growth. It was further discussed in Section 5.7 that while it is expected that the calculated ERR is reasonably accurate prior to the onset of transverse cracking, the value of G_c that is extracted by the above approach cannot be used to determine a valid toughness subsequent to transverse crack initiation. It is expected, however, that G_c will still reflect a measure of the energy expended in the overall growth process that is useful for the comparison of the various geometries to each other and to previously reported results, and it is in this sense that it is used subsequently.

6.3.3. Stress Intensity Factors

Stress intensity factors for SST specimens can be determined from the components of ERR given by Equation (6.1). The relationships between G_i and K_i ($i=I, II, III$) for orthotropic materials are given by Suo (1990) and Bao et al. (1992) in a traditional coordinate system, where y is the thickness and z the width direction. Hu (1995) transformed these equations to the conventional laminated plate theory coordinate system used in Figure 6.1 and Figure 6.3 (Whitney, 1987), where they were applied to cracks between two dissimilar orthotropic materials. For a single, homogeneous, transversely isotropic material, they reduce to

$$K_I = \sqrt{\frac{4 G_I}{H_{11}}}, \quad K_{III} = \sqrt{\frac{2 G_{III}}{H_3}} \quad (6.4)$$

where

$$H_3 = \frac{1}{\sqrt{G_{23}G_{12}}} \quad (6.5)$$

and for $\sigma_{y'y'} = 0$

$$(6.6)$$

$$H_{11} = 2 \left\{ 2 \sqrt{\frac{1}{E_{11}^3 E_{33}}} \left(1 + \left(\frac{1}{2G_{13}} - \frac{\nu_{13}}{E_{11}} \right) \sqrt{E_{11} E_{33}} \right) \right\}^{1/2}$$

whereas for $\varepsilon_{y'y'} = 0$

$$H_{11} = 2 \left\{ 2 \sqrt{\left(\frac{1}{E_{11}} - \frac{\nu_{13}^2 E_{33}}{E_{11}^2} \right)^3 \left(\frac{1}{E_{33}} - \frac{\nu_{23}^2}{E_{33}} \right)} \left(1 - \frac{\frac{\nu_{13}}{E_{11}} + \frac{\nu_{13}\nu_{23}}{E_{11}} - \frac{1}{G_{13}}}{\sqrt{\left(\frac{1}{E_{11}} - \frac{\nu_{13}^2 E_{33}}{E_{11}^2} \right) \left(\frac{1}{E_{33}} - \frac{\nu_{23}^2}{E_{33}} \right)}} \right) \right\}^{1/2}$$

(6.7)

In the above, conventional laminated plate theory notation is used (Whitney, 1987). For isotropic materials, these reduce to the more familiar relationships

$$K_I = \sqrt{E' G_I}, \quad K_{III} = \sqrt{2\mu G_{III}} \quad (6.8)$$

where $E' = E$ for $\sigma_{y'y'} = 0$, and $E' = E/(1-\nu^2)$ for $\varepsilon_{y'y'} = 0$. Here, E is the Young's modulus, ν is the Poisson's ratio, and μ is the shear modulus.

6.3.4. Transverse Crack Angle

In this work, transverse crack orientation will be measured experimentally and correlated to predictions based on the calculated mode I-III conditions at the delamination front. To make these predictions, the most promising criterion from Section 2.4.2.1 were considered. The minimum strain energy density (SED) criterion (Sih et al., 1962; Sih, 1974), maximum ERR criterion (Erdogan and Sih, 1963; Lawn, 1993), and maximum principal tensile stress (MPTS) criterion (Lin et al., 2010; Pons and Karma, 2011; Pham and Ravi-Chandar, 2014; Cooke and

Pollard, 1996; Yates and Miller, 1989) were all considered. Sih (1974) showed that the minimum SED criterion predicts a crack rotation angle of 0° , that is, no rotation at all, for mode III loading. As such, this criterion is considered insensitive to mode III loading Sih (1974), and is not appropriate for this work. Therefore only the MPTS and max ERR criterion were considered further. Considering the maximum ERR criterion, Cooke and Pollard (1996) showed that this criterion exhibits a bifurcation at a value of K_{III}/K_I that depends on material properties. As shown in Appendix C, predicted crack angles by the maximum ERR criterion agree with those from the MPTS criterion prior to this bifurcation. Subsequent to it, the maximum ERR predictions are different and contain two branches whose meanings are unclear and whose results are contradicted by experiment. Consequently, in this work the MPTS criterion is adopted. A full derivation of the MPTS criterion with orthotropic material properties can be seen in Appendix D.1.

Formulating the MPTS criterion for orthotropic material properties yields the predicted echelon array crack angle, θ , as

$$\theta = \frac{1}{2} \tan^{-1} \left(\frac{K_{III}}{\frac{1}{2} K_I (1 - \gamma)} \right) \quad (6.9)$$

where $\gamma = 0$ for $\sigma_{y'y'} = 0$, and, for $\varepsilon_{y'y'} = 0$

$$\gamma = \frac{v_{12} E_{22}}{E_{11}} + v_{23} \quad (6.10)$$

For isotropic materials, Equation (6.10) reduces to the more familiar form $\gamma = 2\nu$ (Cooke and Pollard, 1996). For comparison to experimental results, a predicted echelon crack orientation may be obtained from the measured specimen rotation angle ϕ by substituting Equation (6.1) and Equation (6.4) into Equation (6.9), resulting in

$$\theta = \frac{1}{2} \tan^{-1} \left(\sqrt{\frac{2H_{11}}{H_3} \frac{\cot \phi}{(1-\gamma)}} \right) \quad (6.11)$$

6.4. Results

6.4.1. Apparent Toughness Tests

At least three delamination toughness tests were performed on each of the SST geometries of Table 6.1. These specimens came from two different 24-ply plates (designated as plates J4 and J6) and a single 48-ply plate (J5). The apparent toughness, calculated using Equation (6.3) and the appropriate value of $C_f(a,h)$ from Table 6.1, is plotted versus specimen rotation angle at the onset of delamination growth in Figure 6.4a, and versus mode mixity at the onset of growth in Figure 6.4b. The plates from which the 24-ply specimens were cut are also provided in these figures, from which it is concluded that no significant plate-to-plate variations occurred. Although delamination length is not explicitly shown in Figure 6.4a, for each specimen thickness, the angle of rotation at the onset of growth increased with increasing delamination length. Also, at a given delamination length, the 48-ply specimens showed less rotation but higher apparent toughnesses than the 24-ply specimens, and these differences became more pronounced with increasing delamination length. By plotting the results in the manner shown in Figure 6.4a, it may be observed that the apparent toughness correlates well with the amount of rotation at the onset of growth, regardless of specimen thickness or delamination length. Using the analyses above, Figure 6.4b shows the underlying cause: SST tests that have heretofore been interpreted as essentially mode III, as in Chapter 4 and Chapter 5, actually produce mixed mode I-III conditions. Figure 6.4a and b combined show that the amount of mode I increases with increasing amounts of rotation, and that the apparent toughness correspondingly decreases.

Likewise, small rotations are associated with larger apparent toughnesses and larger mode III components, and Figure 6.4b appears to show the apparent toughness approaching an asymptotic value as the rotation angle, and percentage of G_{III} , becomes small.

Table 6.1. Geometries tested and associated correction factors for ERR determination.

Delamination Length, a	32	70	127	32	70
Thickness, $2h$ (mm)	3.0	3.0	3.0	6.0	6.0
$C_f(a,h)$	1.93 ¹	3.72	5.70	2.24	4.02

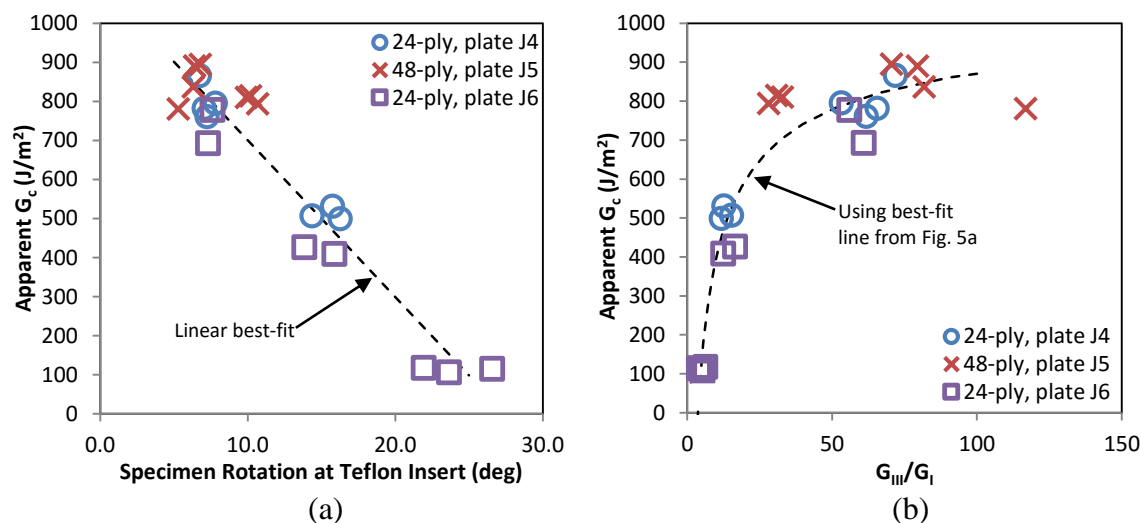


Figure 6.4. Plots of apparent G_c versus (a) specimen rotation at delamination tip, (b) mode mixity.

¹ The value of 1.98 published in Horner and Davidson (2015) was a typographical error.

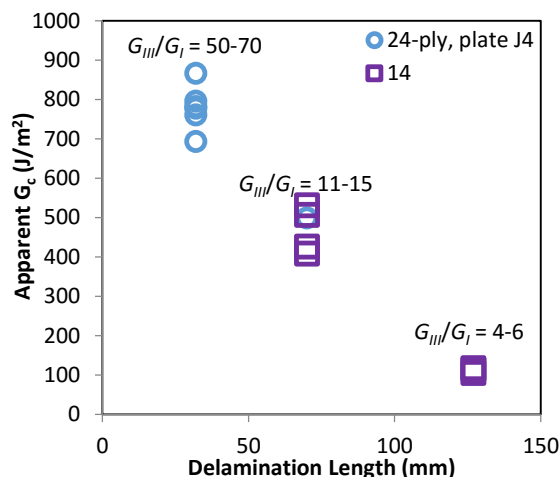


Figure 6.5. Plot of apparent G_c versus delamination length for 24-ply specimens.

Figure 6.5 presents apparent toughness data for the 24-ply specimens versus delamination length. Additionally, the range of G_{III}/G_I calculated for the specimens of each delamination length is noted above each set of data. Data for the 48-ply specimens is in agreement with the data presented in Figure 6.5. These results agree with those of Figure 4.11 and Figure 5.5, where apparent toughness decreases with increasing delamination length. It can now be seen that this trend is directly related to specimen rotation and the ratio of G_{III}/G_I .

At the smallest values of G_{III}/G_I shown in Figure 6.4 and Figure 6.5, the lowest apparent toughness that was measured is below the IM7/8552 mode I delamination toughness of approximately 200 J/m^2 (Czabaj and Ratcliffe, 2013). However, as discussed in Section 5.4, the near-tip transverse cracks initiate well before the onset of delamination advance in these specimens and, for all geometries, the point of macroscopic advance reflected in the apparent toughness represents the growth of the coupled system of transverse cracks and the planar delamination after the transverse cracks have initiated. Note that this physical system has some unknown distribution of ERR and mode mixity along the segmented delamination front and along the boundaries of the transverse cracks. However, the model that is used to extract

toughness does not include these features and the only experimental input to this model is the critical load from the test. Therefore, the approach that has been employed does not reflect any additional toughening (energy absorption) due to the presence of the transverse cracks, nor does it reflect any early growth behaviors due to possible high energy release rate and/or high mode I localizations that may occur due to the presence of the transverse cracks. This methodology is a direct extension of that used thus far in this dissertation and agrees with that used historically for other composite split beam type anti-plane shear tests (Davidson and Sediles, 2011; Szekrényes, 2009; 2011). Therefore, it is used here for continuity with previous results and to provide insight into the reasons for the geometry dependence that has been observed in this and similar tests. Thus, the toughness calculations do not fully represent the physical situation, and clearly cannot be interpreted in the conventional sense as the conditions necessary for the advance of a single planar delamination. For this reason, the term “apparent toughness” has been utilized. As described above, this apparent toughness provides a convenient relative measure to compare the results of the different geometries tested herein to each other and to those previously reported.

6.4.2. Effect of Geometry on Matrix Cracking

Figure 6.6 presents photomicrographs from three 24-ply SST specimens tested with different delamination lengths. These sections are from a plane approximately 2 mm ahead of the Teflon insert tip in each specimen (cf. Figure 5.6), where the fracture surfaces are well developed. Each image also shows the value of G_{III}/G_I at which planar delamination advance occurred, calculated from the associated specimen rotation angle using Equation (6.2). All three sections shown in Figure 6.6 display the coupled matrix cracking and planar delamination that is expected for unidirectional SST specimens. The thick, jagged path running horizontally is the

interlaminar delamination, which is at the mid-plane of the specimen. These photomicrographs display approximately 8 plies of material, although the ply interfaces are not distinct. Also evident are a number of matrix cracks emanating from the mid-plane. These matrix cracks extend both above and below the mid-plane, and their growth is unaffected by the locations of the ply interfaces for all geometries. However, it is clear from Figure 6.6 that the fracture surfaces are evolving differently within the three geometries. For the 24-ply, $a = 32$ mm specimen shown in Figure 6.6a, G_{III}/G_I is relatively high, and the transverse matrix cracks emanate from the mid-plane in approximately straight lines at angles close to 45° . It is pointed out that the fracture surfaces of 48-ply specimens of both $a = 32$ mm and $a = 70$ mm, where G_{III}/G_I is also typically high, look very similar to the fracture surface presented in Figure 6.6a.

For the 24-ply, $a = 70$ mm specimen shown in Figure 6.6b, where G_{III}/G_I is notably lower, the transverse cracking behavior is different. Here, large transverse cracks clearly emanate from the mid-plane, but there are also small branch cracks extending from the mid-plane and intersecting the larger matrix cracks, as noted by the arrows in this figure. Additionally, while the transverse matrix cracks are very straight in Figure 6.6a, in Figure 6.6b they are more s-shaped. Because of this, the vertical height of the matrix cracks in the $a = 70$ mm specimens may be limited, as after some amount of growth these cracks are more likely to turn, and in some cases extend a short amount horizontally. Note that there is no apparent propensity for the horizontal extension of the transverse cracks to occur at the interlaminar interfaces.

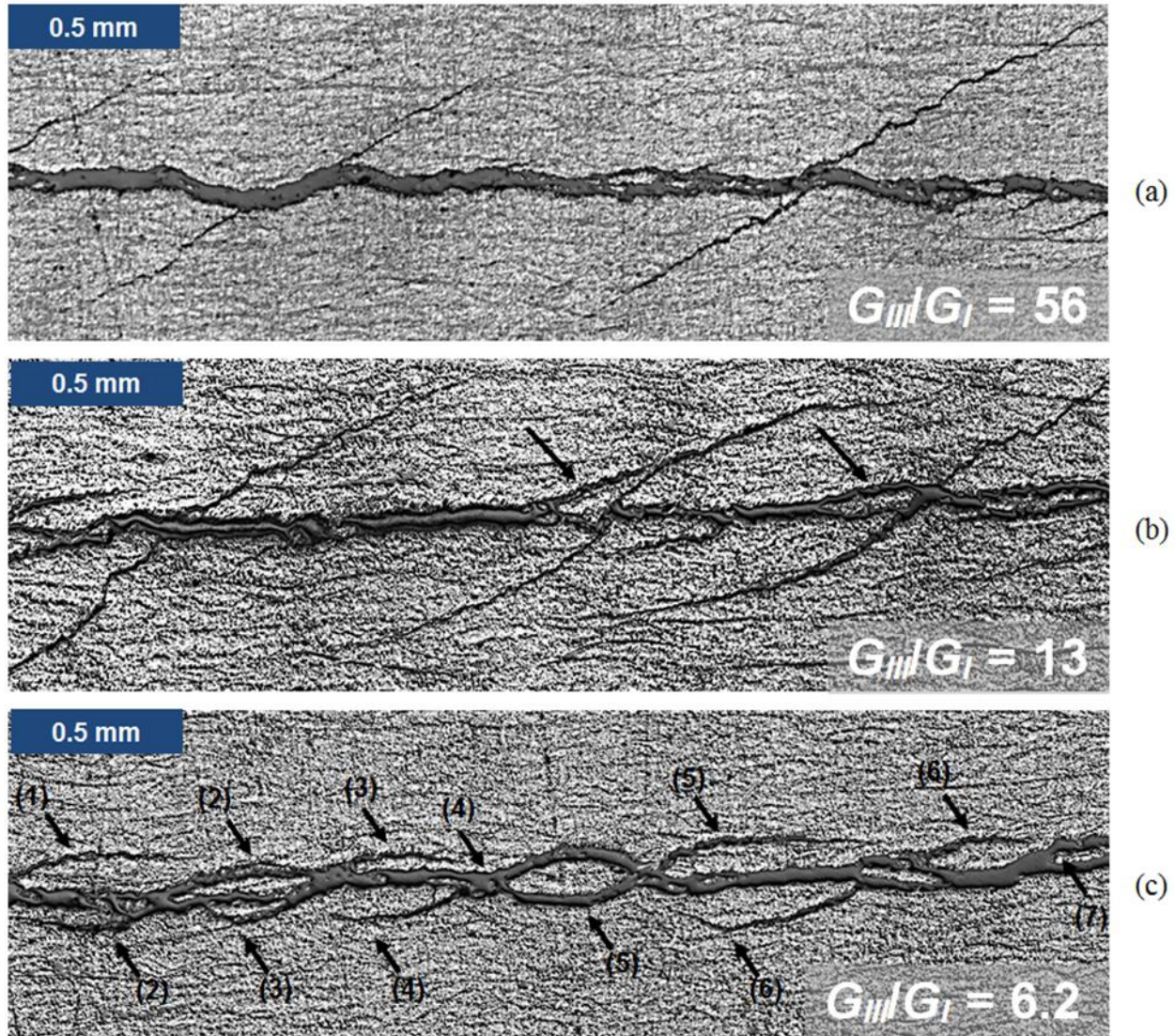


Figure 6.6. Representative transverse section photomicrographs of 24-ply specimens with different delamination lengths (a) 32 mm, (b) 70 mm, (c) 127 mm, taken approximately 2 mm ahead of the Teflon insert tip.

The transverse section in Figure 6.6c is from a 24-ply, $a = 127$ mm specimen. Here, matrix cracks initiate at very shallow angles, and almost immediately turn to approximately horizontal orientations. This is consistent with the relatively large mode I component in these specimens, and is a more dramatic manifestation of the behaviors observed in the specimen of Figure 6.6b. The arrows in Figure 6.6c point to those locations where the transverse cracks curve

and turn back to re-link with the mid-plane. For subsequent use, there are assumed to be five full and two partial transverse cracks in Figure 6.6c. That is, only the beginning or end of cracks (1) and (7) are visible, whereas the full length of transverse cracks (2) – (6) are evident in the figures. Note that the transverse cracks in these specimens rarely extend past the first ply bounding the delamination on either side, and in some locations it is difficult to differentiate the planar delamination from the transverse cracks.

6.4.3. Matrix Crack Orientation

Figure 6.7 presents photomicrographs from the same specimens as Figure 6.6. However, these photomicrographs were obtained from section cuts obtained near the center of each specimen's width and within 0.5 mm of the end of the original Teflon insert tips. The transverse matrix cracks in Figure 6.7 are much smaller than those in the corresponding images of Figure 6.6, and the matrix crack turning observed in Figure 6.6b-c has not yet developed. Whereas the images of Figure 6.6 depict well-developed fracture surfaces, those of Figure 6.7 represent the way that they initially form. That is, the cracks shown in Figure 6.6 developed to their particular size and shape under the influence of an already cracked matrix, whereas those in Figure 6.7 formed adjacent to the original, undamaged configuration associated with the preimplanted Teflon insert. It follows that predictions of transverse crack orientations using Equation (6.11) would be expected to correlate more closely to what is displayed in the images shown in Figure 6.7. Note, however, that these images represent only a small portion of each specimen's width. Therefore, in order to accurately obtain and compare the matrix crack orientations within the different geometries to each other and to predicted results, graphical analyses were used to measure the orientations of every crack across the specimens' width.

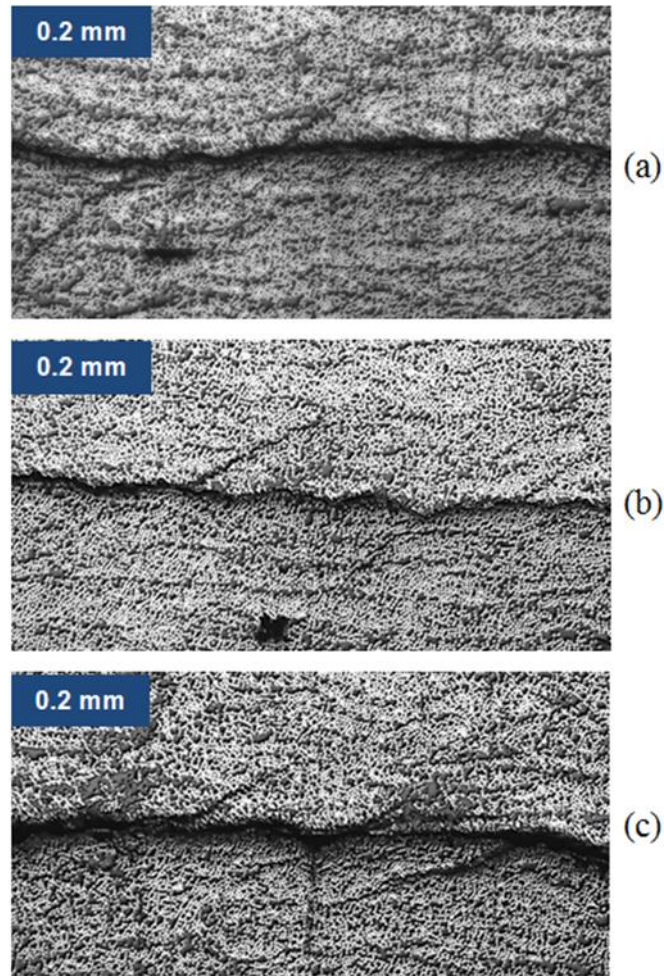


Figure 6.7. Representative transverse section images of 24-ply specimens just ahead of the Teflon insert tip for different delamination lengths (a) 32 mm, (b) 70 mm, (c) 127 mm.

In order to predict the transverse crack orientation, θ , by the MPTS criterion (Equation (6.11)), one requires the experimentally measured rotation of the delamination front, ϕ , the full set of material properties for a transversely isotropic material, and an assumption about whether the transverse strain, $\varepsilon_{y'y'}$, or stress, $\sigma_{y'y'}$, equals zero. Table 6.2 presents properties utilized by O'Brien and Krueger (2003) for IM7/8552. As the values of E_{11} and G_{12} in this table are different than those determined experimentally in Section 5.2.2, and as it is likely that $\varepsilon_{y'y'} = 0$ is more appropriate for the center of the specimen whereas $\sigma_{y'y'} = 0$ is more appropriate near its edges, a sensitivity study was conducted to assess how the predicted value of ϕ would be affected. To this

end, the various values of material properties were considered, including isotropic material properties with $\nu = 0.32$, under conditions of both $\varepsilon_{y'y'} = 0$ and $\sigma_{y'y'} = 0$. It is shown in Appendix D.2 – D.3 that, over the range of angles measured in this work (3-26°), there is some sensitivity to the transverse constraint condition but very little to the assumed material properties². As a result of this insensitivity, the values from Table 6.2 and the assumption that $\varepsilon_{y'y'} = 0$ are used in what follows.

Figure 6.8 presents the ratio of the measured to the predicted transverse crack angle as a function of mode mixity. These data include all five of the geometries tested (cf. Table 6.1) and represent all specimens for which section cuts were taken within 0.5 mm of the original Teflon insert tips. Each value of $\theta_{\text{Experimental}}$ is taken as the average angle from all transverse cracks present across the width of that specimen, and each value of $\theta_{\text{Theoretical}}$ is taken from Equation (6.11) and the measured value of ϕ at the onset of growth. It can be seen that Equation (6.11) over-predicts the transverse matrix crack angle, and that the accuracy of the predictions improves with increasing $G_{\text{III}}/G_{\text{I}}$. The accuracy of the predicted values of θ in Figure 6.8, and the trend of the comparisons of theory to experiment as a function of mode mixity, are quite similar to what has been reported for homogenous materials (Cooke and Pollard, 1996; Yates and Miller, 1989; Seifi and Omidvar, 2013; Liu et al., 2004). In this sense, the results in the figure provide corroborating evidence for the presence of the mode I field.

Table 6.2. IM7/8552 material properties (O'Brien and Krueger, 2003).

$E_{11} = 161.0 \text{ GPa}$	$E_{22} = 11.38 \text{ GPa}$	$E_{33} = 11.38 \text{ GPa}$
$\nu_{12} = 0.32$	$\nu_{13} = 0.32$	$\nu_{23} = 0.436$
$G_{12} = 5.17 \text{ GPa}$	$G_{13} = 5.17 \text{ GPa}$	$G_{23} = 3.98 \text{ GPa}$

² The sensitivity to material properties of 3.5% published in Horner and Davidson (2015) was an error.

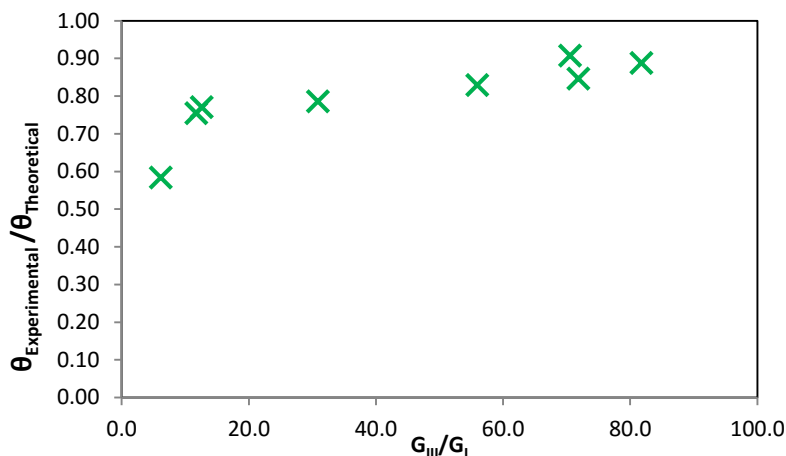


Figure 6.8. Ratio of experimentally measured transverse crack angles ($\theta_{\text{Experimental}}$) with predictions from maximum principal tensile stress criteria ($\theta_{\text{Theoretical}}$) versus mode ratio.

6.4.4. Effect of Geometry on Fracture Surface Evolution

The manner in which the fracture surfaces evolve with increasing delamination growth was examined using the methodology described in Section 5.5.3. Multiple transverse sections cuts, at increasing distances from the Teflon insert tip, were made in 24-ply SST specimens which had 12 – 14 mm of delamination growth. All visible cracks in each image were counted and measured, and the number of matrix crack “groups” and the average matrix crack size were evaluated as a function of the distance from the Teflon insert tip. A single matrix crack group is defined as a large, primary matrix crack and any small, branch cracks emanating from the primary matrix crack. Matrix cracks are counted as groups in order to better compare fracture surfaces between different specimens. For example, although Figure 6.6b contains a number of branch cracks, Figure 6.6a and b were both assumed to show three matrix crack groups. As stated previously, there are seven matrix cracks groups shown in Figure 6.6c, and Figure 6.7a-c each show three matrix crack groups. Matrix crack size was measured using the secant line approach of Section 5.5.3, where a straight line was superposed on each transverse crack and the length of the crack was approximated by the length of this line. This was straightforward for

specimens such as those shown in Figure 6.6a-b, where a straight line extending between the crack's two tips represents the length of the crack quite well. For cracks such as those shown in Figure 6.6c, where the crack is poorly represented by a straight line, a slightly modified technique had to be used. A secant line approach was still employed, but only the portion of the crack in between the pairs of arrows designating the end points was measured. That is, the portions of the crack which had turned horizontal or turned back to re-link with the delamination plane were not included, as it is hypothesized that this portion of crack growth is caused by a different mechanism (Lin et al., 2010). Additionally, between matrix cracks (4) and (5), the upper curved segment is assumed to be the interlaminar delamination, and for this reason matrix crack (4) was assumed to end at the locations that are indicated.

Figure 6.9 presents plots of the average matrix crack size and number of matrix crack groups for transverse sections taken at increasing distances ahead of the insert tip. Figure 6.9a indicates that transverse matrix crack sizes are similar in all of the specimens for the first few millimeters ahead of the Teflon insert tip, although average matrix crack length in the $a = 127$ mm specimen quickly plateaus. This is attributed to the increasingly curved fracture path with increasing mode I, as evidenced in Figure 6.6c. For predominantly mode III conditions, it was hypothesized in Section 5.5.3 that the average matrix crack length will plateau at a value that is approximately half of the specimen thickness due to the influence of the specimen's free surfaces, and the data for the $a = 32$ mm and $a = 70$ mm specimens support this hypothesis. Considering Figure 6.9b, it can be seen that the number of crack groups decreases with increasing distance ahead of the insert tip similarly in all specimens. It has been observed in previous SST specimens as well as in homogenous materials with cracks propagating under anti-plane shear loading (Goldstein and Osipenko, 2012A; 2012B), that as the crack array extends

ahead of the initial Teflon insert tip, the spacing between cracks increases. As their spacing increases, however, so does their length. That is, there is a coarsening process, with, on average, many small, closely-spaced transverse cracks where planar delamination growth first initiates from the insert, which gradually changes to fewer, larger transverse cracks as the planar delamination grows. However, the combination of Figure 6.6c and Figure 6.9 show that when there is a significant amount of specimen rotation, as for the $a = 127$ mm specimen, the coarsening process consists of a decrease in the number of transverse cracks groups and an increase in crack branching, rather than a measurable increase in transverse crack length.

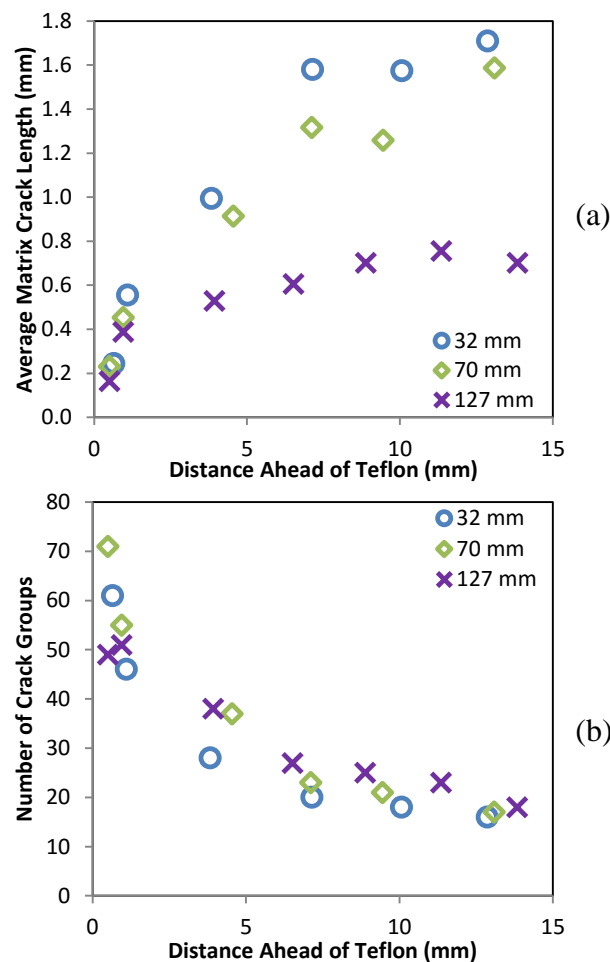


Figure 6.9. Crack surface evolution data for 24-ply specimen of three different delamination lengths. Evolution of (a) matrix crack length, (b) number of crack groups.

In addition to the above, the data was used to select an “average” or “typical” transverse crack for each specimen and trace that crack as it grew through each transverse section. These results are presented in Figure 6.10, which illustrates the evolution of transverse cracking for the three different 24-ply specimens. In this figure, the value at which any transverse crack profile intersects the horizontal axis represents the distance in mm from the Teflon insert tip to the section cut in which that crack was measured. In this way, the horizontal distance from the origin to any crack profile in the figure is scaled to its physical distance ahead of the Teflon insert tip in the specimen, where the exact distance ahead of the Teflon insert tip is given in the figure legend. Otherwise, the millimeter y- and z-scales on the vertical and horizontal axes are used to present the dimensions of the “average crack” profile from each cut section as viewed with the DIC microscope. The left-most data set in each figure therefore represents a typical transverse crack that forms quite close to the Teflon insert tip, and the data sets to the right of it show how that crack evolves, i.e., they depict the appearance of that crack at subsequent cross sections, while the millimeter scales on the vertical and horizontal axes give the exact dimensions of the crack.

Figure 6.10a-b show transverse crack profiles from the $a = 32$ mm and $a = 70$ mm specimens, respectively. In both cases, there is a significant increase in crack length over the first few millimeters of growth, after which the crack length only increases slightly. These results correlate with those depicted in Figure 6.9a. Figure 6.10a and b show that the small increases in crack length in the profiles furthest ahead of the Teflon insert tip are also accompanied by the development of a slight s-shape. Note that the orientation of the cracks near the specimen’s mid-plane remains relatively constant, and that the development of the s-shape is somewhat more pronounced in the $a = 70$ mm than in the $a = 32$ mm specimen. The s-shape crack profiles likely

develop due to the combination of the fiber constraints on crack path and the changing mode mixity during delamination growth. As discussed in Section 5.5.2, growth of the transverse matrix cracks lead the growth of the planar delamination by approximately 2 mm. As the planar delamination grows, the amount of specimen twist at the delamination front increases, which increases the mode I component. As predicted by Equation (6.9), this should result in increasingly shallow matrix cracks. One would expect this to occur in a manner similar to that observed in homogenous materials, where crack segments twist as they extend (Lin et al., 2010; Cooke and Pollard, 1996; Yates and Miller, 1989). However, in the composite laminates studied herein, the presence of the carbon fibers prevents the matrix cracks from significantly rotating once they have formed. That is, while the transverse cracks are able to further extend in the y-z plane without being constrained by the carbon fibers (c.f. Figure 6.7 versus Figure 6.6), those portions that already exist are unable to rotate as growth proceeds in the x-direction. This accounts for the relatively stable shape of the cracks at the specimen mid-plane. As the transverse cracks increase in length with delamination advance, additional crack growth occurs in the local orientation that is dictated by the MPTS criterion. This produces an s-shape that becomes more pronounced with increasing mode mixity.

Figure 6.10c presents the crack profile from the $a = 127$ mm specimen and reflects a continuation and extension of the above phenomenon. In agreement with Figure 6.7c, the first increment of matrix crack growth is straight. However, very soon thereafter, the crack develops an s-shaped profile due to the large amount of rotation and the associated large mode I component. The relinking of these cracks with the mid-plane is similar to the factory roof profile produced by the linking of type A and B zones in homogeneous materials, and energetically follows a similar argument (Lin et al., 2010).

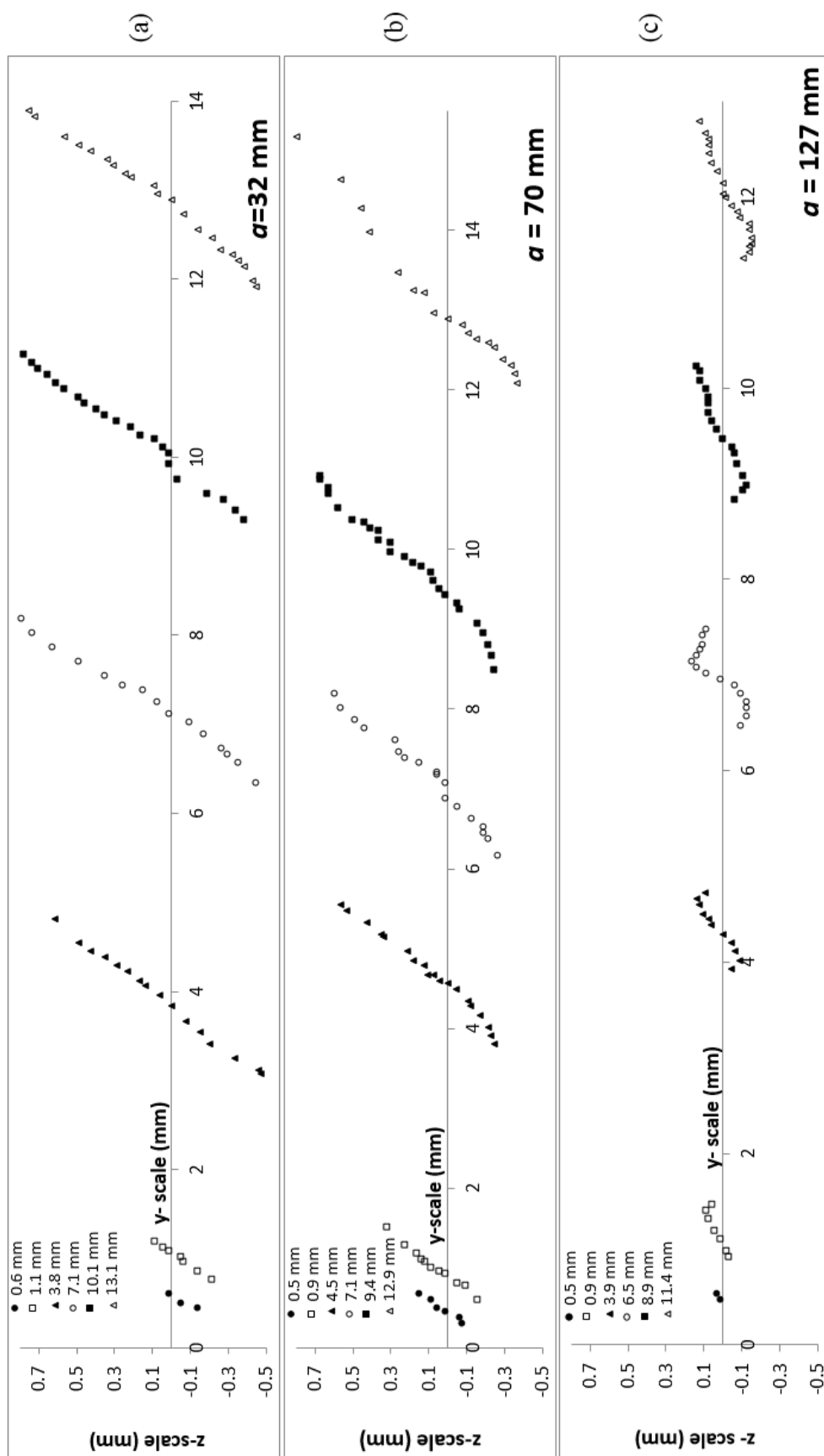


Figure 6.10: Evolution of representative cracks from transverse sections of 24-ply specimens with delamination lengths of (a) 32 mm, (b) 70 mm, (c) 127 mm. Legend represents distance ahead of the Teflon insert tip from which each profile was taken.

6.4.5. Comparison of Composite Fracture Surface Evolution to Homogenous Materials

Fracture surface evolution in composite and homogenous materials subjected to predominantly mode III loadings starts off identically, via the emergence of an echelon array of transverse cracks along the front of the initial planar macro-crack or delamination. This produces crack front segmentation and faceting. In homogeneous materials, the transverse cracks twist as they extend and, if growth of the initially planar macro-crack occurs, it is accompanied by twisting in-between facets (Goldstein and Osipenko, 2012A; 2012B). The twisting of both the transverse cracks and of the initially planar macro-crack represent the tendency of cracks in homogenous materials to grow under mode I conditions. In laminated composites, however, both types of twisting are constrained. Once a matrix crack is created it is not able to substantially change its orientation due to its bounding fibers. Thus, rather than the twisting that occurs in homogenous materials, in composite laminates the transverse cracks will become s-shaped under mixed mode I-III loadings. Further, the amount by which transverse cracks can extend in a composite laminate is limited by the close proximity of the laminate's free surfaces. This is not generally an issue in homogeneous specimens. The composite fibers also constrain the delamination from twisting, and this fact, combined with the presence of an interlaminar interface and the limited ability of the transverse cracks to absorb energy due to limitations on their length, results in a coupled, concurrent planar advance in composites that is not observed in homogenous materials. Thus, the constraints that the fibers place on both transverse crack and planar delamination twisting, the proximity of the free surfaces, and the presence of an interlaminar interface combine to produce a very different fracture surface evolution in the unidirectional SST specimens studied herein in comparison to that which has been observed in homogeneous materials.

6.5. Application to Mode III Delamination Toughness Testing

While the studies presented in this dissertation concentrated on carbon/epoxy composites, it is hard to envision that the sequence of events leading up to delamination advance would be different in any unidirectional laminated polymeric matrix composite. Fundamentally, the observations presented in this chapter and in Chapter 5 confirm the well-documented preference for mode I growth in homogeneous materials, regardless of the mode mixity of the loading, and the architecture of the reinforcing fibers is such that it does not significantly alter this situation. Thus, it is likely that the mechanisms described herein not only explain the dependence of toughness on delamination length for the SST test, but also explain the dependency that has been observed in unidirectional MSCB tests (Szekrényes, 2011; 2009). For ECT tests, note that the laminate layup is typically chosen such that mode III delamination advance will occur along the direction of the fibers of the two bounding plies. That is, it is locally identical to the SST geometry. One would therefore expect that “mode III growth” in conventional ECT tests would proceed similarly to what was observed herein, and this has been confirmed in parallel studies by Czabaj et al. (2014) and Horner et al. (2015). Thus, the apparent variation in toughness with delamination length in ECT testing is also explained by the same mechanisms as those observed herein. These further agree with earlier observations in both homogeneous test specimens and in rock formations containing cracks that are subjected to anti-plane shear loadings.

The results presented herein and in related studies of the ECT (Czabaj et al., 2014; Horner et al., 2015) indicate two fundamental problems with mode III toughness tests of composite tape laminates. First, for any geometry, small transverse cracks initiate prior to delamination advance. For unidirectional specimens where the fibers are oriented in the direction of intended interlaminar delamination growth, such as the geometries used for mode I and mode

II testing and those that have been used herein, these transverse cracks grow prior to the onset of macroscopic delamination advance. As seen in this dissertation for the SST, and in Czabaj et al. (2014) and Horner et al. (2015) for the ECT, transverse crack growth is unconstrained by the fibers of the bounding plies, and “mode III delamination advance” is in fact a linking and coalescence of these cracks. This invalidates the data reduction techniques that have been employed, and is one of the reasons for the dependence of the apparent toughness on test and specimen geometry that has been observed in mode III testing of laminated composites. As discussed in Czabaj et al. (2014) and Horner et al. (2015), one solution to this problem is to employ alternative layups that will bound the length of the transverse cracks to be quite small. This would allow an engineering measure of mode III toughness to be extracted, and the overall process of small transverse cracking accompanied with delamination advance would be analogous to that which occurs in unidirectional mode II delamination toughness testing (O’Brien, 1998). However, in practice delamination advance will often occur under conditions with coupled near-tip matrix cracking, and it is not clear whether this approach will have any appreciable practical applicability. Further, considering the strong dependence of the apparent toughness on test geometry for those ply orientations where coupled matrix cracking occurs, it is also unlikely that approaches which express toughness as a function of bounding ply angle, such as those used in modes I and II (Davidson, 2010), will be valid.

The second problem with mode III testing relates specifically to split beam geometries, where the mode mixity at the onset of delamination advance depends on specimen twist and therefore on specimen and test geometry. To obtain mode III conditions, it would be necessary to restrain the twisting during testing, for example by using a very short, thick specimen with extremely high torsional rigidity, or employing rigid rollers as in the shear-torsion-bending test

(Davidson and Sediles, 2011), or by incorporating thick steel blocks that are bonded to the specimen as in the improved split cantilever beam test (Robinson and Song, 1994). In view of the first issue above, however, solely preventing specimen rotation would not produce a valid mode III toughness; one would also need to change the specimen geometry to a non-unidirectional layup in order to restrict transverse crack growth. This would create considerable problems in the development of an accurate data reduction methodology. Thus, rather than pursuing split beam geometries, a variation of the edge-crack torsion test with an appropriate fiber architecture, as proposed in Czabaj et al. (2014) and Horner et al. (2015), is perhaps the more promising approach, but additional study of this issue is warranted.

6.6. Conclusions

The influence of specimen twisting during global anti-plane shear loading was studied using the split-shear torsion test. It was shown that specimen twisting causes a mode I stress intensity factor to develop that is proportional to the angle of twist, thereby producing mixed mode I-III conditions along the delamination front. The orientations of the near-tip transverse matrix cracks that develop were shown to agree fairly well with predictions based on a maximum principal tensile stress criterion. This was shown to influence the apparent toughness, in that a larger angle of twist at fracture corresponded to larger mode I conditions and a smaller value of apparent G_c . This effect, combined with the fact that the transverse cracks initiate prior to delamination advance, appears to explain the observed dependency of the apparent toughness on test geometry in split-shear torsion specimens. The amount of twist was also shown to affect the way that the fracture surfaces evolve, and explanations were provided why this evolution differs from that observed in homogeneous materials. These findings were used to make some

observations and recommendations regarding future delamination toughness testing. They also have strong implications for predictions of the onset and growth of delaminations in practical structural geometries, in that the amount of mode III that is present can produce behaviors that heretofore have not commonly been recognized to occur.

Chapter 7. Model Formulation and Validation

7.1. Introduction

In order to gain insight into the mechanisms leading to complex fracture surface development in composite laminates subjected to anti-plane shear loading, it is of interest to first model how an echelon array develops and grows. As discussed in Section 2.5.3, an ideal method for studying the development of an echelon array is to use discretely modeled echelon cracks in a FE model. This chapter will present the model formulation and the steps taken to verify the accuracy of a discrete echelon crack model developed for this dissertation. The verified model will then be used in Chapter 8 to study the development of an array of echelon cracks.

This chapter will first cover the overall goals of modeling and the plans for what will be modeled in Chapter 8. Details of how the model will be created are then discussed. The VCCT will be used to extract ERRs for both the planar delamination and echelon cracks, and the necessary equations for this technique are presented. The model validation steps are then discussed. These results are summarized in this chapter, while full details of the model validation can be found in Appendix E. A final overview and summary is then presented.

7.2. Model Plans

7.2.1. Overall Goals of Modeling

The goal of the work presented in Chapter 8 is to determine the energetics of echelon array development and growth. In order to do this, key stages of echelon crack array development will be modeled. The bulk of this work will consider echelon array development prior to any planar delamination advance. The results of this modeling will be used in

conjunction with the experimental findings of Chapters 4-6 to understand the mechanisms controlling echelon crack array development.

7.2.2. Modeling Plans

The stages of echelon array development to model will be heavily influenced by the experimental findings discussed in Chapters 5-6. The actual modeling results will be presented in Chapter 8, however the plans are discussed here because the desired events to model determine how the FE model is formulated and verified. For each stage of echelon array development that will be modeled, the energy release rates will be calculated along both the delamination and echelon crack front. The differences in energy release rates on the echelon crack and delamination front in different stages will be used to draw conclusions regarding the energetics driving that stage of development.

The first stages of modeling will consider a single echelon crack which has initiated at a location along the delamination front based on a pre-existing flaw distribution. The echelon crack will initially be modeled as a circle centered on the delamination tip, and the ERRs around the echelon crack front will be used to determine how a single echelon crack grows. Comparisons of the ERRs on the echelon crack during multiple stages of growth to the ERRs on the delamination front will be used to determine a point when the growth of a single echelon crack may become self-limiting, and further growth would be unlikely.

Subsequent to modeling the growth of a single echelon crack, an array of echelon cracks will be considered. The ERRs along multiple echelon crack fronts will be calculated, along with the ERRs on the delamination front, to determine how the array of echelon cracks is likely to advance and grow. Similar arguments to those used with a single echelon crack will be made to

determine when the echelon crack array may become self-limiting, and further growth of the array without planar delamination growth would become unlikely. The study of an array of echelon cracks will also be used to gain some insight on echelon crack spacing, although this is not the focus of this work.

7.2.3. Intended Model Details

All modeling will be conducted using Abaqus Standard 6.14. Linear eight-noded solid brick elements with full integration will be used for the entire model. The modeled geometry is shown in Figure 7.1. The geometry will consist of a thick block with a mid-plane delamination and an echelon crack (or cracks) coincident with the delamination tip. As seen in Figure 7.1b, the echelon crack is located in the center of the specimen width and is oriented 45° from the x-z plane towards the positive y axis such that the maximum principal tensile plane due to the applied anti-plane shear load, P , is perpendicular the plane of the echelon crack. In cases when multiple echelon cracks are modeled, they will be spaced symmetrically around the center of the specimen width.

The echelon crack(s) will be modeled as an Abaqus seam crack, which has zero thickness. The profile of the echelon crack will consist of circular and/or ellipsoidal shapes. These shapes are chosen to approximate the profile of an echelon crack at different stages of development. Although, as seen in Chapters 5 and 6, the true shapes of echelon cracks are not explicitly circular or ellipsoidal, this is a necessary approximation due to limitations in both Abaqus modeling and post-processing of ERRs. While not fully replicating the profiles of echelon cracks that arise in experiments, it is expected that the mechanisms for echelon array development and growth can still be extracted from the simplified geometries.

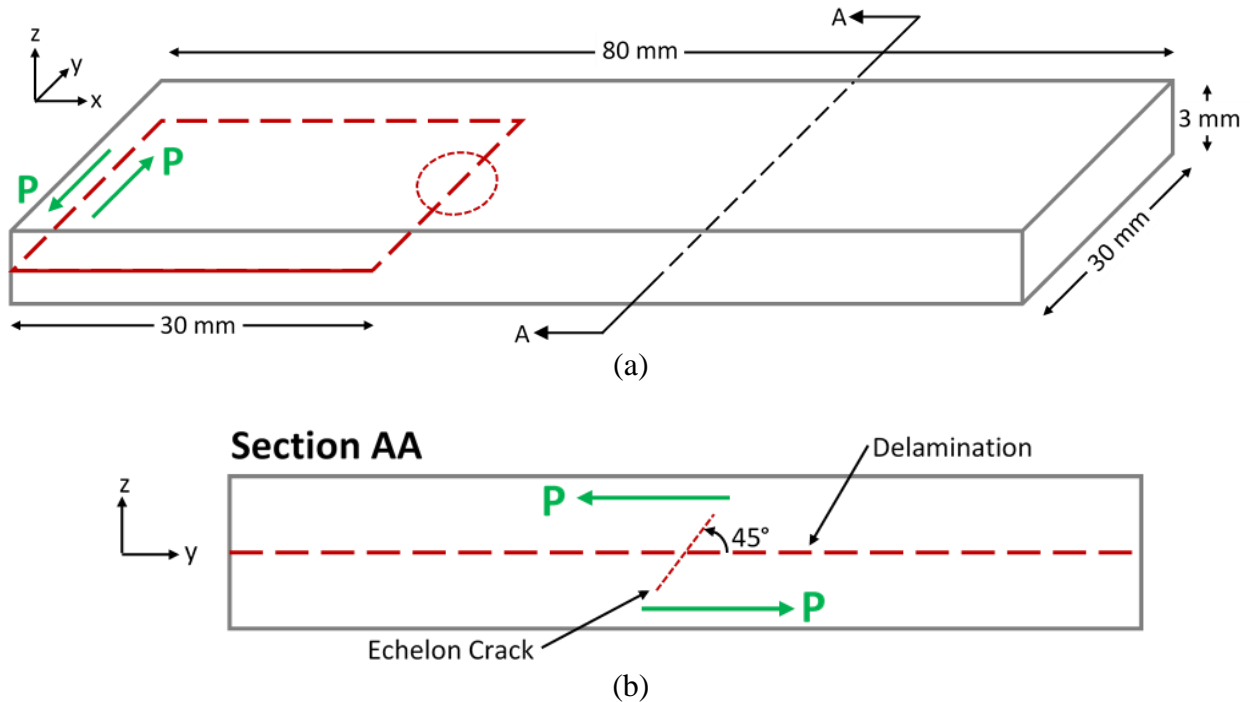


Figure 7.1. (a) FE model geometry with a single echelon crack intersecting the delamination front in the center of the specimen. (b) Cross-sectional view with delamination front and echelon crack positions labeled.

As noted above, the echelon crack will be modeled as an Abaqus seam crack with zero thickness. Due to current limitations in Abaqus, it is not possible to model both the echelon crack and the mid-plane delamination as seam cracks because they intersect each other. Therefore, the mid-plane delamination will be modeled as a very narrow, but finite thickness, wedge which will come to a sharp point at the delamination tip. The nodes on the cracked faces above and below the delamination plane will not be coincident, but the distance between them will be very small such that the delamination can be approximated as infinitesimally thick.

This geometry and loading of the model is intended to represent the SST NE specimen geometry and loading studied experimentally in Chapters 4-6 if the specimen was constrained to

prevent the rotation discussed in Chapters 6. For simplicity, the load tabs of the SST specimen are not modeled, but the boundary conditions applied are equivalent to those imposed by the load tabs. Therefore, the faces on the cracked ends of the model (left side in Figure 7.1a) are loaded with an anti-plane shear displacement, u_y , while rotation on those faces is constrained, $\theta_z = 0$. This represents the loading and constraints on an SST specimen at the very edge of the load tabs, which are not modeled. Additionally, the upper and lower (30 mm x 80 mm) faces of the model are constrained by $\theta_x = 0$ such that there will be no global rotation due to the anti-plane shear loading. This geometry and loading results in almost pure mode III in the center of the specimen, with some mode II near the specimen edges. However, the area of interest, where the delamination intersects the echelon crack, will be under essentially pure mode III loading.

7.3. Energy Release Rate Calculations

Energy release rates on both the delamination and echelon crack fronts of the FE model will be calculated using the VCCT. This technique was briefly introduced in Section 2.2.3.3. It was used in Section 4.7 and 5.3.1 to calculate energy release rates along the delamination fronts of STB and SST specimens.

The VCCT was initially formulated by Rybicki and Kanninen (1977) based on Irwin's crack closure integral. As discussed in Section 2.2.3.3, the VCCT is based on the theory that the energy released when a crack of area A is extended to $A + \Delta A$ is equal to the energy required to close a crack of area $A + \Delta A$ by an amount ΔA (Krueger, 2004). The VCCT uses the nodal forces at the crack tip and nodal displacements just behind the crack tip, both of which are determined by FE analysis, to determine the local components of ERR along the crack front.

7.3.1. Straight Crack Fronts

Krueger (2004) gives VCCT equations for G_I , G_{II} , and G_{III} for three dimensional, eight noded linear brick elements. His equations have been formulated to give the ERR components at each node. However, in this work ERRs are calculated at the center-point of each element, rather than at the nodes. Therefore, the equations from Krueger (2004) are slightly modified to be used in this work. For the element center-point shown as a black circle in Figure 7.2, the mode I, mode II, and mode III components of ERR are calculated by Equation (7.1).

$$\begin{aligned}
 G_I &= \frac{1}{2 \Delta A} \left[\frac{Z_{Mj}}{2} (w_{Mi} - w_{Mi*}) + \frac{Z_{Nj}}{2} (w_{Ni} - w_{Ni*}) \right] \\
 G_{II} &= \frac{1}{2 \Delta A} \left[\frac{X_{Mj}}{2} (u_{Mi} - u_{Mi*}) + \frac{X_{Nj}}{2} (u_{Ni} - u_{Ni*}) \right] \\
 G_{III} &= \frac{1}{2 \Delta A} \left[\frac{Y_{Mj}}{2} (v_{Mi} - v_{Mi*}) + \frac{Y_{Nj}}{2} (v_{Ni} - v_{Ni*}) \right]
 \end{aligned} \tag{7.1}$$

Here, Δa is the length of the elements at the delamination front and b is the width of the element, such that the virtually closed area is $\Delta A = \Delta a * b$. In Figure 7.2, nodal columns are denoted by capital letters and nodal rows by small letters. Thus, X_{Mj} , Y_{Mj} , and Z_{Mj} are nodal forces at the crack tip in column M, row j. The displacements behind the crack in column M of the upper crack face are u_{Mi} , v_{Mi} , and w_{Mi} , and on the lower crack face are u_{Mi*} , v_{Mi*} , and w_{Mi*} . Similar definitions apply for column N.

Equation (7.1) represents the ERRs for interior elements. For edge elements, a slight modification to the equations must be made, as all of the force on the edge node is applied to that element, rather than split between two adjacent elements as it is for interior nodes. If column N is on an edge, then the terms $X_{Nj}/2$, $Y_{Nj}/2$, and $Z_{Nj}/2$ in Equation (7.1) are replaced by X_{Nj} , Y_{Nj} , and Z_{Nj} respectively, while all other terms remain as they are.

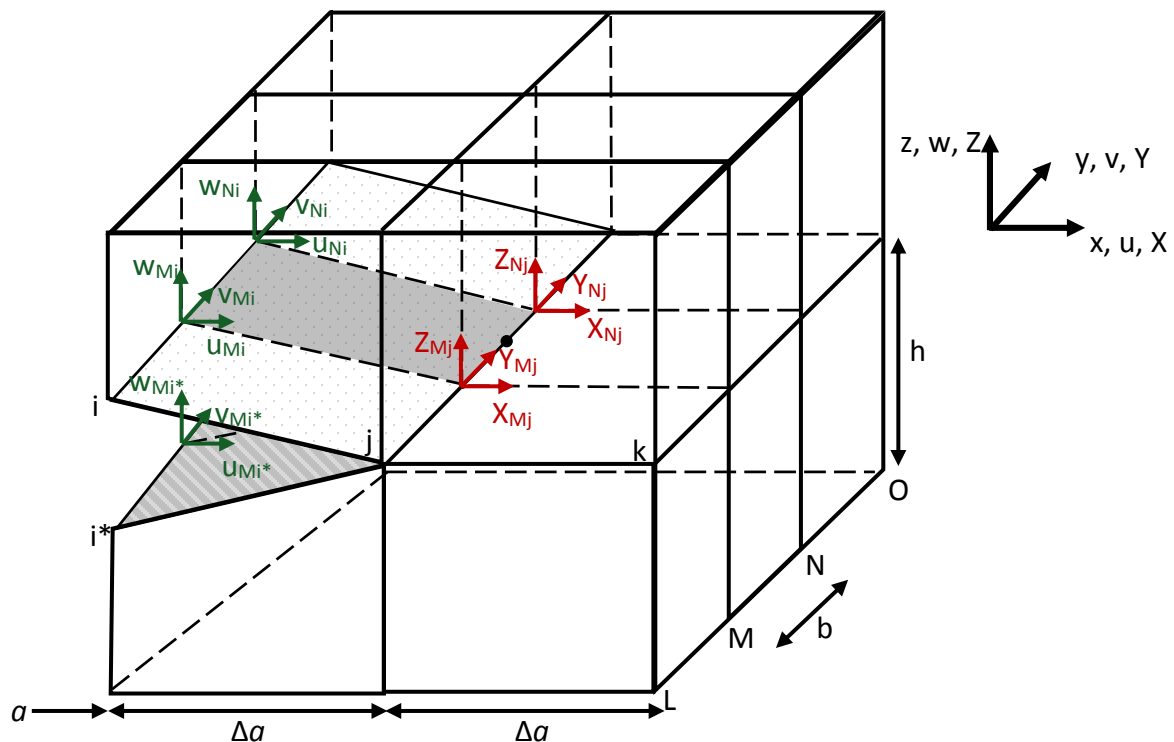


Figure 7.2. Nodal force and displacement labels for eight-noded solid element VCCT calculations.

7.3.2. Curved Crack Fronts

As discussed by Krueger (2004), when the crack front is straight, as it is in Figure 7.2, the definition of modes is intuitive and constant across the entire front. Mode I is caused by out of plane opening (z direction), mode II is caused by in-plane shearing (x direction, normal to the crack front), and mode III is caused by out of plane shearing (y direction, tangent to the crack front). For a curved crack front, such as will be used to model echelon cracks, the mode definition is not so straightforward. In this case, the forces and displacements must be transformed from the global (x, y, z) system to a local (x', y', z') system, where x' is in-plane normal to the local crack front, y' is tangent to the local crack front, and z' is out-of-plane normal to the local crack front.

Figure 7.3 presents a planar view of an arbitrarily curved mesh. A linear transformation must be used at each node to transform between the global and local coordinate systems. The transformed (primed) forces and displacements may then be used in Equation (7.1) in place of the global (non-primed) forces and displacements. Additionally, the closed area, ΔA , must be calculated for each element and used in Equation (7.1), as for a curved crack front $\Delta A \neq \Delta a \cdot b$. For a circular crack front, ΔA can be calculated exactly, as it is a sector of an annulus. For more complex shapes, ΔA may be approximated.

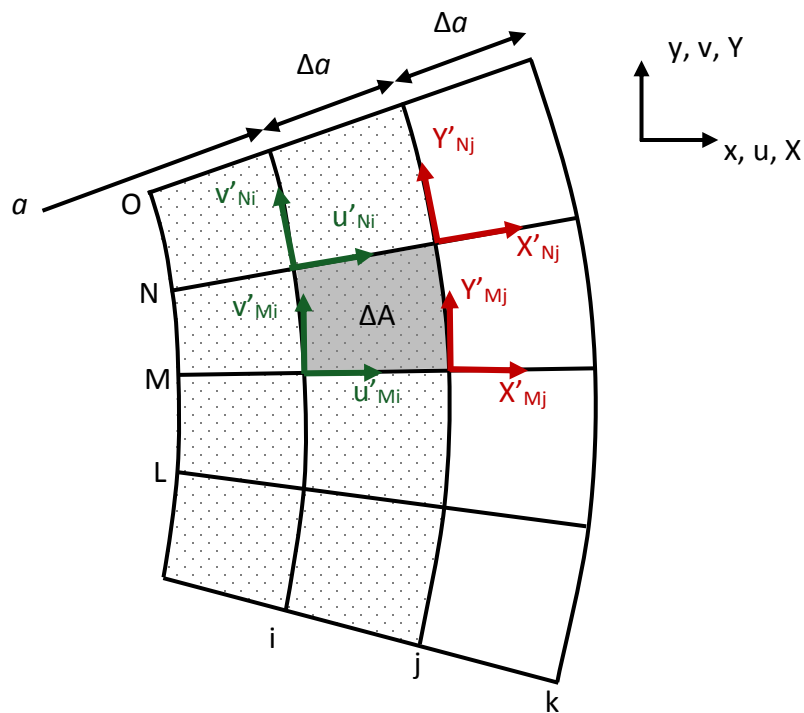


Figure 7.3. Nodal force and displacement labels for eight noded solid elements with arbitrarily curved crack fronts (lower face omitted for clarity).

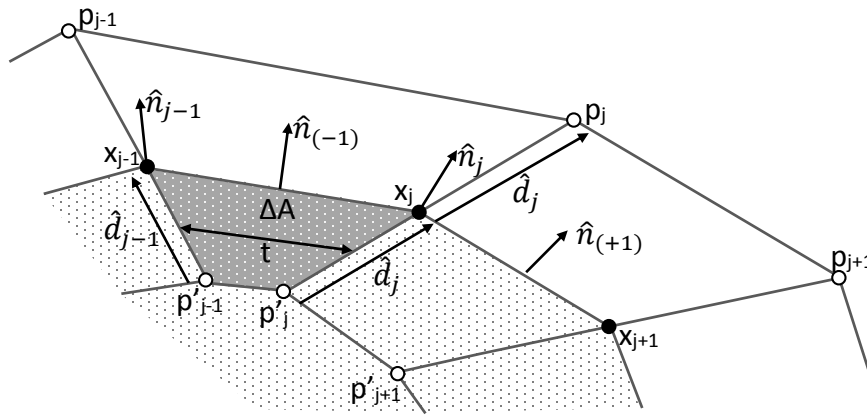


Figure 7.4. Definition of terms defining element area for a crack plane with a mesh that is not orthogonal to the crack front.

The above discussion of curved crack fronts assumes the mesh is orthogonal. That is, for each column node (L, M, N, O) in Figure 7.3, the line of action of the row nodes (i, j, k) is parallel to the direction locally normal to the crack front. However, for some complexly curved crack fronts, such as the example shown in Figure 7.4, the mesh may not be orthogonal. In a non-orthogonal mesh, the locally oriented nodal forces at the crack tip and the nodal displacements behind the crack tip are not aligned, and ERRs calculated via Equation (7.1) will be inaccurate. Instead, the procedure of Smith and Raju (1999) may be used to correctly calculate the ERRs. Here, the nodal forces and displacements are still used, as they are expected to be more accurate than performing interpolation (Smith and Raju, 1999), however the area term is corrected. The correct area for VCCT calculations with a non-orthogonal mesh is $\Delta A = \Delta h * t$, where Δh is a corrected element length and t is a corrected element width. The value of Δh is calculated by

$$\Delta h = \hat{r} \cdot \hat{n}_{(-1)} \quad (7.2)$$

where

$$\hat{r} = \left(\frac{(\hat{n}_{j-1} \cdot \hat{d}_{j-1}) + (\hat{n}_j \cdot \hat{d}_j)}{2} \right) \hat{n}_{(-1)} \quad (7.3)$$

As shown in Figure 7.4, $\hat{n}_{(-1)}$ is the unit normal to the line segment connecting node x_{j-1} and node x_j on the crack front. Similarly, $\hat{n}_{(+1)}$ is the unit normal to the line segment connecting node x_j and node x_{j+1} on the crack front. \hat{n}_j and \hat{n}_{j-1} are the outward pointing normals at points on the crack tip x_j and x_{j-1} respectively, and are defined as the average of the outward pointing normal on the line segments such that

$$\hat{n}_j = \frac{\hat{n}_{(-1)} + \hat{n}_{(+1)}}{\|\hat{n}_{(-1)} + \hat{n}_{(+1)}\|} \quad (7.4)$$

\hat{n}_{j-1} can be obtained similarly. Points p'_j and p'_{j-1} are points located behind the crack tip, and the vector from these points to their respective crack tip nodes x_j and x_{j-1} are defined by \hat{d}_j and \hat{d}_{j-1} . \hat{r} is therefore a vector defining the element length using the distance vectors \hat{d}_j and \hat{d}_{j-1} projected orthogonally to the local crack front. Note that, as shown in Figure 7.4, the mesh must be constructed such that the distance between p'_j and x_j and the distance between x_j and p_j are both of length d_j .

The value of t defines an average element width, and is determined by averaging the distance between the nodes at the crack front, x_j and x_{j-1} , and the nodes behind the crack front, p'_j and p'_{j-1} , according to the equation

$$t = \frac{\|(p'_j - p'_{j-1})\| + \|(x_j - x_{j-1})\|}{2} \quad (7.5)$$

Thus, for a non-orthogonal mesh, ΔA is calculated using Equations (7.2) – (7.5), and is input into Equation (7.1). Forces and displacements are then defined at nodes x_j and x_{j-1} in locally orthogonal coordinate systems based on \hat{n}_j and \hat{n}_{j-1} respectively. \hat{n}_j and \hat{n}_{j-1} define the in-plane normal to the local crack front at each node, described as the x' direction above. The out of plane normal, the z' direction described above, is defined perpendicular to the crack plane. Finally, the y' direction, which is tangent to the local crack front, is defined as the cross product of the x' direction vector and z' direction vector.

7.4. Model Validation

As discussed in Section 7.2.2, the development of echelon cracks at the front of a planar delamination will be modeled in Chapter 8. However, in order to have confidence in the results obtained using the finite element model, a series of validations will be undertaken to determine the accuracy of ERR predictions for both the planar delamination and the echelon cracks. This validation will take place for (1) a model of only the planar delamination, (2) a model containing only an embedded circular crack, and (3) a model combining the geometries of both (1) and (2). Additional cases, for an ellipsoidal echelon crack shape and for multiple echelon cracks on the plane of a delamination, will also be validated for use in Chapter 8.

7.4.1. Model Benchmarks

The models created for this dissertation must be verified against validated, published results in order to ensure the accuracy of both the FE mesh/model, and the post-processor that extracts ERRs. Therefore, benchmark cases will be used to verify the results for each step of the validation process. As no analytical solutions exist for the mode III split beam specimen, the

ERRs on the planar delamination will be verified using the STB model developed by Davidson and Sediles (2011). Note that using the published STB model data for validation would require the creation of a complex model that contains significant geometry components, loading, and boundary conditions that would not be used for the investigations conducted herein. As it was undesirable to add unnecessary complexity to the model developed for this dissertation solely for validation purposes, a different approach was taken. Davidson and Sediles' (2011) STB model was developed at the SU-CML, and remains accessible for modification and use with this dissertation. Therefore, the loading and boundary conditions in this STB model were changed to coincide with those used herein. However, the model partitions, near-tip mesh, quadratic element shape, and the VCCT code written to extract ERRs for the STB model were all left unchanged. This results in a "simplified STB model" that can still be trusted as a benchmark.

It should be noted that while the STB model is used for validation, it cannot be repurposed for this work. This is because the STB model contains quadratic elements, while the models created herein uses linear elements. Initially, it was intended that ERRs on the echelon crack front would be calculated using the internal VCCT function in Abaqus, and this function can only be used with linear elements. It was later found that the Abaqus VCCT function was not satisfactory for this work, and that echelon crack front ERRs should be calculated using the same post-processor created for calculating ERRs on the delamination front. This post-processor was already written to handle linear elements, and so instead of altering the model to higher-accuracy quadratic elements, and rewriting the post-processor, linear elements were retained. Considering the validation of the model containing only a delamination front, it is expected that the model with linear elements will require many more elements than a model with quadratic elements in

order to achieve the same accuracy. This therefore represents the starting point for the delamination model mesh refinement studies described subsequently.

Analytical solutions are available, and will be used, to validate ERRs extracted on the embedded circular crack (Kassir and Sih, 1975) and the embedded ellipsoidal crack (Newman and Raju, 1983). The analytical solution used to calculate G_I on an embedded circular crack due to tension is (Kassir and Sih, 1975)

$$G_I = \frac{\left(\frac{2}{\pi} \sigma \sqrt{\pi a}\right)^2}{E'} \quad (7.6)$$

Where σ is the applied tensile stress, a is the radius of the embedded circular crack, and E' is the plane strain elastic modulus. Kassir and Sih (1975) can also be used to determine the analytical solution for G_{II} and G_{III} on an embedded circular crack due to shear.

$$G_{II} = \frac{\left(\frac{4(2-\nu)}{\pi} \tau \sqrt{\pi a} * \cos(\phi)\right)^2}{E'} \quad (7.7)$$

$$G_{III} = \frac{\left(\frac{4(1-\nu)}{\pi(2-\nu)} \tau \sqrt{\pi a} * \sin(\phi)\right)^2}{\mu} \quad (7.8)$$

Here, τ is the applied shear stress, μ is the shear modulus, and ϕ is an angular position on the crack front, where $\phi=0$ is aligned with the direction of the shear stress. For an embedded ellipsoidal crack, an analytical solution only exists for the case of mode I loading. From the work of Newman and Raju (1983), the mode I energy release rate is

$$G_I = \frac{(\sigma \sqrt{\pi a Q} * F_e(\phi))^2}{E'} \quad (7.9)$$

Where σ is the applied tensile stress and a is the minor ellipsoidal radii. Q is the ellipsoidal shape factor which has been approximated by Newman and Raju (1979) as $Q = 1 + 1.464 * (a/c)^{1.65}$, where c is the major ellipsoidal radii. $F_e(\phi)$ is a boundary correction factor that accounts for the

influence of the ellipsoid aspect ratio, the proximity of free surfaces, and which depends on the angular location, ϕ , along the crack front.

7.4.2. Validation of Delamination Model

The model of the delamination front was verified using two steps. The first step was to model a plate geometry with a mid-plane delamination. This model is referred to as a “geometry without diagonal partition,” as it does not include a 45° partition for the plane of the echelon crack. The second step was to model an identical plate geometry, but to include a 45° partition in the center of the specimen’s width which will later be the plane of the echelon crack. That is, in this latter step, the nodes that would define the echelon crack faces are constrained to deform together so that there is no echelon crack present. Schematics of these two model geometries are shown in Figure 7.5.

For both models, the nominal specimen geometry given in Section 7.2.3 and Figure 7.1 was used. A number of partitions, which are faces or edges created to subdivide the specimen geometry, were used to control the element shapes and sizes in these models. A partition was added around the delamination tip in the x-z plane to impose a square delamination tip element shape that was as small as possible within the constraints of Abaqus. The smallest possible delamination tip partition was $t/96$, where t is the full specimen thickness of 3 mm. The delamination tip elements were then sized to $t/96$, which is equal to both Δa and h in Figure 7.2. Additionally, a “near-tip refined region” was created using another partition in the x-z plane (cf. Figure E.1 – E.4). The partition extended through the entire specimen thickness and extended ahead and behind the delamination tip. This partition was created in order to control the transition between small near-tip elements and large far-field elements.

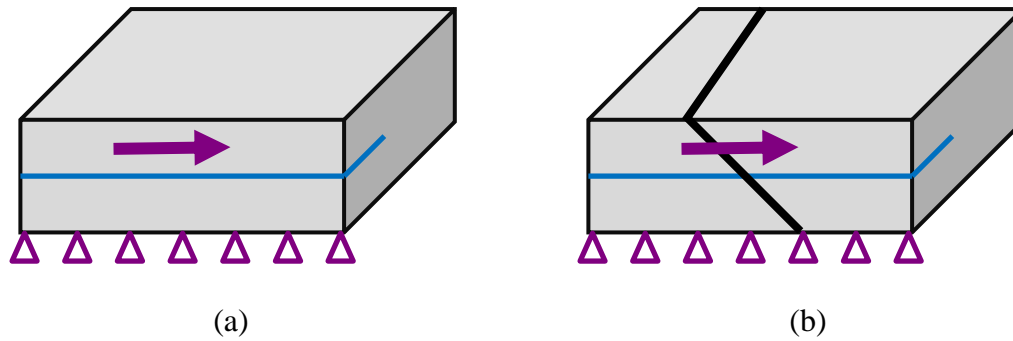


Figure 7.5. Schematics of models created for delamination validation (a) without diagonal partition, and (b) with diagonal partition.

An anti-plane shear displacement was applied to the upper cracked leg, while the lower cracked leg was fixed in both the x and z directions. The top and bottom specimen surfaces were fixed against rotation. To coincide with the experimental work presented in Chapters 5-6, the orthotropic material properties for IM7/8552, as given in Table 6.2 (O'Brien and Krueger, 2003), were used.

7.4.2.1. Geometry without Diagonal Partition

The first step of this study was to determine the details of a mesh with linear elements that could obtain the same ERR distributions as the simplified STB model. A number of different models were created in which the refinement across the width of the specimen as well as in the near-tip region was varied. The number of elements across the width was varied between 30 and 150. Three different element sizes in the near-tip refined region were considered, and in one case the length of the refined region was increased. Details and images of the different meshes used are given in Appendix E.1.

Full results from this step of model validation are given in Appendix E.1. This includes plots of ERR distributions for the models developed herein in comparison to those obtained using the simplified STB model originally developed by Davidson and Sediles (2011). Numerical comparisons of both average ERRs and local values of ERR at the specimen's center and near the edges are also presented. It was found that using FineMeshA-60, which had 60 elements across the specimen width and elements with lengths and heights of 0.08 mm in the x-z plane at the near-tip refined region partition, had the finest near-tip mesh studied, was sufficient to obtain accurate ERRs. For example, for FineMeshA-60, the error in average G_{II} was less than 2%, while the error in average G_{III} was less than 0.002%. Figure 7.6 shows plots comparing the extracted ERR distributions for FineMeshA-60 with those generated using the simplified STB model with the geometry and boundary conditions used herein. It can be seen that the agreement between the model used herein and the results from the simplified STB model are quite good.

It should be noted that for the FineMeshA-60 model, as well as all other models created for this step, very small, but non-zero, values of G_I arise near the specimen edges. This was traced to the difference in how the delamination was modeled herein compared to how it is modeled for the STB. As discussed on Section 7.3.2, the delamination is modeled as a finitely thick wedge. The nonzero values of G_I for the models created herein are due to apparent closure of this finite thickness delamination. That is, there is no interpenetration occurring, but the nodes just behind the delamination tip move slightly towards each other. In the STB, where the delamination is modeled as a seam crack and there is no gap between faces, G_I is zero everywhere. Thus, the small values of G_I found herein are artifacts of the finite thickness delamination, but cannot be removed. As can be seen in Appendix E.1 and Figure 7.6, these small values of G_I do not appear to affect the other ERR distributions.

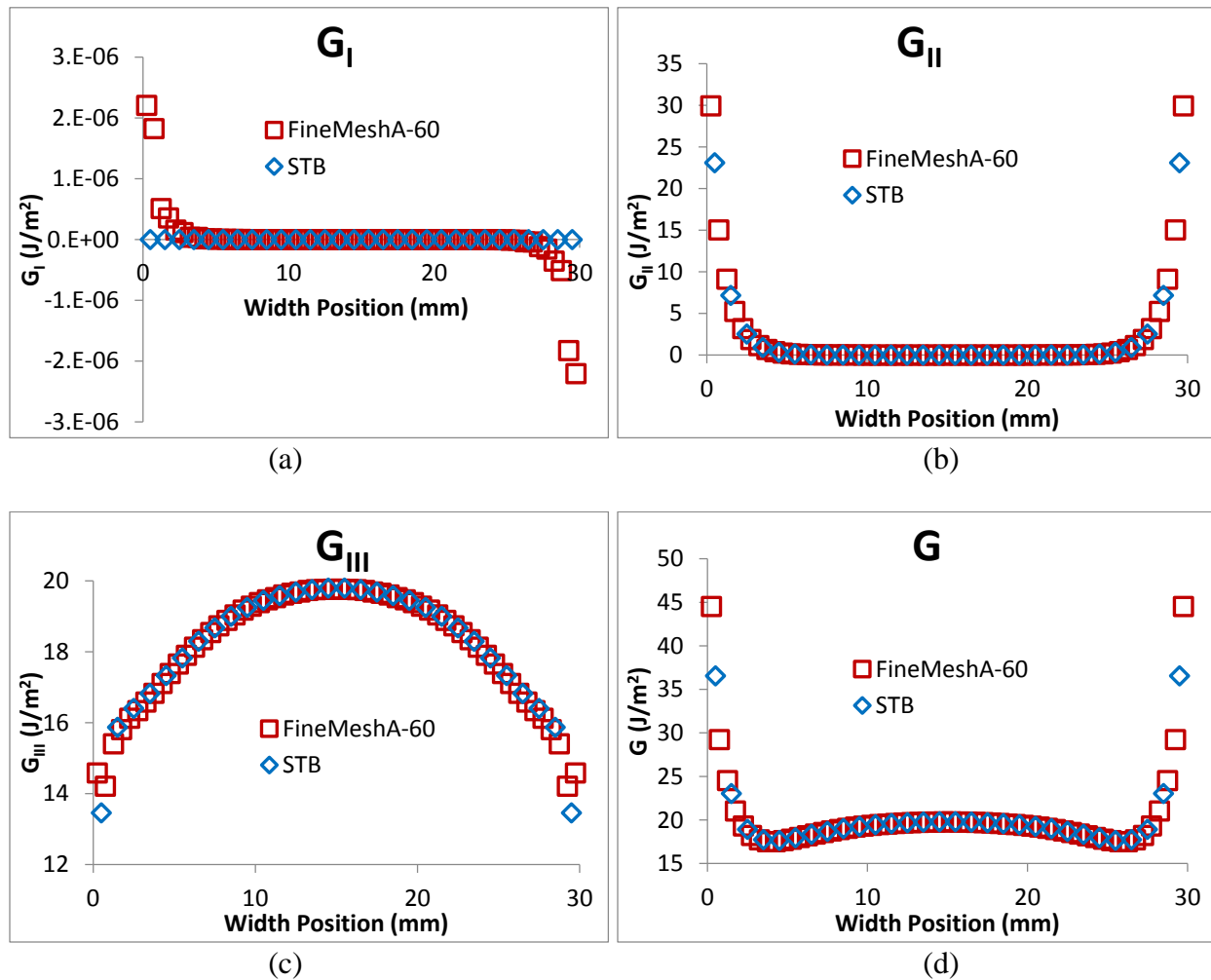


Figure 7.6. ERR distributions comparing the FineMeshA-60 model and the simplified STB model. (a) G_I , (b) G_{II} , (c) G_{III} , (d) G .

7.4.2.2. Geometry with Diagonal Partition

Several models were created containing a diagonal, 45°, partition in the center of the specimen's width. As in Section 7.4.2.1, the near-tip refined region element size and through-width element size were varied. Near-tip region refinement was conducted and the meshes used are separated by increasing fineness and labeled A, B, and C, where A is identical to the

suggested mesh, FineMeshA, found in the previous section. The number of elements across the width was varied from 66 to 94 elements. Note that due to the addition of the diagonal partition and the way that Abaqus creates the mesh, it was not possible to model exactly 60 elements across the width. The element sizes for FineMeshA-60 from the previous section are therefore most closely approximated using FineMeshA-66 in this section. Additionally, a circular partition was included on the diagonal face to represent the future echelon crack location, but the echelon crack itself was not modeled. The element sizing around the circular partition was varied, but only to determine its effect on the accuracy of ERRs along the delamination front. The number of elements around the circumference of the circular partition was varied from 20 to 60 elements. In order to verify that the meshing determined in this step was appropriate for multiple echelon crack sizes, three circular partitions were studied. The circular partitions were sized to represent echelon cracks that were $t/20$, $t/10$, and $t/5$ in diameter.

Similar to the discussion of validation in Section 7.4.2.1, the full results for this step of model validation with the diagonal partition, are given in Appendix E.2. All meshes resulted in good overall accuracy for average G_{II} , G_{III} , and G when compared to results from the simplified STB model. There was some small discrepancy in the local values of G_{II} and G_{III} near the specimen edges for the coarser meshes and the echelon crack size of $t/20$. For this reason, a mesh of FineMeshB and 82 elements across the width, was determined to be necessary for accurate modeling. This represents a slight increase in the through-width refinement but a fairly significant increase in near-tip element refinement. ERR distributions for FineMeshB-88 are shown in Figure 7.7. Similar to the results given in Section 7.4.2.1, and as shown in Figure 7.7a, using a diagonal partition resulted in small non-zero values of G_I near the specimen edges. The exact values are highly dependent on the mesh, and the refinement undertaken for this step was

not able to reduce the effect. It is unclear how much, if any, further improvement could be obtained. However, this is an edge effect that has been traced to the finite delamination thickness, and $G_I = 0$ in the center region of the specimen where the echelon crack will be modeled.

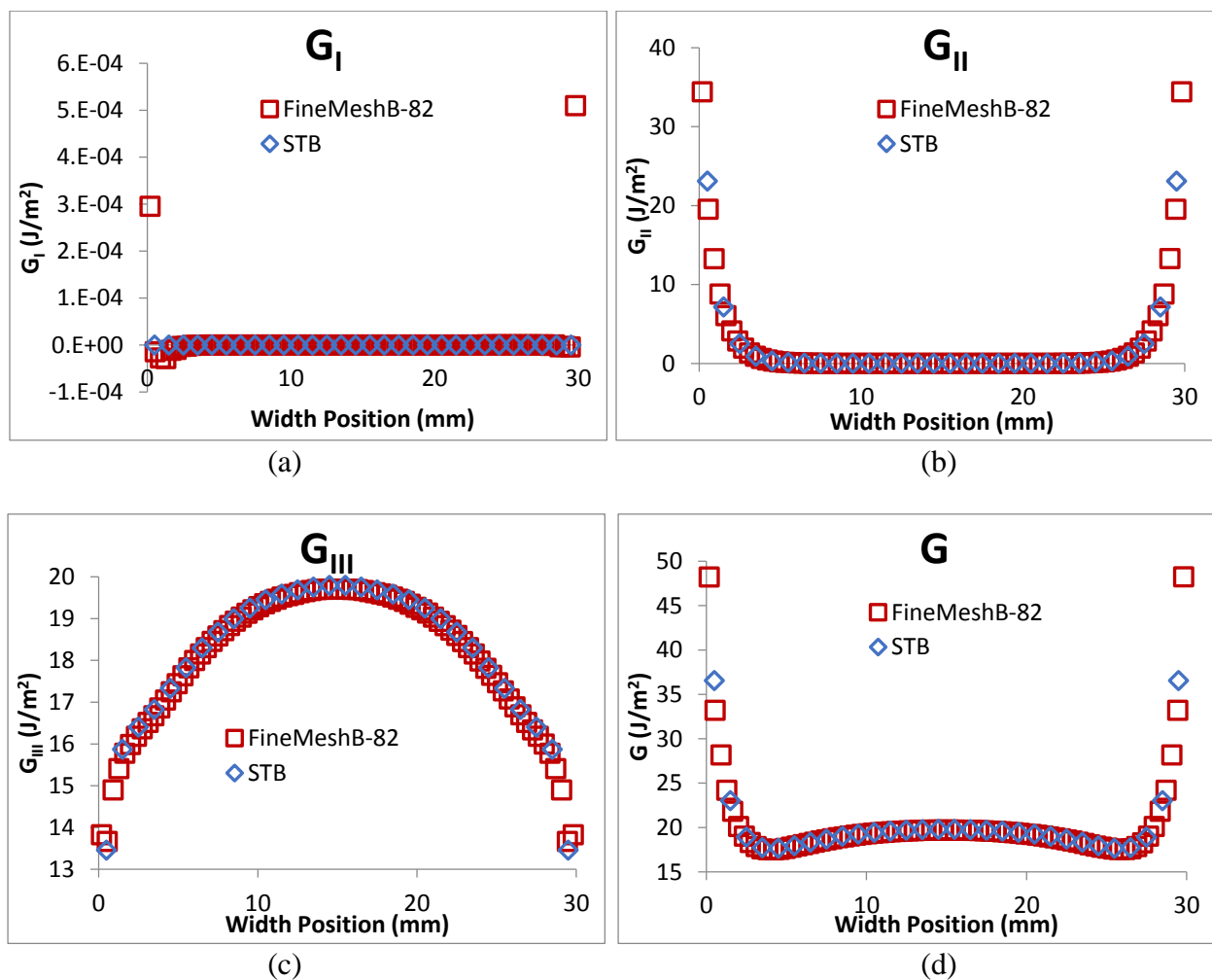


Figure 7.7. ERR distributions comparing the FineMeshB-82 model with a $t/20$ circular partition and the simplified STB model. (a) G_I , (b) G_{II} , (c) G_{III} , (d) G .

7.4.3. Validation of Echelon Crack Model

The echelon crack model was verified using two steps. In both cases an embedded circular crack was placed at the mid-plane of a 4x4x4 mm cube and oriented parallel to the top and bottom surfaces. In the first step, pure mode I loading was applied to the echelon crack by applying tension to the top and bottom surfaces. In the second step, different mixed mode I-II/III loadings were applied to the echelon crack by superposing tensile and shear tractions to the appropriate surfaces of the cube. Schematics of the loads applied in each of the steps are shown in Figure 7.8.

Echelon crack diameters of $t/20$ and $t/5$ were both studied, where t is still 3 mm, the nominal thickness of the model. Using a 4x4x4 mm cube ensured that the echelon crack ERRs remained unaffected by the free surfaces (Newman and Raju, 1983). In order to compare the ERR results to analytical solutions (Kassir and Sih, 1975), isotropic materials properties of $E = 11.38$ GPa and $\nu = 0.32$ were used. These correspond to E_{22} and ν_{12} for IM7/8552 (O'Brien and Krueger, 2003), which was the material used in Section 7.4.2.

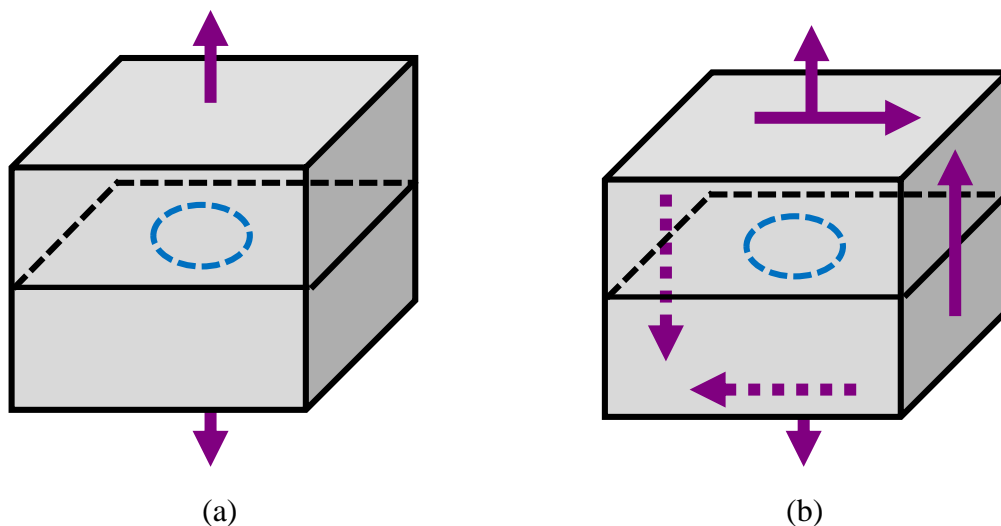


Figure 7.8. Schematics of models created for delamination validation (a) pure mode I, (b) mixed-mode I-II/III.

7.4.3.1. Pure Mode I Loading

Mesh refinement for the embedded circular crack considered both near-tip and far-field refinement. Near-tip refinement considered the number of elements around the crack, from 60 to 120, as well as the length of the elements at, and normal to, the crack front, from 0.0005mm to 0.1 mm. Additionally, the distance over which the elements were constrained to be normal to the crack front was varied. This was done by partitioning additional circles both in front of and behind the echelon crack front, which created additional layers of elements oriented normal to the front. Between one and 18 additional circle partitions were used on each side of the crack front. Far-field refinement was varied both through the thickness and on the planar edges of the modeled cube. Through-thickness element sizes were biased to be small near the embedded crack while becoming larger further away. The minimum through-thickness element size varied from 0.01 mm to 0.08 mm. The maximum through-thickness element size was not studied as a variable, and was 0.4 mm for all models. Far-field planar refinement was unbiased, and the far field element length was varied between 0.038 mm and 0.1 mm.

A summary of the results from this step is given below, while full results are given in Appendix E.3. Both displacement-controlled and traction-controlled tension were applied to induce mode I loading, and there was found to be negligible effect on the results, thus all results presented in this section are for an applied tensile displacement. It was found that increasing the number of elements around the crack front above 60 resulted in no improvement in accuracy for either echelon crack size. For a given echelon crack size, decreasing the near-tip element length itself does not result in improved accuracy. However, for any near tip element size, additional circular partitions controlling the elements size and shape near the crack front resulted in significant improvements in accuracy. This indicates that it is not simply the number of partitions

or the near-tip element size that produces good accuracy, but the distance over which the element size and shape are controlled. For the $t/5$ echelon crack, a near tip element size of 0.04 mm and 18 partitions was determined to be necessary. For the $t/20$ echelon crack, a near tip element size of 0.01 mm and 18 partitions was determined to be necessary. Additionally, both the through-thickness refinement and the in-plane far-field refinement were extremely important, and the smallest element sizes modeled resulted in the most accurate results.

For pure mode I loading on an embedded circular crack, the value of G_I is independent of angular position. Thus, it is easiest to simply report an average error in G_I , compared to the analytical solution given in Equation (7.5), rather than plot the results. For the model with a crack diameter of $t/20$, using a 0.01 mm near-tip element size and 18 circular partitions on either side of the crack front along with an in-plane far-field element size of 0.038 mm and a minimum through-thickness element size of 0.01 mm resulted in less than 3% error in G_I . For the model with an echelon crack diameter of $t/5$, using a 0.04 mm near-tip element size and 18 circular partitions on either side of the crack front along with an in-plane far-field element size of 0.050 mm and a minimum through-thickness element size of 0.015 mm resulted in 0.55% error in G_I . These meshes details are recommended for moving forward.

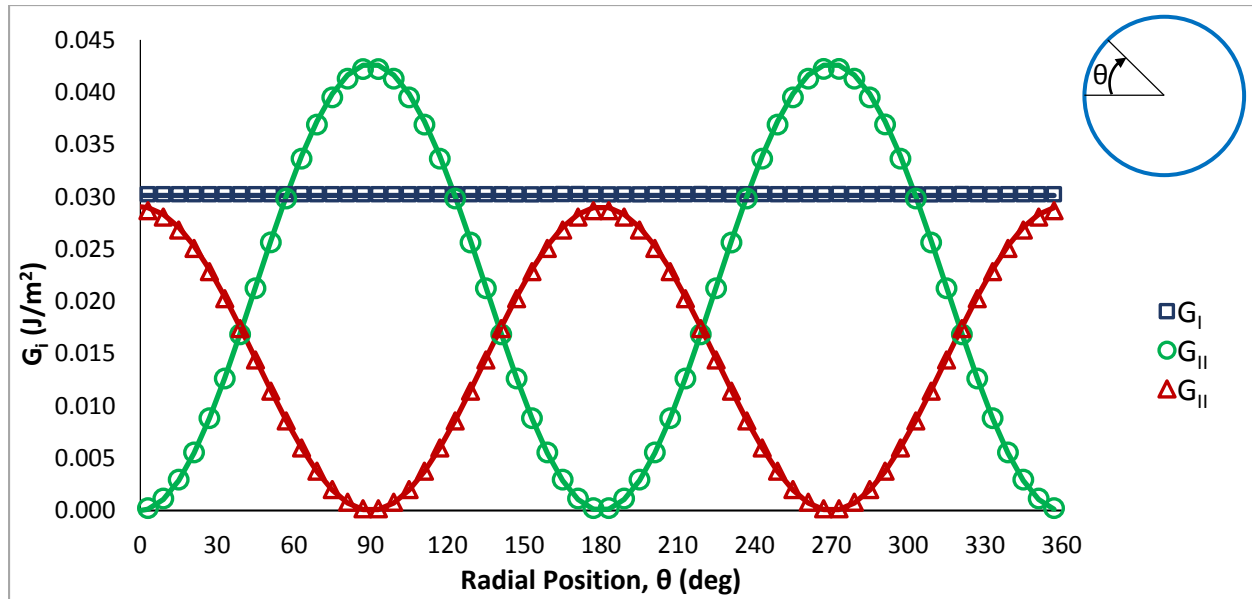


Figure 7.9. ERR distributions for an embedded circular crack of size $t/5$ with mode mixity $G_I/G = 0.46$. Solid lines are for the analytical solution (Kassir and Sih, 1975), symbols are FE results.

7.4.3.2. Mixed Mode I-II/III Loading

The mesh requirements in Section 7.4.3.1 were used as a starting point for this step. The same near-tip and far-field refinement variables studied in the previous section were considered here. It was found during the modeling of this step that in order to create a uniformly applied stress distribution, traction-controlled loading was required, and displacement-controlled loading was not appropriate. Different surface tractions were applied in order to generate mode mixities of $G_I/G = 0.0, 0.46, 0.93, \text{ and } 1.0$ on the crack front.

A summary of the results from this step is given below, while full results are given in Appendix E.4. Results were quite good, compared to the analytical solutions given by Equations (7.6) – (7.8), for all of the meshes considered with the $t/5$ crack diameter. Typical results for $G_I/G = 0.46$ are shown in Figure 7.9, for which the average error in all ERR components was less

than 2%. For the $t/20$ crack diameter, results were better with smaller far-field and through thickness element sizes. For the minimum mesh requirements for a $t/20$ crack determined in Section 7.4.3.1, which included a far-field element size of 0.038 mm, a through thickness element size of 0.01 mm, and a near-tip element length of 0.01 mm with 18 partitions, average errors were 4% or less for all G components except G_{III} , which was 6.2%. In all meshes, there was a trend where the highest errors were for G_{III} , while the lowest errors were for G_I . Additionally, the results were independent of mode mixity. This indicates that accurate results can be expected for the modeling conducted in Chapter 8, where the global mode mixity will be unknown, using the mesh details determined in this step. Based on these results, the mesh requirements given in Section 7.4.3.1 for pure mode I loading are also acceptable for mixed-mode loading.

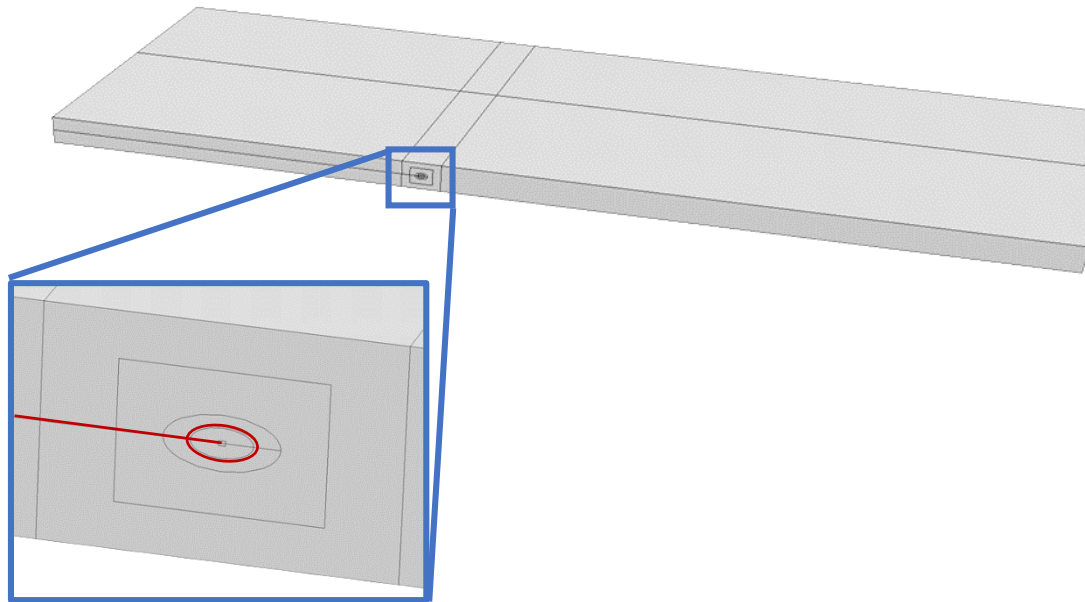


Figure 7.10. Combined FE Model. Partitions shown were used with both delamination-only model and echelon crack-only model. The delamination front and the profile of the echelon crack are highlighted in the inset image.

7.4.4. Validation of Combined Model

The combined model, described as such because the geometry includes both a planar delamination and an echelon crack, was designed to be identical to the single crack model that will be used in Chapter 8. Therefore the specimen geometry is a rectangular plate 30 mm x 80 mm x 3 mm thick as discussed in Section 7.2.3. An image of the model is shown in Figure 7.10. As seen most clearly in the inset to this image, a number of partitions were created in order to obtain a highly controlled mesh where the model element sizes could be based on the result from the previous steps of validation. Partitions used to create the delamination and echelon crack were made across the entire width of the model, and their position on the model edge is highlighted. A small square partition is located around the delamination tip in order to create square near-tip elements of $t/96$ or smaller. Smaller near-tip elements may be obtained by refining the mesh within this partition. In addition to the circular partition creating the echelon crack, 18 partitions were created ahead of, and 10 partitions were created behind, the echelon crack. The smaller number of partitions behind the echelon crack tip was due to the proximity of square delamination tip partition. Most of the circles were only partitioned faces in the echelon crack plane. However, the smallest circle, the echelon crack circle, and the largest circle were all partitioned through the entire specimen width. Outside of the largest circle is a rectangular partition, subsequently referred to as the Level 2 refinement partition. The Level 2 refinement partition is used to set the element size similarly to the planar far-field element size determined for the echelon crack models in Section 7.4.3. Outside of the Level 2 partition is the final refinement partition, referred to as the Level 1 refinement partition, which is equivalent to the refined region in Section 7.4.2. Both the Level 1 and Level 2 refinement partitions extend through the entire model thickness. Figure E.21 in Appendix E shows a schematic with call-outs

for the Level 1, Level 2, and echelon crack partitions. Note that all partitions were included regardless of whether only the echelon crack or only the delamination was modeled. In this way, the same geometry is used for validation of both the echelon crack and planar delamination, and can then be directly transferred for use in Chapter 8.

7.4.4.1. Geometry with Only Echelon Crack

In order to verify ERR results for the embedded echelon crack, it was necessary to apply isotropic material properties to the combined model, such that the results could be compared to the analytical solution (Kassir and Sih, 1975). The material properties used for this step are identical to those used in Section 7.4.3. The delamination was not included in this step, but all of the partitions were in place as if it was modeled. Loading was applied to the echelon crack as a tensile traction on the 3 mm x 80 mm specimen edges. The echelon crack geometry was modeled in two stages. In a preliminary stage, the crack was oriented at 90° , such that the applied tension resulted in pure mode I loading. Next, the echelon crack was oriented at 45° , which is the orientation that will be used for subsequent modeling, such that the same applied tension resulted in mixed-mode I-II/III loading. Both $t/20$ and $t/5$ echelon cracks were used.

Due to the proximity of the echelon crack to the rectangular partition which will later represent the elements surrounding the delamination tip, it was necessary to refine the element size at the delamination tip to be smaller than the $t/96$ that was found to be acceptable in Section 7.4.2.1. Thus, in this step the elements surrounding the delamination tip were sized between $t/864$ and $t/384$. Further, although Section 7.4.2.2 determined that 82 elements across the width (resulting in an element width of 0.37 mm) of the thick plate was acceptable for the delamination front, it was necessary to refine the element width near the echelon crack based on the results

from Section 7.4.3. Thus, a single-direction bias was used near the echelon crack faces such that the width-direction element sizes were biased with a minimum element size between 0.01 mm – 0.03 mm at the echelon crack front and a maximum element size no larger than 0.6 mm at the specimen edges. Edge element sizes of 0.6 mm were deemed acceptable, even though they are larger than allowed based on the results of Section 7.4.2.2, because these large elements will only occur at the very edges of the specimen, far from the echelon crack location, where the accuracy of the model is not as important. The element size on the edges representing the Level 2 refinement partition was varied between 0.030 mm and 0.080 mm, and depended on which echelon crack size was used. For all cases, 60 elements were used around the echelon crack front. Due to the change to a thick plate geometry, and the additional partitions added to control the delamination tip, the elements immediately surrounding the echelon crack tip had to be reduced from those recommended in Section 7.4.3, and so in this step were 0.001 mm for $t/20$ echelon cracks and 0.004 mm for $t/5$ echelon cracks. All other element sizes, including those along the Level 1 refinement partition and the far-field edges, were equivalent to those used in Section 7.4.1.

A summary of the results from this step is given below, while full results are given in Appendix E.5. The results for an echelon crack oriented at 90° were identical to those in Section 7.4.3.1, and no further study was conducted. All of the meshes used with an echelon crack oriented at 45° , and considering echelon crack diameters of both $t/20$ and $t/5$, had relatively small errors in average ERRs when compared to the analytical solutions given in Equations (7.6) – (7.8). Average G_I , G_{II} , and G were 3.3% or less. The most significant errors were in average G_{III} , although this error was still less than 5% for the worst mesh considered. An example of typical results are shown in Figure 7.11 for an echelon crack diameter of $t/20$.

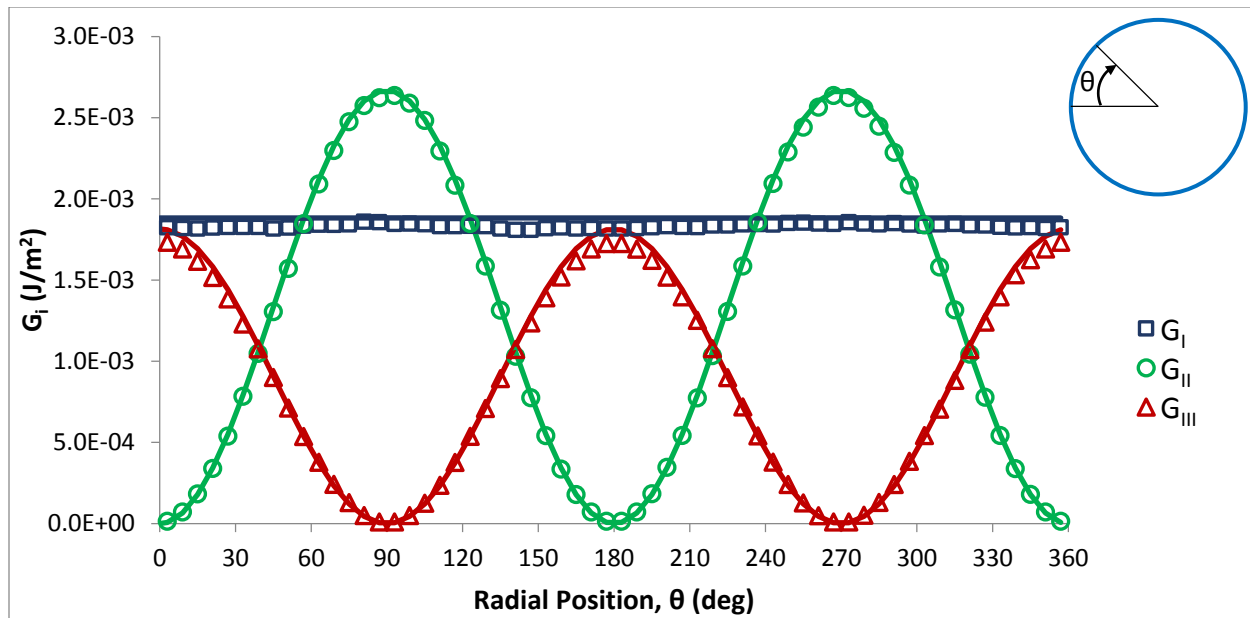


Figure 7.11. ERR distributions for an embedded circular crack of size $t/20$ oriented at 45° in the combined model. Solid lines are for the analytical solution (Kassir and Sih, 1975), symbols are FE results.

Based on the results from this step, it was determined that for a $t/5$ echelon crack, Level 2 refinement of 0.08 mm, width-wise element sizes biased from 0.03 – 0.6 mm, and a delamination tip element size of $t/576$ was required. For a $t/20$ echelon crack, Level 2 refinement of 0.04 mm, width-wise element sizes biased from 0.012 – 0.06 mm, and a delamination tip element size of $t/576$ was acceptable. This was not the most accurate mesh for the $t/20$ echelon crack, but due to a tradeoff between only slight improvements in ERRs and extreme increases in model processing time, it was decided that this mesh would be sufficient.

7.4.4.2. Geometry with Only Delamination

The two meshes determined in Section 7.4.4.1, one each for the $t/20$ and $t/5$ diameter echelon cracks, were studied in this step. For each echelon crack geometry, the full mesh from the previous step was retained, and the delamination was modeled while the nodes on the

echelon crack faces were constrained to deform together such that the echelon crack was not present. As the two meshes studied in this step were formulated based on all of the previous validation steps, and are significantly more refined than the meshes found to be acceptably accurate for a planar delamination as studied in Section 7.4.2, it was predicted that they would give accurate results in this step, and thus no further study was planned unless it was apparent that these meshes were insufficient. In order to compare the results to those from the simplified STB model, the orthotropic material properties from Table 6.2 were again used. Full results are given in Appendix E.6, while a summary of the results is given below.

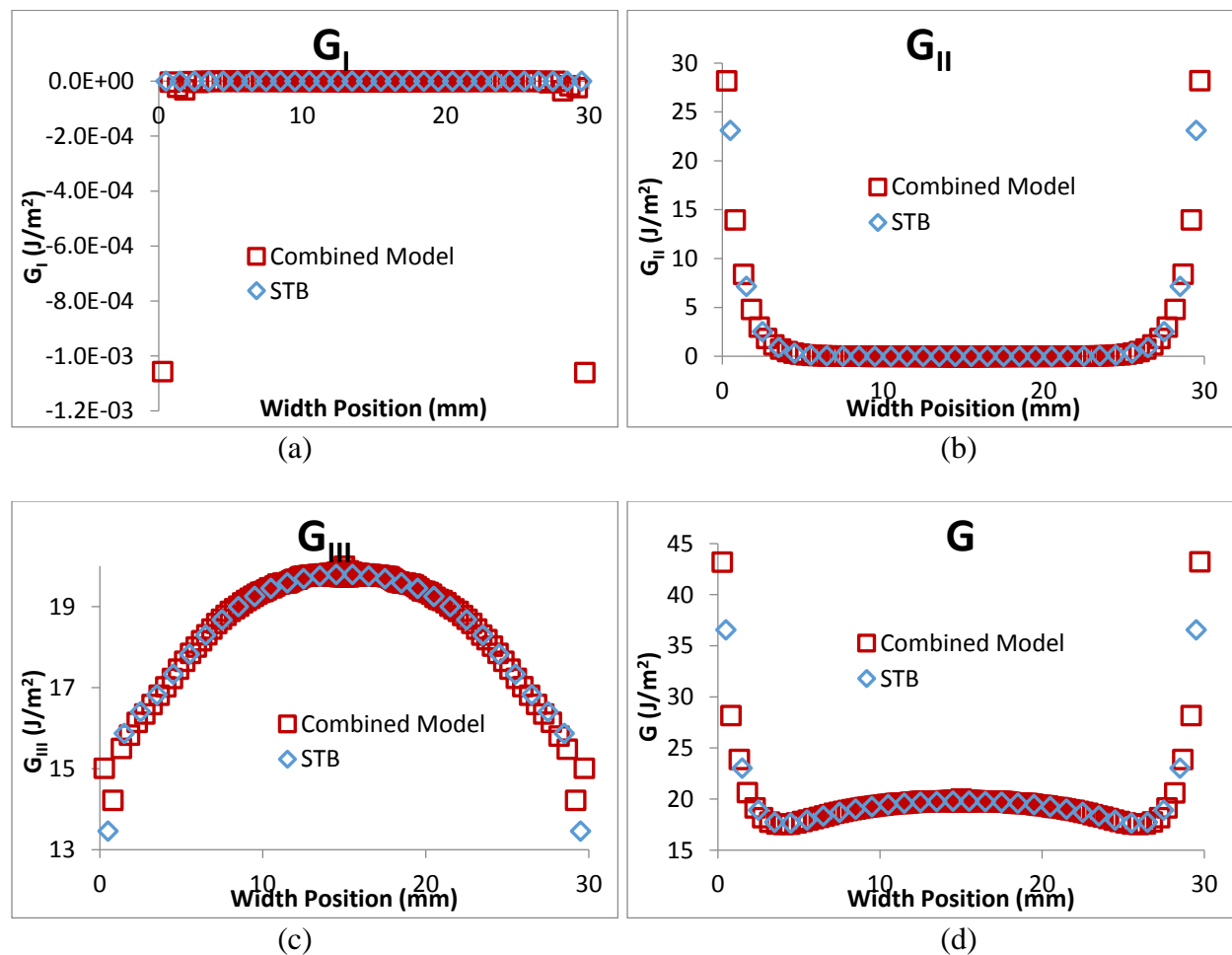


Figure 7.12. ERR distributions for the delamination front in the combined model and the simplified STB model. (a) G_I , (b) G_{II} , (c) G_{III} , (d) G .

The results for delamination front ERRs using the meshes described in Section 7.4.4.1 for both the $t/20$ and $t/5$ echelon crack diameters resulted in very accurate results along the majority of the delamination front. The results for the mesh designed for a $t/5$ diameter echelon crack are shown in Figure 7.12. For both meshes, the average error is under 4% for G_{II} , and under 0.3% for G_{III} and G . Slight discrepancies in G_{II} and G_{III} near the specimen edges remain. However, the specimen edges are far from the region near the echelon crack, and it is expected that slight errors in these edge results will not affect the results of subsequent studies. Thus, the meshes described in Section 7.4.4.1 are also acceptably accurate for modeling the planar delamination.

7.4.5. Validation of Ellipsoidal Echelon Cracks

A model was developed for an embedded ellipsoidal echelon crack based on the geometry, partitioning, and mesh used in Section 7.4.3. The block geometry was lengthened to 8 mm x 4 mm x 4mm to maintain enough distance between the echelon crack and the block edges. The echelon crack was ellipsoidal in shape with a major diameter of 0.75 mm and a minor diameter of 0.3 mm. Isotropic material properties identical to those used in Section 7.4.3 were used for this step. The mesh included ten face partitions behind and eighteen partitions ahead of the crack tip, similar to those used in Section 7.4.4, and crack contained 60 elements around the perimeter with a near-tip element length of 0.002 mm. As determined to be necessary for a circular echelon crack in Section 7.4.3, the ellipsoidal echelon crack model contained a far-field element size of 0.034 mm, and a through-thickness element size of 0.01 mm at the plane of the echelon crack.

In order to compare the FE results to an available analytical solution (Newman and Raju, 1983), only pure mode I loading could be applied, as analytical solutions are not available for an

embedded ellipsoidal crack subjected to mixed-mode loading. The ellipsoidal shape of the crack resulted in a non-orthogonal mesh, and so the area correction factors discussed in Section 7.3.2 were used. A plot comparing the results from the FE model to the analytical solution given in Equation (7.9) is shown in Figure 7.13. It can be seen that there is very good agreement between the FE results and the analytical solution. Since the mesh used in this step is so similar to the circular near-echelon crack mesh used in the combined model, it is expected that using an embedded ellipsoidal crack in the combined model will also give good results. The full results for this step can be found in Appendix E.7.

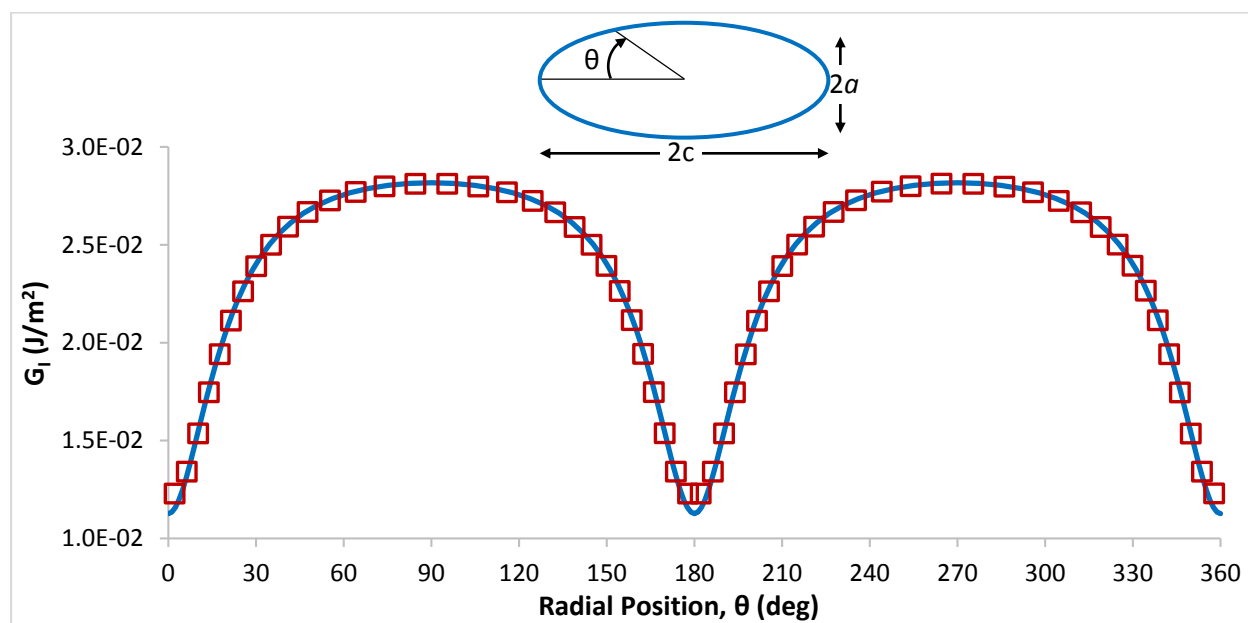


Figure 7.13. ERR distributions for an embedded ellipsoidal crack with $a/c = 0.4$. Solid line is for the analytical solution (Newman and Raju, 1983), symbols are FE results.

7.4.6. Validation of Multiple Echelon Cracks

Validation of a model with multiple echelon cracks proceeded following a similar process to that used for the combined model in Section 7.4.4. A model was created with three diagonal partitions in order to model three echelon cracks of diameter $t/20$ spaced a distance of $3t/20$ away from each other along the delamination front, with the middle echelon crack located at the center of the specimen width. The near-tip and far-field element sizes determined in Section 7.4.4 were used in this step, with the only change that the through-thickness refinement was modified to account for multiple echelon cracks. The regions between echelon cracks used constant sized elements of length 0.012 mm. The regions between the outside echelon cracks and the specimen edges were biased such that the elements closest to the echelon cracks were 0.012 mm and the elements closest to the specimen edges were 0.6 mm, which is the same biasing as was used in Section 7.4.4.

First, isotropic material properties were used and, while the entire mesh was in place, only the middle echelon crack was modeled while the outside two echelon cracks and the delamination were not modeled. As in Section 7.4.4.1, tension was applied to the narrow (3 mm x 80 mm) specimen edges. The results were indistinguishable from those in Section 7.4.4.1. Next, only an outside echelon crack was modeled, and the results were again almost identical to the results given in Section 7.4.4.1. Finally, orthotropic material properties were used and only the delamination was modeled, while the echelon crack mesh was included but the echelon cracks themselves were not. An anti-plane mode III load was applied and the upper and lower (30 mm x 80 mm) specimen faces were constrained against rotation, as in Section 7.4.4.2. The results were very similar to the results given in Section 7.4.4.2. Thus, it was clear that no

additional refinement was necessary beyond that determined in Section 7.4.4 to produce accurate results with multiple echelon cracks. The full results for this step can be found in Appendix E.8.

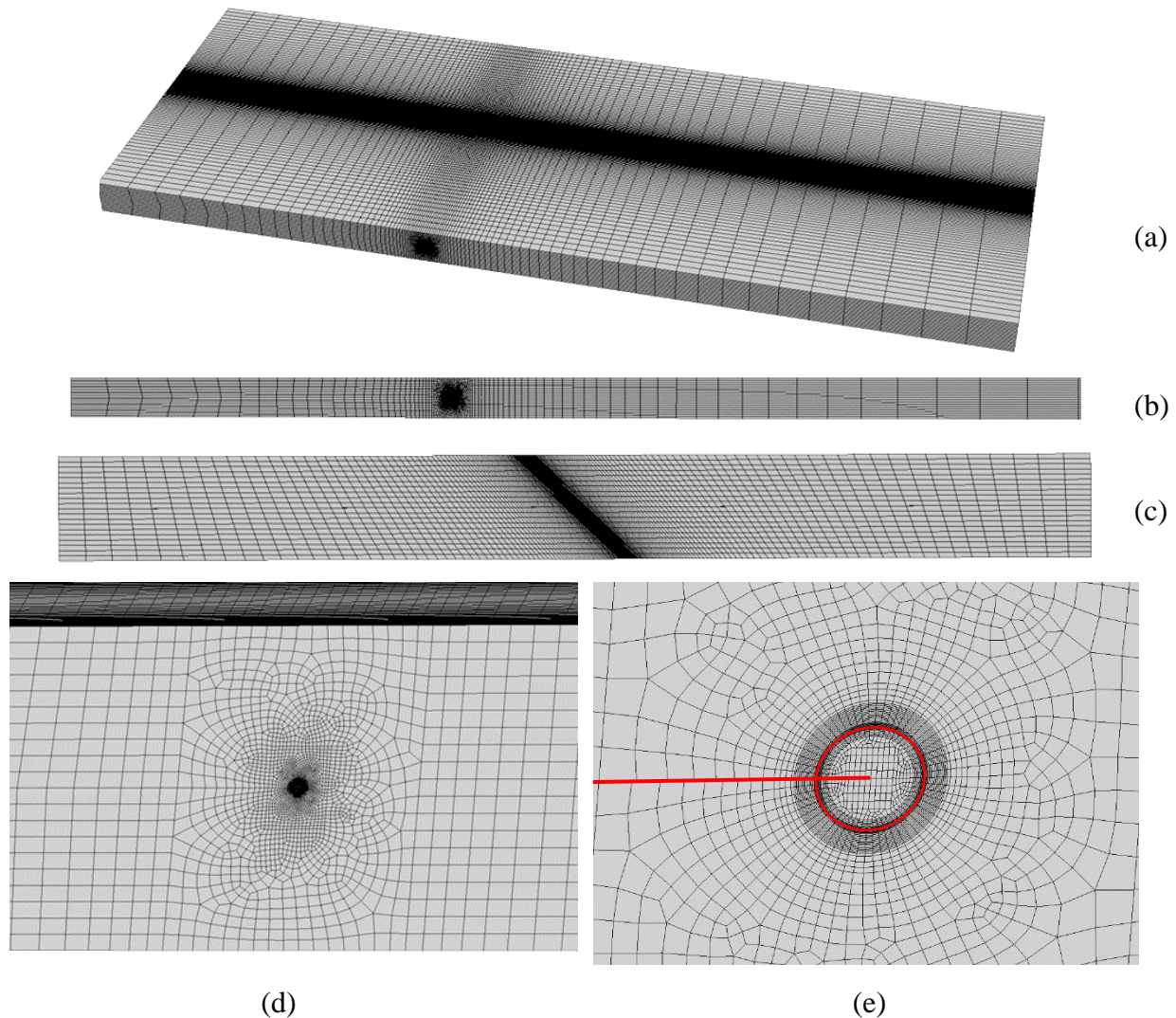


Figure 7.14. Final model of a $t/20$ diameter echelon crack for use in Chapter 8. (a) Isometric view of model. (b) Edge-view of length-wise mesh with several stages of refinement. (c) Edge-view of width-wise mesh with 45° partition and element sizes from 0.012 mm to 0.6 mm. (d) 45° plane view of echelon crack with ordered element shapes surrounding crack tip. (e) Close-up 45° plane view of echelon crack (outlined in red) with 60 elements around the crack tip and 0.001 mm element length. Delamination plane also highlighted in red.

7.5. Final Model Details

The model that will be used in Chapter 8 to study the mechanisms leading to echelon array development under anti-plane shear loading contains all of the intended details from Section 7.2.3. The echelon crack will be modeled with 10 layers of ordered partitioned faces behind the crack front and 18 layers ahead of the crack front. Sixty elements will be modeled around the echelon crack front. The planar element length immediately surrounding the echelon crack will vary between 0.001 mm and 0.004 mm depending on the modeled echelon crack diameter. The delamination tip element length and height will be $t/576$. Depending on echelon crack diameter, the through-width element size will be biased from 0.012 mm or 0.3 mm (nearest the echelon crack) to 0.6 mm (nearest the free edges). Slight variations to these element sizes may be necessary when modeling echelon cracks of different sizes, geometries, or when modeling multiple echelon cracks. However, any changes will be based on the findings in this chapter, and changes to the mesh described above will only result in a more refined mesh. Images of the mesh used with a $t/20$ diameter echelon crack are shown in Figure 7.14.

7.6. Conclusions

The FE model intended for use in Chapter 8 to study the development of an echelon array was formulated in this chapter. A series of mesh validation steps were conducted, and VCCT was used to calculate the ERRs on the echelon crack front or delamination front in each step and compare it to a benchmark. Validation was first conducted for individual models representing either a planar delamination or an embedded echelon crack. Subsequently, a combined model was created that contained the necessary partitions to represent an echelon crack intersecting a planar delamination. Validation was again conducted, using this combined model, on only an

echelon crack and then only a planar delamination. Further mesh validation was conducted considering an ellipsoidal echelon crack and a model with multiple echelon cracks. The details of the model developed that will be used in Chapter 8 were determined based on the results of these validation steps.

Chapter 8. Modeling of Echelon Crack Array Development

8.1. Introduction

This chapter uses numerical modeling to study how an array of echelon cracks develops ahead of planar delamination advance under global mode III loading. In Chapter 7, the modeling plans and data reduction technique were introduced, and a series of model validation steps were carried out. In this chapter, the verified model is used to generate new results. To study the development of an echelon array, this chapter first covers the modeling of a single echelon crack intersecting a planar delamination front. Several stages of echelon crack growth are modeled. Subsequently, multiple echelon cracks are modeled on the planar delamination front. Initially, these modeling results are presented in Sections 8.2-8.3 with limited interpretation. These results are then used in Section 8.4, where a discussion of echelon array development is presented. Additionally, the modeling results are interpreted in order to describe the mechanics behind planar delamination advance occurring slightly behind continued echelon crack growth. These discussions are compared to experimental results presented in Chapters 5-6, and it is found that the modeling results generated herein support the experimental observations of echelon array development.

8.2. Modeling Results for a Single Echelon Crack

The first step to understanding how an array of echelon cracks develops is to model the behavior of a single echelon crack at the delamination front. Several different shapes of echelon crack will be modeled, representing different stages of echelon crack growth. For each stage of

growth, several different echelon crack sizes will be modeled. The first stage of development will be assumed to be a circular echelon crack centered along the delamination front. Subsequent echelon crack shapes that are modeled will be based on predictions from the echelon crack ERRs for a given shape.

8.2.1. Centered Circular Echelon Crack

The first geometry modeled was a circular echelon crack centered at the delamination tip. An image of a typical mesh cross section for this geometry is shown in Figure 8.1, where the echelon crack and delamination tips are highlighted. Note that the echelon crack is oriented at 45° to the plane of the delamination, as described in Section 7.2.3 and Figure 7.1. Several different echelon crack diameters were modeled: $t/20$, $t/15$, $3t/40$, $t/10$, $t/5$, and $t/3$, where t is the model thickness of 3.0 mm. This represents a significant range of sizes, from the smallest size that can be modeled within the constraints of the Abaqus programming using the approach described in Chapter 7 ($t/20$), to a significantly large echelon crack ($t/3$) that is still fairly far from the model's free surfaces. For each case considered, a mode III load was applied, consistent with that discussed in Section 7.2.3, and the VCCT was used to extract energy release rates along both the delamination and the echelon crack fronts.

8.2.1.1. Delamination Front Results

Energy release rates on the delamination front for centered circular echelon cracks of different diameters are presented in Figure 8.2. The mode I ERR component is shown in Figure 8.2a. From this plot it can be seen that G_I is small, but non-zero, near the location of the echelon crack. This appears similar to the apparent G_I observed at the delamination edges in the model

validation process described in Section 7.4.2, although in this case the mode I component arises at the edges created by the echelon crack, rather than the outside free surfaces. It should be noted that the results presented in Figure 8.2a actually show a much smaller value of G_I than was initially obtained with this model. An investigation of the cause of the apparent G_I determined there was some localized delamination surface interpenetration occurring near the echelon crack front. A surface-to-node contact constraint was implemented in the model on the delamination front to limit this, and the ERRs presented in Figure 8.2a, and in all subsequent modeling, are for cases that include this contact constraint. The non-zero values of G_I right at the echelon crack persist because the mode III loading translates some of the delamination tip nodes into the region where the echelon crack has opened. In this region, the nodes immediately behind the delamination tip appear to close, but due to the mode III translation, there is no interpenetration occurring. Therefore, it can be concluded that the small, localized values of G_I seen here are an artifact of the model created, and do not represent true mode I loading.

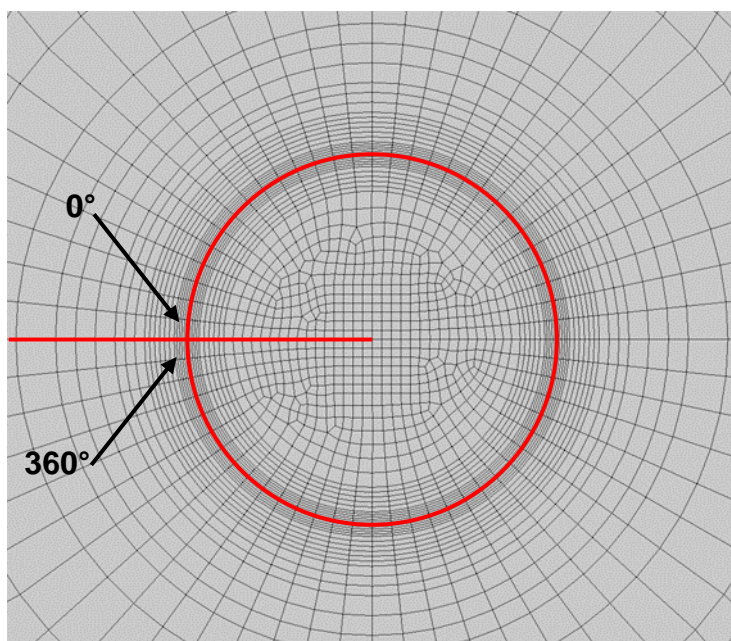


Figure 8.1. Echelon crack plane-view of model with delamination and centered echelon crack shape highlighted.

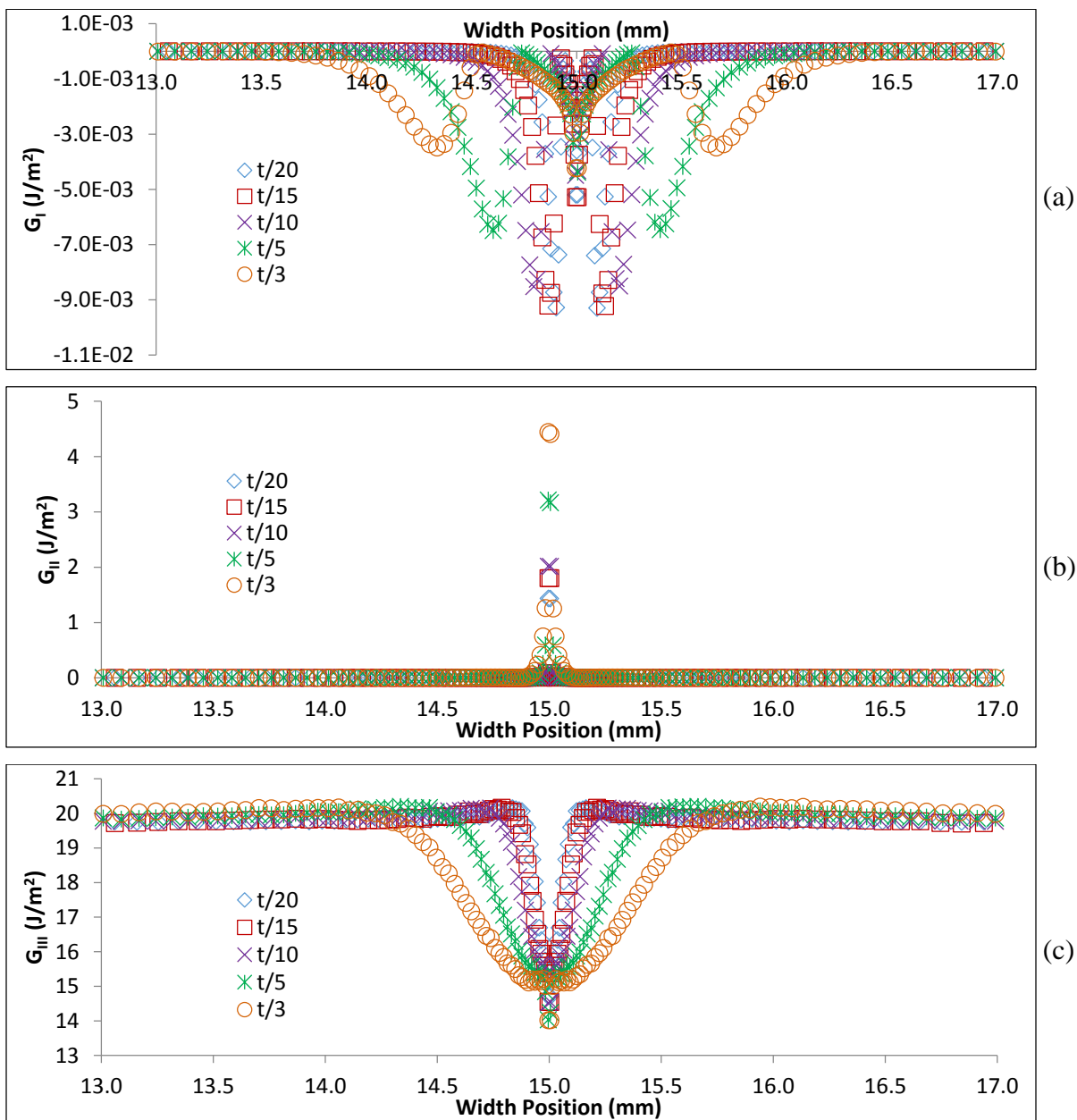


Figure 8.2. ERRs on delamination front for centered circular echelon cracks of diameters $t/20$, $t/15$, $t/10$, $t/5$, and $t/3$. (a) G_I , (b) G_{II} , (c) G_{III} .

Figure 8.2b shows G_{II} along the delamination front for centered circular echelon crack models with different diameter echelon cracks. The value of G_{II} in the interior region of the specimen is approximately zero, however, a non-zero G_{II} arises in the center of the delamination

front at the edges created by the echelon crack. It is unclear if the peak value of G_{II} at the echelon crack depends on echelon crack diameter, or if there is an effect of the slightly different meshes used for each geometry. It looks like the peak G_{II} at the center of the delamination front may be increasing for increasing echelon crack diameters, but further study of this phenomenon is required.

The distribution of G_{III} on the delamination front for centered circular echelon crack models with different diameter echelon cracks is presented in Figure 8.2c. The results for the regions far away from the location of the echelon crack are identical to those discussed in Section 7.4.4.2. However, G_{III} drops in the vicinity of the echelon crack. The amount that G_{III} drops (i.e., the minimum value of G_{III}) appears to be independent of the echelon crack diameter. However, the range over which G_{III} is affected by, or decreased due to, the presence of the echelon crack is highly dependent on diameter. For all of the cases modeled, the value of G_{III} is affected over a distance of ± 1 echelon crack diameter. For example, for an echelon crack of diameter $t/10$ (0.3 mm) located at the midpoint of the model's width (15 mm), G_{III} is affected from 14.7 mm to 15.3 mm.

The G_{II} and G_{III} distributions near the echelon crack front reveal an interesting result. In a traditional thick-plate geometry without an echelon crack, the traction free edges of the specimen require that the shear stress τ_{yz} , and therefore G_{III} , goes to zero at the specimen edges. A G_{II} component then arises near the free edges to enforce equilibrium. This has been recognized by numerous authors (Bažant and Estenssoro, 1979; Buchholz et al., 2004; Davidson and Sediles, 2011; Dhondt et al., 2001; Nakamura and Parks, 1989), and is in agreement with the results shown in Figure 7.12 for a planar delamination without an echelon crack. The free surface created by the echelon crack intersecting the delamination has a different result. Because the

echelon crack is oriented at 45° , the echelon crack surface is not a y-face, and therefore τ_{yz} and G_{III} are not required to go to zero, although they do decrease. This in turn limits the peak value of G_{II} that arises to enforce equilibrium to be much lower than that which occurs at a free edge. Thus, it can be seen that the effect of a 45° echelon crack is different from that of a traction free specimen edge, and this may mean that the magnitude and presence of G_{II} is less important to the localized onset of delamination growth in the vicinity of an echelon crack than it may be at the specimen's free edges.

As discussed in Section 2.5.3, there is limited data available in the literature to compare to the modeling results produced for this dissertation. However, the above results, considering energy release rates calculated along the delamination front for a model with a centered circular echelon crack, do have some analogs in the literature that can be used for comparison. The data presented in Figure 8.2b-c is qualitatively similar to results presented by Pham and Ravi-Chandar (2014). Note that only qualitative comparisons can be made because of the differences in loading and echelon crack orientation between this study and the one conducted by Pham and Ravi-Chandar (2014). However, both studies show the mode III component decreasing and the mode II component rising in the vicinity of the echelon crack. Pham and Ravi-Chandar (2014) also see that the range over which the mode III component is affected by the echelon crack is approximately one diameter on either side of the echelon crack location, which is identical to the result found herein. The results of Ressel and Theilig (2012) may also be considered, although the comparison is also qualitative due to differences in both loading and model geometry. Rather than a thick plate geometry under anti-plane shear loading, they used a cylinder with an internal circular delamination with echelon cracks oriented at 45° and subjected to pure torsion. Similar to the above results, Ressel and Theilig (2012) describe a decrease in mode III and a rise in mode

II loading near the echelon crack. However, Ressel and Theilig (2012) report a non-zero mode I component everywhere, even though a pure mode III loading was apparently applied. As this paper was a short communication, it does not contain enough information to verify the accuracy of the results, or determine what might be causing the apparent mode I component. Despite uncertainty in the results of the Ressel and Theilig (2012) paper, the agreement between this dissertation and the two literature results is encouraging, and particularly in view of the validation studies described in Chapter 7 and Appendix E, indicates that the delamination front ERRs presented in Figure 8.2 are likely accurate.

8.2.1.2. Echelon Crack Front Results

The energy release rates calculated along the echelon crack front for the different echelon crack diameters are presented in Figure 8.3. The horizontal axis for each plot gives an angular position in degrees. As indicated by the schematics inset in each plot, 0° starts behind the delamination front on the upper face, 180° is the point furthest ahead of the delamination front, and 360° is in the same location as 0° , but on the lower face of the delamination front.

Figure 8.3a presents the values of G_I calculated on the echelon crack front for the different echelon crack diameters modeled for this section. G_I is highest at 180° , which is directly ahead of the delamination tip. It then decreases to zero at the back edges that intersect the delamination plane. The peak value of G_I decreases monotonically with increasing echelon crack diameter, although the difference is difficult to see for the smaller echelon crack diameters. The decrease in the peak value of G_I between echelon crack diameters of $t/20$ and $t/3$ is approximately 30%.

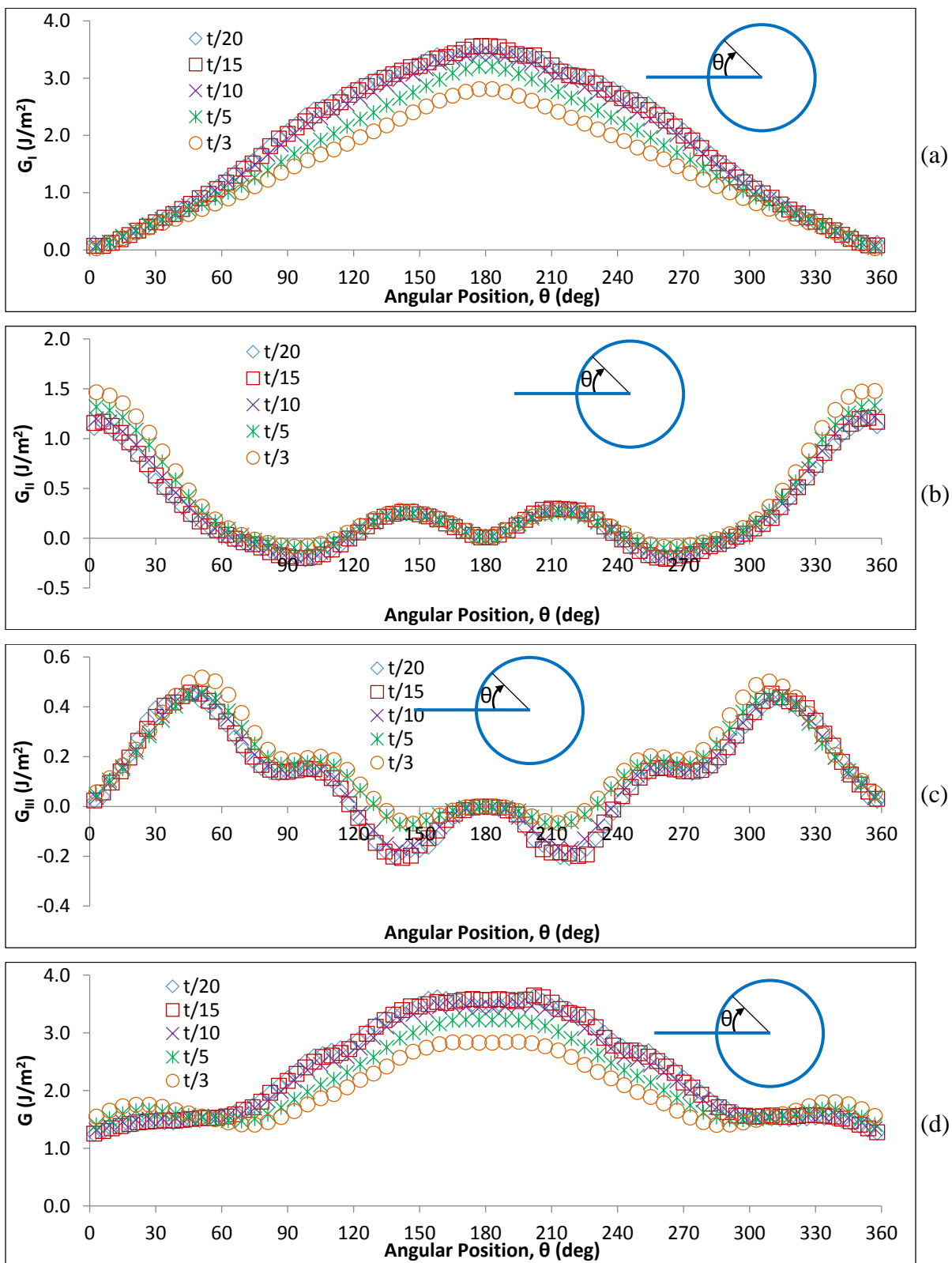


Figure 8.3. ERRs on echelon crack front for centered circular echelon cracks of diameters $t/20$, $t/15$, $t/10$, $t/5$, and $t/3$. (a) G_I , (b) G_{II} , (c) G_{III} , (d) G .

The value of G_{II} calculated on the echelon crack front for different diameter echelon cracks is presented in Figure 8.3b. As can be seen in this figure, G_{II} is approximately independent of echelon crack diameter. It can also be seen that G_{II} varies around the echelon crack front with the highest magnitude of G_{II} located at the back edges of the echelon crack which are contacting the delamination plane, and $G_{II} = 0$ at 180° where G_I is a maximum. The cause of the negative G_{II} values around 90° and 270° is unclear. Considering the VCCT, this means that locally, the force is in the opposite direction to what is expected for “closing” the crack. It is expected that this is caused by some global-local deformation interaction, the meaning of which is not clear.

Figure 8.3c presents the values of G_{III} calculated on the echelon crack front for different echelon crack diameters. As seen with the G_{II} distribution, G_{III} is variable around the echelon crack front. It is highest in the region behind the delamination front (near 60° and 300°), and is zero at the very front (180°) and very back (0° and 360°). Note that the peak values of G_I , G_{II} , and G_{III} all occur at different locations, and that the peak values of G_I (at 180°) are quite a bit larger than for G_{II} and G_{III} . As observed in the G_{II} distribution, there are some regions where G_{III} is negative, also likely caused by a global-local deformation interaction.

Total G along the echelon crack front is shown in Figure 8.3d. Note that only positive values of G_{II} and G_{III} are included in the calculation of G . As seen from a comparison of this plot to the other plots in Figure 8.3, the majority of the total ERR is caused by G_I , although near 0° and 360° G_{II} and G_{III} make notable contributions. It is clear, however, that the highest ERR is predominantly mode I and is directly ahead of the delamination tip.

The only available literature to compare these results to is the work of Ressel and Theilig (2012). There has already been concern expressed in Section 8.2.1.1 over the accuracy of these

results, but as the only available option, it will still be considered. Ressel and Theilig (2012) extract mode I distributions that look quite similar to those given in Figure 8.3a, where G_I is highest at 180° and decreases towards zero at the edges that intersect the planar delamination. Ressel and Theilig (2012)'s mode II and mode III distributions both go to zero at 180° , which is in agreement with the results presented in Figure 8.3b-c, but otherwise their results are quite different. Ressel and Theilig (2012) report unsymmetric mode II and mode III distributions, although based on their geometry and loading these distributions should be symmetric, which makes it more likely that there is an issue with their analysis. Therefore, even though there is agreement between the mode I distributions, their results should not be used as support for the results presented herein.

8.2.2. Semi-Ellipsoidal Echelon Crack

The results in Section 8.2.1 show that, for a centered circular echelon crack, G_I is the most significant contributor to the ERR, and likely drives echelon crack growth. As will be discussed further in Section 8.4, the high ERRs near 180° indicate that a centered circular echelon crack would likely grow forward into the uncracked region, though the echelon crack would be unlikely to increase in ‘height’ (growth in 90° or 270° directions). Therefore, the next model used a semi-ellipsoidal echelon crack. That is, the half of the echelon crack behind the delamination tip remained circular, while the half of the echelon crack ahead of the delamination tip was modeled as an ellipse. An image of a mesh with the semi-ellipsoidal echelon crack and the delamination plane highlighted is shown in Figure 8.4. As in the case of Figure 8.1 (and all other echelon cracks described subsequently), this echelon crack is oriented at 45° to the plane of the delamination.

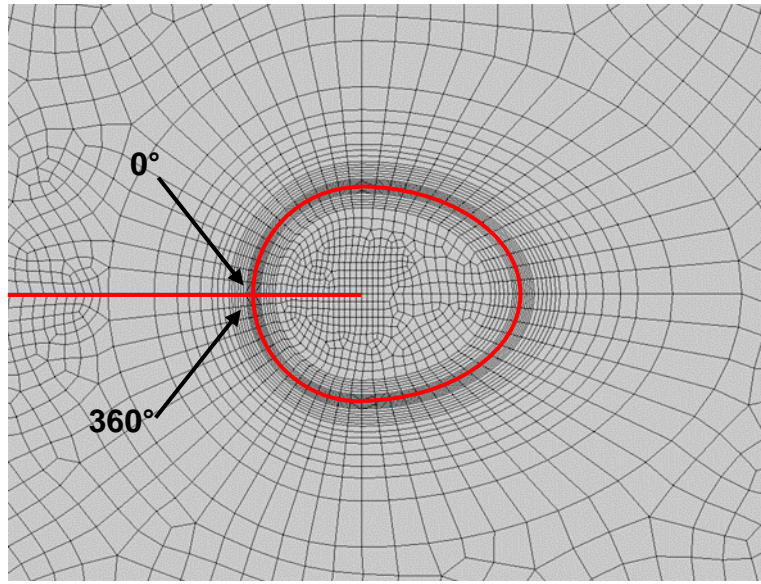


Figure 8.4. Echelon crack plane-view of model with delamination and semi-ellipsoidal echelon crack shape highlighted.

In order to represent the case where a centered circular echelon crack had advanced ahead of the planar delamination, models were created with semi-ellipsoidal echelon cracks that had “nominal diameters” of $t/20$ and $t/10$. Here, the nominal diameter refers to the diameter of the circular portion, and therefore to the minor diameter of the ellipsoidal portion, of the echelon crack. The major diameter of the ellipsoidal portion of the echelon crack is modeled as either 1.0x, 1.5x, or 2.0x the nominal diameter. Note that with these definitions, the case where the major ellipsoidal diameter is 1.0x the nominal diameter is simply the centered circular echelon crack from Section 8.2.1. Models were run for the new cases ($t/20$ and $t/10$ with 1.5x and 2.0x major diameters), and ERRs were extracted along both the delamination and the echelon crack fronts.

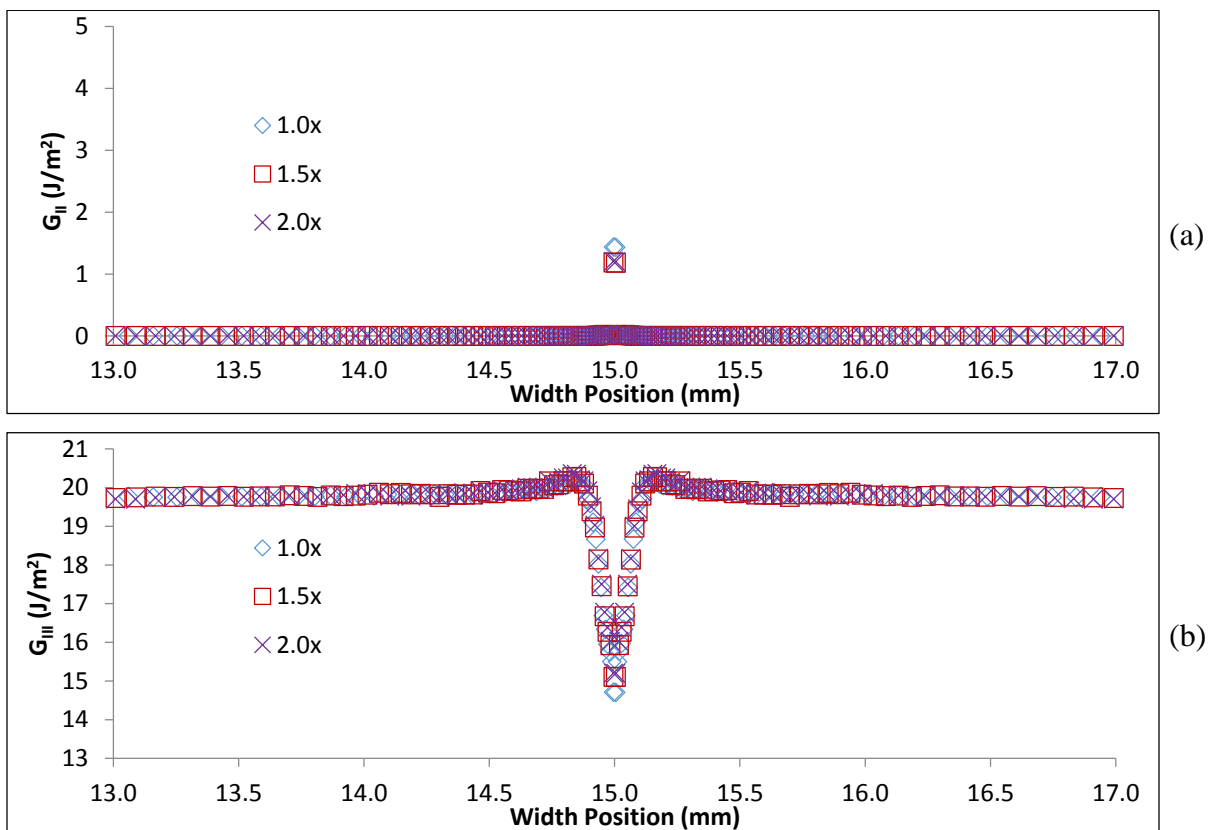


Figure 8.5. ERRs on delamination front for semi-ellipsoidal echelon cracks of nominal diameter $t/20$ with major ellipsoidal diameters of 1.0x, 1.5x, and 2.0x. (a) G_{II} , (b) G_{III} .

Figure 8.5 presents the energy release rates G_{II} and G_{III} on the delamination front for semi-ellipsoidal echelon cracks with a nominal diameter of $t/20$. G_I is not shown as it is essentially zero, and quite similar to the centered circular echelon crack results presented in Figure 8.2a. However, in contrast to Figure 8.2, Figure 8.5 indicates that G_{II} and G_{III} on the delamination front both appear to be independent of the major ellipsoidal diameter. The region over which G_{III} is affected by the echelon crack is the same as for the circular crack, indicating that the distance the circular portion of the echelon crack extends back into the delaminated region may be controlling this. It is possible that G_{II} is slightly lower for the 1.5x and 2.0x major ellipsoidal diameters than the circular case, but this could also be an effect of slight differences

in meshing the different geometries. The trends for the $t/10$ nominal diameter models are identical to those shown in Figure 8.5.

Energy release rates along the front of semi-ellipsoidal echelon cracks are given in Figure 8.6. The results are very similar for $t/20$ and $t/10$ nominal diameters, which is unsurprising considering the similarity between the results for centered circular echelon cracks of these diameters. G_I distributions are given in Figure 8.6a. In comparison to the result for the centered circular echelon crack (1.0x), the distribution of G_I for the semi-ellipsoidal echelon cracks has changed significantly. G_I at 180° is notably lower, while the local values on either side are much higher. The peak values of G_I now occur around 150° and 210° . The behavior of G_I on the circular portion of the echelon cracks, in the delaminated region, is quite similar to the centered circular result. This makes sense, as the shape of the semi-ellipsoidal echelon crack in that region is the same as the centered circular echelon crack. There are small “kinks” in the semi-ellipsoidal echelon crack G_I distributions near 90° and 270° . The cause of these is unclear, but is possibly related to the transition in the mesh between the two halves of the echelon crack shape. Regardless, they are relatively small and occur over a very small range. Figure 8.6b-c show G_{II} and G_{III} for semi-ellipsoidal echelon crack fronts. There are some shifts to the magnitude and location of the local G_{II} and G_{III} peaks for the different major diameters, but overall the results are similar to the centered circular echelon crack results. Thus, changing to a semi-ellipsoidal echelon crack shape appears to have a strong effect on G_I , but only a small effect on G_{II} and G_{III} .

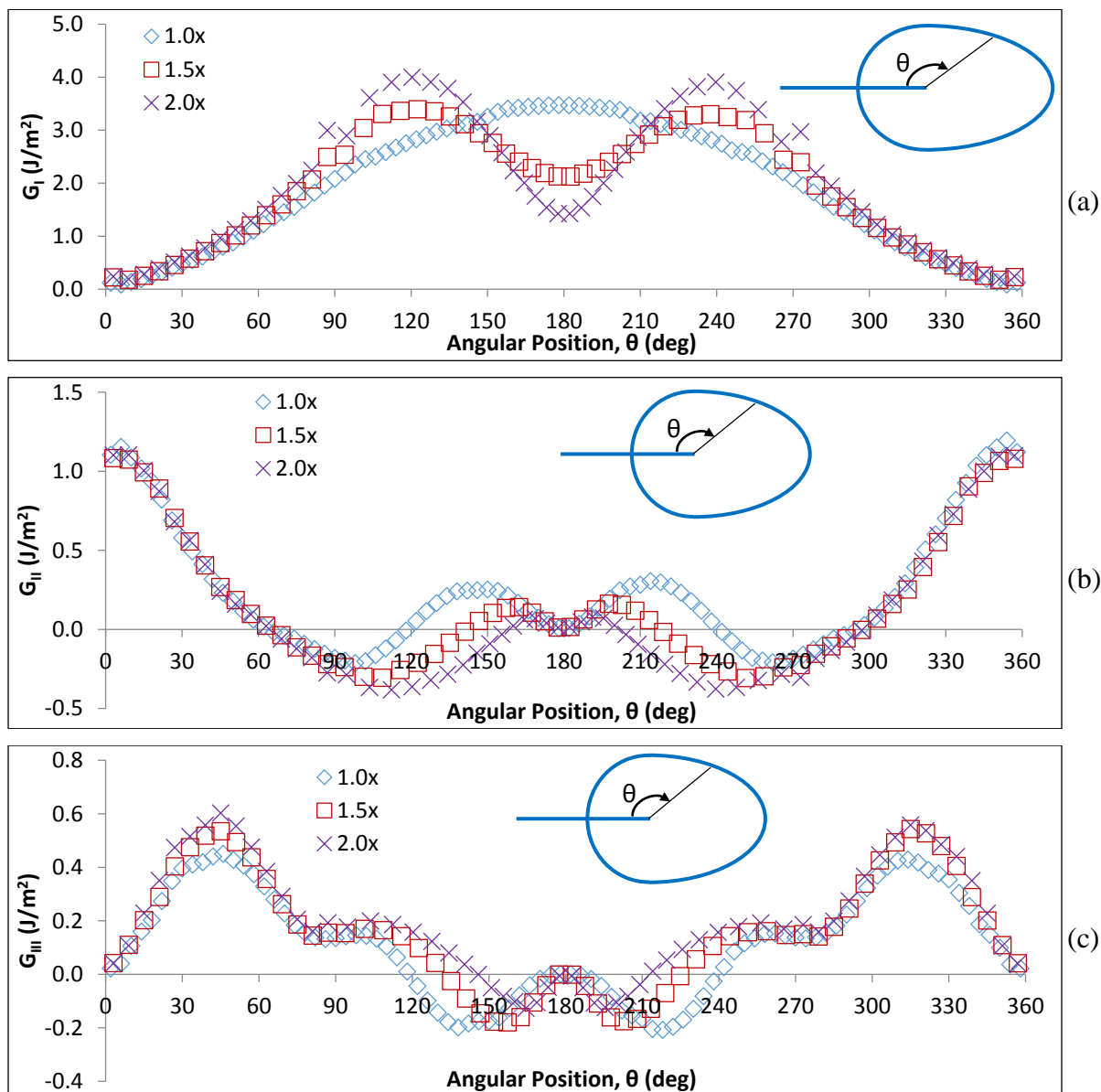


Figure 8.6. ERRs on echelon crack front for semi-ellipsoidal echelon cracks of nominal diameter $t/20$ with major ellipsoidal diameters of 1.0x, 1.5x, and 2.0x. (a) G_I , (b) G_{II} , (c) G_{III} .

8.2.3. Offset Circular Echelon Crack

The results in Section 8.2.1 indicate that G_I will cause growth in a centered circular echelon crack in the vicinity of 180° . The results in Section 8.2.2 show that G_I likely drives further crack growth from the semi-ellipsoidal shape, but that this advance will occur in the

vicinity of the 150° and 210° locations. As will be discussed further in Section 8.4, the high ERRs near 150° and 210° indicate that a semi-ellipsoidal portion of the echelon crack ahead of the delamination tip will likely grow towards a larger semi-circular shape without further advance into the undelaminated region, while the portion of the echelon crack behind the delamination tip is unlikely to change shape. This will be idealized as a circular echelon crack with a center that is offset from the delamination tip, and will hereafter be referred to as an offset circular echelon crack shape. The offset circular echelon crack shape will be defined in terms of its “nominal offset position.” This means that for the various echelon crack diameters, the point furthest behind the delamination tip is coincident with the back point of a centered circular echelon crack of a smaller diameter. In this way, an offset circular echelon crack with, e.g., a diameter of $t/16$ and a nominal offset position of $t/20$ would represent the second stage of growth of an initially centered circular echelon crack of diameter $t/20$. A schematic of the idealized stages of growth is shown in Figure 8.7.

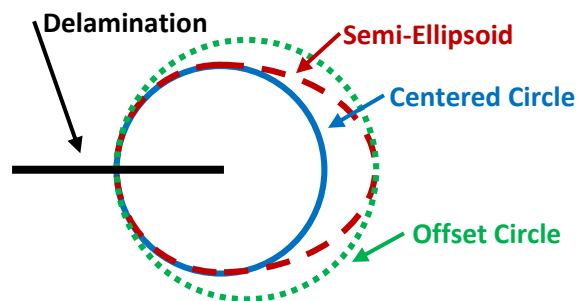


Figure 8.7. Representation of idealized stages of echelon crack growth from a centered circular echelon crack to a semi-ellipsoidal echelon crack and then an offset circular echelon crack.

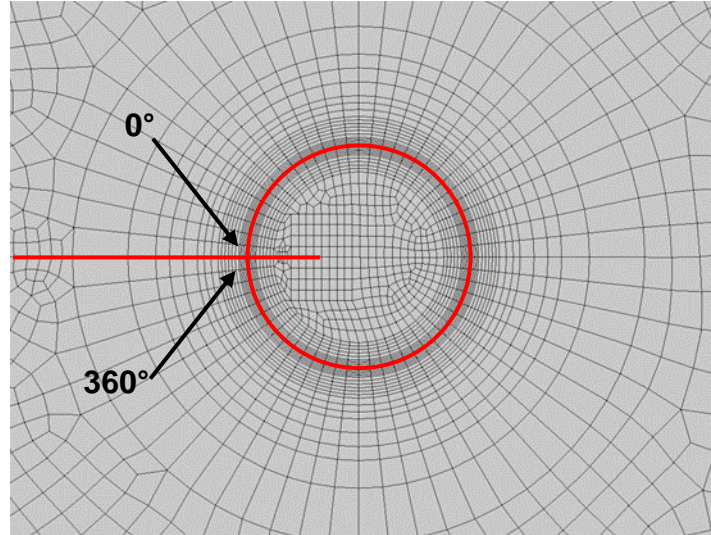


Figure 8.8. Echelon crack plane-view of model with delamination and offset circular echelon crack shape highlighted.

An image of a mesh with an offset circular echelon crack and the delamination plane presented is shown in Figure 8.8. In this figure, the diameter of the echelon crack is $3t/40$, but the echelon crack has been offset in the x-direction such that the 0° and 360° position is coincident with the position of a centered $t/20$ echelon crack. That is, the center point of the offset circular echelon crack is $(3t/40)/2 - (t/20)/2 = t/80$ ahead of the delamination tip. In addition to the $t/20$ positions shown, an offset of $t/10$ was also considered for this stage of modeling. For the nominal offset position of $t/20$, the offset circular echelon crack diameters modeled were $t/20$ (i.e. no offset), $t/16$, and $3t/40$. For the nominal offset position of $t/10$, the offset circular echelon crack diameters were $t/10$ (no offset), $t/8$, and $t/5$. Models were run for the new cases ($t/16$ and $3t/40$ offset to $t/20$, and $t/8$ and $t/5$ offset to $t/10$), and ERRs were extracted on both the delamination and the echelon crack fronts.

Energy release rates along the delamination front for models with a nominal offset position of $t/20$ are shown in Figure 8.9. The results for the $t/10$ offset look similar. Once again,

G_I is not shown because it is essentially zero. From this figure, it can be seen that both the G_{II} and G_{III} distributions are independent of echelon crack diameter for a given nominal offset position. As observed for the semi-ellipsoidal echelon crack, the region over which G_{III} is affected appears to depend on the distance the echelon crack extends back into the delaminated region, and not on the actual diameter of the echelon crack. It is possible that the peak value of G_{II} is a little lower for the larger diameter echelon cracks. However, the peak G_{II} values are exactly the same as they were for the semi-ellipsoidal crack shapes, and it is only the $t/20$ centered circular echelon crack that has a slightly higher G_{II} peak than the other echelon crack shapes.

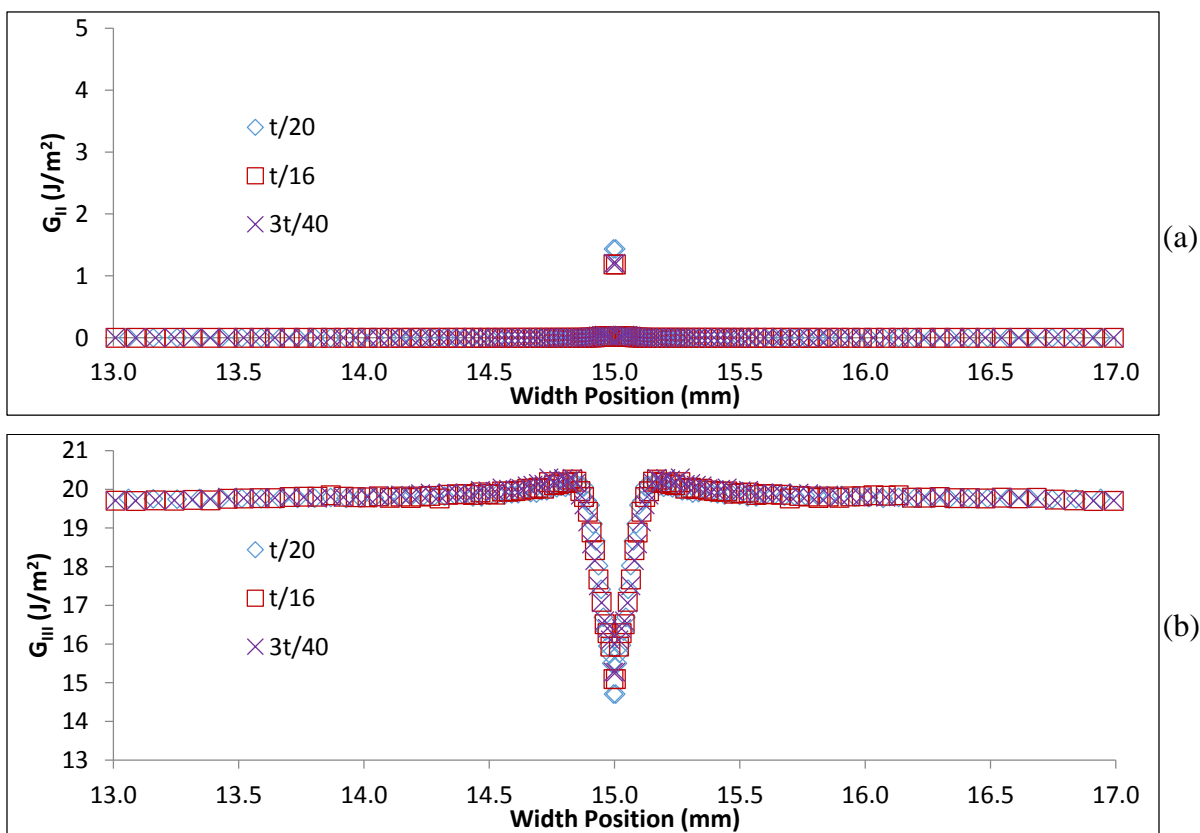


Figure 8.9. ERRs on delamination front for offset circular echelon cracks offset to $t/20$ position with echelon crack diameters of $t/20$, $t/16$, and $3t/40$. (a) G_{II} , (b) G_{III} .

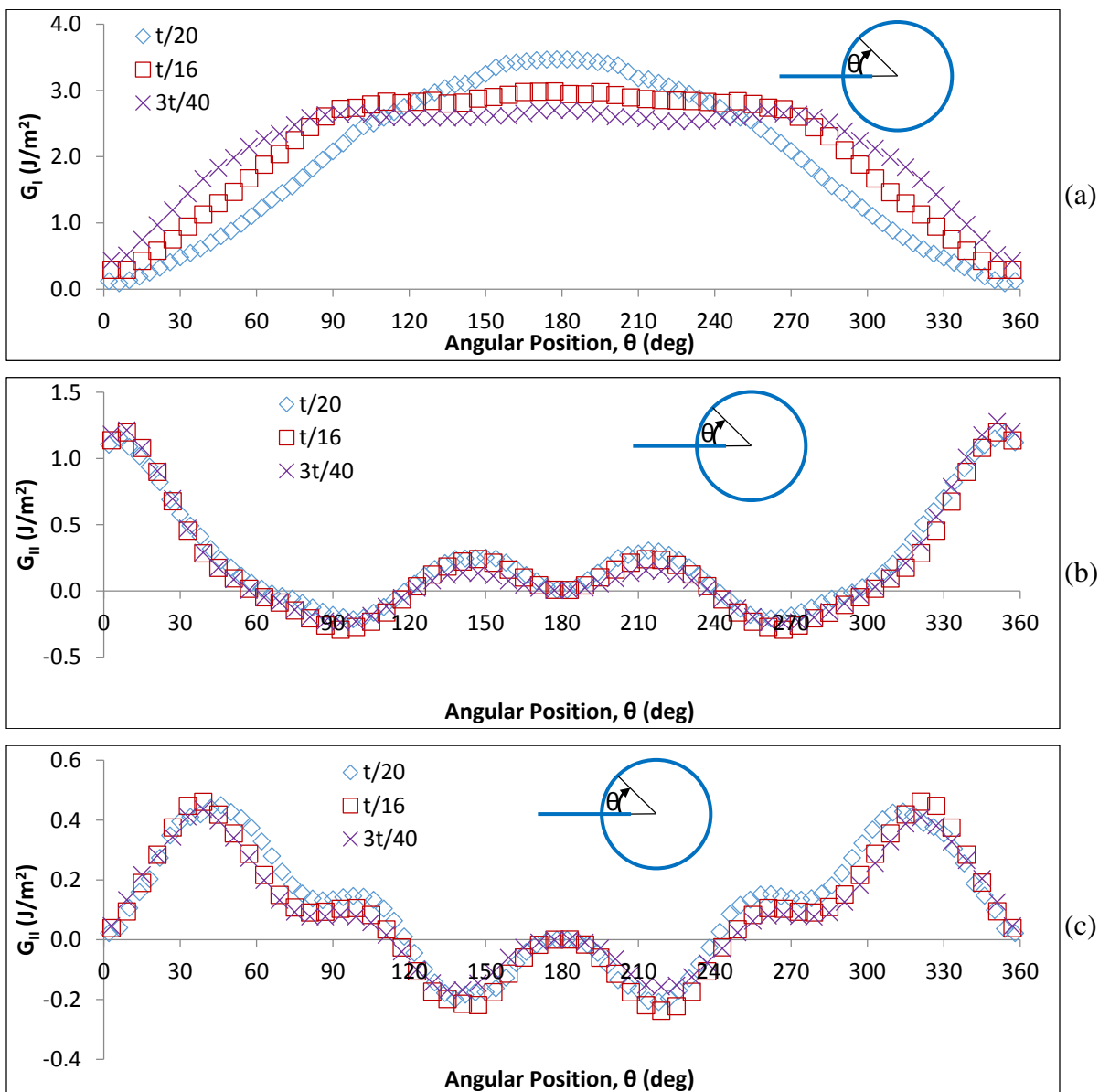


Figure 8.10. ERRs on echelon crack front for offset circular echelon cracks offset to $t/20$ position with echelon crack diameters of $t/20$, $t/16$, and $3t/40$. (a) G_I , (b) G_{II} , (c) G_{III} .

Figure 8.10 shows ERRs around the echelon crack front for the three different diameters modeled with an offset position of $t/20$. The results for an offset position of $t/10$ look similar. Figure 8.10a shows the G_I distribution for offset circular echelon cracks. It can be seen here that as the echelon crack diameter increases, the peak value of G_I drops. Additionally, the distribution

becomes much flatter in the region ahead of the delamination tip. This is accompanied by an overall increase in G_I in the regions behind the delamination tip, but the values are still much lower than those ahead of the delamination tip. The G_{II} and G_{III} distributions for the offset circular echelon cracks can be seen in Figure 8.10b-c. While there are differences in the peak values of G_{II} and G_{III} for the different echelon crack diameters, the overall trends are the same as for the centered circular echelon cracks.

8.3. Modeling Results for Multiple Echelon Cracks

As discussed in Section 7.4.6, three echelon cracks will primarily be used to investigate the behavior of an array of echelon cracks. Using three cracks allows for the study of the primary interactions between the cracks while limiting the overall model size. These echelon cracks will be spaced an equal distance apart and the middle crack will remain located at the center of the model's width. Different echelon crack geometries, sizes, and spacings will be modeled. Based on the results of these studies, a small number of additional runs with five echelon cracks are conducted. This allows for further insight into the behavior of the echelon crack array as the number of echelon cracks increases, while still limiting the overall model size. The studies with five echelon cracks consider different echelon crack spacings, but only use $t/20$ centered circular echelon cracks.

8.3.1. Three Centered Circular Echelon Cracks

The first models created using multiple echelon cracks considered a centered circular echelon crack geometry where all of the echelon cracks were either $t/20$ or $t/10$ in diameter. The spacing between cracks was defined in terms of the number of diameters between the centers of

two echelon cracks. For $t/20$, center-to-center distances of 1, 2, 3, and 10 diameters were modeled. Due to the similarity between the $t/10$ and $t/20$ results for a single echelon crack given in Section 8.2, it was expected that the results for multiple echelon cracks would also be similar, and therefore only the single case of three diameter spacing was modeled for the $t/10$ echelon crack. For these models, ERRs were extracted along the delamination front as well as on each of the three echelon cracks.

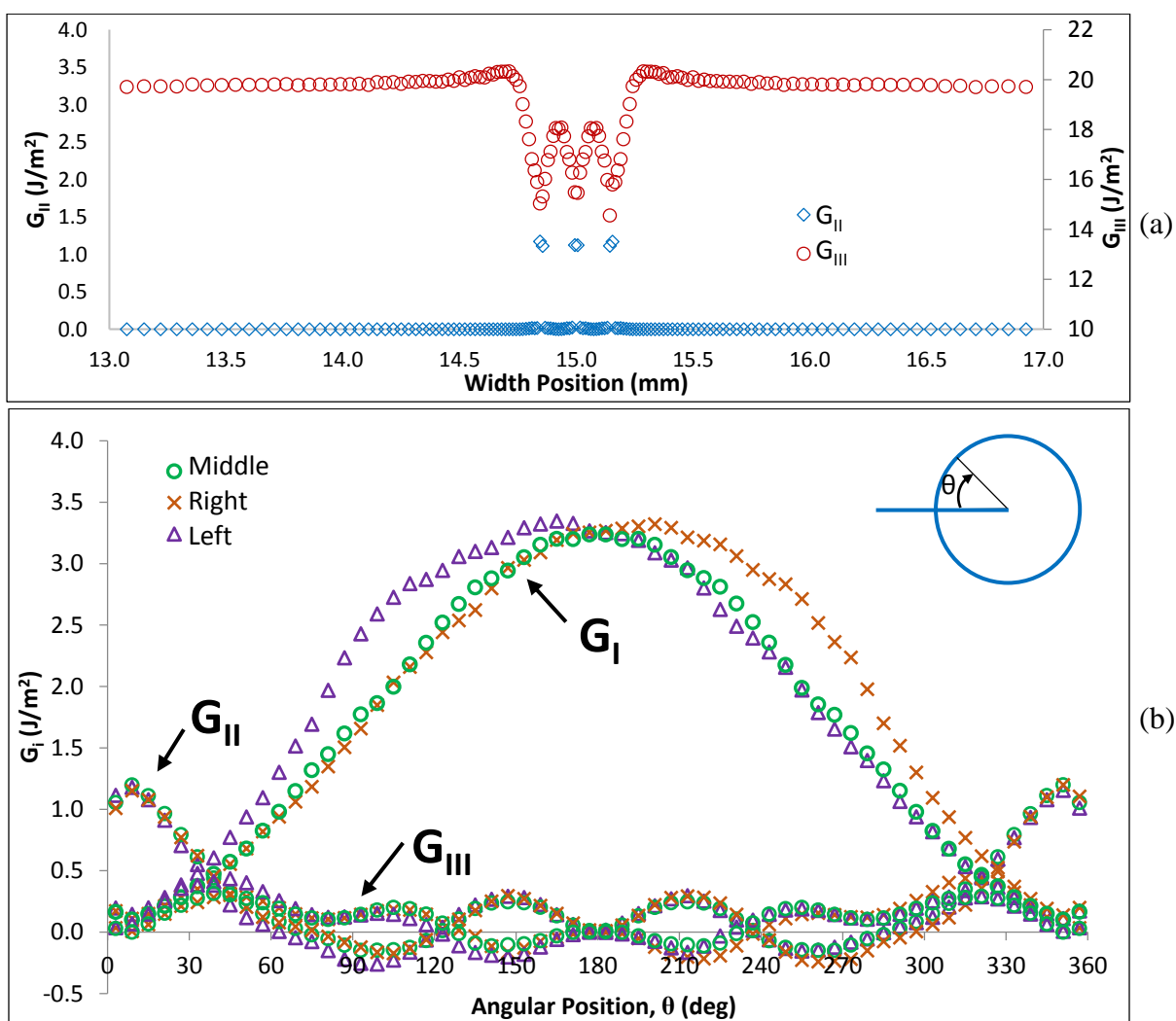


Figure 8.11. ERRs on delamination front and echelon crack fronts for three centered circular echelon cracks of diameter $t/20$ and center-to-center crack spacing of one diameter. (a) Delamination front G_{II} and G_{III} , (b) Echelon crack front G_I , G_{II} , and G_{III} .

Energy release rates for centered circular $t/20$ echelon cracks with one diameter spacing are presented in Figure 8.11. Figure 8.11a shows G_{II} and G_{III} on the delamination front. G_I was also calculated, but once again was found to be approximately zero everywhere, and so is not presented. In Figure 8.11a it can be seen that G_{III} drops to a minimum at the location of each echelon crack, and then rises back up as the distance away from the echelon crack increases. However, due to the close spacing between the echelon cracks, G_{III} does not return to its nominal value between the echelon cracks. There is some variation in the minimum values of G_{III} , but they are all similar to the minimum value for the $t/20$ echelon crack given in Figure 8.2c. G_{II} also shows a similar behavior as for a single echelon crack. It is approximately zero except right at the echelon crack locations; however, the peak values of G_{II} are somewhat lower for the multiple echelon crack results than for the single crack result given in Figure 8.2b. It is not clear whether this is due to effects from localized differences in the mesh or whether there is truly a difference between the two results.

Figure 8.11b shows the ERR distributions for the three echelon cracks. The echelon cracks are labeled as “left,” “middle,” and “right.” The middle echelon crack is located at the midpoint of the model’s width. The left echelon crack is located on the $-z$ direction side of the middle crack, and the right echelon crack is located on the $+z$ direction side of the middle crack (cf. Figure 7.1). The G_{II} and G_{III} distributions are almost completely unaffected by the presence of additional echelon cracks. G_{II} and G_{III} on all three cracks are almost identical to that of the single echelon crack result, although there is some very slight asymmetry apparent between $30^\circ - 150^\circ$ for the left echelon crack and between $210^\circ - 330^\circ$ for the right echelon crack. The distribution of G_I on the middle echelon crack is symmetric and similar to the result for a single echelon crack of the same diameter. The G_I distributions on the left and right echelon cracks,

however, are clearly non-symmetric, and are mirror images of each other. From this it can be seen that when echelon cracks are spaced very closely together, there is some kind of interaction occurring. The peak G_I values for the right and left echelon cracks are slightly higher than for the middle echelon crack, which may indicate that the outside cracks are “shielding” the middle crack, such that the ERR for the middle crack is lower than for the outside cracks. However, there does not appear to be any significant effect from the delamination front ERRs on the echelon crack ERRs. That is, although G_{III} on the delamination front is unable to return to its nominal value (known from Figure 8.2c) between the echelon cracks, there is not a significant decrease in G_I on the echelon crack fronts. These behaviors will be considered further when five echelon cracks are modeled.

Energy release rates for centered circular $t/20$ echelon cracks with a spacing of two diameters are presented in Figure 8.12. G_{II} and G_{III} on the delamination front are shown in Figure 8.12a. As seen with previous delamination front ERR results, G_{III} decreases dramatically at the location of each echelon crack. However, with a center-to-center crack spacing of two diameters, G_{III} is just able to return to the nominal value between the echelon cracks, similar to the results shown in Figure 8.12a. Thus, a spacing of two diameters appears to be approaching a “minimum spacing” at which the delamination front ERRs for a single echelon crack are valid for representing the delamination front ERRs for multiple echelon cracks. G_{II} shows similar behavior at each echelon crack as for the single crack results. G_{II} is approximately zero with a local peak right at the echelon crack fronts. Figure 8.12b presents the echelon crack front ERRs for a spacing of two diameters. G_{II} and G_{III} are unaffected by the presence of additional echelon cracks, and there is no asymmetry evident. For this case, G_I for each crack is also unaffected by the other cracks, and each result is similar to the single echelon crack results, although the peak

value of G_I is slightly lower and the distribution is slightly flatter. Therefore, when the echelon crack spacing is large enough, which may possibly be determined by the fact that G_{III} on the delamination front is able to return to its nominal value between echelon cracks, each echelon crack behaves as if it were the only echelon crack present, and there is no interaction between cracks.

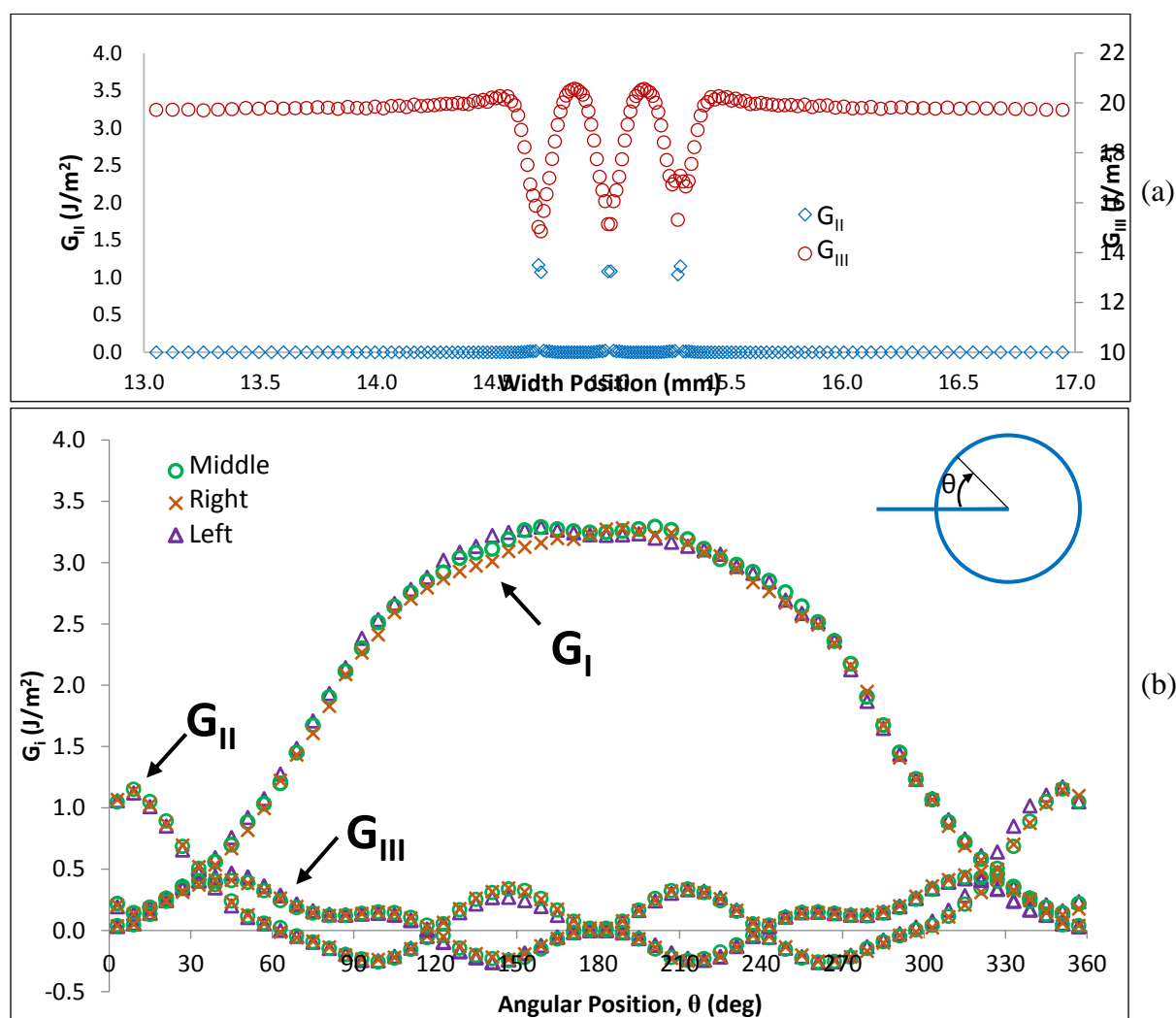


Figure 8.12. ERRs on delamination front and echelon crack fronts for three centered circular echelon cracks of diameter $t/20$ and center-to-center crack spacing of two diameters. (a) Delamination front G_{II} and G_{III} , (b) Echelon crack front G_I , G_{II} , and G_{III} .

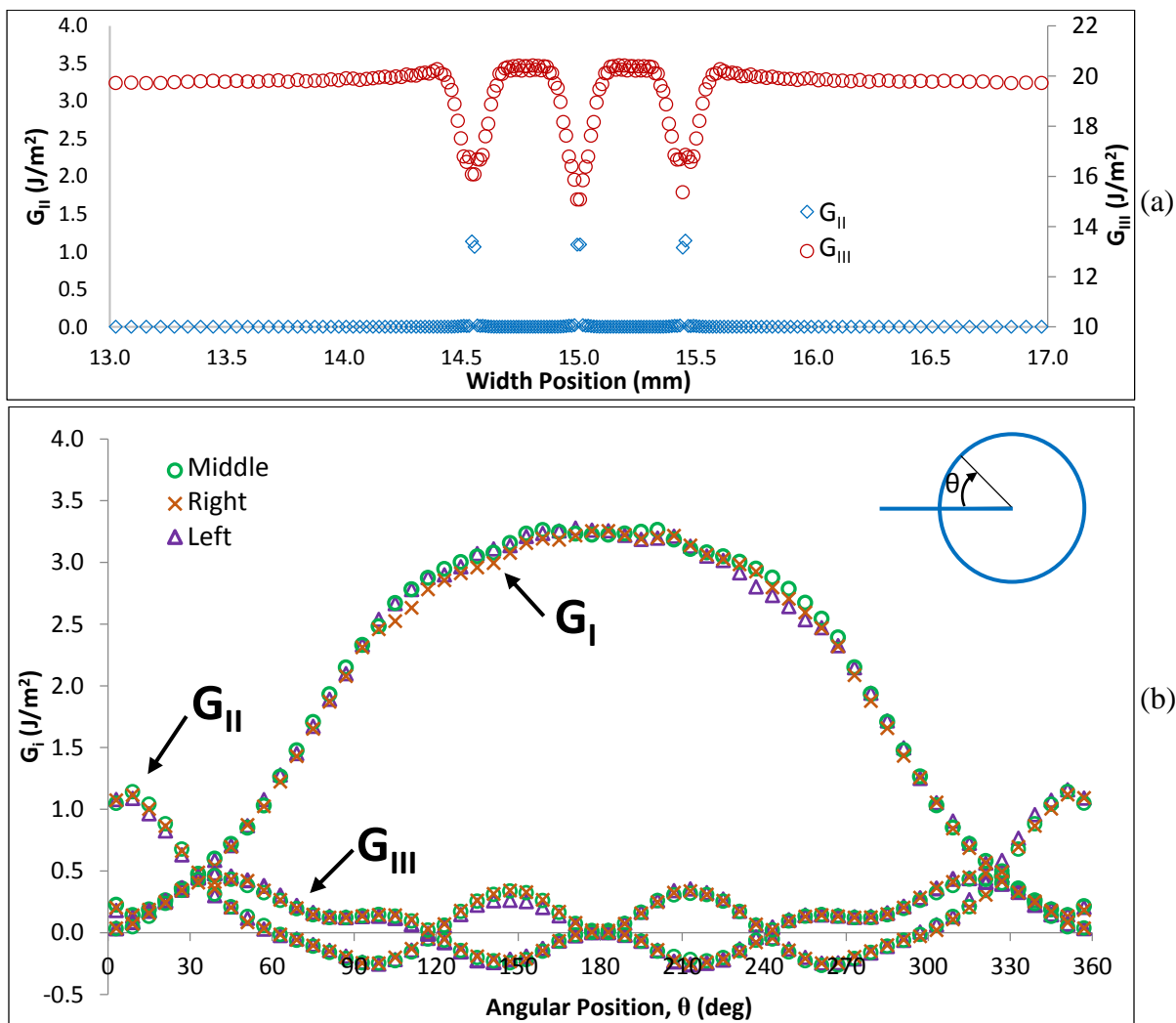


Figure 8.13. ERRs on delamination front and echelon crack fronts for three centered circular echelon cracks of diameter $t/20$ and center-to-center crack spacing of three diameters. (a) Delamination front G_{II} and G_{III} , (b) Echelon crack front G_I , G_{II} , and G_{III} .

Cases were also run with echelon crack spacings of three diameters, which are shown in Figure 8.13, and ten diameters, which are not shown. In both of these cases, G_{III} on the delamination front drops in the vicinity of the echelon crack but is able to return to its nominal value between cracks, and G_{II} peaks at each echelon crack front. Additionally, the ERRs on each echelon crack were similar to the two diameter spacing, again showing no interaction between echelon cracks.

It should be noted that the echelon crack G_I distributions shown in Figure 8.11 - Figure 8.13 are slightly lower than the distribution for a single echelon crack, as shown in Figure 8.3a. For the one diameter spacing case, the peak value of G_I is 3.5% to 6.7% lower on the multiple echelon cracks than the peak value of G_I for the single crack case. The average G_I is 6.1% to 12.9% lower on the multiple echelon cracks than it is for the single echelon crack. These differences are quite significant. However, if the 2, 3, and 10 diameter spacing results are all considered, the peak values of G_I are lower by 5.3% to 6.2%, and the average G_I is 1.5% lower to 1.5% higher. Thus, while the results for multiple cracks are generally somewhat lower than the results for a single echelon crack, the differences appear to be independent of echelon crack spacing for the cases where there does not appear to be interaction between echelon cracks. The percent differences for G_{II} and G_{III} are similar to those given for G_I , and are also independent of spacing above the one diameter spacing case. These percent differences are calculated considering all three echelon crack in each of the three different spacing models. It is not clear whether this behavior is due to differences in meshing for the various models, or whether there really is a difference in the ERR distributions for a single crack compared to multiple cracks. This will be investigated further, including a graphical comparison of results, in Section 8.3.4 where five centered circular echelon cracks will be modeled.

8.3.2. Three Offset Circular Echelon Cracks

A model with three offset circular echelon cracks was next created in order to determine whether the effects of modeling multiple cracks, compared to a single crack, are consistent for geometries other than the centered circular echelon cracks studied in Section 8.3.1. This model consisted of three $t/16$ offset circular echelon cracks with an offset location of $t/20$. The spacing

between the echelon cracks in this model was three diameters, which, based on the results of Section 8.3.1, was a distance expected to result in echelon cracks that did not interact with each other. As in previous cases, the model was run and ERRs were extracted on the delamination front as well as on each of the three echelon cracks.

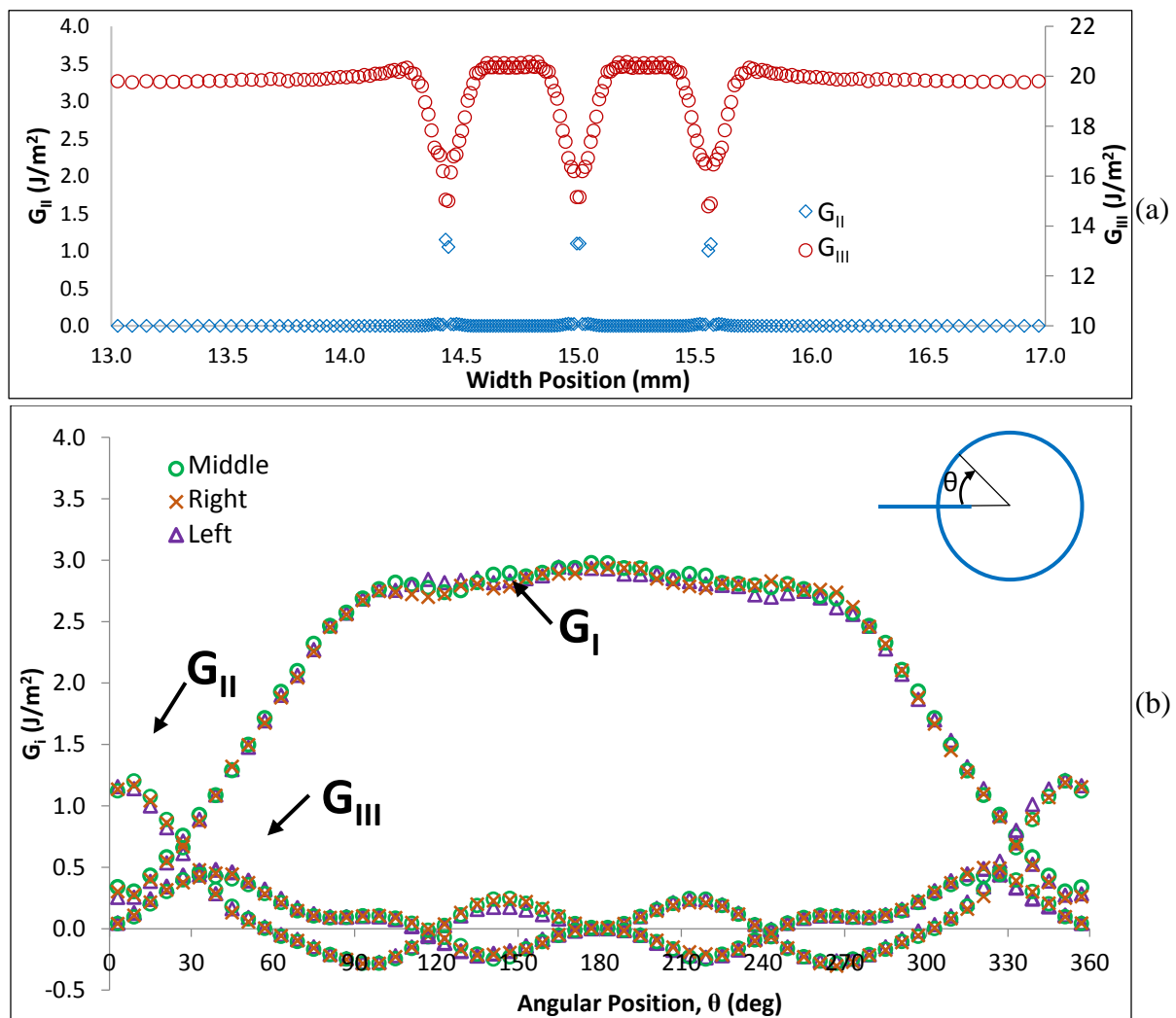


Figure 8.14. ERRs on delamination front and echelon crack fronts for three offset circular echelon cracks of diameter $t/16$ and nominal offset position of $t/20$ and center-to-center crack spacing of three diameters. (a) Delamination front G_{II} and G_{III} , (b) Echelon crack front G_I , G_{II} , and G_{III} .

Energy release rates for centered circular $t/20$ echelon cracks with three diameter spacing are presented in Figure 8.14. G_{II} and G_{III} on the delamination front are shown in Figure 8.14a. G_I on the delamination front is once again omitted as it is negligible. As expected, the crack spacing is large enough that G_{III} is able to return to the nominal value between echelon cracks. Figure 8.14b presents the ERRs on the delamination front for the offset circular echelon cracks. G_I , G_{II} , and G_{III} are almost identical for each of the three cracks, and are similar to the results for a single offset circle echelon crack.

The issue with slight differences between the results for a single centered echelon crack and multiple echelon cracks, discussed above in Section 8.3.1, is much less noticeable here. For the offset circular echelon cracks, the peak values of G_I vary from the single offset circular crack result from 1.6% lower to 0.3% higher. Average G_I varies from the single echelon crack result from 1.5% to 0.2% lower.

8.3.3. Three Centered Circular Echelon Cracks of Different Diameters

The results presented for multiple echelon cracks in Section 8.3.1 and 8.3.2 consider cracks with the same geometry and diameter. For this section, a model is created using centered circular echelon cracks that have different diameters. The model created has a middle echelon crack of diameter $t/15$, with $t/20$ left and right echelon cracks. The spacing between the echelon cracks is 2.5 middle-crack diameters, which is equal to a spacing of $t/6$. As the goal of this section is to model non-uniform echelon cracks, it is a drawback that the echelon crack geometries are all centered circles and that the diameters are not dramatically different. However, meshing constraints in Abaqus preclude the modeling of different geometry echelon

cracks, and model size constraints limit the differences in echelon crack diameter that can be modeled.

Energy release rates for the model with a middle $t/15$ and outside $t/20$ centered circular echelon cracks with 2.5 middle-crack diameter spacing are presented in Figure 8.15. G_{II} and G_{III} on the delamination front are shown in Figure 8.15a. G_I on the delamination front is once again omitted as it is negligible. As seen in previous results, the distance over which the delamination front value of G_{III} is affected by the presence of the echelon cracks is approximately one diameter on either side of each echelon crack. This remains true here, and it can be seen that the range over which G_{III} is decreased is slightly larger for the larger echelon crack. Additionally, the peak G_{II} value at the echelon crack is higher for the larger echelon crack diameter, which is in agreement with the results presented in Figure 8.2b, where the peak G_{II} value on the delamination front is higher for larger echelon cracks. Figure 8.15b presents ERRs along the echelon crack fronts. Although a spacing of 2.5 middle-crack diameters was used, it appears that there is still some interaction occurring between the echelon cracks. There is a slight asymmetry in the ERR distributions for the outside echelon cracks, similar to that seen for the centered circular echelon cracks with one diameter spacing shown in Figure 8.11b. This is interesting, as it indicates that the distance over which echelon cracks can influence each other is not necessarily dependent solely on the echelon crack diameter.

The differences between the G_I distributions for these cracks and their respective single echelon crack results are mixed. The peak value of G_I for the two $t/20$ echelon cracks is 1.8% lower than the single crack result while the average value of G_I is 0.5% lower. For the center $t/15$ echelon crack, the peak value of G_I is 4.4% lower, while the average value of G_I is 2.5% lower than the result for the single crack. Thus, there is some variation between the results for single

and multiple echelon cracks, but the results are all more similar than those given for the equal diameter centered circular echelon cracks.

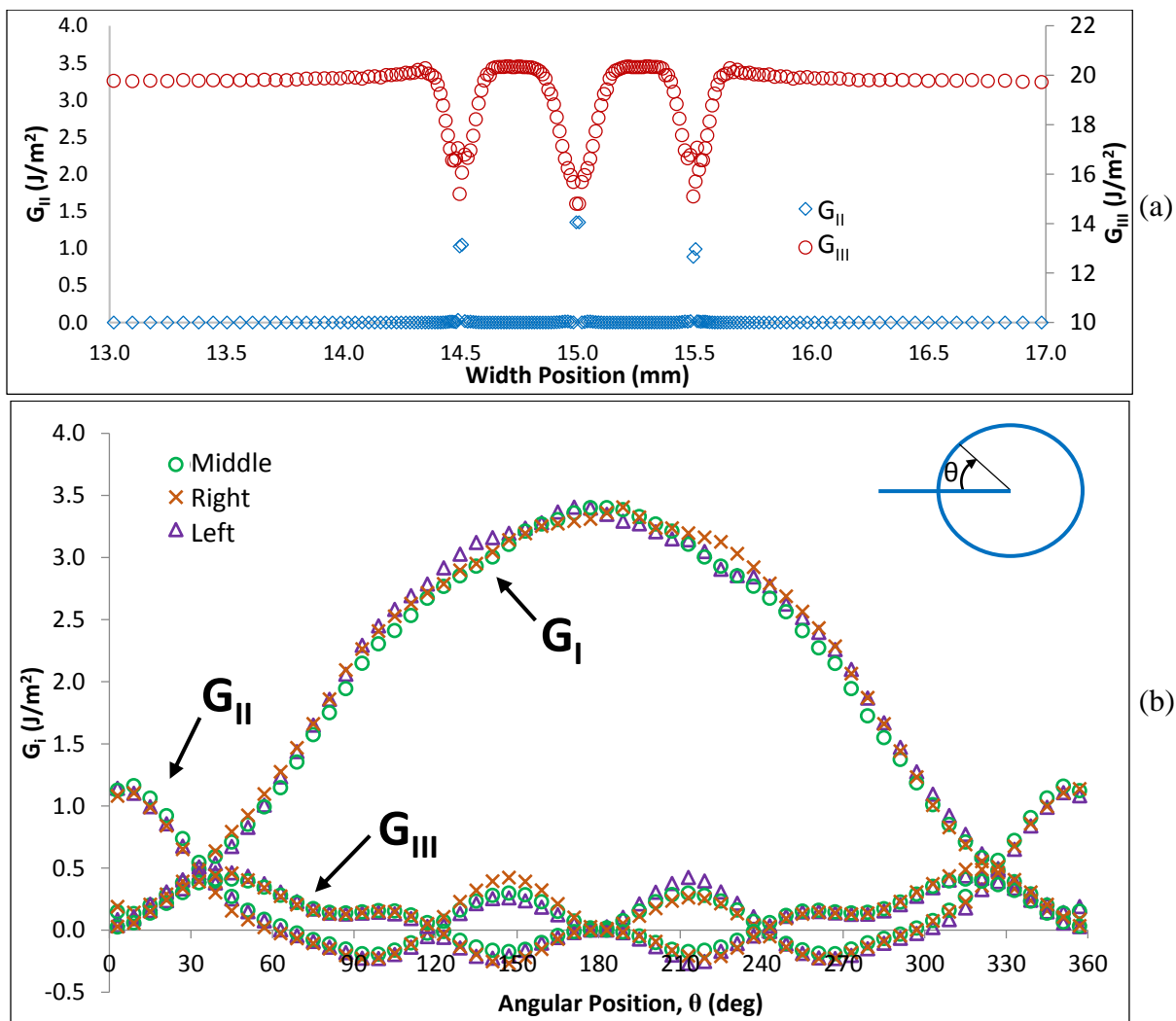


Figure 8.15. ERRs on delamination front and echelon crack fronts for a middle $t/15$ circular echelon crack and two outside $t/20$ circular echelon cracks with center-to-center crack spacing of 2.5 center-crack diameters. (a) Delamination front G_{II} and G_{III} , (b) Echelon crack front G_I , G_{II} , and G_{III} .

8.3.4. Five Centered Circular Echelon Cracks

The studies of three echelon cracks described above show the primary interactions between echelon cracks. However, both the case with one diameter spacing for the centered circular echelon crack and the case of centered circular echelon cracks of different sizes showed asymmetry in the ERRs of the outside echelon cracks. The cause of this asymmetry is unclear, and so a small number of cases with five echelon cracks have been conducted to further study this behavior. The models created for this section use $t/20$ centered circular echelon cracks with several different spacings. The cracks will be defined as “outside left,” “inside left,” “middle,” “inside right,” and “outside right” where, as before, the left side is in the $-z$ direction from the middle crack and the right side is in the $+z$ direction from the middle crack.

Figure 8.16 presents delamination front and echelon crack front ERRs for five centered circular echelon cracks of diameter $t/20$ with a spacing of one diameter. In Figure 8.16a it can be seen that the effect of five echelon cracks spaced this close together is similar to the result seen in Figure 8.11. That is, G_{III} on the delamination front decreases near each echelon crack but is unable to return to its nominal value between the cracks. Additionally, the minimum values of G_{III} and maximum values of G_{II} at the echelon crack fronts are almost identical to those for three echelon cracks. ERRs on the five echelon cracks are shown in Figure 8.16b. Here it can be seen that while the inner and middle echelon cracks have symmetric G_I distributions, the outermost echelon cracks have asymmetric G_I distributions. The asymmetry is consistent with the results shown in Figure 8.11, where the left most echelon crack G_I distribution is skewed towards 0° and the right-most echelon crack G_I distribution is skewed towards 360° . This may indicate that the outermost echelon cracks are providing some shielding to the inner echelon cracks. Figure 8.16b shows how the results of Figure 8.11b will scale to many cracks; the outside cracks would have

the skewed distributions, but all inside cracks would not. A comparison of the results for five echelon cracks to the case of a single centered circular $t/20$ echelon crack shows that both the peak and average values of G_I for each of the five echelon cracks are lower than the single crack result. This behavior, will be discussed further in Section 8.4.3 and Section 8.4.4.

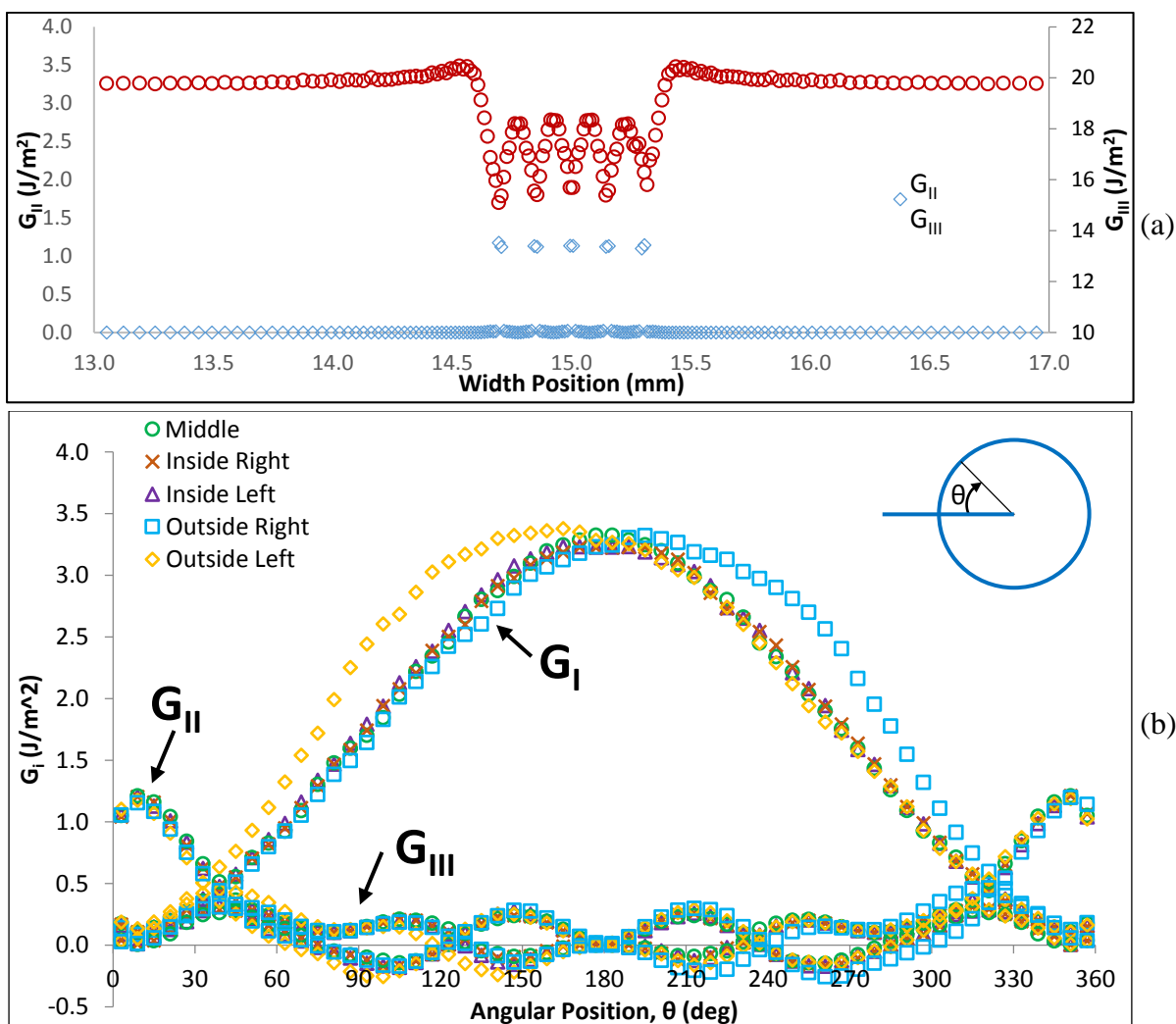


Figure 8.16. ERRs on delamination front and echelon crack fronts for five centered circular echelon cracks of diameter $t/20$ and center-to-center crack spacing of one diameter. (a) Delamination front G_{II} and G_{III} , (b) Echelon crack front G_I , G_{II} , and G_{III} .

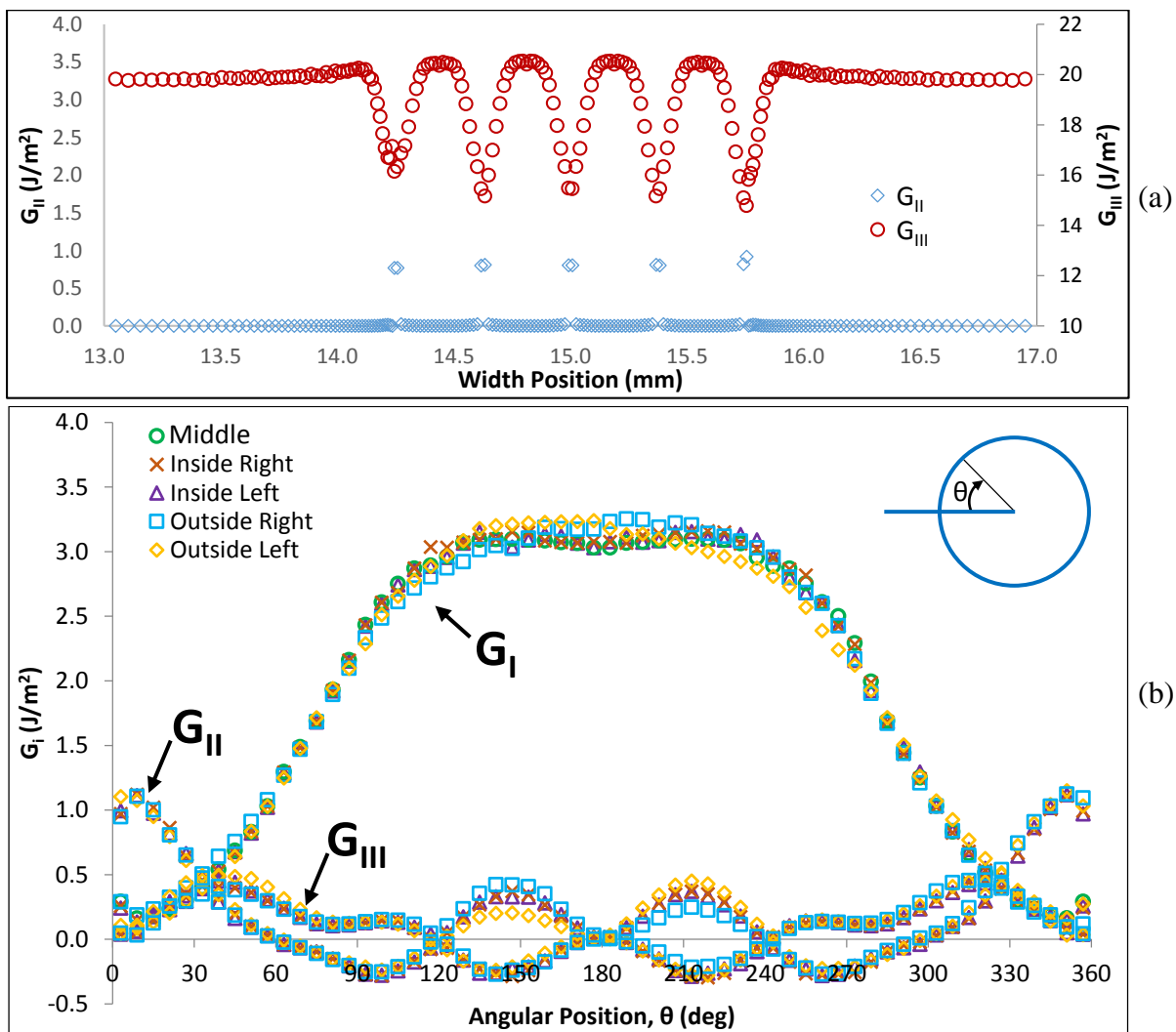


Figure 8.17. ERRs on delamination front and echelon crack fronts for five centered circular echelon cracks of diameter $t/20$ and center-to-center crack spacing of 2.5 diameters. (a) Delamination front G_{II} and G_{III} , (b) Echelon crack front G_I , G_{II} , and G_{III} .

Figure 8.17 presents delamination front and echelon crack ERRs for five centered circular echelon cracks of diameter $t/20$ with a spacing of 2.5 diameters. In Figure 8.17a it can be seen that the delamination front G_{III} is able to return to its nominal value between echelon cracks. There is not data with this spacing and three echelon cracks to compare these results to, but the maximum values of G_{II} and minimum values of G_{III} are similar to the other results presented

herein. That is, there is nothing in these delamination front energy release rate results that are remarkably different than other cases with larger than one diameter spacing. Figure 8.17b shows the echelon crack front ERRs for the five cracks. Even though the spacing is 2.5 diameters, the outside echelon crack distributions still show a slight asymmetry. This type of asymmetry has previously been used as an indication of interactions between closely spaced echelon cracks. This provides further evidence that that there are more factors involved in whether echelon cracks interact than simply the echelon crack spacing, i.e., three echelon cracks do not interact at this spacing, but there is interaction among five echelon cracks. It is interesting that, for this case, the peak values of G_I for the middle and inside cracks do not occur at 180° . Instead, there is a slight decrease in G_I at 180° , and the peak values of G_I occur on either side of 180° . This behavior is not present in the other results discussed thus far.

Figure 8.18 presents delamination front and echelon crack ERRs for a final case of five centered circular echelon cracks of diameter $t/20$ with a spacing of five diameters. As the above case of 2.5 diameters appears to show some interaction between echelon cracks, the spacing used in this case was intended to be large enough that the echelon cracks would not interact with each other. Figure 8.18a shows the delamination front ERRs. Once again, G_{II} peaks at each echelon crack location while G_{III} decreases in the vicinity of each echelon crack. G_{III} is also able to return to its nominal value between each echelon crack. Figure 8.18b presents the echelon crack ERRs. For this spacing, all of the echelon cracks have symmetric ERR distributions, indicating no interactions between echelon cracks. However, the G_I distributions appear fairly flat, and a comparison to the single $t/20$ centered circle result shows that the single crack has both a higher peak and higher average G_I than any of the five echelon cracks. This behavior will be discussed further in Section 8.4.3 and Section 8.4.4.

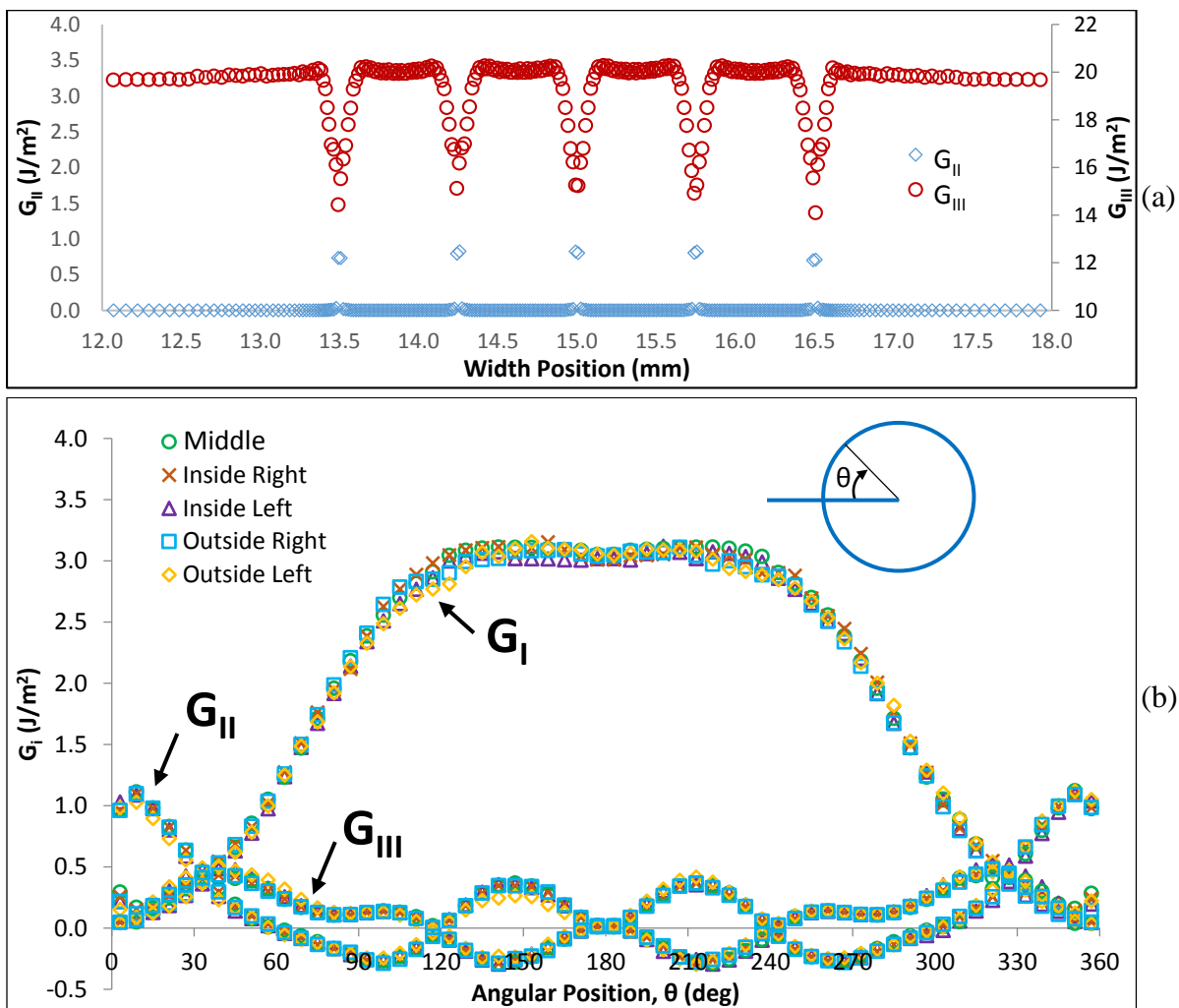


Figure 8.18. ERRs on delamination front and echelon crack fronts for five centered circular echelon cracks of diameter $t/20$ and center-to-center crack spacing of five diameters. (a) Delamination front G_{II} and G_{III} , (b) Echelon crack front G_I , G_{II} , and G_{III} .

8.4. Discussion

In what follows, the development of an array of echelon cracks will be discussed. The modeling conducted in this chapter will be used to support this discussion and explain the mechanisms that result in echelon array development and coupled planar delamination growth.

The modeling in Section 8.2 began by considering a single centered circular echelon crack. This may be thought of as representing a small crack that has initiated at the delamination tip from some pre-existing flaw. Considering the results presented in Figure 8.3, it can be seen that G_I is the largest component of the ERR across most of the echelon crack front, and G_I is the largest component of the ERR in the region where total G is the highest. Additionally, G_{Ic} is the smallest delamination toughness (c.f. Czabaj and Ratcliffe (2013) for G_{Ic} and O'Brien et al. (2010) for G_{IIIc}), and $G_I = G_{Ic}$ is likely to occur far earlier than where $G_{II} = G_{IIc}$, $G_{III} = G_{IIIc}$, or a mixed-mode growth criterion is satisfied. From this, it can be inferred that G_I likely drives echelon crack growth. In what follows, G_I distributions on the echelon crack fronts will therefore be used to discuss how an echelon array develops.

8.4.1. Initiation and Development of an Echelon Array

To understand the development of an array of echelon cracks, first consider a delamination front which contains a distribution of pre-existing flaws and which is subjected to mode III loading. At some critical load, an echelon crack will initiate from the “most favorable” pre-existing flaw. This echelon crack will “pop in” at a load which is based on the size, shape, and location of the most favorable flaw. When this crack pops in, it will immediately grow until G_I at all points on the crack front is less than the critical ERR, and further the echelon crack growth will not occur until additional load is applied. With increasing load, the condition $G_I = G_{Ic}$ will again be satisfied at one or more points (discussed subsequently) on the echelon crack front, at which point the echelon crack will grow under constant load until $G_I < G_{Ic}$, after which additional loading would again be necessary for further growth. After the initial echelon crack pops in from the most favorable pre-existing flaw, and additional load is applied, other echelon

cracks will pop in from other pre-existing flaws. These cracks will also grow, under constant load, whenever $G_I = G_{Ic}$, and will arrest when enough growth has occurred such that $G_I < G_{Ic}$.

The shapes the echelon cracks grow into can be described using the FE results presented in this chapter. The shape of an echelon crack when it initially pops in will be idealized as a centered circle. Based on the G_I distributions presented in Section 8.2.1, an echelon crack that was originally a centered circular shape is likely to grow forward into the uncracked region into a shape that can be idealized as semi-ellipsoidal. Following this, the ERRs on a semi-ellipsoidal echelon crack, for example the 1.5x case from Figure 8.6a, indicate that further advance at the echelon crack's 180° circumferential position would be unlikely. Instead, the regions with high G_I , in the vicinity of 110° and 240°, will advance the geometry of the echelon crack into a shape approximating an offset circle. This corresponds to the discussion surrounding Figure 8.7, and leads to the offset circle shape that it presents. Based on the G_I distribution for the offset circle, as shown in Figure 8.10a, additional advance would likely occur along the echelon crack front between 90° and 270°, which can be idealized as further growth into a larger diameter offset circle. The G_I distributions for progressive echelon crack shapes are shown in Figure 8.19. The centered circle is stage A, and growth progresses through the semi-ellipsoid shape of stage B and into the offset circular shapes of stage C and stage D. Further growth has not been modeled in this work, but based on the G_I distribution for stage D, the echelon crack would most likely evolve into a “fan shape.” This fan shape would be characterized by both an increase in echelon crack height and growth further into the undelaminated region, as shown in the schematic given in Figure 8.20. This next stage of development is supported by the experimental results in Chapter 6 and is evidenced in Figure 6.10. Additionally, it has been seen in many experiments that the echelon cracks are fan shaped. It has also been seen many times that the echelon cracks

do not grow back into the delaminated region, which is also in agreement with the results of this modeling where G_I always approaches zero at the delamination plane. The ability for an echelon crack initially modeled as a centered circle to grow into a shape that is in agreement with experiments is evidence that the assumed starting shape has not negatively impacted the results.

As the echelon array develops, echelon cracks will continue to pop in from pre-existing flaws at different times depending on the applied load and pre-existing flaw distribution. Consider one echelon crack that popped in at a low load level and, as the load was increased, reached a state where $G_I = G_{Ic}$, after which additional growth occurred, as described above, until $G_I < G_{Ic}$. Consider also, a second crack that has popped in at this higher load level. The applied load is already high enough that the second crack will grow, and this growth will continue at a constant load until $G_I < G_{Ic}$ on the echelon crack front. If the two echelon cracks are sufficiently far apart that no interaction occurs, this will occur when the second crack reaches a size and shape similar to the first crack. Additional advance of both echelon cracks will then occur when additional load is applied. This is supported by the results for centered circular echelon cracks of different diameters presented in Figure 8.15. Here it was seen that if one echelon crack is larger than other echelon cracks, its peak G_I will be lower. Thus, at a constant load, the smaller echelon cracks will advance before there is further growth of the larger echelon crack. For non-interacting cracks of similar sizes, for example the $t/20$ centered circular echelon cracks used in Figure 8.12 and Figure 8.13, the G_I distribution are the same for all cracks. In this way the echelon cracks in the array will advance relatively uniformly, which is supported by the experimental results presented in Section 5.5.2 where it was observed that the echelon array consisted of relatively uniformly sized cracks.

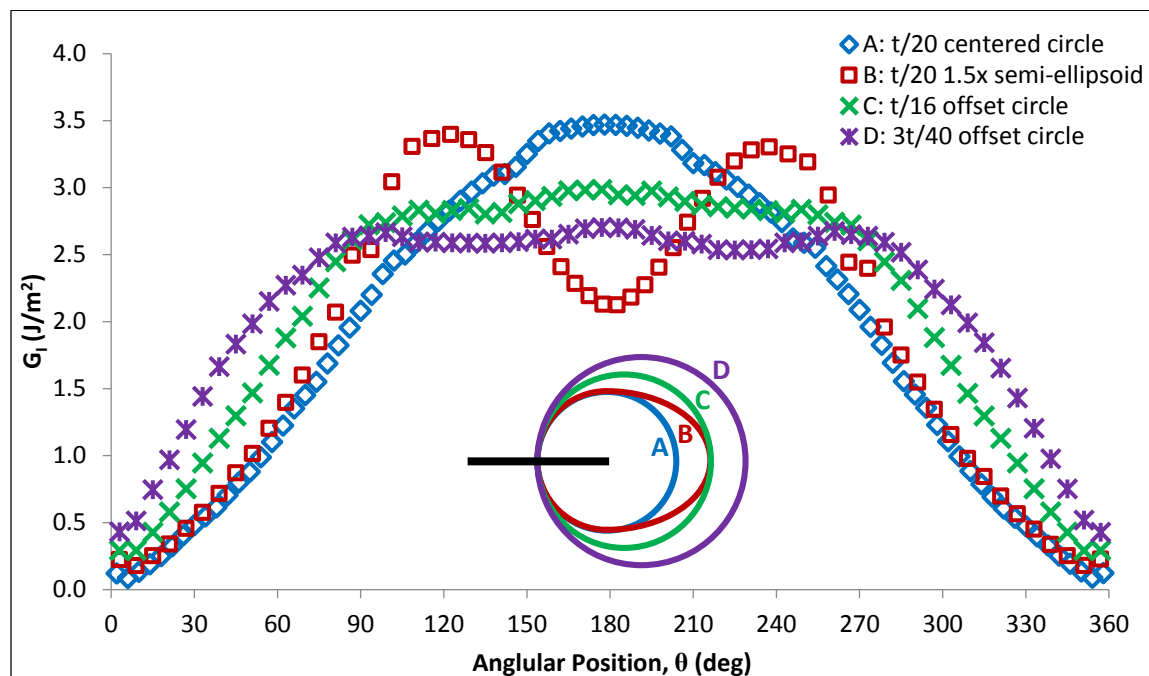


Figure 8.19. G_I on echelon crack front for progressive stages of growth starting at a $t/20$ centered circular crack.

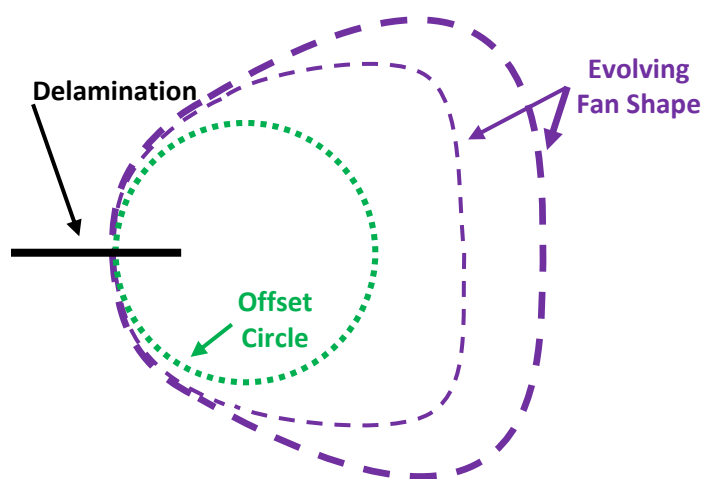


Figure 8.20. Representation of idealized stage of echelon crack growth from an offset circular echelon crack to a fan shaped echelon crack.

8.4.2. Effect of Increasing Echelon Crack Number on Development

As the number of echelon cracks in the array increases, the ERRs on the individual echelon crack fronts will be affected. It was noted in Section 8.3 that the cases of multiple echelon cracks had both peak and average values of G_I that were generally lower than the single echelon crack result. These differences are shown graphically in Figure 8.21. In Figure 8.21a-b, the percent differences between the three crack results and the single crack results for average and peak G_I of centered circular echelon cracks are given. Figure 8.21c-d give similar data for five echelon cracks. Consider first, the cases where the spacing is large and there is no interaction between echelon cracks. For these cases, the results presented in Figure 8.21 are relatively independent of crack location. From this figure it can be seen that increasing the number of echelon cracks decreases the peak G_I along all of the echelon crack fronts, while the average values of G_I are almost unchanged. Thus, at a constant load, there is flattening of the G_I distributions as the number of echelon cracks increases, which is shown in Figure 8.22. Thus, while there is almost the same amount of total mode I energy going into each echelon crack, the peak G_I for a given amount of applied mode III load is decreasing for an increasing number of echelon cracks. This same trend holds when the data for three offset circular cracks and three centered circular cracks of different diameters are considered, although the decreases in peak G_I are not quite as high. Therefore, as additional echelon cracks initiate from pre-existing flaws, the amount of additional load needed for further growth of the echelon cracks increases.

The effect increasing the number of echelon cracks has on the delamination front G_{III} can be seen in Table 8.1. This table presents the decrease in average G_{III} on the delamination front, for a given applied load, for each of the multiple crack cases when compared to the single crack result. It can be seen here that the average value of G_{III} on the delamination front is almost

unchanged for all of the cases of multiple echelon cracks. From the above results it can be seen that, for a constant amount of applied load, increasing the number of echelon cracks results in a decreased peak G_I on the echelon crack fronts while negligibly affecting the overall delamination front G_{III} distribution. Therefore, as the applied mode III load increases, and additional echelon cracks initiate from pre-existing flaws, the ratio of peak G_I/G_{Ic} on the echelon crack fronts to peak G_{III}/G_{IIIc} on the delamination front will decrease. That is, as the number of echelon cracks in the array increases, in order for G_I to be high enough for further growth of the array, G_{III} on the delamination front will approach its critical value. Thus, delamination growth becomes easier to achieve, relative to driving the echelon array forward, as more echelon cracks appear. At some level of applied load the most favorable event will be the advance of the planar delamination.

The above discussion considered the cases where echelon cracks were spaced far enough apart that the cracks will not interact. However, as a result of pre-existing flaw spacing, some echelon cracks may form at a close spacing where there is interaction between cracks. Additionally, it is evident from Figure 8.21 that the spacing over which there is interaction depends on the number of echelon cracks, and cracks which did not initially interact may start to interact as the number of echelon cracks that pop in increases. In the modeling results, interaction between cracks was indicated by asymmetric distributions in the echelon crack ERR plots. This can also be seen in Figure 8.21, where the differences between the single echelon crack result and the results for multiple echelon cracks are shown to depend on the crack location. In the cases where there are interactions, the outside cracks have higher ERRs, and “shield” the inside cracks such that the inside cracks have a lower peak and average values of G_I . Because the shielded cracks have a lower peak G_I for a given applied load, they may be less

likely to advance than the cracks with higher ERRs. This may be the mechanism behind coarsening discussed in Section 5.5.3, although pursuing this further is beyond the scope of the present investigation.

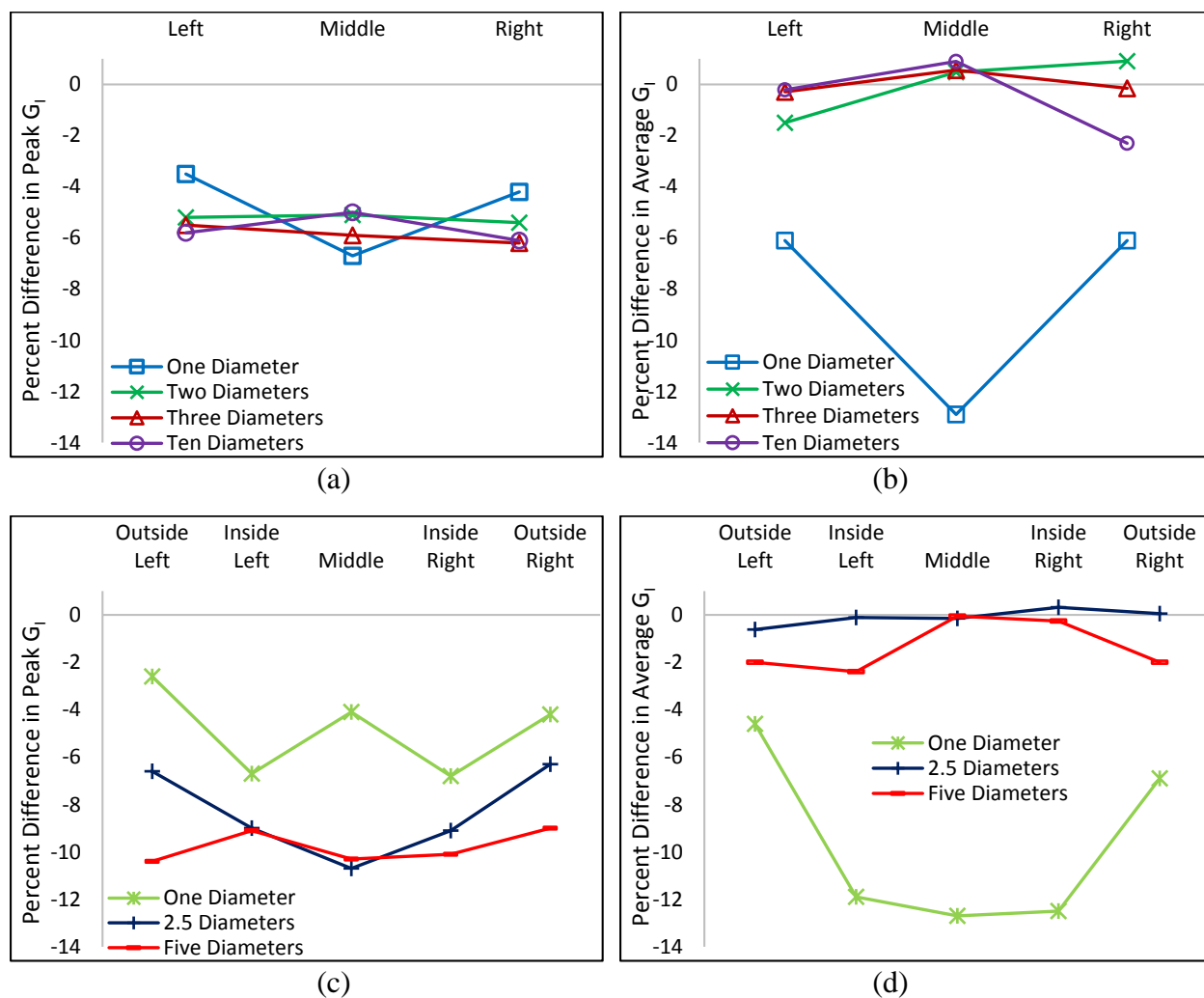


Figure 8.21. Percent differences between multiple crack results and single crack result for centered circular $t/20$ echelon crack. (a) Peak G_I for three cracks, (b) average G_I for three cracks, (c) peak G_I for five cracks, (d) average G_I for five cracks.

Additionally, from Table 8.1 it can be seen that the behavior of the delamination front G_{III} distribution does not reflect whether echelon cracks are interacting. Thus, the relationship between peak G_I/G_{Ic} on the echelon crack fronts to peak G_{III}/G_{IIIc} on the delamination front can also be used here to describe the propensity for delamination growth to become the next likely event as the applied load is increased.

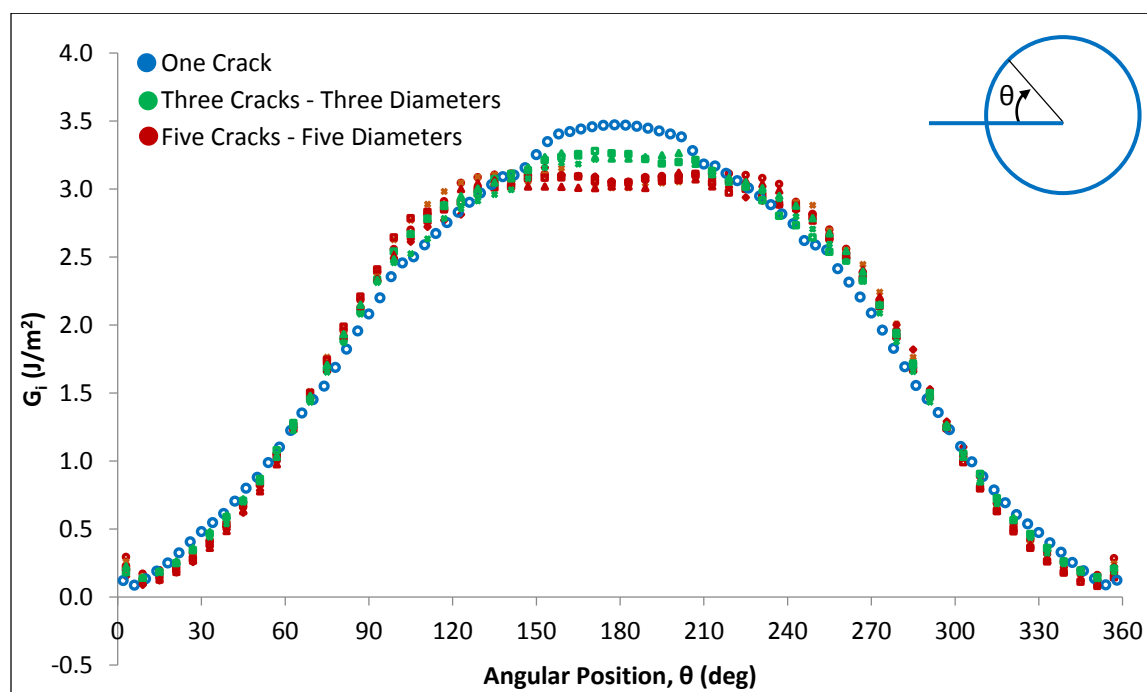


Figure 8.22. G_I distribution flattening on echelon crack fronts shown for a single crack, three cracks with three diameters spacing, and five cracks with five diameters spacing.

Table 8.1. Percent difference in average G_{III} on delamination front for multiple echelon cracks.

Number of Echelon Cracks	3	3	3	3	5	5	5
Echelon Crack Spacing (diameters)	1	2	3	10	1	2.5	5
% Difference in Avg G_{III} on Delam	-0.16	-0.15	-0.14	-0.15	-0.26	-0.22	-0.14

8.4.3. Coupled Advance of an Echelon Array and the Planar Delamination

As noted above, at some ratio of peak G_I/G_{Ic} on the echelon cracks to peak G_{III}/G_{IIIc} on the planar delamination, conditions become favorable for the delamination front to advance. To illustrate what happens when this occurs, consider an offset circular echelon crack of $3t/40$, which is stage D in Figure 8.19. The G_I distribution for this crack shape is also shown as stage D in Figure 8.23. Assume the delamination advances such that this crack becomes a $3t/40$ centered circular echelon crack, as represented by stage E in this figure. When this occurs, the echelon crack G_I distribution returns to the result for a centered circle, while the G_{III} distribution on the delamination front will remain unchanged (assuming the amount of delamination growth is small). Therefore, after the planar delamination advances at a constant load, the ratio of peak G_I/G_{Ic} on the echelon cracks to G_{III}/G_{IIIc} on the planar delamination will likely be high enough for further echelon crack growth. In the above example, the next stage of echelon crack growth would again be semi-ellipsoidal in shape, as shown by stage F. Further growth would again proceed through the stages represented in Figure 8.19. In this way, the echelon crack size will continue to increase, and it will be “pushed” forward into the undelaminated region by the planar delamination growth. This agrees with the experimental observations in Section 5.5.2 that echelon crack growth leads ahead of planar delamination growth.

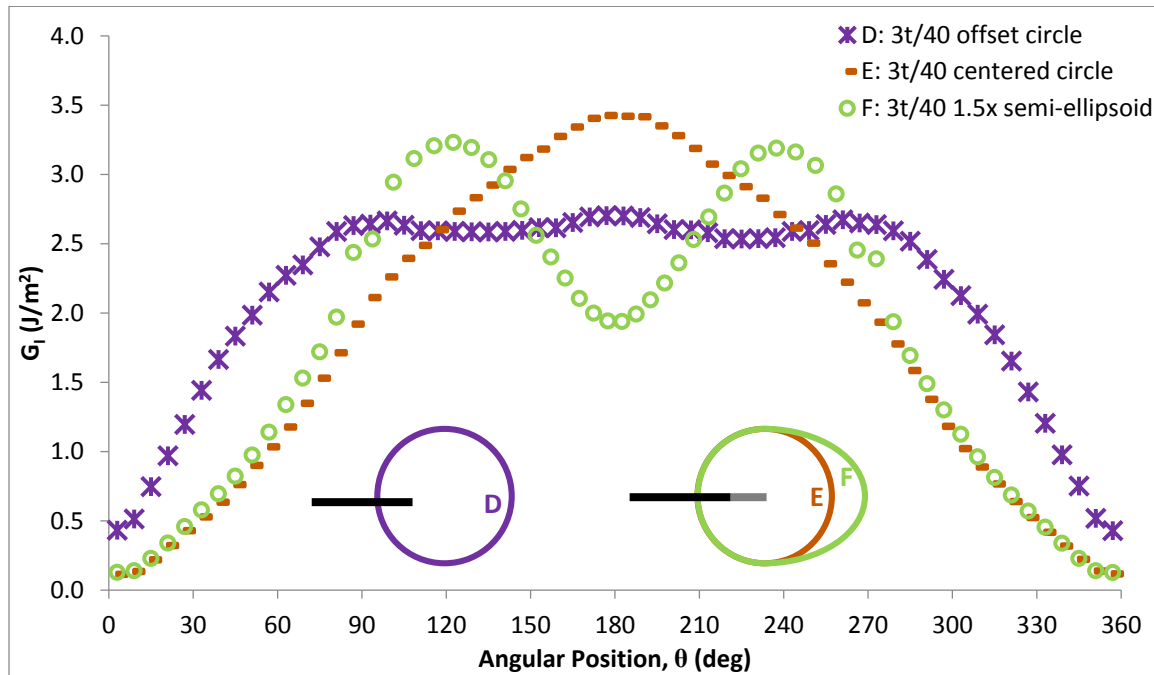


Figure 8.23. G_I on echelon crack front for coupled planar delamination and echelon crack growth of a single echelon crack.

As discussed above and represented schematically in Figure 8.20, echelon cracks in experiments developed into a fan shape. Coupled growth of the planar delamination and fan shaped echelon cracks will be qualitatively similar to that described above. Growth of the planar delamination will push the array forward into the undelaminated region as well as increase the size of the echelon cracks. This process can continue repeatedly as the loading is increased and conditions for delamination growth occur. However, at some point the influence of the model's free surfaces, as discussed in Section 5.5.3, are likely to limit the maximum echelon crack length in the z -direction. Growth would then likely advance in some sort of offset full-ellipsoidal shape, were growth continues forward into the undelaminated region, but there is no increase in echelon crack size in the direction of the free surfaces. This is in agreement with the experimental observations presented in Figure 6.10a.

The above discussion holds for an array of echelon cracks that are spaced far apart, such that there is no interaction occurring between cracks, as well as echelon cracks that are spaced closely together. From Table 8.1 it was shown that the delamination front ERRs are generally unaffected by whether the echelon cracks are interacting. This indicates that, even if there is interaction occurring between echelon cracks in experiments, the delamination front would be expected to advance fairly uniformly. That is, there should not be any “lagging” areas where some portion of the delamination front has not advanced. This is consistent with the experimental results presented in Section 5.5, where the delamination advance is generally fairly uniform.

8.5. Conclusions

This chapter covered the modeling of both a single echelon crack and multiple echelon cracks at the tip of a planar delamination which was subjected to global mode III loading. Energy release rates were calculated for the echelon cracks and the planar delamination to understand how an array of echelon cracks develops ahead of planar delamination advance. It was found that echelon cracks will advance ahead of the planar delamination in progressive shapes that can be idealized by a centered circle, semi-ellipsoid, and offset circle. At a constant load, as echelon cracks grow, the peak ERR on the echelon crack decreases while the energy release rates on the delamination front remain constant. It was determined that, for an array of echelon cracks, close spacing between cracks results in interactions that may lead to some cracks growing preferentially over others. Well-spaced echelon cracks behave independently, although there is a flattening in the echelon crack G_I distribution as the number of cracks increases, which results in the increasing likelihood of favorable conditions for delamination advance to occur. It was also

found that the coupled growth of a single echelon crack and the planar delamination will “push” the echelon cracks ahead of the planar delamination as well as cause them to increase in size. The results of the modeling conducted in this chapter are in agreement with the experimental findings in Chapters 5 – 6. Thus, the energetics along the planar delamination and echelon crack fronts found herein can be used to describe echelon array growth in unidirectional composite laminates subjected to global mode III loading.

Chapter 9. Conclusions and Future Work

9.1. Conclusions

This dissertation focused on the study of the mechanisms for crack growth in composite laminates subjected to anti-plane shear loading. The objectives of this dissertation were to (1) develop an experimental technique that can be used to study anti-plane shear loading in composite laminates, (2) determine the mechanisms associated with delamination advance under anti-plane shear loading, (3) develop a model that will contribute to crack growth prediction capabilities with emphasis on the events associated with mode III initiation, and (4) apply the findings from the above to issues of delamination toughness assessment and growth prediction under mixed mode loadings where mode III is present.

In Chapter 4, four different mode III toughness test methods were introduced and evaluated. A constant apparent mode III toughness was obtained for these four test methods at a single delamination length. However, it was later determined that the apparent toughness depended on the geometry, indicating that a true mode III toughness was not measured. Assessments of the fracture surfaces in specimens where delamination growth had occurred found matrix cracks oriented at approximately 45° to the delamination plane. In Chapter 5 a study was conducted to determine if these matrix cracks initiate prior to the onset of planar delamination advance. It was confirmed that the initiation of matrix cracks within the resin rich interlaminar interface, and their growth into the plies surrounding the delamination tip, occurred before any planar delamination advance, indicating that “mode III advance” does not occur. The fracture surface evolution in SST specimens was then studied and it was found that while crack growth was analogous to that in homogenous materials, the composite laminate architecture

resulted in several key differences. These differences were caused by a preferential fracture path along the interlaminar interface, the prevention of echelon crack twisting due to constraint by the composite's fibers, and a limitation in echelon crack size due to the proximity of free surfaces. In Chapter 6, the previous experimental results were reinterpreted considering the specimen twisting that occurred during loading. It was found that this twisting results in mode I-III conditions along the delamination front. This amount of twisting, and therefore the mode mix, affects the way the fracture surfaces evolve, and the angle between matrix cracks and the planar delamination is in fairly good agreement with the MPTS criterion.

Two key problems were identified from the experimental investigations described above that have prevented the development of a mode III delamination toughness test method. First, small transverse cracks initiate prior to delamination advance, which invalidates any data reduction methodology assuming an uncracked matrix and indicates that, at least for 0/0 interfaces, "pure mode III growth" does not appear to be possible. Second, split-beam geometries will twist during loading resulting in a changing mode mix that depends on geometry. The experimental investigations have also brought up several issues regarding the understanding of crack growth under anti-plane shear loading. These issues are (1) whether there are ply interface combinations that will constrain matrix cracking such that what is commonly called mode III interlaminar delamination could be approximated, (2) how to predict growth for the general problem of anti-plane shear loading where transverse cracks occur, and (3) what experiments and analyses are required for prediction of growth in the general anti-plane shear problem. It was discussed in Section 6.5 that although a variation of the SST test could be used for (1), it may be better addressed using a variation of the ECT test. Use of the ECT test for this purpose is currently being pursued in a parallel study by Czabaj, Ratcliffe, and Davidson, and for this

reason was not pursued further as part of this research. However, the SST test could also potentially be used to address this issue. This will be discussed further in Section 9.2.1. Rather, this dissertation research focused on issues (2) and (3), which may be addressed simultaneously by studying the fundamental mechanics of crack growth under anti-plane shear loading. This motivated the computational portion of this study.

In Chapter 7, a computational model was formulated and validated for the study of echelon array development under mode III loading on a planar delamination. This model was used in Chapter 8 to study the development of an array of echelon cracks. A small echelon crack was first assumed to have grown from a pre-existing flaw on the delamination front. This has been shown to happen in experiments, where matrix cracks were observed to initiate at the discontinuity between the fiber and matrix material, as shown in Figure 5.8a, or from a small void, as shown in Figure 5.7a. It was shown using the model that as the first echelon crack grows, it will develop into a shape that can be approximated by a fan, which is in agreement with the results discussed in Section 6.4.4 and by Figure 6.10a. The modeling work shows that as the echelon crack grows, the ratio of G_I/G_{Ic} on the echelon crack to G_{III}/G_{IIIc} on the delamination front decreases such that increasing applied load is necessary for further echelon crack growth. At some G_{III}/G_{IIIc} on the delamination front, additional echelon cracks will initiate and grow from other pre-existing flaws. As individual cracks in the array grow, G_I on the advancing echelon cracks will decrease relative to other cracks, resulting in temporary arrest of the further advanced cracks and continued growth of the less advanced cracks. In this way, the array develops relatively uniformly. Further, as the number of echelon cracks increases, the modeling results show that there is a flattening in the G_I distributions, which likely contributes to the self-limiting of the echelon array prior to the onset of planar delamination advance. As the echelon

cracks grow and increase in number, the ratio of G_I/G_{Ic} on the echelon cracks to G_{III}/G_{IIIc} on the delamination decreases until planar delamination advance becomes the next likely event. It was also found that the coupled growth of the echelon crack array and the planar delamination will “push” the echelon cracks ahead of the planar delamination as well as cause them to increase in size. This is in agreement with the experimental results discussed in Section 5.5.2, where the echelon cracks extended a uniform amount ahead of the planar delamination. As planar delamination growth proceeds, the echelon cracks will continue to grow in size. However, as the echelon cracks become larger, the specimens’ free surfaces will limit the overall through-thickness size of the cracks, which was shown experimentally in Figure 5.5.3. At this point, additional echelon crack growth will continue forward into the undelaminated region without additional increase in length in the transverse plane. This is supported by the transverse sections presented in Section 5.5.2 and the echelon crack profiles shown in Figure 6.10.

9.2. Future Work

This section presents proposals for future work that will continue to advance the understanding of crack growth in composite laminates subjected to anti-plane shear loading. These proposals consider both experimental approaches and modeling approaches.

9.2.1. Mode III Delamination Toughness Test Development

While the work presented in this dissertation reveals that delamination growth will be coupled to matrix cracking in most practical laminates and structures subjected to anti-plane shear loading, there is still interest in the development of a test method to determine the delamination toughness under anti-plane shear loading where echelon cracks are constrained to

the interlaminar interface. While uncommon, there may be situations where the laminate architecture constrains matrix cracks to the interlaminar interface, and growth under anti-plane shear loading would approximate pure interlaminar delamination advance. Additionally, delamination growth where matrix cracks are constrained to the interlaminar interface likely requires significantly less energy to initiate planar delamination advance than when the matrix cracks are unconstrained. An anti-plane shear delamination toughness test with constrained matrix cracks could therefore represent a lower limit of a general laminates' resistance to growth of a planar delamination. As discussed above and in Section 6.5, this type of test could possibly be achieved with either a variation of the ECT or the SST test geometries. While the ECT test is proposed as the preferable method, and is being investigated in a parallel study, it is possible a variation of the SST test could be used. This would require addressing several issues with SST testing, which are described below.

As discussed in Section 6.5, there are several issues with current split-beam tests, such as the SST, that need to be addressed before they could be applied to measuring the delamination toughness under anti-plane shear where matrix cracking is constrained to the interlaminar interface. First, with the current SST laminate architecture, the growth of matrix cracks is unconstrained. Second, SST specimen rotation is unconstrained, resulting in mixed-mode I-III loading that depends on geometry. Additionally, as discussed in Chapter 4, the SST test is non-linear. Achieving a linear test is important for wide-scale use of the SST as a delamination toughness test method, as a nonlinear test will likely confound the accurate determination of energy release rates or stress intensity factors. .

In the current unidirectional, 0° SST specimen layup, where the applied shear stress is perpendicular to the fiber direction, matrix crack growth is unconstrained. As seen in

unidirectional mode II testing, where the applied shear stress is parallel to the fiber direction, matrix cracks are constrained to the interlaminar region (O'Brien, 1998). It is therefore possible that modifying the SST specimen layup could constrain matrix cracks. However, in order to prevent damage to the specimen prior to planar delamination advance, a multidirectional layup is necessary. Davidson and Schapery (1988) and Davidson et al. (1996) propose non-dimensional constants for multidirectional layups to ensure the uniformity of ERR distributions and minimization of bend-twist coupling, respectively. Davidson and Schapery (1988) introduce a term defined as one minus the ratio of plane stress to plane strain bending rigidities, for which

$$D_c = \frac{D_{12}^2}{D_{11}D_{22}} \quad (9.1)$$

can be used. Davidson et al. (1995) recommend $D_c < 0.25$ to minimize of finite width effects and ensure a uniform ERR distribution. Davidson et al. (1996) introduce a term to measure the amount of bending-twisting coupling which correlate to ERR distribution uniformity. They use

$$B_t = \frac{D_{16}}{D_{11}} \quad (9.2)$$

and recommend $B_t < 0.0001$. Note that both B_t and D_c are defined for the sub-laminate representing each "cracked leg." A multidirectional layup should satisfy both of these conditions. One set of such layups to satisfy these conditions are the 48-ply [((φ / 0 / - φ / 0 / $\pm\varphi$)_s)_{as} ||]_s where || refers to the location of the Teflon insert and $\varphi < 35^\circ$ (for IM7/8552 material properties given in Table 6.2). It will need to be determined experimentally whether matrix cracks can be constrained within this range of φ , otherwise a different layup with a larger range of allowable φ would need to be used.

The final two issues, constraining the rotation of the specimen and achieving a linear test, may be able to be addressed simultaneously. As noted in Chapter 5, there have been various

approaches to constrain rotation in split-beam tests such as the method used for the STB (Davidson and Sediles, 2011) or the improved SCB (Robinson and Song, 1994). These or other, new, methods may be attempted, although it was found in the investigations of Chapter 4 that correctly imposing the STB constraints proved challenging. However, it is possible that if specimen rotation can be constrained, the load-deflection response may become linear. If this is not the case, other approaches to obtain a linear test, such as changing the specimen geometry or method of load introduction, would need to be considered.

The above represents a significant experimental undertaking, as the three issues are coupled together, and it is possible that a solution cannot be found for one issue without solving all three simultaneously. Still, the development of a mode III interlaminar delamination toughness test using a split-beam specimen may be possible. Alternatively, and as discussed in Chapter 6, it may be worthwhile to use an ECT specimen with an appropriate layup, such as those proposed above, for a toughness test. Both test methods warrant further study.

9.2.2. Observation of the Initiation of Echelon Cracks

As discussed in Section 9.1, a significant issue to address is the determination of the experiments and analyses required for prediction of growth in general laminates subjected to anti-plane shear loading. Consideration of the case where echelon cracking is unconstrained may be one path to achieve this. If a variation of the SST test could be developed with a linear load versus deflection response, it may be used to address this issue. A first step would be to use this test to determine when echelon crack growth first initiates. This would be done using in-situ non-destructive evaluation techniques, which are described below, to determine the applied ERR associated with transverse crack initiation for different specimen geometries, and potentially for

different applied mode mixities. This information could then be used for validation purposes of a numerical model intended to predict echelon crack initiation from a pre-existing flaw distribution. This would be useful in order to further the understanding of crack growth in practical laminates and structures where mode III loading is present.

The current work presented in Chapter 5 on echelon array development show the stages of growth in “snapshots.” That is, individual specimens were loaded to a percentage of their apparent G_{IIIc} , then sectioned and viewed under an optical microscope to obtain a single data point. Several data points were then considered together in order to understand the development of an echelon array. It was shown that echelon cracks are present above $G_{III}/G_{IIIc} > 0.70$, but not when they initiate. A much more accurate understanding of which echelon cracks initiate could be obtained if the entire development of an echelon array could be observed for a single specimen. This is possible with in-situ X-Ray CT, where a series of scans could be conducted for many increments of loading without added inaccuracies due to unloading, removing, reinserting, and reloading the specimen between scans or using multiple specimens. Note that it is also possible that these investigations could be accomplished with the ECT test.

In addition to being used for validation of a computational model, this type of work could answer a number of questions. It could be determined whether the initiation of matrix cracking is reflected by some apparent “point of increasing nonlinearity” in the load versus deflection plot. If so, this could be useful for future testing where it is of interest to obtain an ERR associated with the onset of matrix cracking. Along with this, it could be determined whether, for cases where twisting is unconstrained, there is some consistency in when echelon cracks initiate and if there is some set of conditions under which the initiation of matrix cracking may be independent of geometry. These investigations would reveal a significant amount about the initiation of

matrix cracking, and could be used as a first step in fully understanding of how an echelon array develops. From this, it is more likely that an accurate crack growth prediction methodology could be developed for mode III loading, as discussed in Section 3.4.1.

9.2.3. Modeling of Echelon Array Development

The modeling of echelon array development conducted in this dissertation was intended as a preliminary analysis. It has proven useful for determining the energetics that lead to echelon array development, and so there are a number of improvements and future steps that can be made to continue with this area of study. These steps can be categorized as either improving the accuracy and capabilities of the model, or furthering the study of echelon array development.

The numerical model developed was created using the commercial FE program Abaqus. Because of this, there were a number of limitations. Transitioning to a different program with increased capabilities, or creating an in-house program, could reduce or eliminate some of these limitations. One limitation of Abaqus is that either the echelon crack or the planar delamination could be modeled as an infinitesimally thick, but not both. This produced an apparent G_I on the delamination front that most likely did not affect the ERR results, although this was not shown definitively. There is not currently a commercial or open source FE program that can model intersecting seam cracks, and so this would require the creation of a custom program. Another limitation was that, in order for Abaqus to create a mesh, multiple echelon cracks had to be the same geometry and fairly similar in size. This precluded the study of the potential interaction between echelon cracks which had advanced to different stages or had grown to significantly different sizes. Other available FE codes, such as Frank3D, may be able to accomplish this. A final issue with using Abaqus was the constraint on the echelon crack size. Due to partitioning

constraints in Abaqus, the minimum echelon crack diameter that could be modeled was $t/20$. For a 3.0 mm thick, 24-ply IM7/8552 laminate, such as was used in Chapters 5 and 6, this represents an echelon crack on the order of a ply thickness in size. However, Figure 5.4.2.1 shows initial echelon array development for a 24-ply laminate with cracks smaller than the thickness of the interlaminar interface. This is a significant difference in magnitude, and being able to model appropriately small echelon cracks may be useful for further modeling.

There were two interesting findings discussed in Chapter 8 that warrant further investigation. First, the range of spacings over which echelon cracks interact with each other appears to depend on the number of echelon cracks modeled. As more echelon cracks were modeled, the spacing had to be larger to avoid interactions. It was hypothesized that this could be the mechanism for coarsening, but this is not clear. Further study considering more echelon cracks, as well as echelon cracks of different sizes and geometries could help address this. Second, the distance over which an echelon crack decreased G_{III} on the delamination front appears to depend on the distance the crack extends behind the delamination front. In experiments there was never echelon cracking observed behind the Teflon insert tip, and so it is not clear how an echelon crack actually affects delamination front ERRs. Further study considering smaller echelon cracks or cracks with more realistic shapes could shed light on this issue.

A final proposal for future modeling considers the true origins of an echelon cracking. It was shown in Section 5.4.2 that echelon cracks initiate from small flaws at the delamination front. Each specimen tested contains some unknown flaw distribution from which echelon cracks initiate. If the above discussed model issues could be address, and significantly smaller as well as varying geometry echelon cracks could be modeled, it is likely that an inherent flaw distribution

could be approximated. This could be done using a stochastic distribution, and the development of echelon cracks could be modeled from this distribution of flaws. This would be significantly more accurate at representing echelon array development than starting with assumed echelon cracks of fairly significant size at specific locations, as was done in Chapter 8. This would represent a significant step towards developing a mechanistic model that can predict echelon array development and growth in real laminates under loadings that include a mode III component.

Appendix A. Tensile Test procedure for Axial Modulus

Determination

This appendix is intended to provide guidance on the practical issues involved in determining axial Young's Modulus (E_{11}) via the test procedure of ASTM D3039 (2014). It is assumed that all specimens are cut from a plate fabricated for SST or STB tests, as described in Section 4.4.1.

A.1. Specimen Preparation

A.1.1. Specimen Size

- Use c-scan image of composite plate to determine the available area to cut an E_{11} specimen. This area has no delamination present.
- Cut the composite specimen to approximately 8" long and ½" wide.
- Measure the width of the specimen at three points (2.5" from each end and in the center) using the calipers and the specimen thickness at six points (left and right sides each for the three locations of width measurement) using the micrometer.
- Record the specimen width and thickness measurements, and determine whether the width or thickness are out of tolerance according to the standard (ASTM D3039, 2014).

A.1.2. *Tabbing for Extensometers*

- Mix several grams of 3M DP-420 epoxy.
- Apply two “dabs” of epoxy to one of the wide sides of the specimen halfway down the length. The “dabs” should be $\frac{1}{2}$ ” apart.
- Let sit approximately $\frac{1}{2}$ hour.
- Use one of the extensometers, with the pin in place, to put razor marks through the epoxy. These will hold the extensometer in place during testing. Ensure that the razor marks go all the way down to the composite.
- Once cured, repeat epoxy application on the other side, again $\frac{1}{2}$ ” apart. The dabs should be offset from the ones on the other side by $\frac{1}{4}$ ”, so none of the dabs overlap.

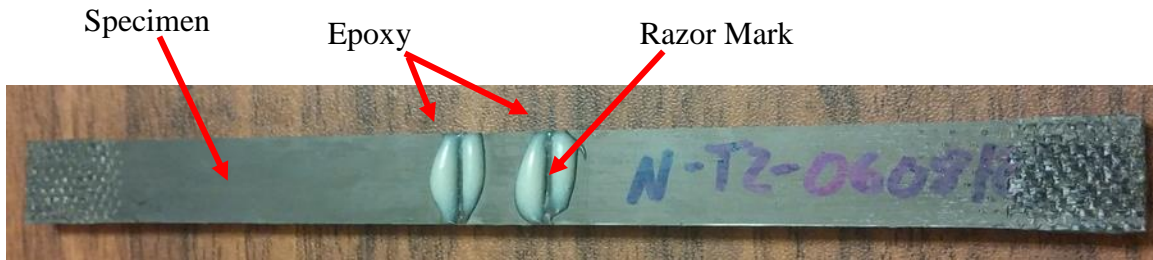


Figure A.1. E₁₁ specimen with razor marked epoxy ready for testing.

A.2. Test Setup

This setup is for the auto-tightening grips shown in Figure A.2 and Figure A.3. A slight modification to this procedure is necessary if a different style of grip is used.

A.2.1. Grip Alignment

- Only modify the grip alignment if there is reason to believe there is misalignment, or when changing fixtures. Otherwise leave grips in place.
- Verify that the top grip has two degrees of freedom to rotate; otherwise the load frame will be too rigid. Add links if necessary.
- Thread the top grip into the load cell until it is threaded all the way in and facing forward. Use a spanner wrench and hammer to tighten it into place.
- Thread the bottom grip into the hydraulic actuator almost all of the way. Loosely align it with the position of the top grip.
- Lower the top grip until it is just touching the bottom grip. Twist the bottom grip until the back faces of the two grips are parallel and in line.
- Use one C-clamp on each side to clamp the grips together where they are touching. Be sure the clamps are fully contacting each grip.
- Use a spanner wrench and hammer to tighten the bottom grip in place.
- Remove the clamps. Verify that the back faces of the grips are still aligned in the same plane.

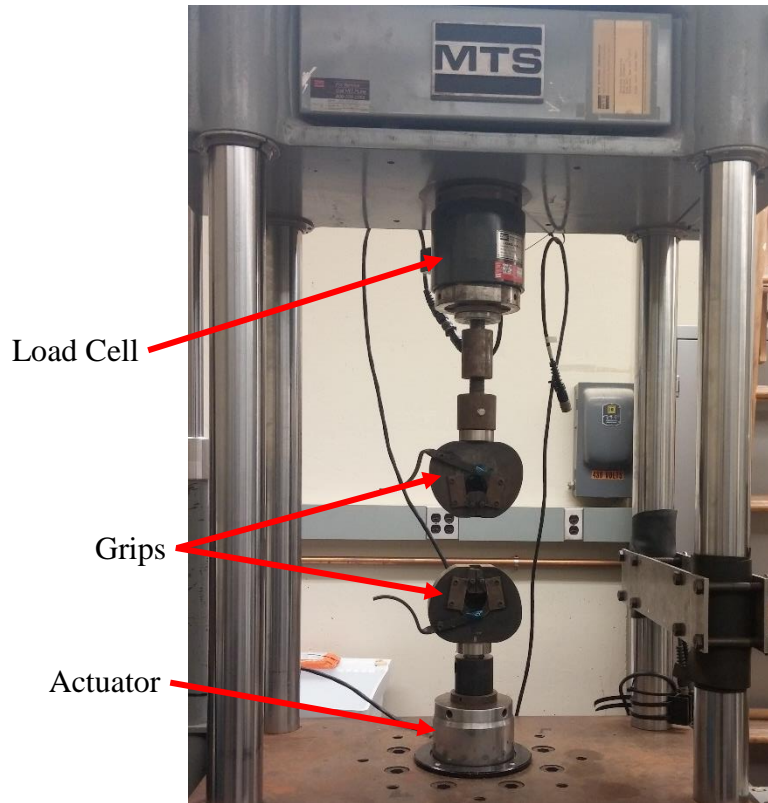


Figure A.2. E₁₁ grips installed in load frame.

A.2.2. Specimen Insertion

- Apply the extensometers using rubber bands. The rubber bands must be tightly holding the extensometer to the specimen. Verify both extensometers are securely on the specimen. Remove extensometer pins when done.
- Use hydraulics to raise or lower the grips so they are a distance apart equal to the length of the E₁₁ specimen plus approximately 1/2".
- Use the top lever to open the top grip and push the specimen against the back of the top grip with approximately 1/4" between the top of the specimen and the grip. It is unlikely to be flush at this point because the bottom grip is still closed. Release the lever so the top grip closes on the specimen.

- Use the bottom lever to open the bottom grip, and push the specimen against the back of the bottom grip with approximately ¼” between the bottom of the specimen and the grip. Release the lever so the grip closes on the specimen. It should be flush against both grips at this time.
- If the specimen is not flush, alternate between opening the top and bottom grips while pushing the specimen against the back of the grips until it is flush. If the top or bottom of the specimen comes in contact with either grip, remove specimen, raise top grip higher, and repeat insertion procedure.
- As the specimen is inserted into the grips, keep an eye on the load cell. If the load cell displays tension (positive force), remove the specimen from the grips and re-do. If the load cell displays compression (negative force), proceed.

A.2.3. Running Programs

- Open the E₁₁ program in TestWare SX. Zero the load, displacement, and extensometers after the specimen is in the load frame.
- Open the ramp program in TestStar.
- Open the data acquisition file in LabVIEW. Verify channels are properly setup. See Table A.1 for recommended channel settings for current hardware.
- Name a file to record data by the following convention: Plate Number – Specimen Number (Test Number). E.g. T-081910-7(2) for the 2nd test of specimen 7 on plate T-081910.
- Set the TestStar program to run at 0.05 in/min crosshead displacement.

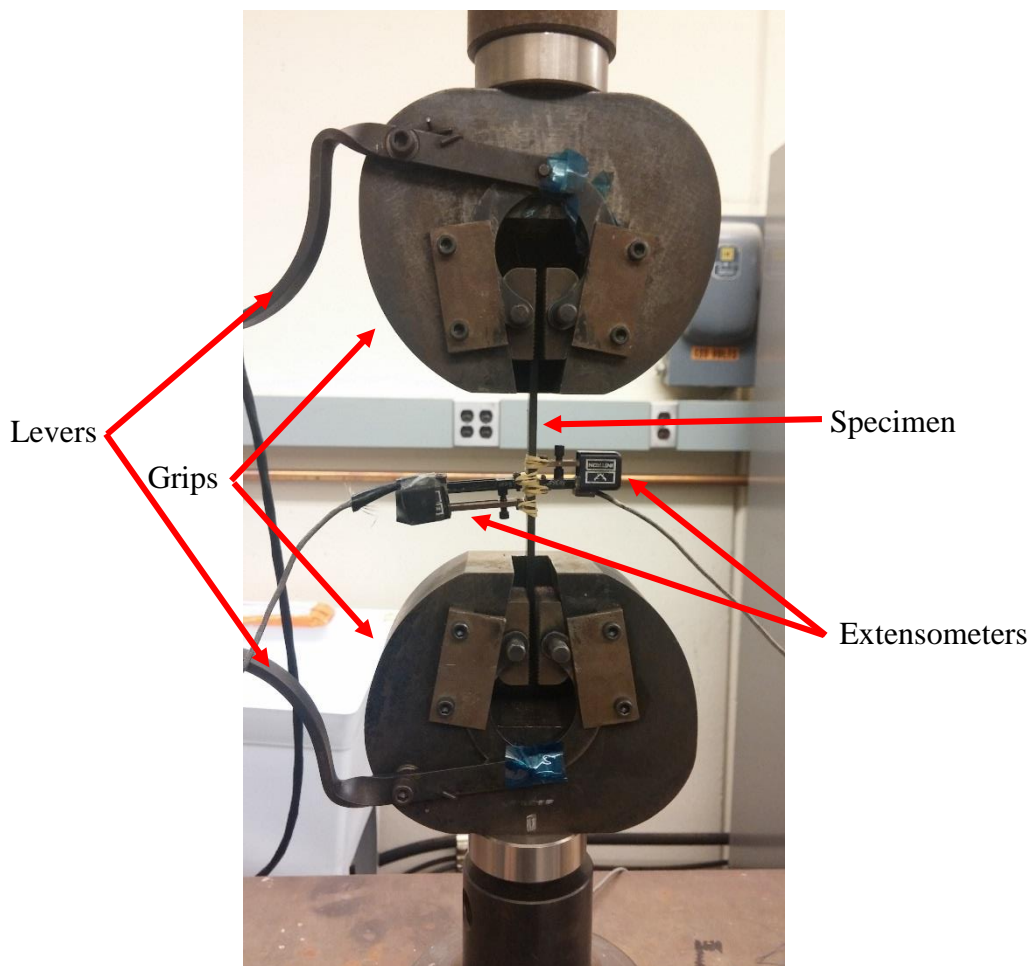


Figure A.3. E₁₁ specimen installed in grips with extensometers.

Table A.1: Recommended channel settings for E₁₁ Testing

Name	Scale (Units/Volt)	Units	Offset	Min (V)	Max (V)
Load	500	lbs/V	0	0	8.5
Displacement	0.05	in/V	0	0	5
Ext1	0.01	mil/V	0	-0.1	1
Ext2	0.01	mil/V	0	-0.1	1

A.3. Test

- Start the LabVIEW data collection.
- Start the TestStar program.

- Run the program until the specimen is loaded to approximately 1500 lbs tension.
- Change the TestStar program to unload the specimen at 0.05 in/min and stop at 50 lbs tension.
- Retighten the top and bottom grips.
- Run the program again until approximately 4000 lbs. Stop data collection. Unload specimen.

Remove specimen from grips and rotate so the extensometer on the left hand side is now on the right hand side, but the specimen remains upright.

- Tighten specimen in grips according to “Specimen Insertion” and retest using the above procedure.

A.4. Data Reduction

- Import the data into excel.
- Use specimen dimensions previously recorded to calculate stress and extensometer length to solve for strain.
- Graph stress vs. extensometer 1, stress vs. extensometer 2, and stress vs. the average value of the extensometers.
- Use the secant line approach, as detailed in the standard, to determine the value of E_{11} for each of the tree plots.
- Record the three values of E_{11} and the specimen dimensions in the workbook for modulus values.

Appendix B. Test Procedure for Shear Modulus

Determination

This appendix is intended to provide guidance on the practical issues involved in determining shear modulus (G_{12}) via the test procedure of ASTM D5379 (2012).

B.1. Specimen Preparation

B.1.1. Plate Layup

- Fabricate a plate using a $[0/90]_{xs}$ layup where x is one quarter the number of desired plies. For example, for IM7/8552 $x = 6$ while for IM7/977-3 $x = 7$.
- Specimens will be cut from the plate such that the 0° and 90° plies will be parallel and perpendicular to the specimen edges.

B.1.2. Specimen Size

- Cut the composite specimen into a rectangle 3" long and $\frac{3}{4}$ " wide. Cut 90° v-notches on each side of the specimen with an interior radius of 0.05in.
- Measure the width of the specimen at the narrowest point of the notches on both sides of the specimen using the calipers. Measure the thickness of the specimen near each notch using the micrometer.
- Record the specimen width and thickness measurements, and determine whether the width or thickness are out of tolerance according to the standard (ASTM D5379, 2012).

B.1.3. Strain Gage Application

- Strain gages used for this research were Vishay Micro-Measurements EA-06-062TH-120/E, which is a two-element 90° torque gage with a 0.062 mm gage length and a 120 V excitation.
- Apply the strain gages using strain gage application procedure that comes with the strain gage epoxy.
- Center a strain gage between the two v-notches, as seen in Figure B.1, on each side of the specimen. Repeat on the other side of the specimen.
- Bond terminals on either side of each strain gage and solder wire between strain gage and terminals. Solder wires onto terminals as seen in Figure B.1.

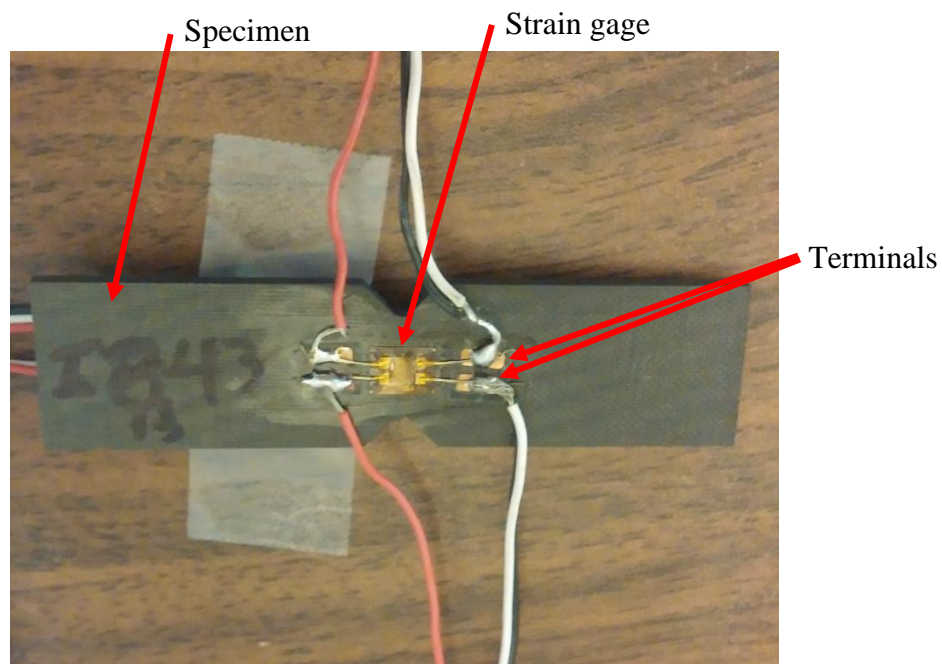


Figure B.1. G₁₂ specimen with strain gages ready for testing.

B.2. Test Setup

B.2.1. Fixture Alignment

- Only modify the fixture alignment if there is reason to believe there is misalignment, or when changing fixtures. Otherwise leave fixture in place.
- Thread the lower half of the fixture into the actuator until it is threaded all the way in and facing forward (Figure B.2). Use a spanner wrench and hammer to tighten it into place.
- Thread the upper half of the fixture into the load cell until it is threaded almost all the way in. Loosely align it with the position of the lower half of the fixture.
- Lower the upper half of the fixture until the upper pair of alignment holes and lower pair of alignment holes are aligned.
- Hold the alignment plate, which contains four aligned holes, against the front faces of the fixture so the four alignment holes in the fixture are aligned with the holes in the plate. Thread small bolts into each of the alignment holes until they are tight.
- Use a spanner wrench and hammer to tighten the upper half of the fixture in place.
- Remove the alignment bolts and plate. Verify that the back faces of the grips are still in plane.

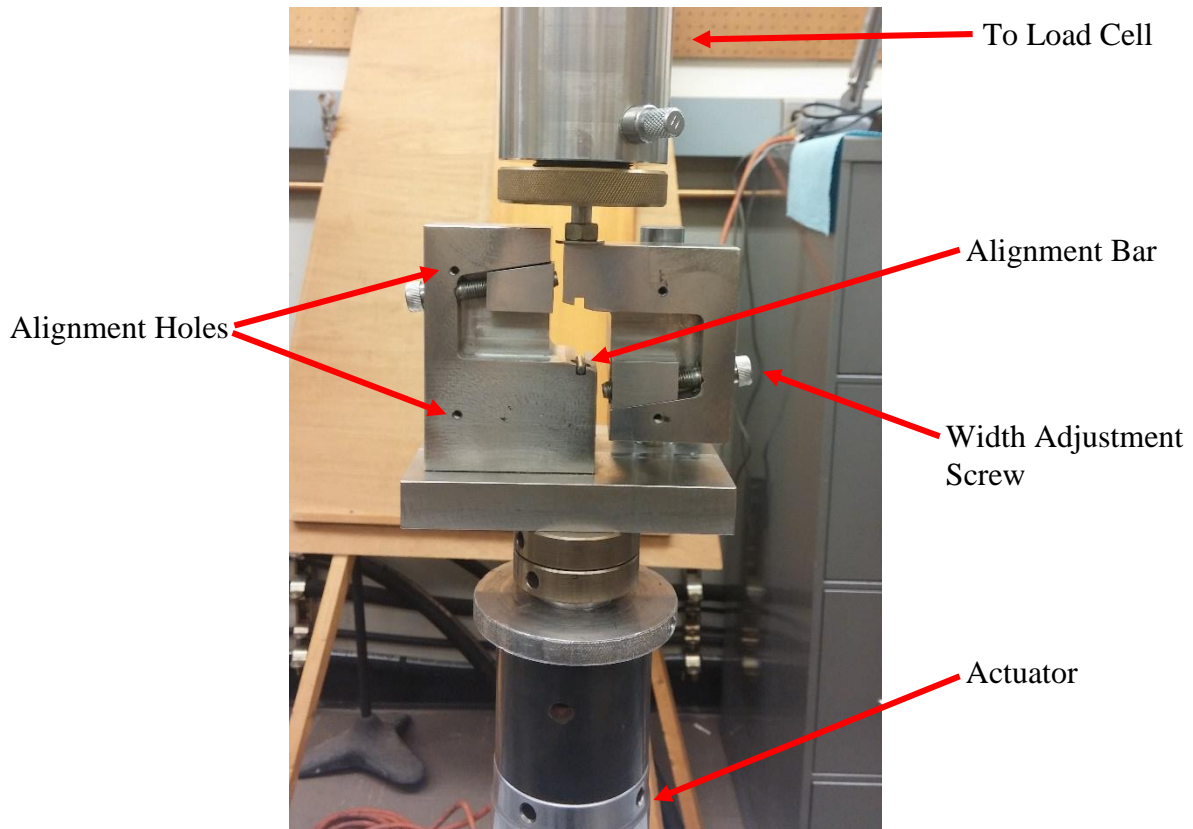


Figure B.2. G_{12} fixture installed in load frame.

B.2.2. Specimen Insertion

- Turn the width adjustment screws until they are all the way open.
- Use the actuator to raise the fixture until the specimen can easily fit into both halves, as shown in Figure B.3.
- Push the specimen flush against the back of the bottom fixture. Raise the alignment bar (shown in Figure B.2) and move the specimen side to side so the center v-notch of the specimen contacts the alignment bar. Tighten one width adjustment screw until it holds the specimen tightly.
- Begin to tighten the other width adjustment screw. Keep an eye on the load cell. If the specimen begins to pick up load while the width adjustment screw is being tightened,

raise or lower the actuator until the load is removed. Continue tightening the screw and watching the load cell until the specimen is tightly in the fixture.

B.2.3. Strain Gage Calibration

- Use the red wire and the white wire for the actual strain gage reading, and fit them into the strain gage breadboard in the appropriate locations. Use the black wire for shunt calibration and fit it into the appropriate location on the breadboard.
- Repeat for all four sets of strain gage wires.
- Conduct strain gage shunt calibration as specified by the calibration manual.

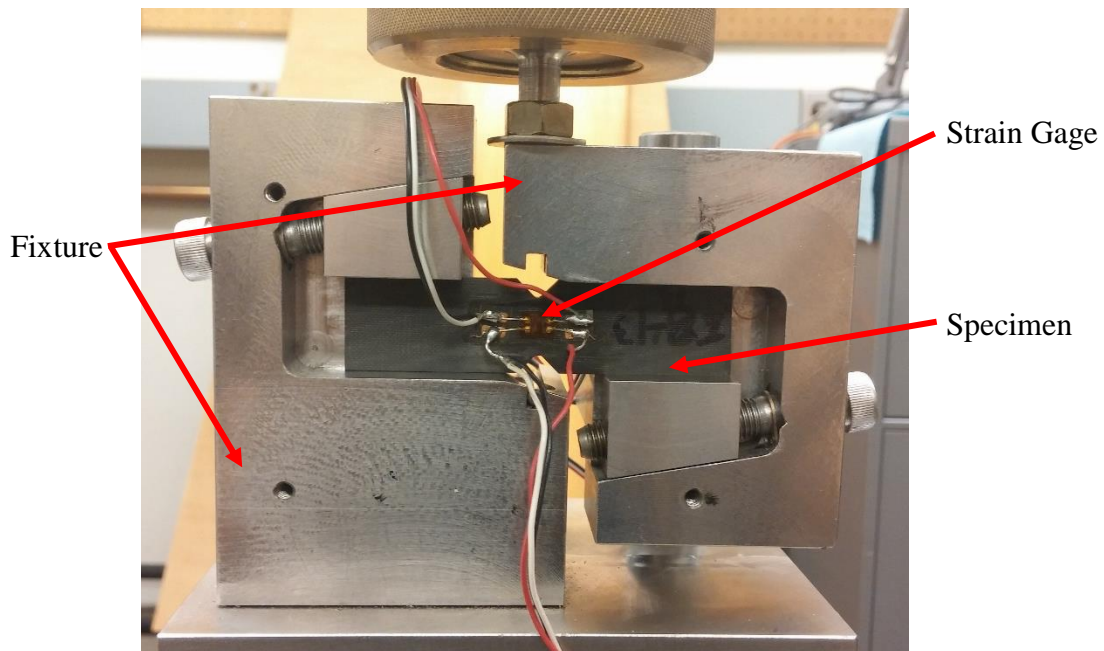


Figure B.3. G_{12} specimen installed in fixture.

B.2.4. Running Programs

- Open the G₁₂ program in TestWare SX. Zero the load before the specimen is in the fixture and the displacement after the specimen is in the fixture.
- Open the ramp program in TestStar.
- Open the data acquisition file in LabVIEW. Verify channels are properly setup. See Table B.1 for recommended channel settings for current hardware.
- Name a file to record data by the following convention: Plate Number – Specimen Number (Test Number). E.g. T-081910-7 for the test of specimen 7 on plate T-081910.
- Set the TestStar program to run at 0.05 in/min crosshead displacement.

B.3. Test

- Start the LabVIEW data collection.
- Start the TestStar program.
- Run the program until the specimen is loaded to approximately 400 lbs compression.
- Stop data collection. Unload specimen.

Table B.1: Recommended channel settings for G₁₂ Testing

Name	Scale (Units/Volt)	Units	Offset	Min (V)	Max (V)
Load	50	lbs/V	0	-10	1
Displacement	0.05	in/V	0	-7	7
Front Strain 1	1000	μ ϵ /V	0	-7	7
Front Strain 2	1000	μ ϵ /V	0	-7	7
Back Strain 1	1000	μ ϵ /V	0	-7	7
Back Strain 2	1000	μ ϵ /V	0	-7	7

B.4. Data Reduction

- Import the data into excel.
- Use specimen dimensions previously recorded to calculate stress.
- Graph stress vs. front strain, stress vs. back strain, and stress vs. the average value of strain.
- Use the secant line method, detailed in the standard, to determine the value of G_{12} for each of the three plots.
- Record the three values of G_{12} and the specimen dimensions in the workbook for modulus values.

Appendix C. Derivation of Maximum Energy Release Rate Criterion for an Orthotropic Material

For applied mode I loading, Irwin's crack tip solutions give

$$\begin{aligned}\sigma_{xx} &= \frac{K_I}{\sqrt{2\pi r}} \left(\cos\left(\frac{\theta}{2}\right) \left[1 - \sin\left(\frac{\theta}{2}\right) \sin\left(\frac{3\theta}{2}\right)\right] \right) \\ \sigma_{yy} &= \frac{K_I}{\sqrt{2\pi r}} \left(\cos\left(\frac{\theta}{2}\right) \left[1 + \sin\left(\frac{\theta}{2}\right) \sin\left(\frac{3\theta}{2}\right)\right] \right) \\ \sigma_{xy} &= \frac{K_I}{\sqrt{2\pi r}} \left(\sin\left(\frac{\theta}{2}\right) \cos\left(\frac{\theta}{2}\right) \cos\left(\frac{3\theta}{2}\right) \right)\end{aligned}\quad (C.1)$$

where K_I is the mode I stress intensity factor and θ , r , σ_{xx} , σ_{yy} , and σ_{xy} are given in Figure C.1.

For an angular position of $\theta = 0$, directly ahead of the crack tip, the normal stresses are

$$\sigma_{xx}(r, 0) = \frac{K_I}{\sqrt{2\pi r}}, \quad \sigma_{yy}(r, 0) = \frac{K_I}{\sqrt{2\pi r}} \quad (C.2)$$

At this location, the out of plane normal stress σ_{zz} is given by

$$\sigma_{zz}(r, 0) = \frac{\gamma}{2} (\sigma_{xx}(r, 0) + \sigma_{yy}(r, 0)) = \gamma \frac{K_I}{\sqrt{2\pi r}} \quad (C.3)$$

where $\gamma = 0$ for $\sigma_{zz} = 0$, and, for $\varepsilon_{zz} = 0$, γ is given by Equation (6.10). Under mode I loading the other shear stress terms are

$$\sigma_{xz} = \sigma_{yz} = 0 \quad (C.4)$$

For the above defined case of $\theta = 0$, let

$$\sigma_{ij} = \frac{K_I}{\sqrt{2\pi r}} f_{ij} \quad (C.6)$$

Such that

$$f_{yy} = 1; f_{yz} = 0; f_{zz} = \gamma \quad (C.7)$$

Considering a coordinate rotation by angle ϕ about the x axis as shown in Figure C.2, the transformed stress components can be defined by

$$\sigma_{ij}' = \frac{K_I}{\sqrt{2\pi r}} g_{ij} \quad (C.8)$$

Considering only the y and z components of stress, g_{ij} are then defined by

$$g_{ij} = B_{ij} f_{ij} B_{ji} \quad (C.9)$$

Where B_{ij} is the transformation matrix. Substituting into the above

$$\begin{pmatrix} g_{yy} & g_{yz} \\ g_{yz} & g_{zz} \end{pmatrix} = \begin{pmatrix} \cos(\phi) & \sin(\phi) \\ -\sin(\phi) & \cos(\phi) \end{pmatrix} \begin{pmatrix} 1 & 0 \\ 0 & \gamma \end{pmatrix} \begin{pmatrix} \cos(\phi) & -\sin(\phi) \\ \sin(\phi) & \cos(\phi) \end{pmatrix} \quad (C.10)$$

Which yields

$$\begin{pmatrix} g_{yy} & g_{yz} \\ g_{yz} & g_{zz} \end{pmatrix} = \begin{pmatrix} \gamma \cos^2(\phi) + \sin^2(\phi) & \left(\frac{\gamma}{2} - \frac{1}{2}\right) \sin(2\phi) \\ \left(\frac{\gamma}{2} - \frac{1}{2}\right) \sin(2\phi) & \gamma \sin^2(\phi) + \cos^2(\phi) \end{pmatrix} \quad (C.11)$$

The ‘transformed stress intensity factors’ under a rotation of angle ϕ are then

$$\begin{aligned} K_I'(\phi) &= K_I g_{zz} \\ K_{II}'(\phi) &= 0 \\ K_{III}'(\phi) &= K_I g_{yz} \end{aligned} \quad (C.12)$$

where $\sigma_{y'y'}$ gives rise to K_I' and $\sigma_{y'z'}$ gives rise to K_{III}' for the case of mode I loading.

For applied mode III loading, Irwin’s crack tip solutions give

$$\begin{aligned} \sigma_{xz} &= \frac{K_{III}}{\sqrt{2\pi r}} \left(-\sin\left(\frac{\theta}{2}\right)\right) \\ \sigma_{yz} &= \frac{K_{III}}{\sqrt{2\pi r}} \left(\cos\left(\frac{\theta}{2}\right)\right) \end{aligned} \quad (C.13)$$

$$\sigma_{xx} = \sigma_{yy} = \sigma_{zz} = \sigma_{xy} = 0$$

where K_{III} is the mode III stress intensity factor and all other terms are identical to those previously defined. For an angular position of $\theta = 0$, directly ahead of the crack tip, the stresses are

$$\sigma_{yz}(r, 0) = \frac{K_{III}}{\sqrt{2\pi r}} \quad (C.14)$$

and all other stresses are zero. For this radial position, the stresses can be defined similarly to Equation (C.8), such that

$$\sigma_{ij} = \frac{K_{III}}{\sqrt{2\pi r}} h_{ij} \quad (C.15)$$

and

$$h_{yy} = 0, \quad h_{yz} = 1, \quad h_{zz} = 0 \quad (C.16)$$

Considering a coordinate transformation by angle ϕ about the x axis, the transformed stress components can be defined by

$$\sigma_{ij}' = \frac{K_{III}}{\sqrt{2\pi r}} l_{ij} \quad (C.17)$$

Again considering only the y and z components of stress, l_{ij} are defined by the transformation matrix and h_{ij} .

$$\begin{pmatrix} l_{yy} & l_{yz} \\ l_{yz} & l_{zz} \end{pmatrix} = \begin{pmatrix} \cos(\phi) & \sin(\phi) \\ -\sin(\phi) & \cos(\phi) \end{pmatrix} \begin{pmatrix} 0 & 1 \\ 1 & 0 \end{pmatrix} \begin{pmatrix} \cos(\phi) & -\sin(\phi) \\ \sin(\phi) & \cos(\phi) \end{pmatrix} \quad (C.18)$$

$$\begin{pmatrix} l_{yy} & l_{yz} \\ l_{yz} & l_{zz} \end{pmatrix} = \begin{pmatrix} -\sin(2\phi) & \cos(2\phi) \\ \cos(2\phi) & \sin(2\phi) \end{pmatrix} \quad (C.19)$$

The 'transformed stress intensity factors' under a rotation of angle ϕ are then

$$\begin{aligned} K_I'(\phi) &= K_{III} l_{zz} \\ K_{II}'(\phi) &= 0 \end{aligned} \quad (C.20)$$

$$K_{III}'(\phi) = K_{III} l_{yz}$$

where $\sigma_{y'y'}$ gives rise to K_I' and $\sigma_{y'z'}$ gives rise to K_{III}' for the case of mode III loading.

For mixed mode I-III loading, the contribution of both Equations (C.12) and Equations (C.20) must be considered. Therefore the rotated mode I and mode III stress intensity factors are calculated by

$$K_I'(\phi) = K_I g_{zz} + K_{III} l_{zz} = K_I (\gamma \sin^2(\phi) + \cos^2(\phi)) + K_{III} \sin(2\phi) \quad (C.21)$$

$$K_{III}'(\phi) = K_I g_{yz} + K_{III} l_{yz} = K_I \left(\frac{\gamma}{2} - \frac{1}{2} \right) \sin(2\phi) + K_{III} \cos(2\phi)$$

Equations (C.21) can then be used to determine the energy release rate using the previously derived orthotropic relationships, which have been rearranged from Equation (6.4) as

$$G_I = \frac{H_{11}}{4} K_I^2 \quad (C.22)$$

$$G_{III} = \frac{H_3}{2} K_{III}^2$$

In absence of mode II loading, the energy release rate is then determined by

$$G(\phi) = G_I(\phi) + G_{III}(\phi) \quad (C.23)$$

$$G(\phi) = \frac{H_{11}}{4} K_I'(\phi)^2 + \frac{H_3}{2} K_{III}'(\phi)^2$$

Combining Equation (C.21) and Equation (C.23), this is equivalent to

$$G(\phi) = \frac{H_{11}}{4} (K_I (\gamma \sin^2(\phi) + \cos^2(\phi)) + K_{III} \sin(2\phi))^2 + \frac{H_3}{2} \left(K_I \left(\frac{\gamma}{2} - \frac{1}{2} \right) \sin(2\phi) + K_{III} \cos(2\phi) \right)^2 \quad (C.24)$$

Thus Equation (C.24) is the energy release rate under a rotation of angle ϕ for mode I-III loading and the assumption of $\epsilon_{zz} = 0$. For plane stress conditions, this equation still holds if $\gamma = 0$ is used.

Also note that for isotropic material properties, Equation (C.24) reduces to the equation given by Cooke and Pollard (1996)

$$G(\phi) = \frac{1 - \nu^2}{E} \left(K_I (2\nu \sin^2(\phi) + \cos^2(\phi)) + K_{III} \sin(2\phi) \right)^2 + \frac{1 + \nu}{E} \left(K_I \left(\nu - \frac{1}{2} \right) \sin(2\phi) + K_{III} \cos(2\phi) \right)^2 \quad (\text{C.25})$$

The maximum energy release rate criterion given in Equation (C.24) has been used to determine the predicted angle of twist, ϕ , based on K_{III}/K_I . The orthotropic material properties of IM7/8552 given by O'Brien and Krueger (2003) and presented in Table 6.2 were used as well as the assumption of $\varepsilon_{zz} = 0$. This is presented in Figure C.3. For each K_{III}/K_I , the value of ϕ for which Equation (C.24) is maximum is given. For these material properties, there is a bifurcation in the solution around $K_{III}/K_I = 0.4$. Below $K_{III}/K_I = 0.4$ the solution is equal to the maximum principal tensile stress criterion prediction. Above $K_{III}/K_I = 0.4$, the average value of the two solutions is equal to the maximum principal tensile stress criterion prediction.

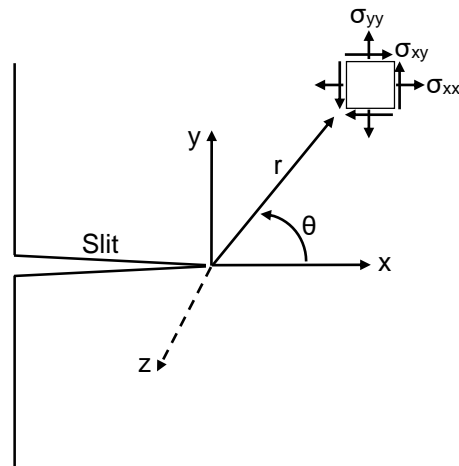


Figure C.1. Stress field at Irwin slit-crack tip, showing rectangular coordinate components.

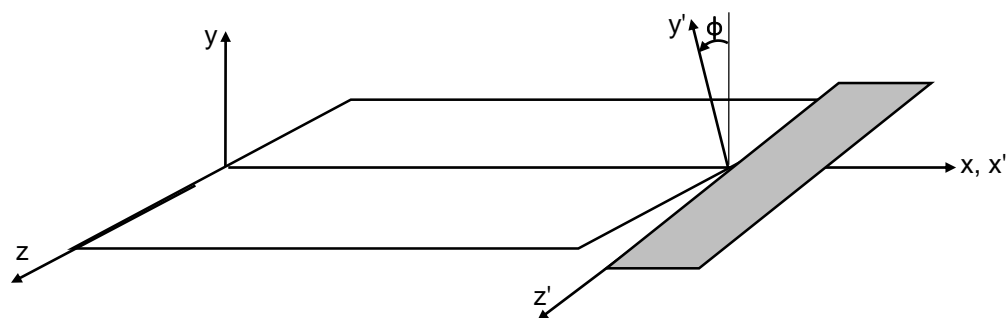


Figure C.2. Model for out-of-plane twisting crack extension.

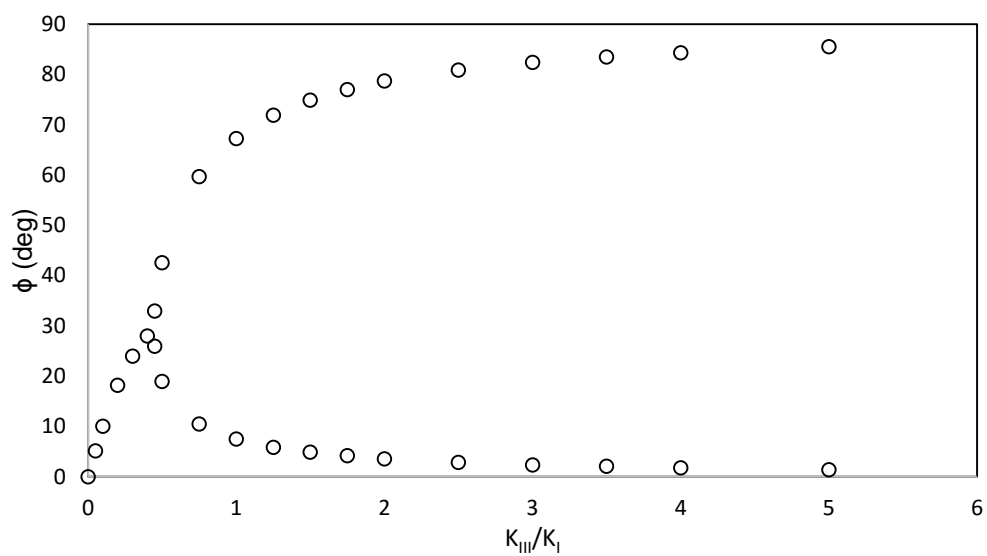


Figure C.3. Maximum energy release rate criterion solution for IM7/8552 material properties and the assumption of $\varepsilon_{zz} = 0$.

Appendix D. Derivation and Evaluation of Maximum Principal Tensile Stress Criterion for an Orthotropic Material

D.1. Maximum Principal Tensile Stress Criterion Derivation

For applied mode I-III loading, Irwin's crack tip solutions give

$$\begin{aligned}
 \sigma_{xx} &= \frac{K_I}{\sqrt{2\pi r}} \left(\cos\left(\frac{\theta}{2}\right) \left[1 - \sin\left(\frac{\theta}{2}\right) \sin\left(\frac{3\theta}{2}\right)\right] \right) \\
 \sigma_{yy} &= \frac{K_I}{\sqrt{2\pi r}} \left(\cos\left(\frac{\theta}{2}\right) \left[1 + \sin\left(\frac{\theta}{2}\right) \sin\left(\frac{3\theta}{2}\right)\right] \right) \\
 \sigma_{xy} &= \frac{K_I}{\sqrt{2\pi r}} \left(\sin\left(\frac{\theta}{2}\right) \cos\left(\frac{\theta}{2}\right) \cos\left(\frac{3\theta}{2}\right) \right) \\
 \sigma_{xz} &= \frac{K_{III}}{\sqrt{2\pi r}} \left(-\sin\left(\frac{\theta}{2}\right) \right) \\
 \sigma_{yz} &= \frac{K_{III}}{\sqrt{2\pi r}} \left(\cos\left(\frac{\theta}{2}\right) \right)
 \end{aligned} \tag{D.1}$$

where K_I is the mode I stress intensity factor, K_{III} is the mode III stress intensity factor, θ , r , σ_{xx} , σ_{yy} , and σ_{xy} are given in Figure D.1, and σ_{yz} , and σ_{xz} can be inferred from the given coordinate system. For an angular position of $\theta = 0$, directly ahead of the crack tip, these stresses reduce to

$$\begin{aligned}
 \sigma_{xx}(r, 0) &= \frac{K_I}{\sqrt{2\pi r}}, & \sigma_{yy}(r, 0) &= \frac{K_I}{\sqrt{2\pi r}}, & \sigma_{yz}(r, 0) &= \frac{K_{III}}{\sqrt{2\pi r}} \\
 \sigma_{xy} &= \sigma_{xz} = 0
 \end{aligned} \tag{D.2}$$

At this location, the out of plane normal stress σ_{zz} is given by

$$\sigma_{zz}(r, 0) = \frac{\gamma}{2} (\sigma_{xx}(r, 0) + \sigma_{yy}(r, 0)) = \gamma \frac{K_I}{\sqrt{2\pi r}} \tag{D.3}$$

where $\gamma = 0$ for $\sigma_{zz} = 0$, and, for $\varepsilon_{zz} = 0$, γ is given by Equation (6.10).

Consider a material point at the tip of the crack in the y - z plane. In this plane, the stresses acting are σ_{yy} , σ_{zz} , and σ_{yz} , which are proportional to K_I , γK_I , and K_{III} respectively. A schematic of this, along with a Mohr's Circle representation, is given in Figure D.2. The principal angle, ϕ , is determined by

$$\tan(2\phi) = \frac{2\sigma_{yz}}{\sigma_{yy} - \sigma_{zz}} \quad (\text{D.4})$$

In terms of stress intensity factors,

$$\tan(2\phi) = \frac{2K_{III}}{K_I - \gamma K_I} = \frac{2K_{III}}{K_I(1 - \gamma)} \quad (\text{D.5})$$

or

$$\phi = \frac{1}{2} \tan^{-1} \left(\frac{2K_{III}}{K_I(1 - \gamma)} \right) \quad (\text{D.6})$$

For the case of $\sigma_{zz} = 0$, $\gamma = 0$, and Equation (D.6) simplifies to

$$\phi = \frac{1}{2} \tan^{-1} \left(\frac{2K_{III}}{K_I} \right) \quad (\text{D.7})$$

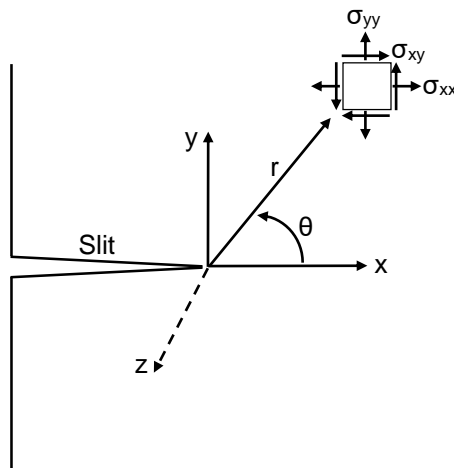


Figure D.1. Stress field at Irwin slit-crack tip, showing rectangular coordinate components.

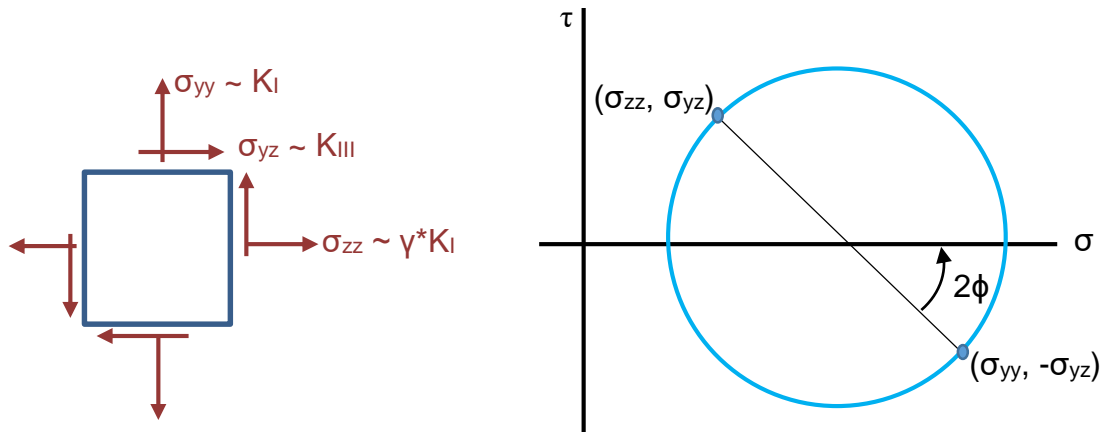


Figure D.2. General expression for stress state in y-z plane and Mohr's Circle representation.

D.2. Sensitivity to Material Properties and Constraint Conditions

A study has been conducted to determine the sensitivity of the MPTS criterion predictions to material properties and constraint conditions. Three sets of material properties have been considered: (1) orthotropic material properties of IM7/8552 given by O'Brien and Krueger (2003) and presented in Table 6.2, hereafter known as the "reference" material properties, (2) orthotropic material properties of IM7/8552 from O'Brien and Krueger (2003) but with the experimentally determined $E_{11} = 187.2$ GPa and $G_{12} = G_{13} = 7.33$ GPa from Section 5.2.2, hereafter known as the "experiment" material properties, and (3) isotropic material properties with $E = 161$ GPa and $\nu = 0.32$, hereafter known as the "isotropic" material properties. Note that these isotropic material properties are equivalent to E_{11} and ν_{12} from Table 6.2. Further, two constraint conditions, $\epsilon_{zz} = 0$ and $\sigma_{zz} = 0$, are considered.

The MPTS criterion was used predict the orientation of transverse cracks initiating under mixed mode I-III loading for the different material properties and constraint conditions. Here,

Equation (6.4) was used to relate G_{III}/G_I to K_{III}/K_I and input into Equation (D.6) and Equation (D.7). G_{III}/G_I was used as a basis of comparison because the specimen loading in Chapter 6 is in terms of G_{III}/G_I , and subsequent comparisons to experimental data necessitate the MPTS predictions to be in terms of G_{III}/G_I as well.

The various MPTS predictions are presented in Figure D.3. Here it can be seen that there is an effect of material properties and constraint conditions, and at low G_{III}/G_I , the differences between the predictions become larger. For a given constraint condition, there is a fairly significant difference between the predictions for the orthotropic and isotropic material properties. However, there is almost no difference between the results for the two different orthotropic sets of material properties. This indicates that for the range of “likely orthotropic material properties” of IM7/8552, that is, considering potential errors in material property determinations, the predictions are relatively insensitive. For a given set of material properties, there is reasonably large sensitivity to the constraint conditions.

The sensitivity of MPTS criterion to material properties and constraint conditions can be quantified in terms of the percent differences between various predictions, which is given in Figure D.4. Here, the differences between predictions are plotted based on the mode mix in terms of G_{III}/G_I . The first comparisons listed in the legend considers the difference between material properties for $\varepsilon_{zz} = 0$, while the second comparison listed in the legend considers the difference between constraint conditions for the reference material properties. The results for these two comparisons are almost identical, and for the range of G_{III}/G_I measured in the experimental data, the differences are less than 10%. From this it can be seen that the differences between predictions will be fairly small for the data obtained in this dissertation, even when significantly different material properties and constraint conditions are considered.

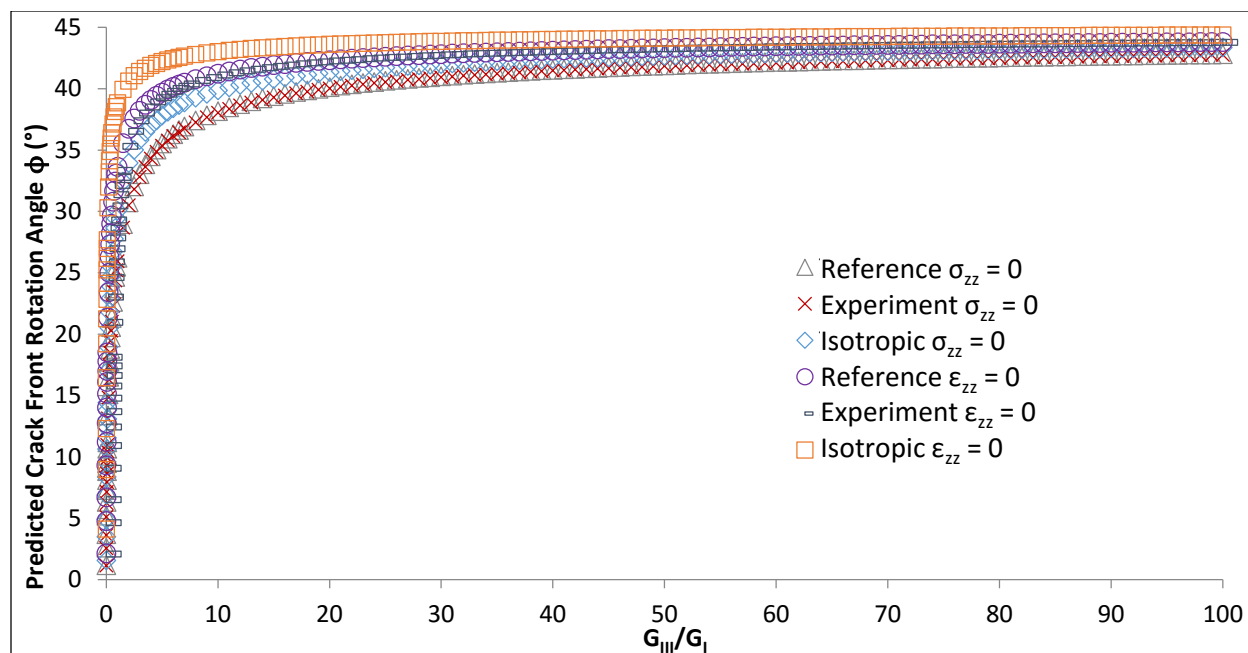


Figure D.3. Maximum principal tensile stress criterion prediction for different material properties and constraint conditions.

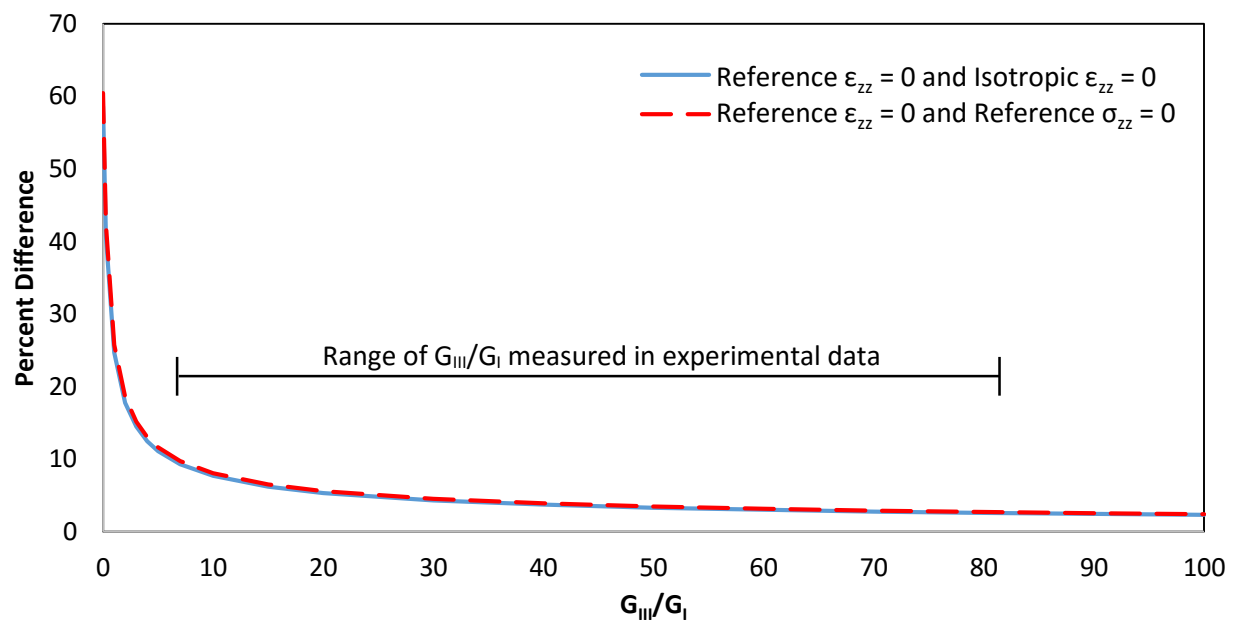


Figure D.4. Plot of percent differences between different material property and constraint conditions for MPTS predictions.

D.3. Appropriate Material Properties and Constraint Condition for Comparison to Experimental Data

The MPTS criterion is used in Section 6.4.3 for comparison to experimental data of matrix crack angle measurements. Section D.2 showed that there is reasonable sensitivity of the MPTS predictions to assumed constraint condition. As SST specimens are wide in comparison to their thickness, the constraint on the through-width strain being equal to zero is true over the majority of the specimen width. Further, in Section 5.4, it is shown that matrix cracks first initiate near the center of the specimen width, which also supports the constraint condition $\varepsilon_{zz} = 0$ ($\varepsilon_{yy} = 0$ in the coordinate system used with SST specimens). Thus, the assumption that $\varepsilon_{zz} = 0$ will be used for the predictions presented in Section 6.4.3.

In Section D.2 above, it was shown that using the reference versus experimental orthotropic material properties resulted in almost identical MPTS predictions. Thus, while it is important to make the correct decision on constraint condition, the choice between these two sets of material properties is not critical. However, this sensitivity study was relatively minor, and did not consider the effect of differences in material constants other than E_{11} or $G_{12} = G_{13}$. A wider sensitivity study could show somewhat more effect, but it would certainly be less than the difference of going from orthotropic to isotropic material properties. Therefore, the differences between predictions for isotropic and orthotropic material properties can be considered as a worst-case scenario. To study the effect of these material properties, the experimental data given in Figure 6.8, which was generated using the reference material properties, is replotted in Figure D.5. Additional predictions using the experimental and isotropic material properties are also presented in this figure. From this figure it can be seen that the material property assumptions have relatively little effect on the accuracy of the prediction with respect to the experimental

data, even for the isotropic material properties. Thus, in the analysis presented in Section 6.4.3, the reference material properties are used.

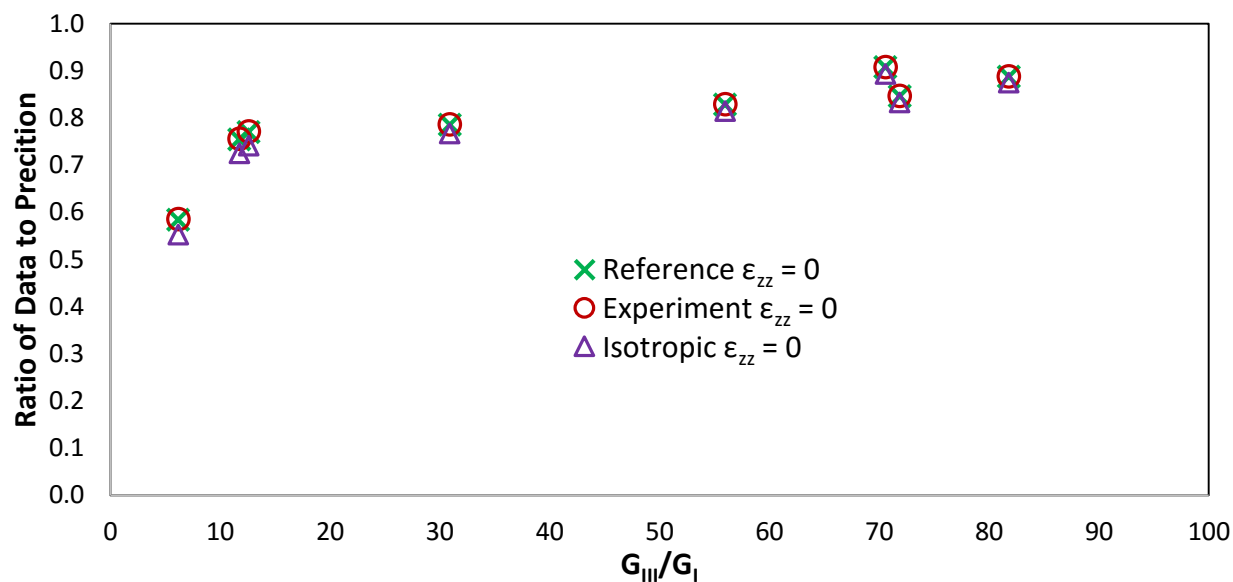


Figure D.5. Ratio of experimental data to MPTS predictions for $\epsilon_{zz} = 0$ and different material properties.

Appendix E. Full Results of Model Validation

E.1. Delamination Model without Diagonal Partition

E.1.1. Model Details

The meshes listed below were created for the delamination model without a diagonal partition.

- Baseline mesh with 0.001mm thick delamination, 30 elements across the width, and a near-tip refined region that extends 1.5 mm ($t/2$) on either side of the delamination tip. **(Linear-30)**
- Baseline mesh with 0.001mm thick delamination, 60 elements across the width, and a near-tip refined region that extends 1.5 mm ($t/2$) on either side of the delamination tip. Shown in Figure E.1 **(Linear-60)**
- Mesh with a thin delamination (0.0005mm, rather than baseline 0.001mm thick), 30 elements across the width, and a near-tip refined region that extends 1.5 mm ($t/2$) on either side of the delamination tip. **(LinearThin-30)**
- Mesh with thin 0.0005mm delamination, 30 elements across the width, and a near-tip refined region that extends 1.5 mm ($t/2$) on either side of the delamination tip with a finer mesh in the length-thickness plane than the “Linear” meshes. Shown in Figure E.2. **(FineMesh-30)**.
- Mesh with thin 0.0005mm delamination, 60 elements across the width, and a near-tip refined region that extends 1.5 mm ($t/2$) on either side of the delamination tip with a finer mesh in the length-thickness plane than the “FineMesh” mesh. Shown in Figure E.3. **(FineMeshA-60)**.

- Mesh with thin 0.0005mm delamination, 60 elements across the width, and a near-tip refined region that extends 4.5 mm ($3t/2$) on either side of the delamination tip with the same mesh in the length-thickness plane as “FineMeshA” but spread across the wider refined region. Shown in Figure E.4. (**RefineMesh3X**).
- Mesh with thin 0.0005mm delamination, 150 elements across the width, and a near-tip refined region that extends 1.5 mm ($t/2$) on either side of the delamination tip with a finer mesh in the length-thickness plane than the “FineMesh” mesh. (**FineMeshA-150**)

Model Dimensions: 30mm width, 3mm thickness, 80mm length, 30mm delamination length

Material Properties

- Orthotropic material properties for IM7/8552 given in Table 6.2.

Boundary Conditions:

- Top and bottom (30mmx80mm faces) $U_2 = 0$
- Lower cracked leg (1.5mmx30mm face) $U_1=U_3=0$
- Upper cracked leg (1.5mmx30mm face) $U_1=0, U_3 = -0.1\text{mm}$

Mesh Details:

- Delamination tip elements are 0.031mm long and high, or $t/96$
- 14-24 elements through-thickness in far field, i.e., outside of the refined region
- 30-60 elements through-width across whole specimen

- Uncracked region element length (outside of refined region) biased from 0.5mm at the edge of the refined region to 2mm at the far end of the specimen
- Cracked region element length (outside of refined region) biased from 0.5mm at the edge of the refined region to 1.5mm at the far end of the specimen
 - Due to decreased size of cracked region outside of the refined region, element length for RefineMesh3X biased from 0.5mm at edge of the refined region to 1.0mm at far end of the specimen.
- Element size in length-thickness plane refined region varies based on whether mesh is Linear, FineMesh, or FineMeshA. See Figure E.1 through Figure E.4 for qualitative comparison.

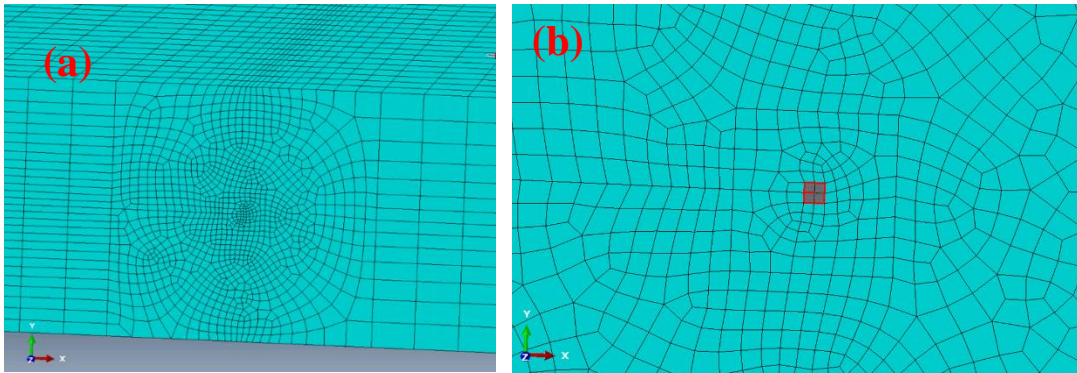


Figure E.1. Linear-60 mesh. (a) edge-view of refined region. Refined region is 3mm long, i.e., it extends 1.5mm ahead and behind delamination tip. (b) edge-view of near-tip region with delamination tip elements highlighted.

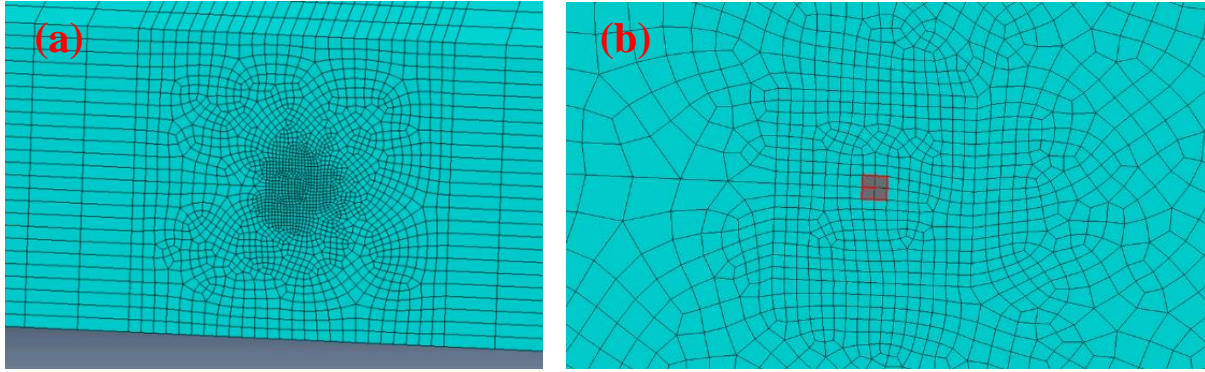


Figure E.2. FineMesh-30 mesh. (a) edge-view of refined region. Refined region is 3mm long, i.e., it extends 1.5mm ahead and behind delamination tip. (b) edge-view of near-tip region with delamination tip elements highlighted.

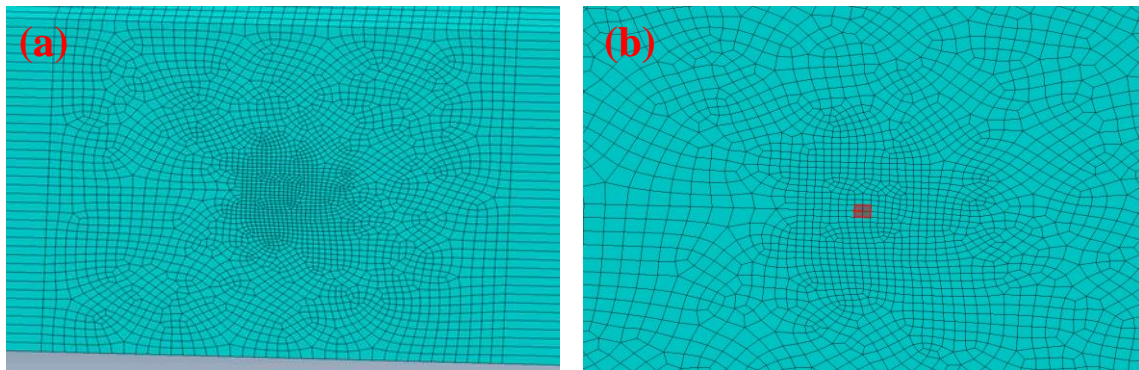


Figure E.3. FineMeshA-60 mesh. (a) edge-view of refined region. Refined region is 3mm long, i.e., it extends 1.5mm ahead and behind delamination tip. (b) edge-view of near-tip region with delamination tip elements highlighted.

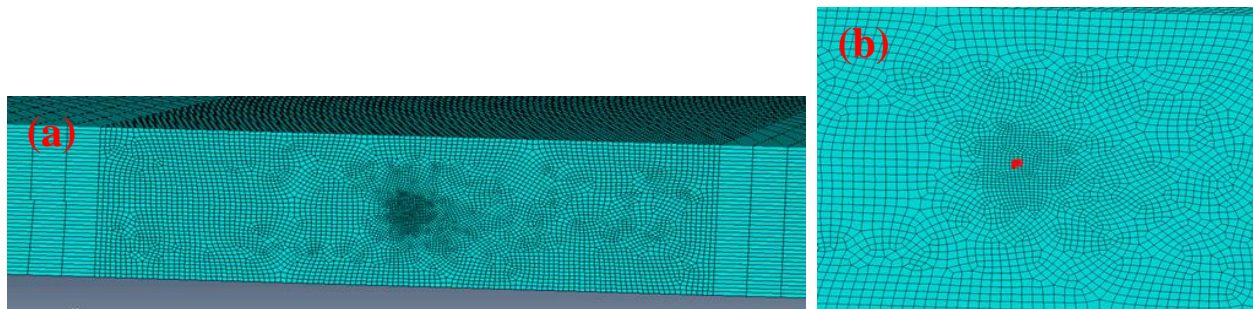


Figure E.4. RefineMesh-3X mesh. (a) edge-view of refined region. Refined region is 9mm long, i.e., it extends 4.5mm ahead and behind delamination tip. (b) edge-view of near-tip region with delamination tip elements highlighted.

E.1.2. Results

The benchmark results for the STB model are given in Table E.1. The benchmark model has 30 elements across the width, and the values given in Table E.1 are averages obtained for the 30 data points across the width. These benchmark results are used with the results from the models generated for this step to determine the percent difference for each mesh. Table E.2 gives percent differences between the average values of ERR for the experimental models, averaged for the total number of width elements, with respect to the benchmark. For G_{II} , G_{III} , and G a negative percent difference indicates that the average value for the STB model was larger. For G_I , the average values from the experimental models are given since the benchmark reports $G_I = 0$, and this results in an infinite percent difference.

Table E.1. Average values of ERR components for benchmark STB model.

G_I (J/m ²)	G_{II} (J/m ²)	G_{III} (J/m ²)	G (J/m ²)
0	2.278	18.08	20.36

Table E.2. Comparative results between benchmark STB model and experimental models for delamination validation without diagonal partition.

	G_I (J/m ²)	G_{II} (%)	G_{III} (%)	G (%)
Linear-30	2.205 E-5	-5.329	0.9727	20.41
Linear-60	2.244 E-5	-6.024	0.919	0.1422
LinearThin-30	2.205 E-5	-5.328	0.973	0.267
FineMesh-30	8.863 E-7	-1.133	0.081	-0.055
FineMeshA-60	1.760 E-7	1.758	0.00199	0.1983
RefinedMesh3X	8.345 E-7	-1.883	0.0310	0.183
FineMeshA-150	1.91E-07	-1.9668	-0.0437	-0.25876

Figure E.5 through Figure E.8 present graphical comparisons of a selection of the models run for this step. For these figures, the horizontal axis represents the location along the delamination front in millimeters. The vertical axis is the component of ERR (in J/m^2) for G_I , G_{II} , G_{III} , and G .

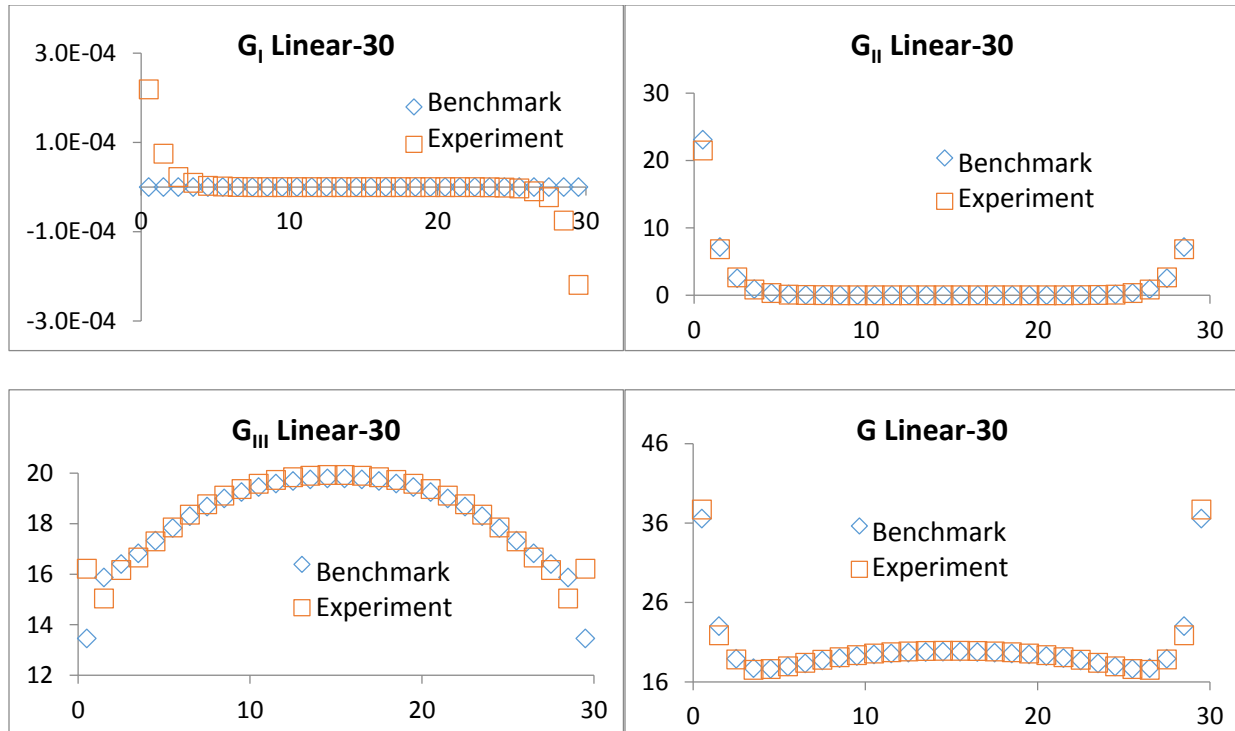


Figure E.5. Plot of ERRs for Linear-30 model.

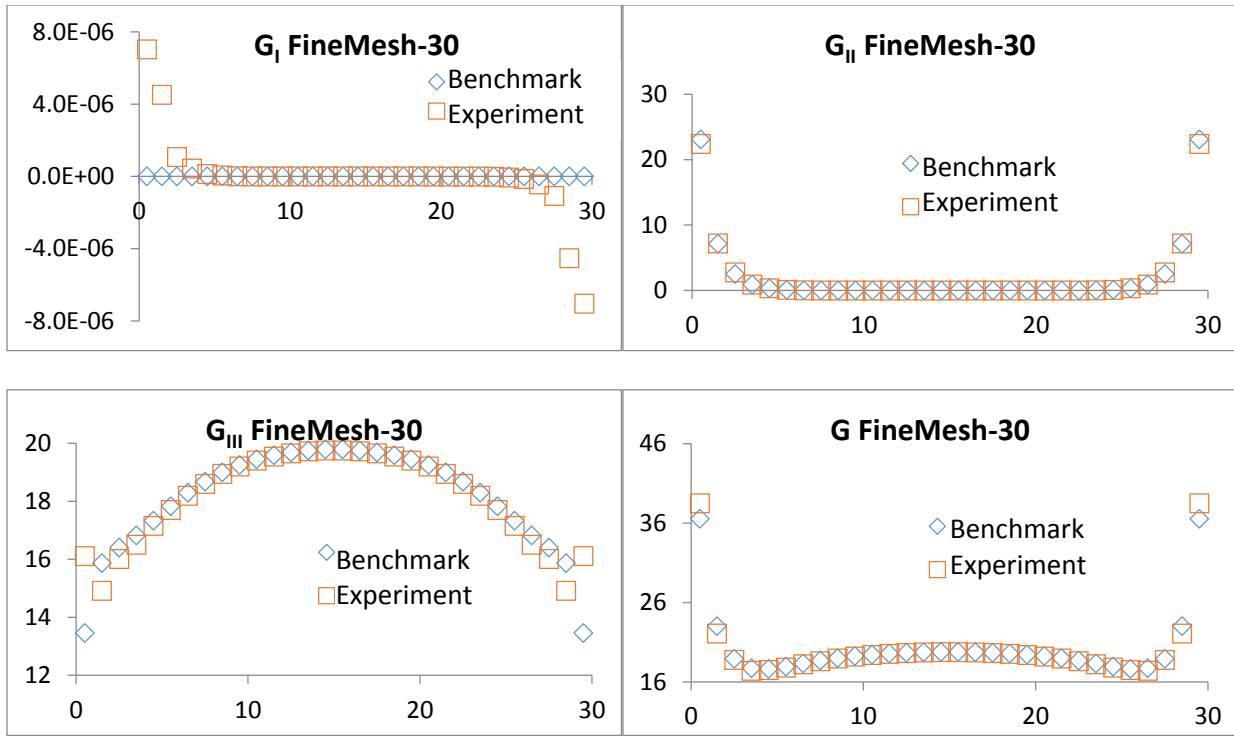


Figure E.6. Plot of ERRs for FineMesh-30 model.

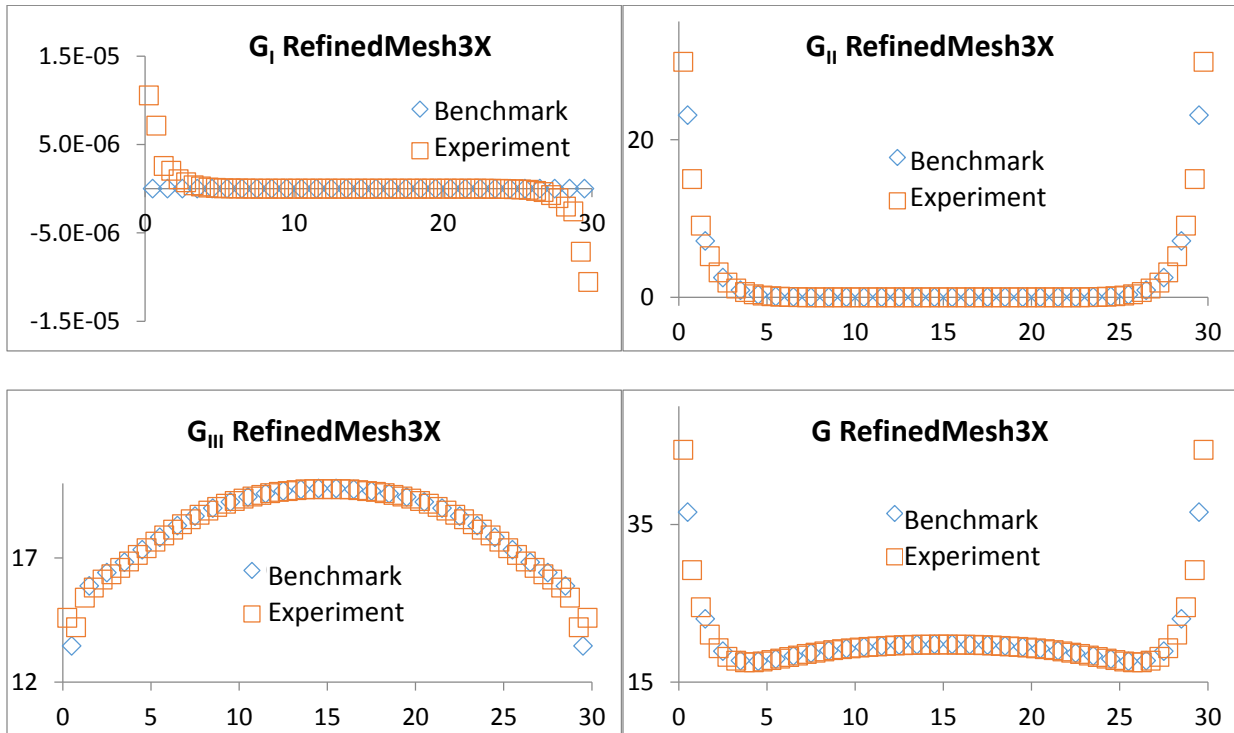


Figure E.7. Plot of ERRs for RefinedMesh3X model.

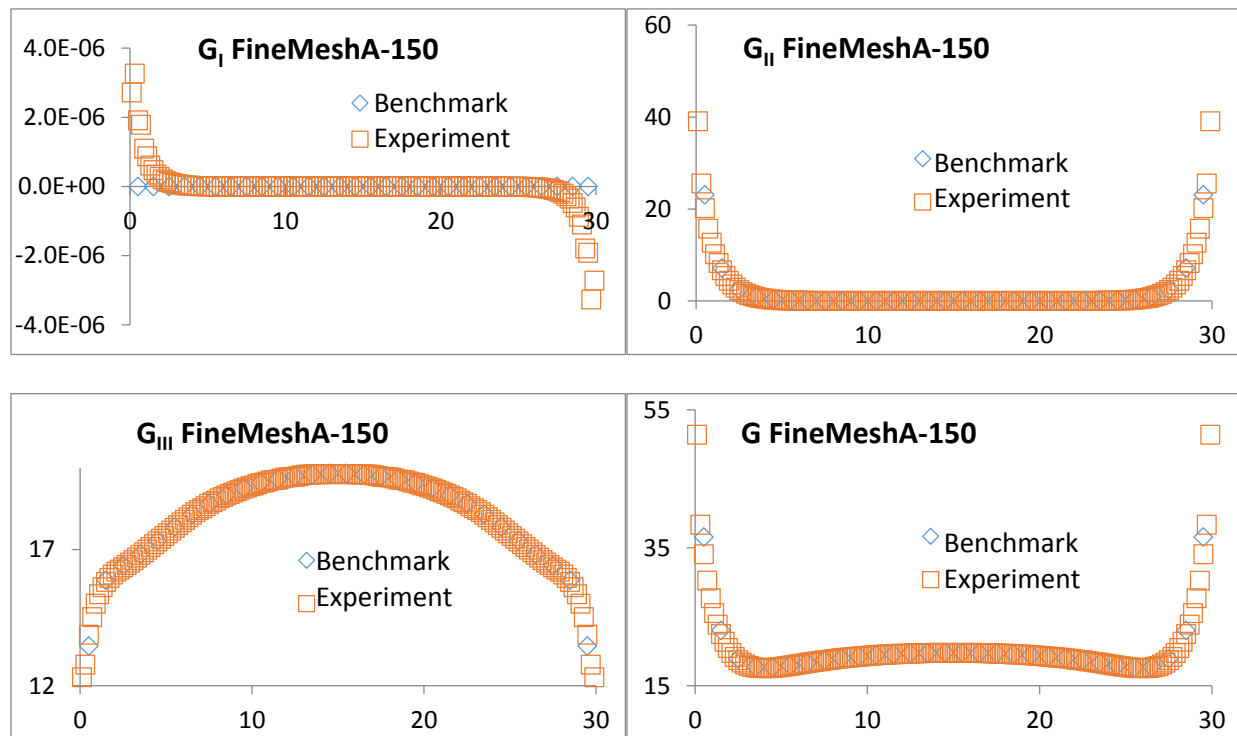


Figure E.8. Plot of ERRs for FineMeshA-150 model.

For the models represented in Figure E.5 through Figure E.8, comparisons are given between the model result at a specific location along the delamination front and the ERRs at that location from the benchmark model. The benchmark results for the STB model are given in Table E.3. The percent differences are given for the different models in Table E.4 through Table E.8. As before, a negative percent difference indicates that the average value for the STB model was larger. The average value of G_I is given since the STB model reports $G_I = 0$, and this results in an infinite percent difference between the two results. For those models with a different number of elements across the width than the benchmark, linear interpolation was used to obtain the values of the ERRs at the location of interest.

Table E.3. Values of ERR components at select locations along the delamination front for benchmark STB model.

Location of Interest	y-location (mm)	G_I (J/m ²)	G_{II} (J/m ²)	G_{III} (J/m ²)	G (J/m ²)
Center Element	14.5	0.0	4.00 E-6	19.79	19.79
Edge Element	29.5	0.0	23.10	13.45	36.55
Near-Edge Element	28.5	0.0	7.157	15.87	23.02

Table E.4. Comparative results between benchmark STB model and experimental model ERRs at select locations along the delamination fronts for Linear-30 mesh.

Linear-30	y-location (mm)	G_I (J/m ²)	G_{II} (%)	G_{III} (%)	G (%)
Center Element	14.5	2.348 E-11	-45.56	0.6877	0.6876
Edge Element	29.5	-2.192 E-4	-6.915	20.50	3.177
Near-Edge Element	28.5	-7.484 E-5	-4.567	-5.232	-5.026

Table E.5. Comparative results between benchmark STB model and experimental model ERRs at select locations along the delamination fronts for FineMesh-30.

FineMesh-30	y-location (mm)	G_I (J/m ²)	G_{II} (%)	G_{III} (%)	G (%)
Center Element	14.5	1.579 E-12	-44.47	-0.2010	-0.2020
Edge Element	29.5	-7.038 E-6	-3.019	19.73	5.35
Near-Edge Element	28.5	-4.523 E-6	0.4012	-6.000	-4.014

Table E.6. Comparative results between benchmark STB model and experimental model ERRs at select locations along the delamination fronts for FineMeshA-60.

FineMeshA-60	y-location (mm)	G_I (J/m ²)	G_{II} (%)	G_{III} (%)	G (%)
Center Element	14.5	4.839 E-14	58.87	0.1484	0.1484
Edge Element	29.5	-2.016 E-6	2.672	-6.972	-0.8780
Near-Edge Element	28.5	-4.326 E-7	-0.1881	1.677	1.097

Table E.7. Comparative results between benchmark STB model and experimental model ERRs at select locations along the delamination fronts for RefinedMesh3X.

RefinedMesh3X	y-location (mm)	G_I (J/m ²)	G_{II} (%)	G_{III} (%)	G (%)
Center Element	14.5	1.371 E-13	58.87	0.1484	0.1485
Edge Element	29.5	-8.842 E-6	2.804	-6.991	-0.801
Near-Edge Element	28.5	-2.298 E-6	-0.0805	1.661	1.119

Table E.8. Comparative results between benchmark STB model and experimental model ERRs at select locations along the delamination fronts for FineMeshA-150.

FineMeshA-150	y-location (mm)	G_I (J/m ²)	G_{II} (%)	G_{III} (%)	G (%)
Center Element	14.5	8.066 E-14	71.87	0.1156	0.1156
Edge Element	29.5	-1.924 E-6	12.51	-3.119	6.755
Near-Edge Element	28.5	-4.745 E-7	6.656	0.3669	2.320

E.1.3. Discussion

For average data:

- Models created herein result in nonzero average G_I . Benchmark STB model with an infinitesimal delamination thickness had $G_I = 0$ everywhere. Going to finer meshes helps average G_I , but does not eliminate it.
- Finer meshes (in the refined region length-thickness plane) improve accuracy of average G_{II} significantly. Increase from 30 to 60 elements across width does not help average G_{II} . Thinner delamination does not help average G_{II} .
- Average G_{III} and G differences are small for all meshes.

For local data:

- Percent difference for G_{II} at center point is very large for all runs.
 - o At this location $G_{II} \sim 10^{-6}$, so the large percent differences are in actuality very small differences
 - o Therefore there is no real issue with the center values of G_{II} .
- G_{III} at edges improves with finer meshes, but is still off by around 3% at best
(FineMeshA-150)

- As seen in Figure E.5 through Figure E.8, there is a small discrepancy in the G_{III} distribution (compared to benchmark) at the very edge of the specimen.
 - G_{III} edge values improved between FineMesh-30 and FineMeshA-60. However, FineMeshA-60 and RefinedMesh3X give almost the exact same results. In fact, FineMeshA-60 gives better results, even though RefinedMesh3X is refined over a larger region.
 - This large percent difference is possibly caused by the finite delamination thickness.
 - Will not be a concern during modeling, because echelon cracks will only be modeled in the center of the specimen, where G_{III} is very accurate.
- G_I at edges is non-zero for all meshes
- G_I edge accuracy appears to have plateaued after FineMesh-30, although it is an improvement over the Linear-30 mesh.
 - The non-zero G_I has to do with the finite delamination thickness. Investigation of the nodes just behind the delamination tip shows that there is some closing occurring that is possible because of the finite delamination thickness. This cannot be avoided because the delamination must be modeled with a finite thickness.

E.1.4. Conclusions

Significant improvements in average and local ERRs come with increasing the length-thickness plane refinement in the refined region up to FineMeshA. Increasing the length of the refined region (RefinedMesh3X) did not result in significant improvements in results. Increasing the width-wise element number from 30 to 60 increased the model accuracy, although there was

only small improvement going to 150 elements. This improvement was primarily with respect to the edge value of G_{III} , which is not of high importance for subsequent modeling. Thus, a mesh of FineMeshA-60 (or higher, depending on model requirements as the model becomes more complex) should be used.

E.2. Delamination Model with Diagonal Partition

E.2.1. Model Details

The meshes listed below were created for the delamination model with a diagonal partition. Every mesh created for this section has a 0.0005mm thick delamination and a near-tip refined region that extends 1.5 mm ($t/2$) on either side of the delamination tip. Included echelon cracks were either $t/20$ (given a code of F20), $t/5$ (F5), or $t/10$ (F10) in diameter.

- Mesh of FineMeshA from Section E.1. with 66 elements across the width and 20 elements surrounding a $t/20$ echelon crack. Shown in Figure E.9. (**A66 F20-20**)
- Mesh with a finer refined region length-thickness mesh than FineMeshA (called FineMeshB) with 82 elements across the width and 32 elements around a $t/20$ echelon crack. (**B82 F20-32**)
- Mesh with a finer refined region length-thickness mesh than FineMeshB (called FineMeshC) with 88 elements across the width and 40 elements around a $t/20$ echelon crack. (**C88 F20-40**)
 - o Results almost indistinguishable from B82 F20-32, so not presented.
- Mesh with FineMeshB and 82 elements across the width, and the diagonal partition used with the echelon crack, but no modeled echelon crack. (**B82 DiagOnly**)

- Mesh with FineMeshA, 66 elements across the width, and 60 elements around a $t/5$ echelon crack. (**A66 F5-60**)
- Mesh with FineMeshB, 94 elements across the width, and 60 elements around a $t/5$ echelon crack. Shown in Figure E.10. (**B94 F5-60**)
- Mesh with FineMeshA, 66 elements across the width, and 32 elements around a $t/10$ echelon crack. (**A66 F10-32**)

Dimensions:

- 30mm width, 3mm thickness, 80mm length, 30mm delamination length
- Echelon crack diameters defined as a fraction of model thickness. E.g., $t/20$ refers to 3mm thickness and 0.15 mm echelon crack diameter

Material Properties

- Orthotropic material properties for IM7/8552 given in Table 6.2.

Boundary Conditions:

- Top and bottom (30mmx80mm faces) $U_2 = 0$
- Lower cracked leg (1.5mmx30mm face) $U_1=U_3=0$
- Upper cracked leg (1.5mmx30mm face) $U_1=0, U_3 = -0.1\text{mm}$

Mesh Details:

- Delamination tip elements are 0.031mm long and high, or $t/96$
- 14-24 elements through-thickness in far field, i.e., outside of the refined region

- 66-94 elements through-width across whole specimen, as it is difficult to reproduce 30, 60, 90, etc., elements with the diagonal partition.
- Uncracked region element length (outside of refined region) biased from 0.5mm at the edge of the refined region to 2mm at the far end of the specimen
- Cracked region element length (outside of refined region) biased from 0.5mm at the edge of the refined region to 1.5mm at the far end of the specimen
- Element size in length-thickness plane refined region varies based on whether mesh is FineMeshA, FineMeshB, or FineMeshC. See Figure E.9 and Figure E.10 for qualitative comparison between FineMeshA and FineMeshB.
- Elements surrounding echelon crack are all 0.01 mm in length. This was not studied as a variable.

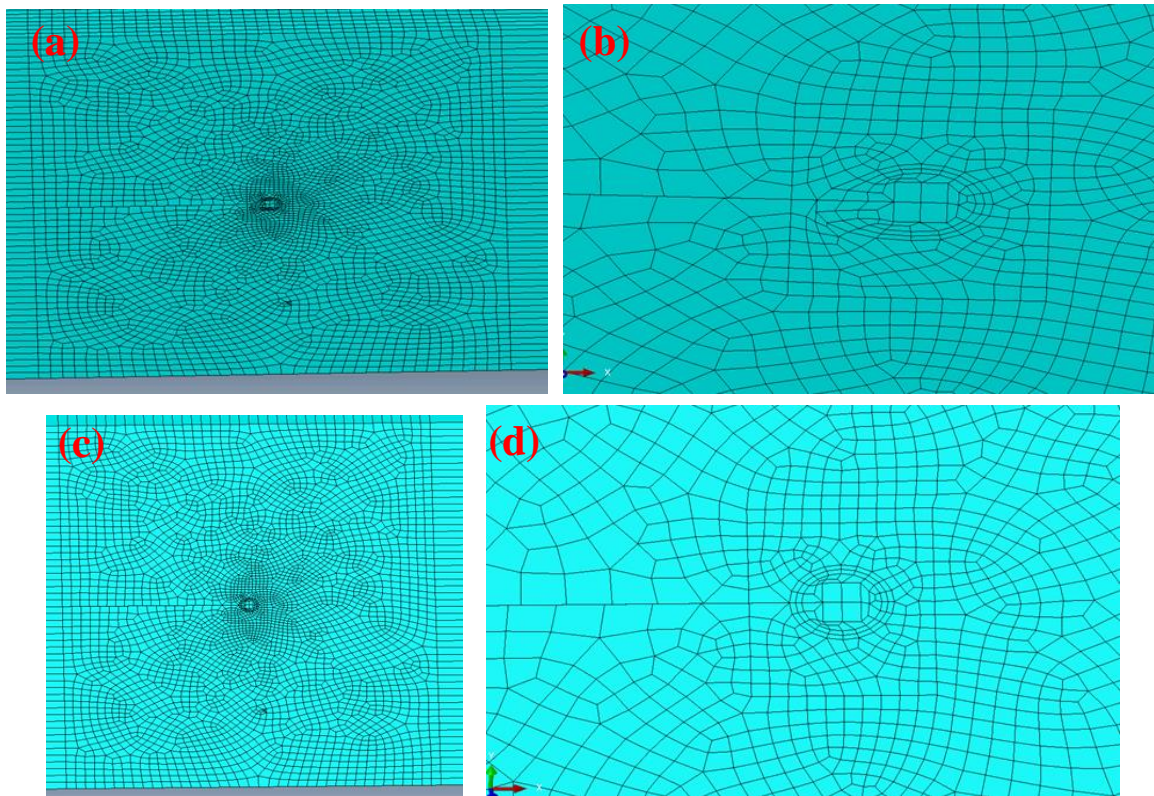


Figure E.9. A66 F20-20 mesh. (a) edge-view of refined region, (b) edge-view of near-tip region, (c) diagonal partition-view of refined regions, (d) diagonal partition-view of near-tip region.

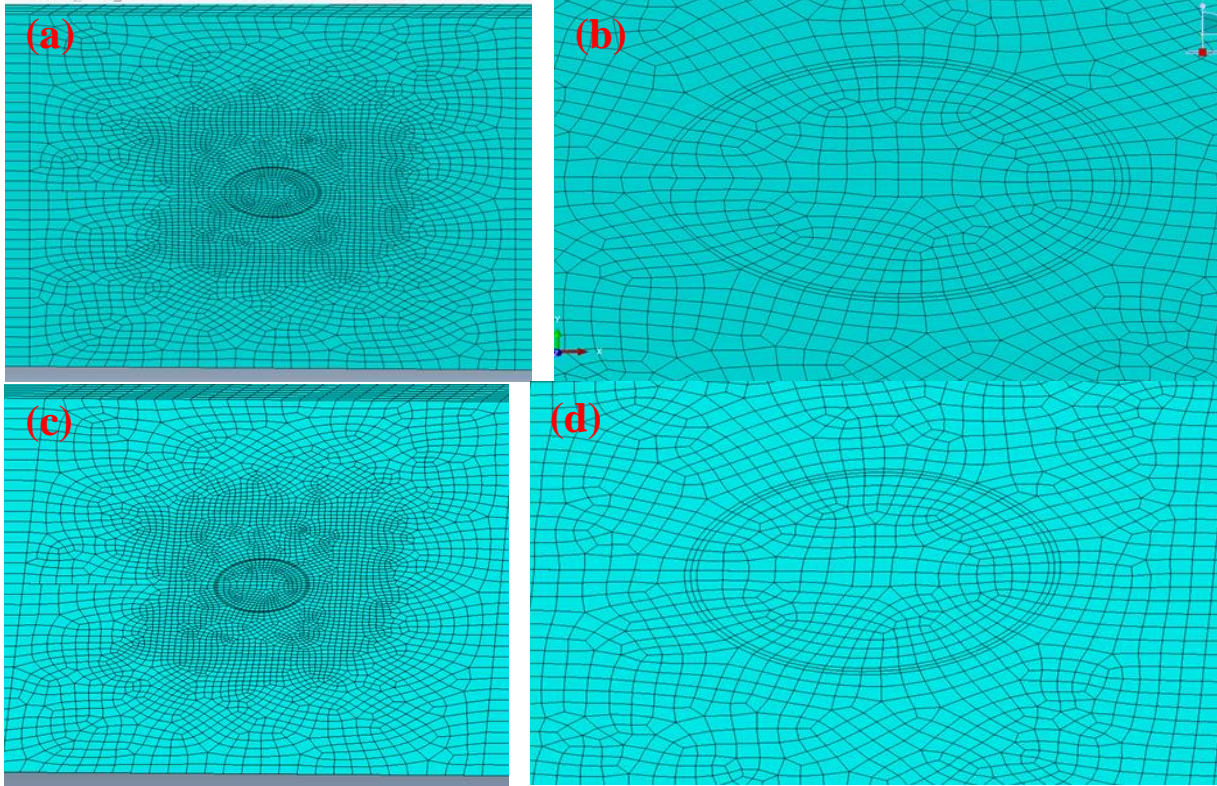


Figure E.10. B94 F5-60 mesh. (a) edge-view of refined region, (b) edge-view of near-tip region, (c) diagonal partition-view of refined regions, (d) diagonal partition-view of near-tip region.

E.2.2. Results

The benchmark results for the STB model are given in Table E.1. These are used with the results from the models generated for this step to determine the percent difference for each mesh. The percent differences are given for G_{II} , G_{III} , and G in Table E.9, where a negative percent difference indicates that the average value for the STB model was larger. The average value of G_I is given since the STB model reports $G_I = 0$, and this results in an infinite percent difference between the two results.

Table E.9. Comparative results between average values of benchmark STB model and experimental models for delamination verification without diagonal partition.

Mesh Code	Mesh Description			Percent Differences in Average ERRs			
	In Refined Region	Width Elements	Echelon Crack Size	G_I (J/m^2)	G_{II} (%)	G_{III} (%)	G (%)
A66 F20-20	FineMeshA	66	t/20	2.281E-5	3.12	0.194	0.522
B82 F20-32	FineMeshB	82	t/20	8.479E-6	1.89	-0.357	-0.105
B82 DiagOnly	FineMeshB	82	--	8.056E-6	0.377	-0.222	-0.155
A66 F5-60	FineMeshA	66	t/5	1.544E-5	-0.338	-0.470	-0.456
B94 F5-60	FineMeshB	94	t/5	4.883E-6	0.303	-0.114	-0.067
A66 F10-32	FineMeshA	66	t/10	1.855E-5	0.369	-0.286	-0.213

Figure E.11 through Figure E.14 present graphical comparisons of a selection of the models run for this step. For these figures, the horizontal axis represents the location along the delamination front in millimeters. The vertical axis is the component of ERR (in J/m^2) for G_I , G_{II} , G_{III} , and G. Note that G_{II} , G_{III} , and G were almost identical for every model considered. For simplicity all the results for these components are shown on combined plots. The G_I results, which show variation between the meshes, are broken out separately.

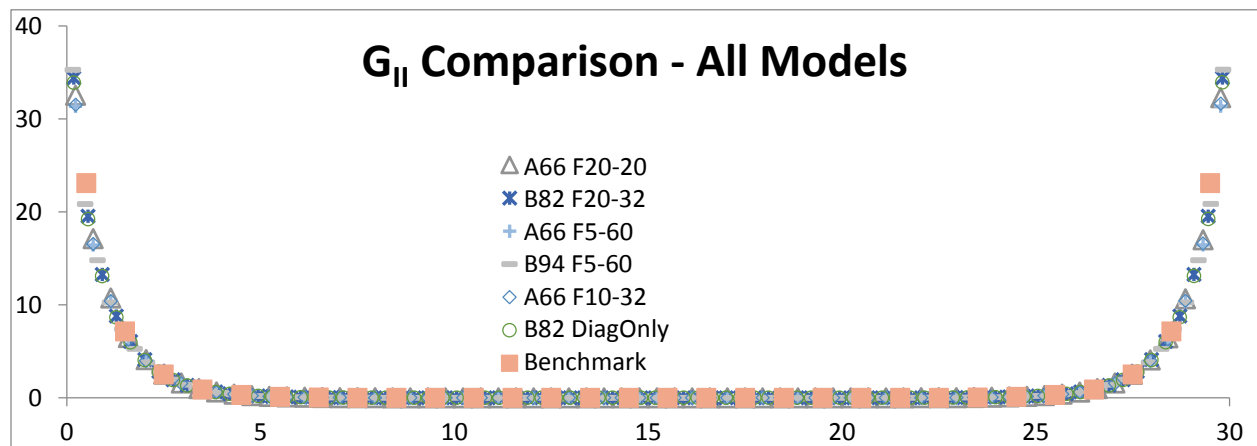


Figure E.11. G_{II} distributions for models with diagonal partitions.

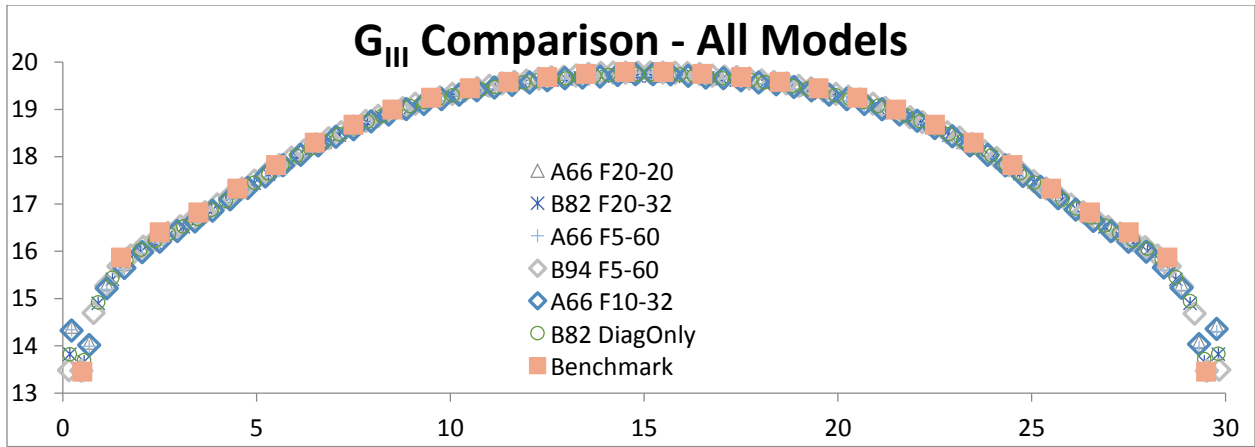


Figure E.12. G_{III} distributions for models with diagonal partitions.

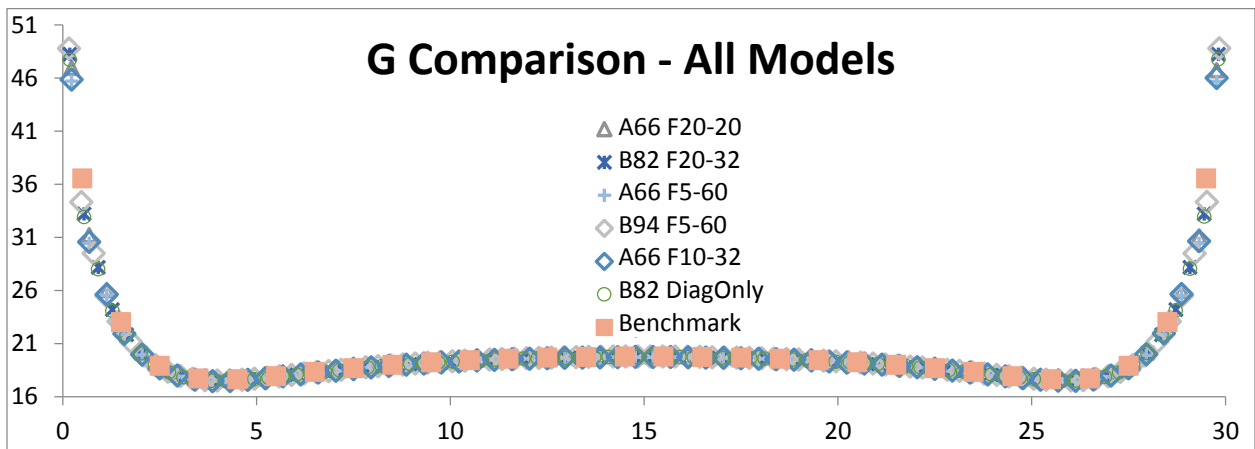


Figure E.13. G distributions for models with diagonal partitions.

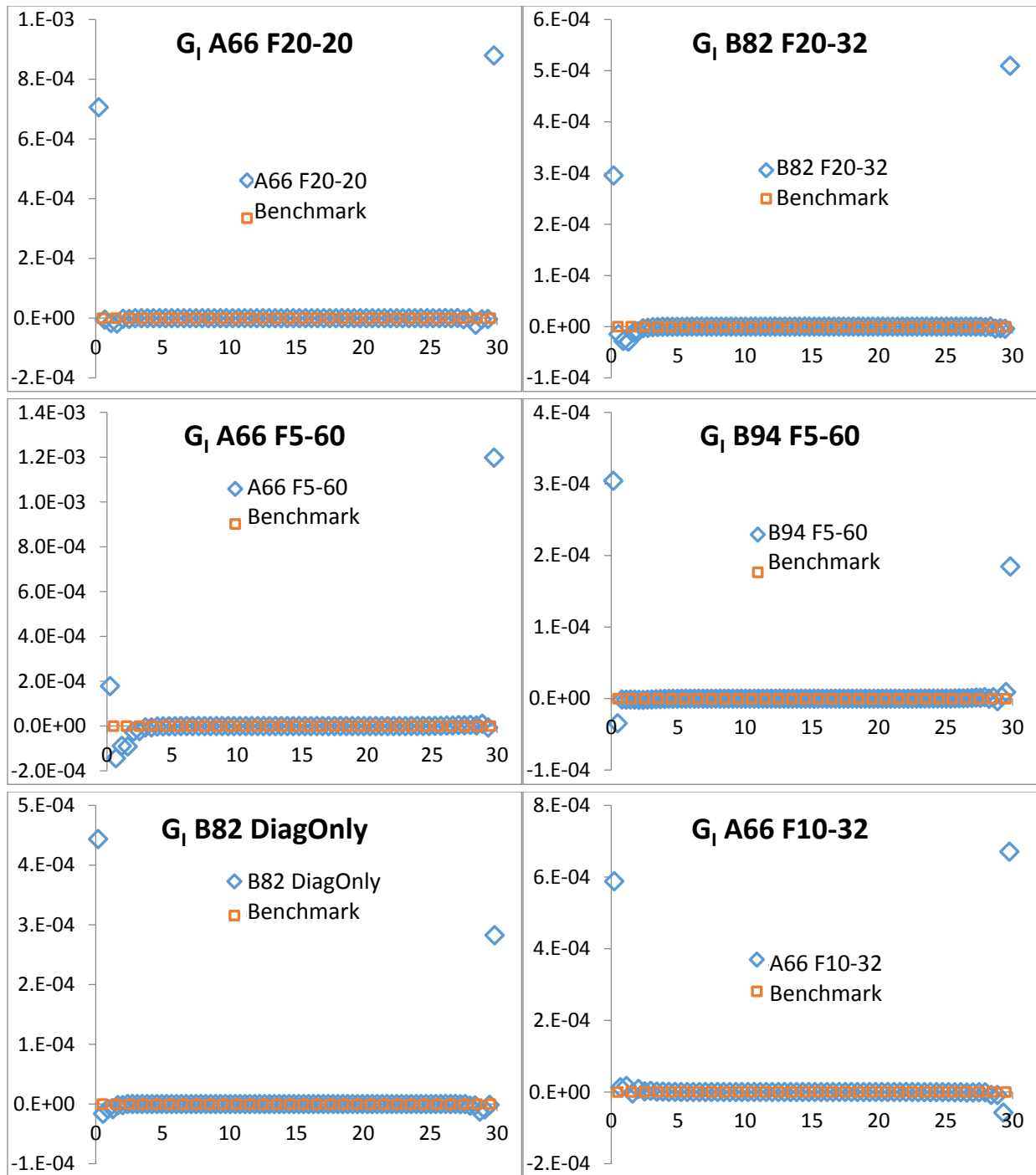


Figure E.14. G_I distributions for models with diagonal partitions.

For a selection of the models run for this step, comparisons are given between the model result at a specific location along the delamination front and the ERRs at that location from the

benchmark model. The benchmark results for the STB model are given in Table E.3. The percent differences are given for the different models in Table E.10 through Table E.13. As before, a negative percent difference indicates that the local value for the STB model was larger. The average value of G_I is given since the STB model reports $G_I = 0$, and this results in an infinite percent difference between the two results. For those models with a different number of elements across the width than the benchmark, linear interpolation was used to obtain the value of ERR at the location of interest.

Table E.10. Values of ERR components at select locations along the delamination front for B82 F20-32, which is a model with FineMeshB in the refined region, 82 elements across the width, and a $t/20$ echelon crack with 32 elements around it.

B82 F20-32	y-location (mm)	G_I (J/m ²)	G_{II} (%)	G_{III} (%)	G (%)
Center Element	14.5	4.24E-10	-66.5	-0.457	-0.457
Edge Element	29.5	6.47E-05	-6.80	1.70	-3.66
Near-Edge Element	28.5	-1.40E-06	-0.141	-1.50	-1.08

Table E.11. Values of ERR components at select locations along the delamination front for B82 DiagOnly, which is a model with FineMeshB in the refined region, 82 elements across the width, and a diagonal partition but no echelon crack.

B82 DiagOnly	y-location (mm)	G_I (J/m ²)	G_{II} (%)	G_{III} (%)	G (%)
Center Element	14.5	-3.03E-11	-70.1	-0.265	-0.265
Edge Element	29.5	3.65E-05	-8.21	2.05	-4.43
Near-Edge Element	28.5	-6.41E-06	-1.56	-1.17	-1.29

Table E.12. Values of ERR components at select locations along the delamination front for A66 F5-60, which is a model with FineMeshA in the refined region, 66 elements across the width, and a $t/5$ echelon crack with 60 elements around it.

A66 F5-60	y-location (mm)	G_I (J/m ²)	G_{II} (%)	G_{III} (%)	G (%)
Center Element	14.5	6.83E-10	-61.1	-0.480	-0.480
Edge Element	29.5	4.76E-04	-2.93	4.793	-0.0867
Near-Edge Element	28.5	4.56E-06	-1.25	-2.31	-1.99

Table E.13. Values of ERR components at select locations along the delamination front for A66 F10-32, which is a model with FineMeshA in the refined region, 66 elements across the width, and a $t/10$ echelon crack with 32 elements around it.

A66 F10-32	y-location (mm)	G_I (J/m ²)	G_{II} (%)	G_{III} (%)	G (%)
Center Element	14.5	6.65E-10	-60.8	-0.291	-0.291
Edge Element	29.5	2.34E-04	-2.08	5.250	0.614
Near-Edge Element	28.5	-8.17E-06	-0.396	-1.88	-1.42

E.2.3. Discussion

For average data:

- G_I is much higher this step here than for the model without diagonal partition in Section E.1. , but is still small compared to G_{II} and G_{III} .
- G_{II} is a little high for A66 F20-20. All other meshes appear reasonable.
 - o Average percent differences between B82 F20-32 and B82 DiagOnly are fairly large considering the distributions in Figure E.11 look identical. However, the differences are small (since average G_{II} is small) and are due to very slight differences in the near-edge and edge values between the two models.
- G_{III} and G quite accurate for all meshes.

For local data:

- Noteworthy that while average data for G_{II} (in Table E.9) generally shows positive percent differences, local data (in Table E.10 through Table E.13) all show negative percent differences.
 - o Average data is strongly affected by edge-most values of G_{II} , since most G_{II} values are close to zero. Experimental models, which have more elements than the

benchmark, have data points closer to the “true edge” located at 30mm, and so the average values of G_{II} are larger for the experimental models.

- Regarding G_{II} , G_{III} and G_I :
 - All meshes resulted in good overall accuracy
 - Some discrepancy in G_{II} and G_{III} at the edges with FineMeshA meshes, but average, center, and near-edge results are all quite accurate..
- Smaller echelon crack size ($t/20$) requires a finer mesh than the larger echelon crack sizes ($t/10$ and $t/5$).
- It was previously hypothesized that the edge issues in G_I has to do with the finite delamination thickness. This was investigated further in this step.
 - Once the echelon crack is added (and, as seen by B82 DiagOnly results, once the diagonal partition is added, even without a echelon crack), the apparent G_I distributions change from those given in Section E1.2.
 - G_I now indicates slight opening at both edges, with apparent closing near-edge on both sides, likely due to the finite delamination thickness.
 - The peak values of G_I are highly dependent on mesh. Finer meshes do help decreasing the edge peaks slightly, but it is unclear how much, if any, further improvement will occur from further mesh refinement.

E.2.4. Conclusions

From the above discussion, it can be seen that a refined region mesh of FineMeshA and 66 elements across the width (A66) is sufficient when the $t/10$ and $t/5$ echelon crack partitions are modeled. For a $t/20$ echelon crack, A66 may be acceptable, but a refined region mesh of

FineMeshB and 82 elements across the width results in better accuracy. For consistency, a mesh of FineMeshB and 82 elements across the width is recommended. It is not clear how effective using between 20 and 60 elements around the echelon crack partition was. A recommendation for this element size will be saved for the next section.

E.3. Echelon Crack Model with Pure Mode I Loading

E.3.1. Model Details

The models run are listed below. Due to the complexity of the models created, a system was developed to describe the different models using a short code. The variables used to generate the code are:

- The echelon crack diameter (e.g., $t/20$ where $t = 3\text{mm}$)
- The number of elements around the echelon crack
- The length of the elements immediately ahead of and behind the echelon crack tip
- The number of circular partitions modeled on each side of the echelon crack tip to control the near-tip element size and shape
- The planar (in the plane of the echelon crack) far-field element size and through thickness (perpendicular to the plane of the crack) element size labeled as nothing, "A," or "B" and quantified in Table E.14.

Models created with a $t/20$ echelon crack:

- 60 elements along the crack front of length 0.1mm and one partitioned circle on either side of the crack front. (**F20-60_D0.1_X1**)

- 60 elements along the crack front of length 0.05mm and one partitioned circle on either side of the crack front. **(F20-60_D0.05_X1)**
- 60 elements along the crack front of length 0.025mm and one partitioned circle on either side of the crack front. **(F20-60_D0.025_X1)**
- 90 elements along the crack front of length 0.05mm and one partitioned circle on either side of the crack front. **(F20-90_D0.05_X1)**
- 60 elements along the crack front of length 0.1mm and three partitioned circles on either side of the crack front. **(F20-60_D0.1_X3)**
- 60 elements along the crack front of length 0.05mm and seven partitioned circles on either side of the crack front. **(F20-60_D0.05_X7)**
- with 60 elements along the crack front of length 0.05mm and fourteen partitioned circles on either side of the crack front. **(F20-60_D0.05_X14)**
- 60 elements along the crack front of length 0.025mm and fourteen partitioned circles on either side of the crack front. **(F20-60_D0.025_X14)**
- 60 elements along the crack front of length 0.01mm and eighteen partitioned circles on either side of the crack front. **(F20-60_D0.01_X18)**
- 60 elements along the crack front of length 0.005mm and eighteen partitioned circles on either side of the crack front. **(F20-60_D0.005_X18)**
- 120 elements along the crack front of length 0.005mm and eighteen partitioned circles on either side of the crack front. **(F20-120_D0.005_X18)**
- 60 elements along the crack front of length 0.01mm and eighteen partitioned circles on either side of the crack front. **(F20-60_D0.01_X18)**

- 60 elements along the crack front of length 0.01mm, five partitioned circles on either side of the crack front, and a finer far-field and through thickness element size labeled “A” (see Table E.14 for values) **(F20-60_D0.01_X5_A)**
- 60 elements along the crack front of length 0.01mm, eighteen partitioned circles on either side of the crack front, and a finer far-field and through thickness element size labeled “A” (see Table E.14 for values) **(F20-60_D0.01_X18_A)**
- 60 elements along the crack front of length 0.01mm, eighteen partitioned circles on either side of the crack front, and very fine far-field and through thickness element sizes labeled “B” (see Table E.14 for values) **(F20-60_D0.01_X18_B)**

Models created with a t/5 echelon crack:

- 60 elements along the crack front of length 0.01mm, five partitioned circles on either side of the crack front, and a finer far-field and through thickness element size labeled “A” (see Table E.14 for values) **(F5-60_D0.01_X5_A)**
- 60 elements along the crack front of length 0.04mm, five partitioned circles on either side of the crack front, and a finer far-field and through thickness element size labeled “A” (see Table E.14 for values) **(F5-60_D0.04_X5_A)**
- 60 elements along the crack front of length 0.04mm, eighteen partitioned circles on either side of the crack front, and a finer far-field and through thickness element size labeled “A” (see Table E.14 for values) **(F5-60_D0.04_X18_A)**

Note: when a large number of faces are partitioned (e.g. X18), they are not all the same distance (e.g., D0.01) away. The distances between further away partitions are larger to create a transition region. This can be seen in the mesh images presented below in Figure E.15 and Figure E.16.

Dimensions:

- 4mm width, 4mm thickness, 4mm length
- $t/20$ and $t/5$ echelon crack diameter (where $t = 3\text{mm}$), with the echelon crack center located 2mm from each edge (center of cube)

Boundary Conditions:

- Top and bottom faces (parallel to echelon crack faces) $U_1 = 0.1\text{mm}$ or 0.001mm

Material Properties:

- Isotropic material properties based on IM7/8552
 - o $E = E_{22} = 11380 \text{ MPa}$, $\nu=0.32$
 - o E' (plane strain) = 12680 MPa

Example Calculations for Analytical Solution (Kassir and Sih, 1975):

For $U_1 = 0.1\text{mm}$, $\varepsilon = 0.025$, $\sigma = 284.5 \text{ MPa}$ (stress by calculation and validated by FEA)

$$K_I = (2/\pi) * \sigma * \sqrt{\pi * a} = 2.78 \text{ MN}\cdot\sqrt{\text{m}}$$

$$G_I = K_I^2/E' = 609.5 \text{ J/m}^2$$

For $U_1 = 0.001\text{mm}$, $\varepsilon = 0.00025$, $\sigma = 2.845 \text{ MPa}$ (stress by calculation and validated by FEA)

$$K_I = (2/\pi) * \sigma * \sqrt{\pi * a} = 27.8 \text{ kN}\cdot\sqrt{\text{m}}$$

$$G_I = K_I^2/E' = 0.06095 \text{ J/m}^2$$

Mesh Details:

- Element length around echelon crack tip 0.1mm to 0.025mm (D0.1 to D0.005)
- 60-120 elements around echelon crack
- 1 to 18 additional circular partitions on either side of echelon crack front
- Far-field planar (non-vertical edge) element size between 0.38mm – 0.10mm
- Far-field through thickness (vertical edge) element size biased smallest towards center with minimum element sizes from 0.01 – 0.10mm and maximum element sizes from 0.08 – 0.20mm

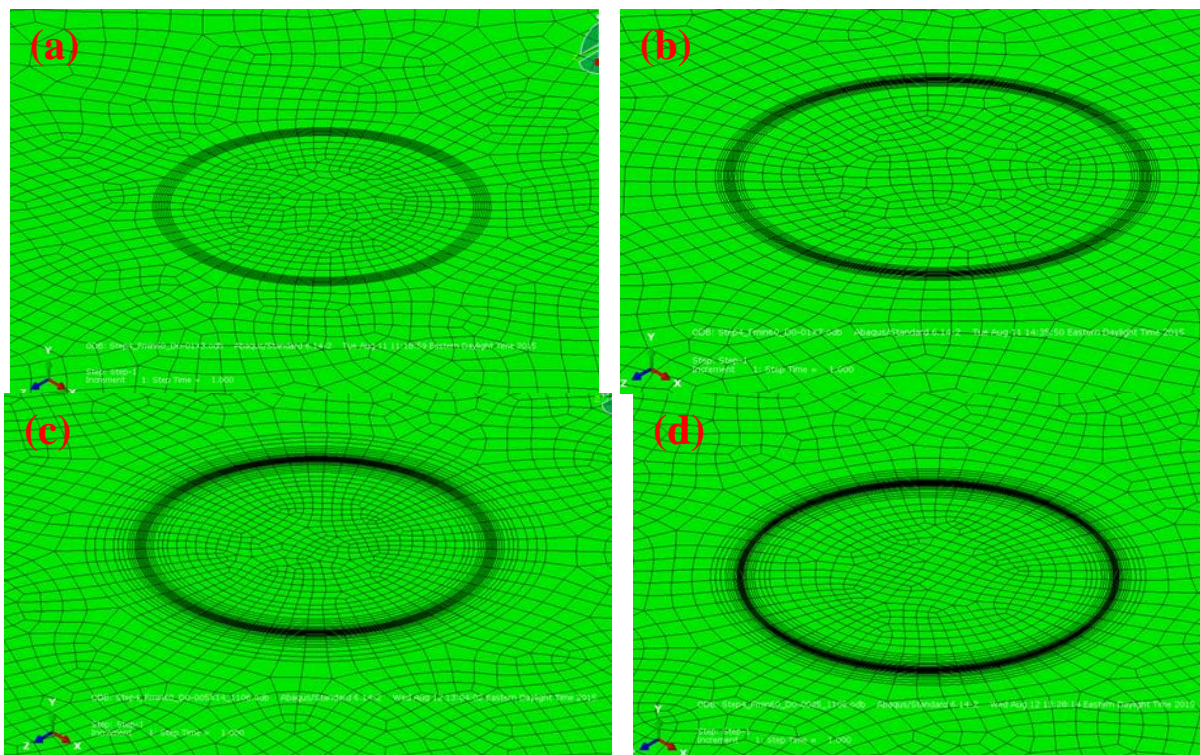


Figure E.15. Echelon crack-view meshes created for mode I loading validation with $t/20$ diameter echelon crack and 60 elements around the crack tip (F20-60). (a) D0.1_X3, (b) D0.05_X7, (c) D0.05_X14, (d) D0.025_X14.

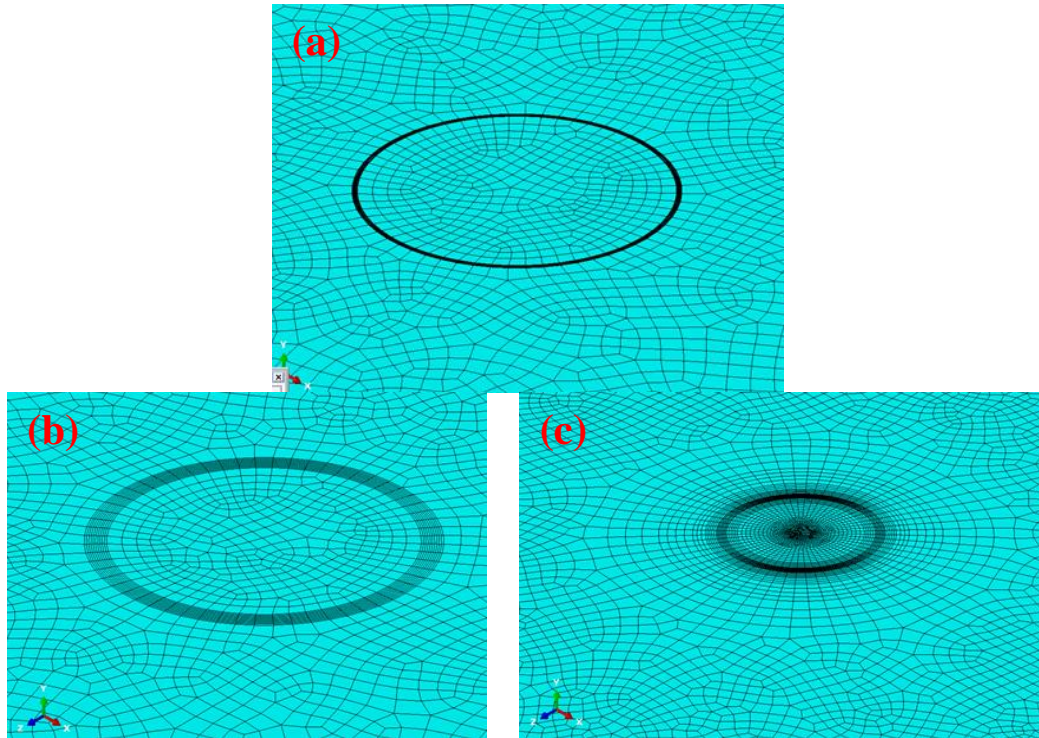


Figure E.16. Echelon crack-view meshes created for mode I loading validation with $t/5$ diameter echelon crack and 60 elements around the crack tip (F5-60). (a) D0.01_X5, (b) D0.04_X5, (c) D0.04_X18.

E.3.2. Results

Example analytical solutions for mode I loading of an embedded echelon crack are given above in Section E.3.1. These are used with the results from the models generated for this step to determine the percent difference for each mesh. The average values of G_I , calculated using every element around the echelon crack front, and percent differences compared to the analytical solution are given in Table E.14. Here, a negative percent difference indicates that the average value for the analytical solution was larger. The coefficient of variation (COV), which is defined as the ratio of the standard deviation to the average value, is also given for each model. The COV gives an idea of the uniformity of the G_I distribution, as for this loading G_I should be uniform

around the entire crack front. Note that a subset of the models run for this step are given in Table E.14 in order focus on the results of interest.

Table E.14. ERR results for echelon crack subjected to mode I loading for different models.

Model	Planar far-field edge element size (mm)	Through thickness min element size (mm)	COV of G_I (%)	G_I (J/m ²)	Percent Difference G_I
F20-60_D0.1_X1	0.080	0.080	0.0452	536.27	-12.03
F20-60_D0.05_X1	0.080	0.080	0.136	502.22	-17.61
F20-60_D0.025_X1	0.080	0.080	0.181	486.03	-20.27
F20-90_D0.05_X1	0.080	0.080	0.017	502.93	-17.50
F20-60_D0.025_X1	0.080	0.080	0.181	0.0486	-20.28
F20-60_D0.01_X18	0.100	0.020	0.00069	0.0577	-5.27
F20-60_D0.005_X18	0.100	0.020	0.0022	0.0575	-5.67
F20-120_D0.005_X18	0.100	0.020	0.00180	0.0575	-5.55
F20-60_D0.01_X5_A	0.050	0.015	0.00019	0.0585	-3.94
F20-60_D0.01_X18_A	0.050	0.015	0.00064	0.0587	-3.69
F20-60_D0.01_X18_B	0.038	0.010	0.00083	0.0591	-2.90
F5-60_D0.01_X5_A	0.050	0.015	1.294	0.2388	-2.05
F5-60_D0.04_X5_A	0.050	0.015	0.2430	0.2415	-0.950
F5-60_D0.04_X18_A	0.050	0.015	~ 0	0.2451	-0.552

E.3.3. Discussion

In order to determine the effect of different variables on the results presented in Table E.14, the model names are color coded. The code is as follows:

- Same mesh for the pair, except for number of elements around echelon crack
- Same mesh, U=0.1mm vs. U=0.001mm
- Same mesh, except for the number of partitioned rings on each side

- **Same mesh, except change in near-tip element length**
 - *Same mesh details, but different echelon crack size.*
 - Same mesh except for planar far-field element size (noted by purple arrows)
- Results appear insensitive to amount of applied strain (blue highlight)
 - Increasing the number of elements around the echelon crack (above 60) does not affect the accuracy of results (green highlights).
 - Simply decreasing the size of the near-tip elements does not improve the accuracy (red text). In all three cases studied, it provided worse results to have a smaller near-tip size.
 - There likely is some critical element size above which the results are worse.
 - As seen with several refinements (improvement in results between some D0.05 and D0.01), there is an effect of the distance over which the element shape is constrained by additional partitions.
 - Adding more near-tip element partitions improves accuracy (yellow highlight).
 - There is interplay between near-tip element size and refined element partitions in order to get the most accurate results.
 - Since the same number of refined element partitions with a smaller near-tip element size will result in an overall smaller partition-refined area.
 - Studies with $t/5$ echelon crack size have much better results than $t/20$ echelon crack size indicating that a coarser mesh may be acceptable for larger echelon cracks (*italic text*).
 - Decreasing the far field element size can notably improve accuracy (purple arrows)

E.3.4. Conclusions

For the model with a crack diameter of $t/20$, the mesh of F20-60_D0.01_X18_B is recommended. That is, 60 elements around the echelon crack front that are 0.01 mm long, 18 circular partitions on either side of the crack front, an in-plane far-field element size of 0.038 mm, and a minimum through-thickness element size of 0.01 mm should be used. For the model with a crack diameter of $t/5$, the mesh of F5-60_D0.04_X18_A is recommended. That is, 60 elements around the echelon crack front that are 0.04 mm long, 18 circular partitions on either side of the crack front, an in-plane far-field element size of 0.050 mm, and a minimum through-thickness element size of 0.015 mm should be used. In this case, two different meshes are recommended for the different geometries, rather than choosing a single mesh as in Section E.2, in order to minimize model size, and therefore computational time, whenever possible.

E.4. Echelon Crack Model with Mixed Mode Loading

E.4.1. Model Details

The models run are listed below. Due to the complexity of the models created, a system was developed to describe the different models using a short code which is almost identical to the code used in Section E.3. The variables used to generate the code are:

- The echelon crack diameter (e.g., $t/20$ where $t = 3\text{mm}$)
- The number of elements around the echelon crack
- The length of the elements immediately ahead of and behind the echelon crack tip
- The number of circular partitions modeled on each side of the echelon crack tip to control the near-tip element size and shape

- The planar (in the plane of the echelon crack) far-field element size and through thickness (perpendicular to the plane of the crack) element size labeled as nothing, “A,” or “B” and quantified in Table E.15.
- The G_I/G mode mix

When a large number of faces are partitioned (e.g. X18), there are not all the same distance (e.g., D0.01) away. The distances between further away faces are larger to create a transition region. This can be seen in the mesh images presented below.

Models created with $t/5$ echelon crack:

- 60 elements along the crack front of length 0.04mm, eighteen partitioned circles on either side of the crack front, far-field element sizes labeled “A” (see Table E.15 for values), and G_I/G of 0.0 (**F5-60_D0.04_X18_A-0.0**)
- 60 elements along the crack front of length 0.04mm, eighteen partitioned circles on either side of the crack front, far-field element sizes labeled “A” (see Table E.15 for values), and G_I/G of approximately 0.5 (**F5-60_D0.04_X18_A-0.5**)

Models created with $t/20$ echelon crack:

- 60 elements along the crack front of length 0.01mm, eighteen partitioned circles on either side of the crack front, far-field element sizes labeled “A” (see Table E.15 for values), and G_I/G of approximately 0.5 (**F20-60_D0.01_X18_A-0.5**)

- 120 elements along the crack front of length 0.01mm, eighteen partitioned circles on either side of the crack front, far-field element sizes labeled “A” (see Table E.15 for values), and G_I/G of approximately 0.5 (F20-120_D0.01_X18_A-0.5)
- 60 elements along the crack front of length 0.01mm, eighteen partitioned circles on either side of the crack front, far-field element sizes labeled “B” (see Table E.15 for values), and G_I/G of approximately 0.5 (F20-60_D0.01_X18_B-0.5)
- 60 elements along the crack front of length 0.01mm, eighteen partitioned circles on either side of the crack front, far-field element sizes labeled “A” (see Table E.15 for values), and G_I/G of approximately 0.9 (F20-60_D0.01_X18_A-0.5)
- 60 elements along the crack front of length 0.01mm, eighteen partitioned circles on either side of the crack front, far-field element sizes labeled “B” (see Table E.15 for values), and G_I/G of approximately 0.9 (F20-60_D0.01_X18_B-0.9)

Dimensions:

- 4mm width, 4mm thickness, 4mm length, $t/20$ and $t/5$ echelon crack diameters
- Echelon crack center located 2mm from each edge (center of cube)

Boundary Conditions:

- Normal tractions on top and bottom faces $S_1 = 1$ MPa for $G_I/G \sim 0.5$ and $S_1 = 3.9$ MPa for $G_I/G \sim 0.93$
- Shear tractions of $S_{12} = S_{21} = 1$ MPa on top and bottom faces, and on two side faces necessary for equilibrium.
- Mid-plane corner point at (2mm, 0 mm, 2mm) pinned $U_1=U_2=U_3=0$

Note that the first attempt at boundary conditions was to apply mode I and mode II/III loads by displacement boundary conditions, as was primarily used in Section E.3. However, the resultant stress field was non-uniform. Thus, this section used traction boundary conditions, which did result in a uniform stress field.

Material Properties:

- Isotropic material properties based on IM7/8552
 - o $E = E_{22} = 11380 \text{ MPa}$, $\nu=0.32$, and $G = 4311 \text{ MPa}$ based on isotropy
 - o E' (plane strain) = 12680 MPa

Example Calculations for Analytical Solution (Kassir and Sih, 1975):

For $\sigma = 1 \text{ MPa}$, $\tau = 1 \text{ MPa}$, and $a = 0.3\text{mm}$ ($t/5$ echelon crack diameter)

$$K_I = 2/\pi * \sigma * \text{sqrt}(\pi*a) = 19544 \text{ N-sqrt(m)}$$

$$G_I = K_I^2/E' = 0.03013 \text{ J/m}^2$$

$$K_{II} = 4/\pi/(2-\nu)*\tau*\text{sqrt}(\pi*a)*\cos(\phi) = 23267 * \cos(\phi) \text{ N-sqrt(m)}$$

$$G_{II} = K_{II}^2/E' = 0.0427*\cos^2(\phi) \text{ J/m}^2$$

$$K_{III} = 4*(1-\nu)/\pi/(2-\nu)*\tau*\text{sqrt}(\pi*a)*\sin(\phi) = 15821*\sin(\phi) \text{ N-sqrt(m)}$$

$$G_{III} = K_{III}^2/2/G = 0.029*\sin^2(\phi) \text{ J/m}^2$$

Mesh Details:

- Element length surrounding tip: 0.01mm for $t/20$ crack and 0.04 mm for $t/5$ crack
- 60-120 elements around echelon crack

- 18 additional circular partitions on either side of echelon crack front
- Far-field planar (non-vertical edge) element size between 0.38mm – 0.50mm
- Far-field through thickness (vertical edge) element size biased smallest towards center with minimum element sizes from 0.01 – 0.15mm and maximum element sizes from 0.10 – 0.20mm

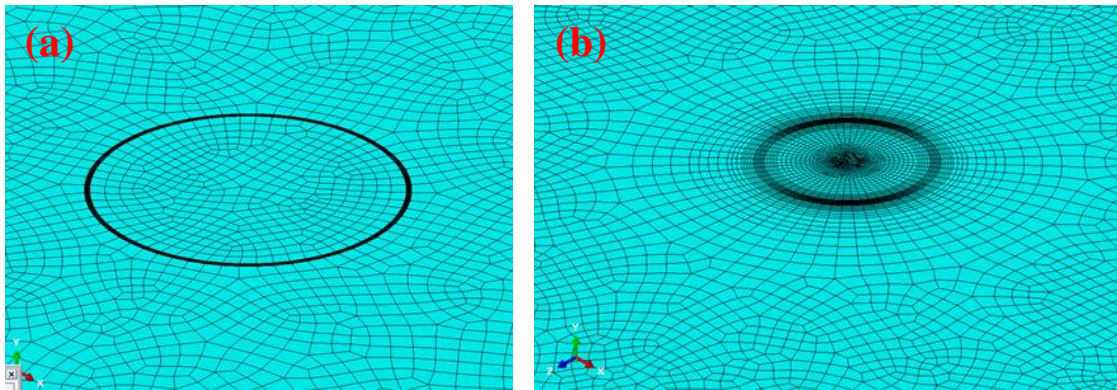


Figure E.17. Echelon crack-view meshes created for mixed mode loading validation with $t/5$ diameter echelon crack and 60 elements around the crack tip (F5-60). (a) D0.01_X5, (b) D0.04_X18.

E.4.2. Results

Graphical results for cases with different meshes, and different mode mixities, are given in Figure E.18 through Figure E.20. These results are presented as polar plots where the circumferential numbers are the angular position around the crack and the radial numbers are the values of the ERR components. In all figures the solid lines represent the analytical solution and the symbols represent the model results.

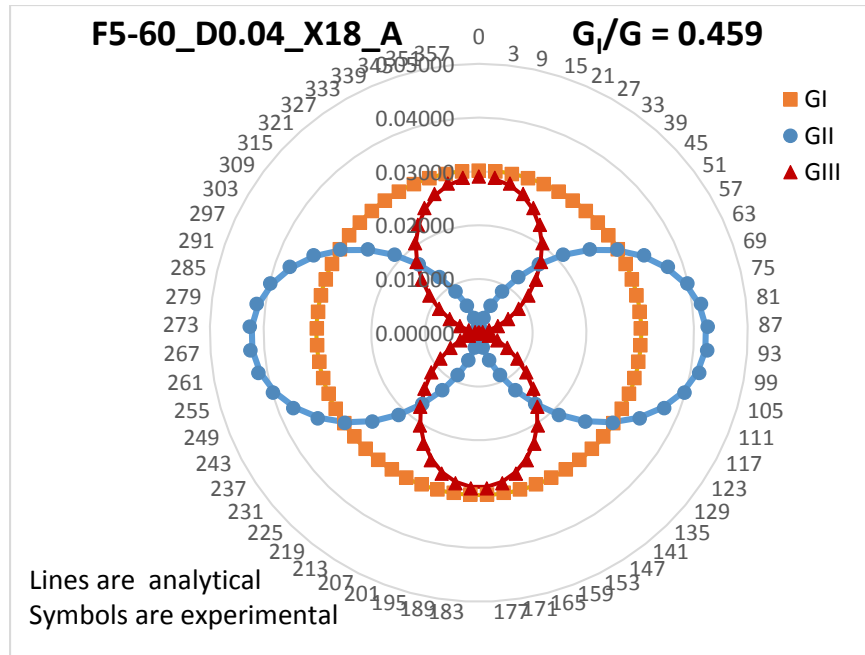


Figure E.18. ERR distributions for mixed mode loading of embedded echelon crack model F5-60_D0.04_X18_A-0.5.

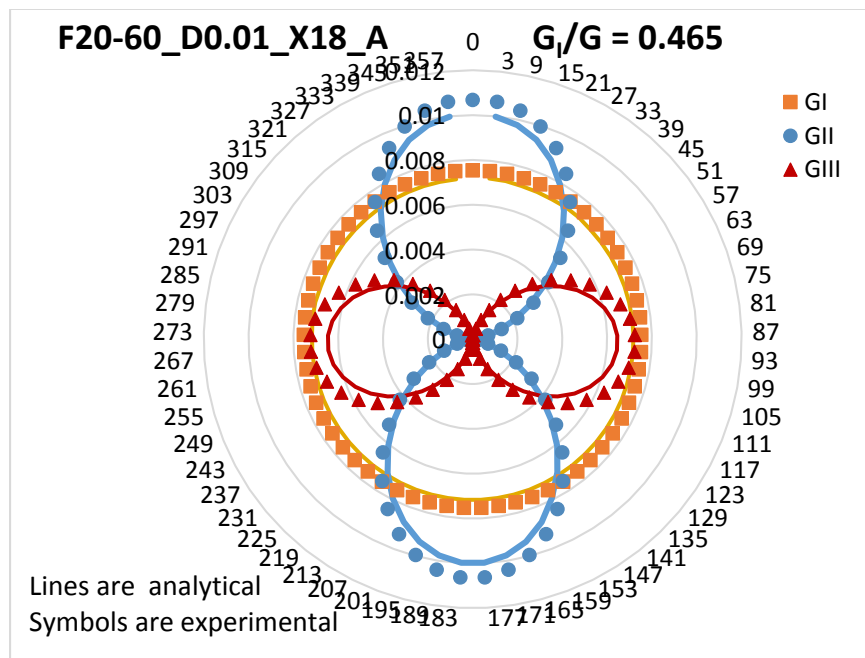


Figure E.19. ERR distributions for mixed mode loading of embedded echelon crack model F20-60_D0.01_X18_A-0.5.

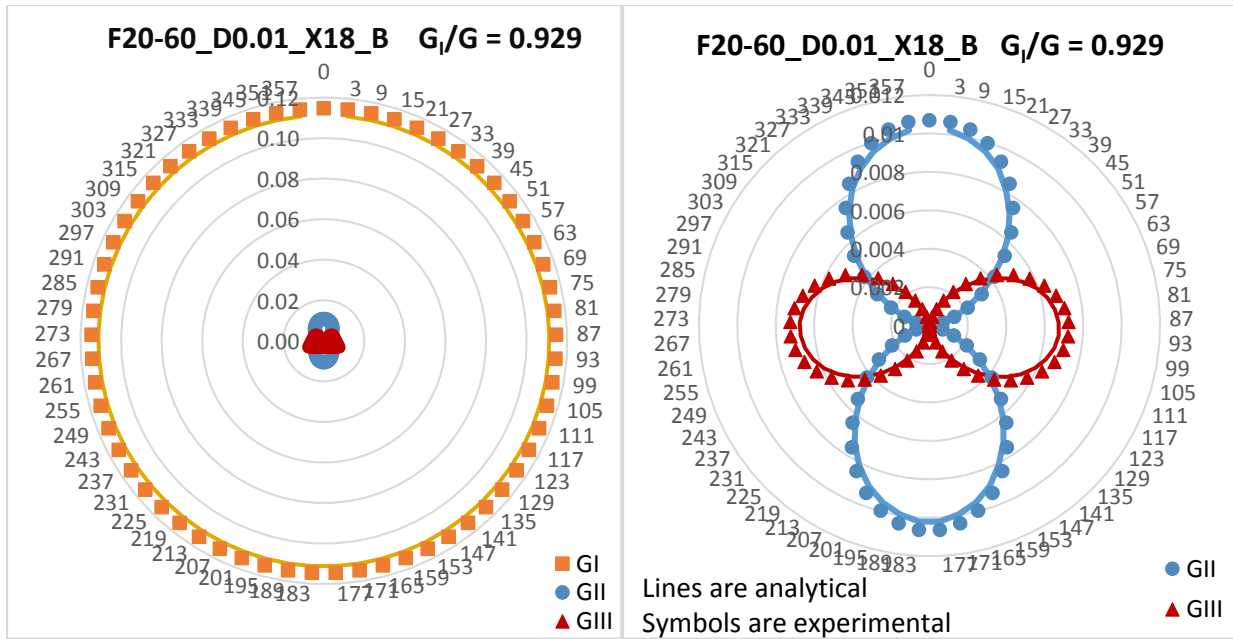


Figure E.20. ERR distributions for mixed mode loading of embedded echelon crack model F20-60_D0.01_X18B. (left) G_I , G_{II} , and G_{III} . (right) G_{II} and G_{III} .

Example analytical solutions for mode I loading of an embedded echelon crack are given above in Section E.4.1. These are used with the results from the models generated for this step to determine the percent difference for each mesh. The percent differences between the ERR components determined experimentally and the analytical solutions are given in Table E.15. The results given are an average percent difference across the entire front. Because of this averaging, it is not possible to use a sign to indicate whether the analytical solution or experimental results were larger or smaller, and so all percent differences are given as positive values.

Table E.15. ERR results for echelon crack subjected to mixed mode I-II/III loading for different models.

Model	Planar far-field edge element size (mm)	Through thickness min element size (mm)	G_I/G	G_I (%)	G_{II} (%)	G_{III} (%)	G (%)
F5-60_D0.01_X5_A	0.050	0.015	1.0	2.05	--	--	2.05
F5-60_D0.04_X18_A-0.0	0.050	0.015	0.0	--	1.40	1.62	0.60
F5-60_D0.04_X18_A-0.5	0.050	0.015	0.459	0.339	1.41	1.64	0.19
F20-60_D0.01_X18_A-0.5	0.050	0.015	0.465	4.71	5.59	9.59	6.45
F20-120_D0.01_X18_A-0.5	0.050	0.015	0.466	5.13	5.96	10.90	7.07
F20-60_D0.01_X18_B-0.5	0.038	0.010	0.462	2.86	3.85	6.26	4.04
F20-60_D0.01_X18_A-0.9	0.050	0.015	0.929	4.72	5.79	9.57	4.95
F20-60_D0.01_X18_B-0.9	0.038	0.010	0.929	2.94	3.91	6.25	3.09

E.4.3. Discussion

- All models show that results are best at non-peak locations (i.e. results are poorest at 0° and 180° for G_{II} and at 90° and 270° for G_{III}). Reason is unclear.
- For $t/5$ models mode I, mode II/III, and mixed mode $G_I/G \sim 0.5$
 - o Errors are very small for all three mode mixities.
 - o Error for pure mode I model here (applied using tractions) is more accurate than same model/mesh using displacement loading (from pure mode I loading in Section E.3)
- For $t/20$ models with $G_I/G \sim 0.5$
 - o Significantly more error than the F5 models, even though both near-field and far-field meshes were identical or finer than the F5 models

- Increasing near-field refinement (from 60 to 120) made results worse (echoed results from pure mode I loading in Section E.3.3, which showed refinement above 60 elements did not improve accuracy)
- Increasing far-field refinement (from mesh A to B) reduced errors. It is expected that further refinement would result in further improvements, but this results in a very large model that takes a lot of computational time to run.
 - Combined model with only echelon crack will be used to double check this.
- For t/20 model comparing $G_I/G \sim 0.5$ to $G_I/G \sim 0.9$
 - For both cases (mesh A and B) the results are almost exactly the same between the two different mode mixities.
 - Indicates that mesh refinement needs are independent of mode mixity, and so unknown/changing mode mixity in actual model should be no issue as long as the mesh is known to work for at least one mode mixity

E.4.4. Conclusions

The above indicate that the same mesh recommendations from Section E.3 are acceptable here. That is, F20-60_D0.01_X18_B for a t/20 echelon crack and F5-60_D0.04_X18_A for a t/5 echelon crack. Further, the results indicate that a variety of mixed mode loadings are well handled in the current model, and the models will not need to be re-validated once the echelon crack loading (in Chapter 8) is known.

E.5. Combined Model with Only Echelon Crack

E.5.1. Model Details

The models run are listed below. Due to the complexity of the models created, a system was developed to describe the different models using a short code which is a modification of the code used in Section E.3 and Section E.4. The variables used to generate the code are:

- The echelon crack diameter (e.g., $t/20$ where $t = 3\text{mm}$)
- The number of elements inside the $t/96$ delamination tip partition used to make the tip element size smaller than possible with partitioning. For the echelon crack oriented at 45° , the delamination tip partition is a rectangle (edge-view of partition is a square and is projected on a 45° face).
- The through-width element size biased small near the echelon crack plane and large at the specimen edges.
- The planar (in the plane of the echelon crack) far-field element size defined for a square partition known as the “Level 2 Refinement” partition which is labeled in Figure E.21 and visible in Figure E.22b and Figure E.22d.
- The echelon crack orientation, which defines the mode mix.

Note that, based on the work in Section E.3 and Section E.4, some variables in these sections are no longer used:

- The number of element around the echelon crack front is always 60.
- The length of the elements surrounding the echelon crack front is always 0.001mm for the $t/20$ echelon crack and 0.004mm for the $t/5$ echelon crack.

- There are 18 circular partitions modeled outside the echelon crack tip and 10 inside the echelon crack tip to control the near-tip element size. As before, these partitions are not all the same distance away. The distances between further away partitions are larger to create a transition region. This can be seen in the mesh image presented in Figure E.22c. Ten circular partitions were used inside the echelon crack tip due to the proximity of the square delamination tip partition.

Models created with $t/20$ echelon crack:

- Delamination tip partition with 6 elements on each edge, width wise refinement biased from 0.03-0.5mm, Level 2 element length of 0.04mm, and a 90° echelon crack (**F20-CT6_W03-5_L04_90**)
- Delamination tip partition with 6 elements on each edge, width wise refinement biased from 0.02-0.6mm, Level 2 element length of 0.03mm, and a 90° echelon crack (**F20-CT6_W02-6_L03_90**)
- Delamination tip partition with 6 elements on each edge, width wise refinement biased from 0.012-0.6mm, Level 2 element length of 0.04mm, and a 90° echelon crack (**F20-CT6_W012-6_L04_90**)
- Delamination tip partition with 6 elements on each edge, width wise refinement biased from 0.012-0.6mm, Level 2 element length of 0.04mm, and a 45° echelon crack (**F20-CT6_W012-6_L04_45**)
- Delamination tip partition with 9 elements on each edge, width wise refinement biased from 0.01-0.6mm, Level 2 element length of 0.034mm, and a 45° echelon crack (**F20-CT9_W01-6_L034_45**)

Models created with t/5 echelon crack:

- Delamination tip partition with 4 elements on each edge, width wise refinement biased from 0.03-0.5mm, Level 2 element length of 0.08mm, and a 90° echelon crack (**F5-CT4_W03-5_L08_90**)
- Delamination tip partition with 6 elements on each edge, width wise refinement biased from 0.03-0.6mm, Level 2 element length of 0.08mm, and a 45° echelon crack (**F5-CT6_W03-6_L08_45**)
- Delamination tip partition with 6 elements on each edge, width wise refinement biased from 0.012-0.6mm, Level 2 element length of 0.08mm, and a 45° echelon crack (**F5-CT6_W012-6_L08_45**)

Dimensions:

- 30mm width, 3mm thickness, 80mm length, t/20 and t/5 echelon crack diameter
- Echelon crack center located 30mm in length direction and in center of width and thickness such that, if there was a delamination tip, it would be centered on the tip in the middle of the specimen's width.

Boundary Conditions:

- Side (3mmx80mm) faces: $S_1 = 1$ MPa (normal tractions)
- Mid-plane corner point at (-40mm, 0 mm, 0mm) pinned $U_1=U_2=U_3=0$
- Resultant stresses on echelon crack:
 - o 90° echelon crack is 1 MPa tension only
 - o 45° echelon crack is 0.5 MPa tension and 0.5 MPa shear

Material Properties:

- Isotropic material properties based on IM7/8552
 - o $E = E_{22} = 11380 \text{ MPa}$, $\nu=0.32$, $G = 4311 \text{ MPa}$
 - o E' (plane strain) = 12680 MPa

Example Calculations for Analytical Solution (Kassir and Sih, 1975):

For 90° echelon crack of $t/5$ diameter: $\sigma = 1 \text{ MPa}$ and $a = 0.3\text{mm}$

$$K_I = 2/\pi * \sigma * \sqrt{\pi*a} = 19544 \text{ N}\cdot\sqrt{\text{m}}$$

$$G_I = K_I^2/E' = 0.03013 \text{ J/m}^2$$

$$K_{II} = K_{III} = G_{II} = G_{III} = 0$$

For 45° echelon crack of diameter $t/5$, $\sigma = 0.5 \text{ MPa}$, $\tau = 0.5 \text{ MPa}$, and $a = 0.3\text{mm}$

$$K_I = 2/\pi * \sigma * \sqrt{\pi*a} = 9772 \text{ N}\cdot\sqrt{\text{m}}$$

$$G_I = K_I^2/E' = 0.00753 \text{ J/m}^2$$

$$K_{II} = 4/\pi/(2-\nu)*\tau*\sqrt{\pi*a}*\cos(\phi) = 11633 * \cos(\phi) \text{ N}\cdot\sqrt{\text{m}}$$

$$G_{II} = K_{II}^2/E' = 0.01067*\cos^2(\phi) \text{ J/m}^2$$

$$K_{III} = 4*(1-\nu)/\pi/(2-\nu)*\tau*\sqrt{\pi*a}*\sin(\phi) = 7911*\sin(\phi) \text{ N}\cdot\sqrt{\text{m}}$$

$$G_{III} = K_{III}^2/2G = 0.007259*\sin^2(\phi) \text{ J/m}^2$$

Mesh Details:

See Figure E.21 for labels identifying different parts of the model

- Bonded region far-field element size: single biased 0.22mm near Level 1 region and 4.0mm at far end of specimen
- Unbonded region far-field: single biased 0.22mm near Level 1 region and 3.0mm at far end of specimen
- Level 1 refined regions horizontal element size: 0.20mm
- Level 1 refined regions vertical element size: 0.22mm
- Level 2 refined region all 4 edges element size: 0.03-0.08mm
- Delamination tip partition: 4-9 elements per edge
- 60 elements surrounding echelon crack
- Element length immediately around the echelon crack is 0.001mm for t/20 crack and 0.004mm for t/5 crack.
- Width-wise refinement: biased at echelon crack with minimum 0.01– 0.03mm to maximum at specimen edges of 0.5 – 0.6mm

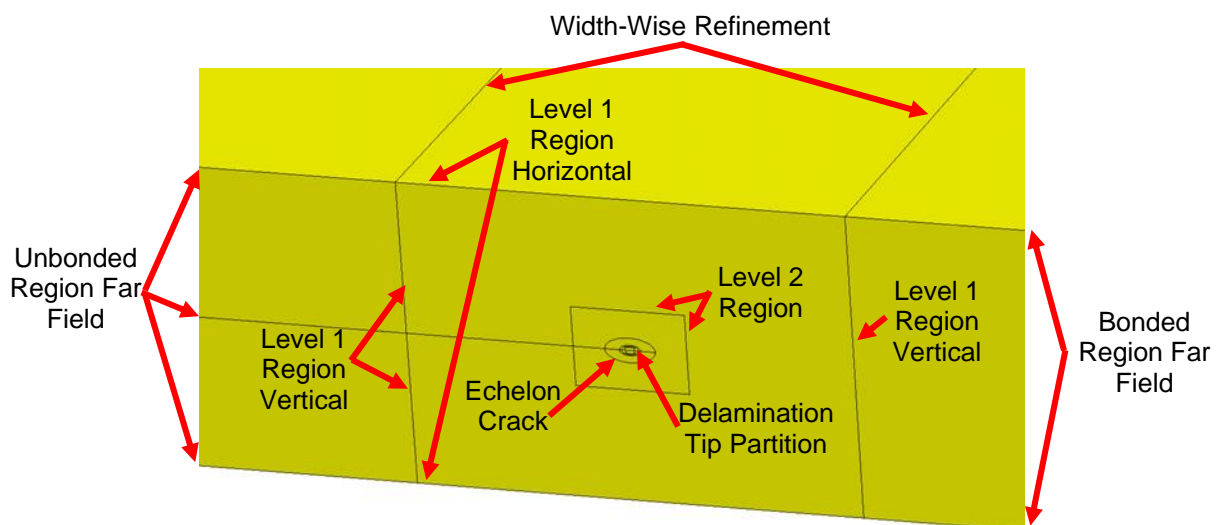


Figure E.21. Description of edges used to define meshing.

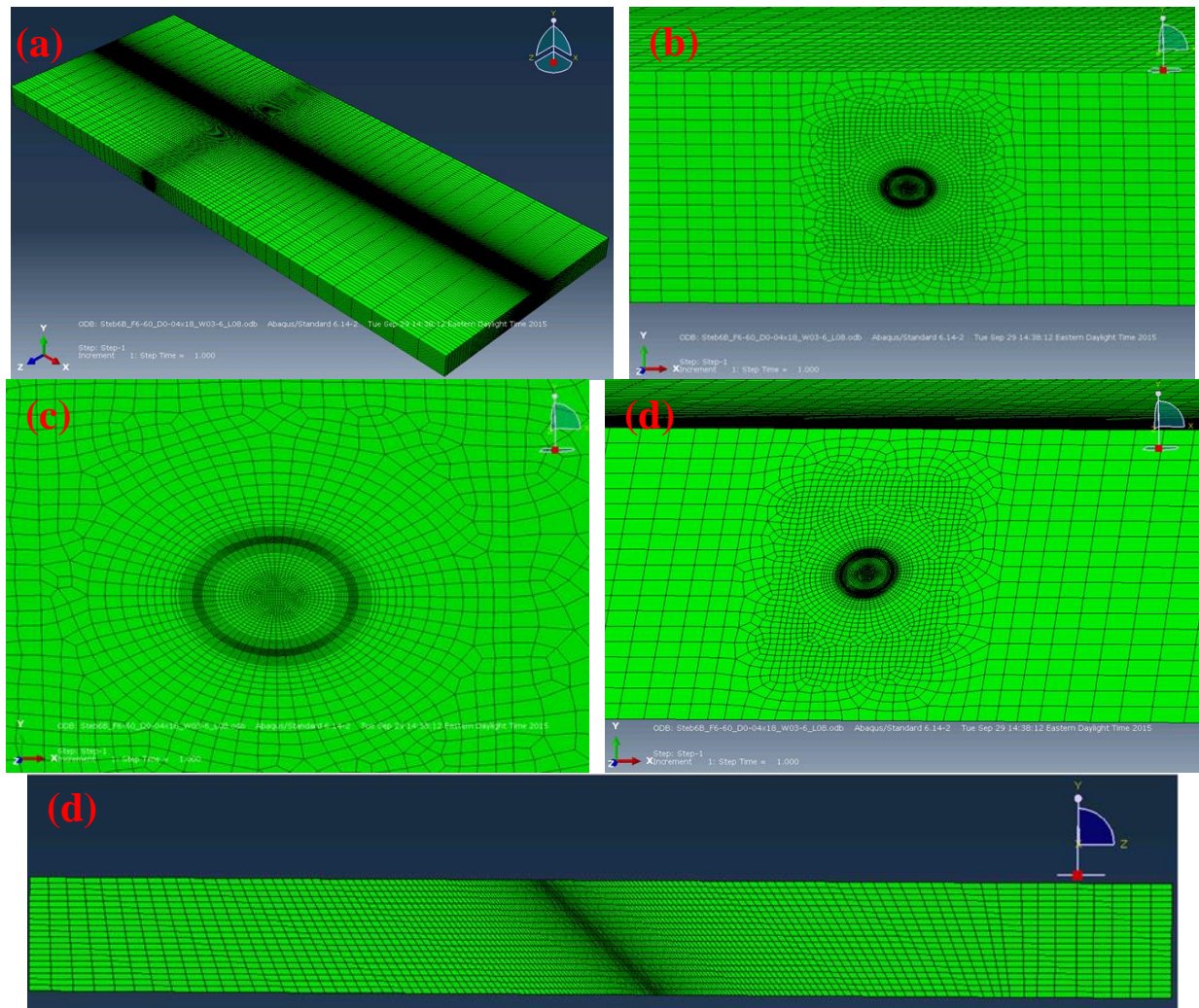


Figure E.22. Views of mesh for $t/5$ echelon crack oriented at 45° with code F5_CT6_W03-6_L08_45. (a) full view of model, (b) edge-view of refined region, (c) edge-view of near-tip region, (d) diagonal partition-view of echelon crack, (e) width-wise refinement view.

E.5.2. Results

Graphical results for cases with different meshes, and different mode mixities, are given in Figure E.23 through Figure E.25. These results are presented as polar plots where the circumferential numbers are the angular position around the crack and the radial numbers are the values of the ERR components.

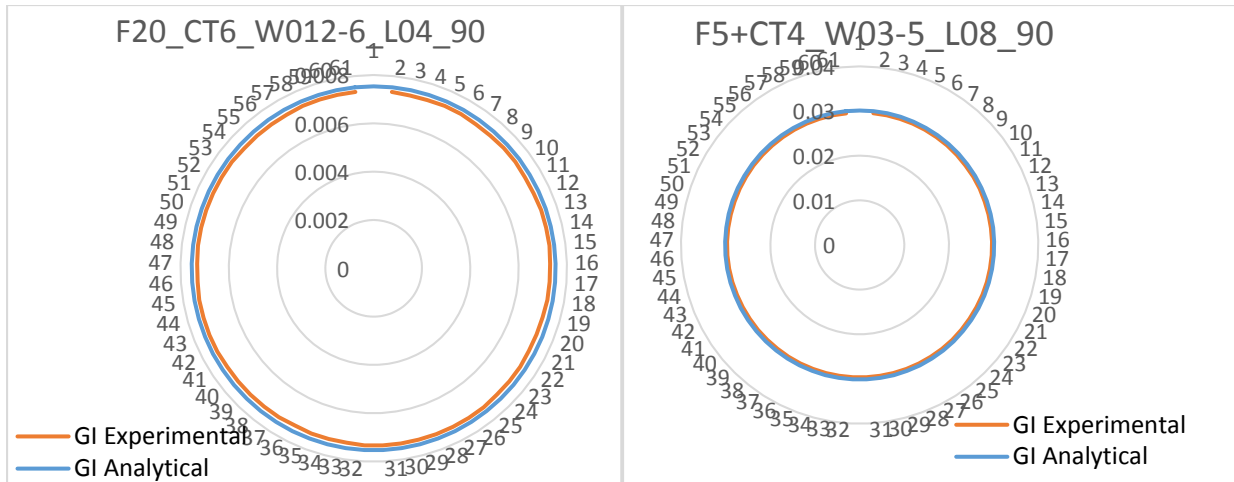


Figure E.23. Mode I ERR distributions for echelon cracks oriented at 90° (left) t/20 crack F20_CT6_W012-6_L04_90, (right) t/5 crack F5_CT4_W03-5_L08_90.

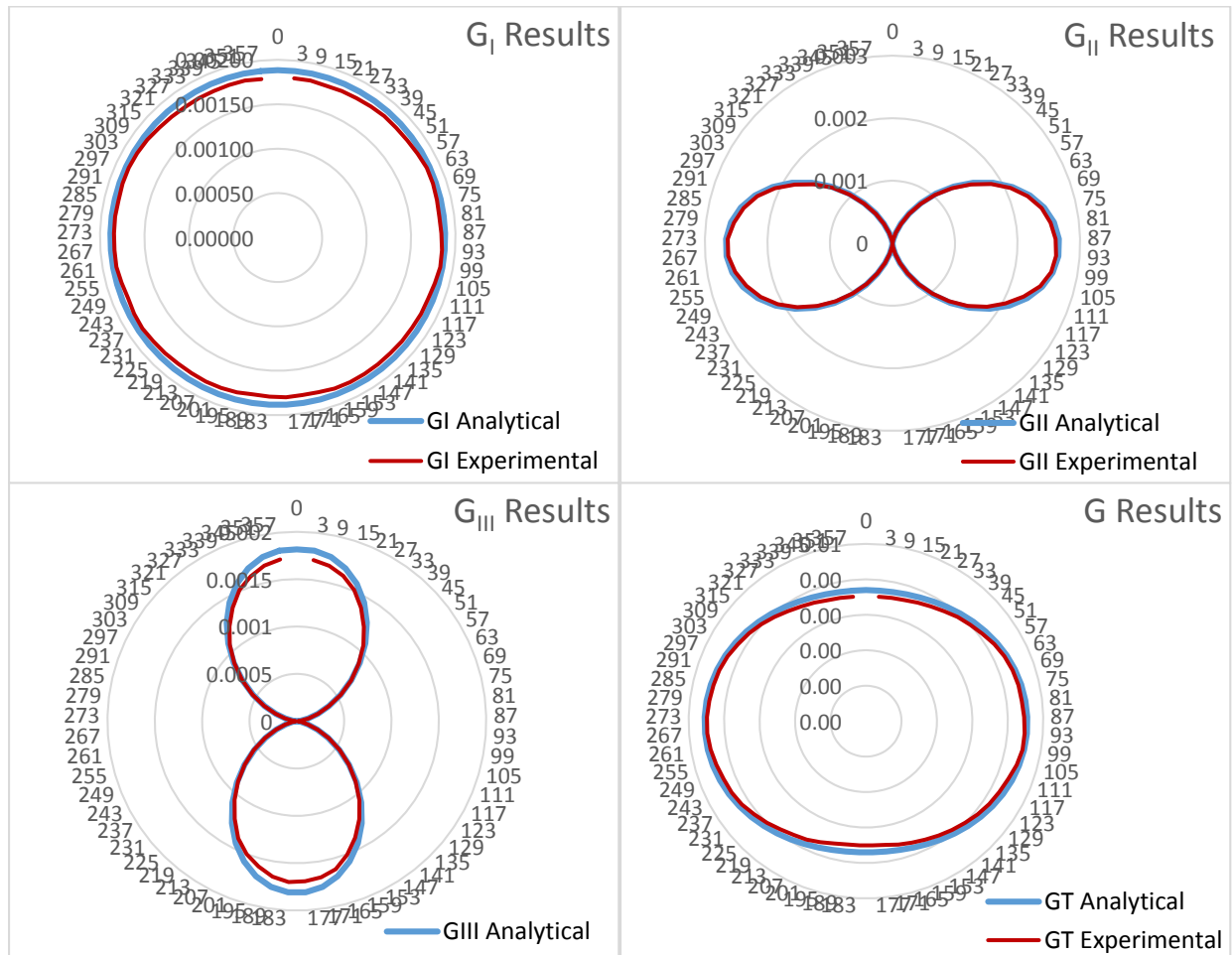


Figure E.24. ERR distributions for t/20 echelon crack oriented at 45° with code F20_CT6_W012-6_L04_45.

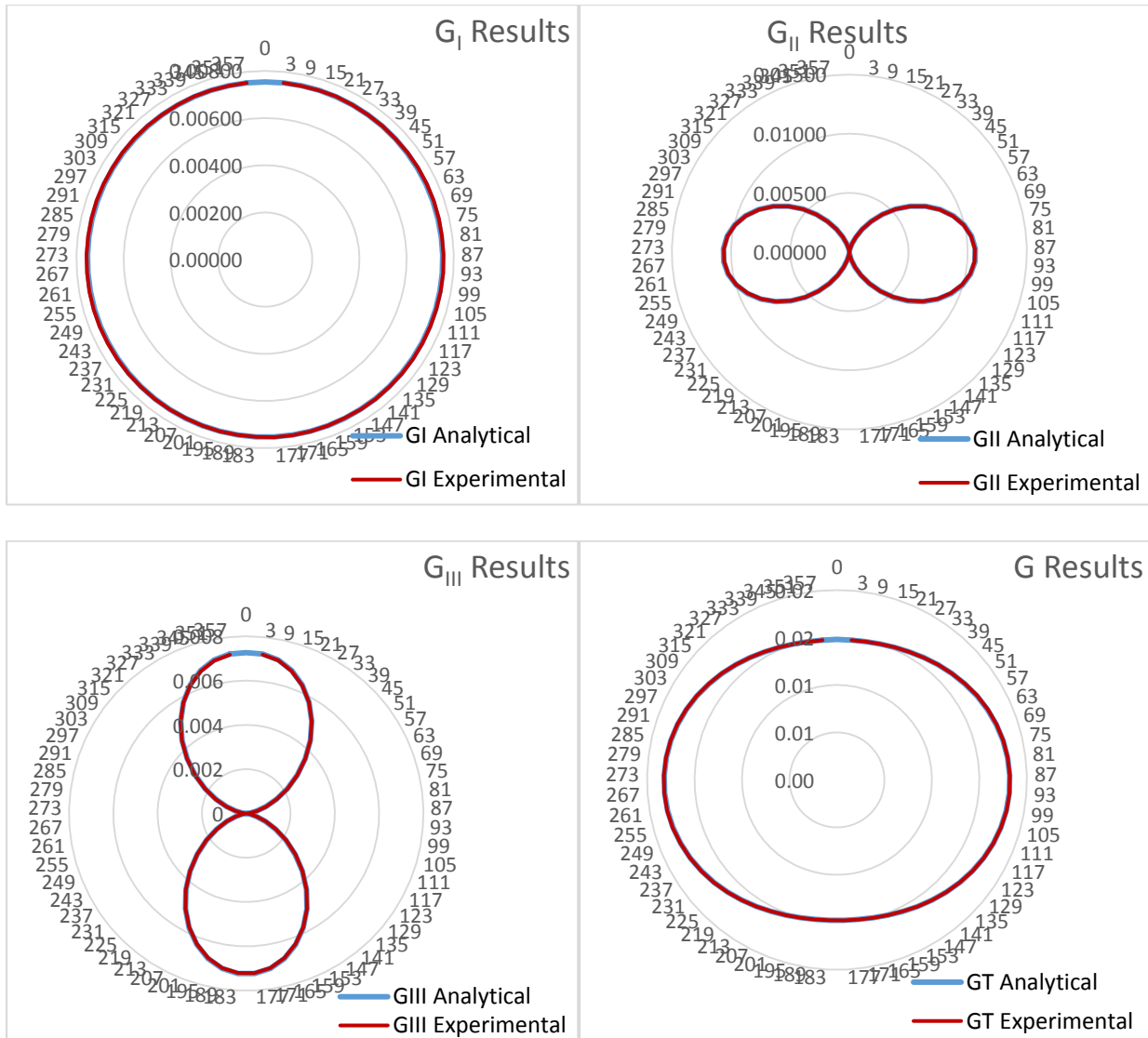


Figure E.25. ERR distributions for $t/5$ echelon crack oriented at 45° with code F5_CT6_W012-6_L08_45.

Example analytical solutions for mode I loading of an embedded echelon crack are given above in Section E.5.1. These are used with the results from the models generated for this step to determine the percent difference for each mesh. The percent differences between the ERR components determined experimentally and the analytical solutions are given in Table E.16. The results given are an average percent difference across the entire front. Because of this averaging,

it is not possible to use a sign to indicate whether the analytical solution or experimental results were larger or smaller, and so all percent differences are given as positive values.

Table E.16. ERR results for combined model with $t/20$ and $t/5$ echelon cracks at 45° and 90° .

Model	Min. Width Size (mm)	Level 2 Size (mm)	Echelon Crack Angle	G_I/G	G_I (%)	G_{II} (%)	G_{III} (%)	G (%)
F20_CT6_W03-5_L04_90	0.030	0.040	90°	1.0	8.05	--	--	8.05
F20_CT6_W02-6_L03_90	0.020	0.030	90°	1.0	5.17	--	--	5.17
F20_CT6_W012-6_L04_90	0.012	0.040	90°	1.0	2.82	--	--	2.82
F5-CT4_W03-5_L08_90	0.030	0.080	90°	1.0	1.57	--	--	1.57
F20_CT6_W012-6_L04_45	0.012	0.040	45°	0.45	3.32	2.34	4.11	3.06
F20_CT9_W01-6_L034_45	0.010	0.034	45°	0.45	2.68	2.06	3.53	2.35
F5_CT6_W03-6_L08_45	0.030	0.080	45°	0.45	1.34	1.60	2.70	1.31
F5_CT6_W012-6_L08_45	0.012	0.080	45°	0.45	0.22	1.25	1.74	0.07

E.5.3. Discussion

- The most refined data for the 90° echelon crack is quite good. No further study was necessary here, as this step was only to prepare for the 45° echelon crack.
- Most significant error with 45° echelon crack models was G_{III} error. Generally under-predicted at the peak values, although the largest under-prediction was only about 5%.
- For the $t/25$ echelon crack at 45° : Width wise refinements of either 0.03-0.6mm or 0.012-0.6mm are acceptable.
 - o Should go with less refined model for faster processing time.

- For the $t/20$ echelon crack oriented at 45° : width wise refinement of 0.01-0.6mm and a Level 2 element size of 0.034mm gives the best results, although there is still a fairly large G_{III} error (peak local error in G_{III} is about 5%).
 - o Processing time is very significant with this recommended model.
 - o Only a small improvement between this and the model with width wise refinement of 0.012-0.6mm and Level 2 element size of 0.04mm. Most likely worth the tradeoff to have slightly more error but also decreased processing time.

E.5.4. Conclusions

For a $t/5$ echelon crack oriented at 45° , Level 2 refinement of 0.08 mm, width-wise element sizes biased from 0.03 – 0.6 mm, and 6 elements along each edge of the delamination tip partition (element size of $t/576$) is required. For a $t/20$ echelon crack oriented at 45° , Level 2 refinement of 0.04 mm, width-wise element sizes biased from 0.012 – 0.06 mm, and 6 elements along each edge of the delamination tip partition (element size of $t/576$) is acceptably accurate.

E.6. Combined Model with Only Delamination

E.6.1. Model Details

Two models were run for this step. They are the models for a $t/20$ and $t/5$ echelon crack that were determined to be necessary in Section E.5. Due to the complexity of the models created, a system was developed to describe the different models using a short code. This code is identical to that used in Section E.5, since the two sections use the same models and partitions.

The two models created were F20_CT6_W012-6_L04 and F5_CT6_W03-6_L08. These codes refer to:

- $t/20$ echelon crack with 6 elements on each edge of the delamination tip partition, a width-wise refinement from 0.012-0.6mm, and a Level 2 refinement of 0.04mm.
- $t/5$ echelon crack with 6 elements on each edge of the delamination tip partition, a width-wise refinement from 0.03-0.6mm, and a Level 2 refinement of 0.08mm.

Dimensions:

- 30mm width, 3mm thickness, 80mm length, $t/20$ and $t/5$ echelon crack diameter
- Echelon crack center located 30mm in length direction and in center of width and height such that, if there was a delamination tip, it would be centered on the tip in the middle of the specimen's width.

Boundary Conditions:

- Top and bottom (30mmx80mm) faces: $U_2 = 0$
- Upper mode III (1.5mm x 30mm) face $U_1 = 0$, $U_3 = 0.1\text{mm}$
- Lower mode III (1.5mm x 30mm) face $U_1 = U_3 = 0$

Material Properties

- Orthotropic material properties for IM7/8552 given in Table 6.2.

Mesh Details:

See Figure E.21 for labels identifying different parts of the model

- Bonded region far-field element size: single biased 0.22mm near Level 1 region and 4.0mm at far end of specimen
- Unbonded region far-field: single biased 0.22mm near Level 1 region and 3.0mm at far end of specimen
- Level 1 refined regions horizontal element size: 0.20mm
- Level 1 refined regions vertical element size: 0.22mm
- Level 2 refined region all 4 edges element size: 0.04 for t/20 crack and 0.08mm for t/5 crack
- Delamination tip partition: 6 elements per edge
- 60 elements surrounding echelon crack
- Element length immediately around the echelon crack is 0.001mm for t/20 crack and 0.004mm for t/5 crack.
- Width-wise refinement: biased smallest at echelon crack 0.012-0.6mm for t/20 crack and 0.03-0.6mm for t/5 crack

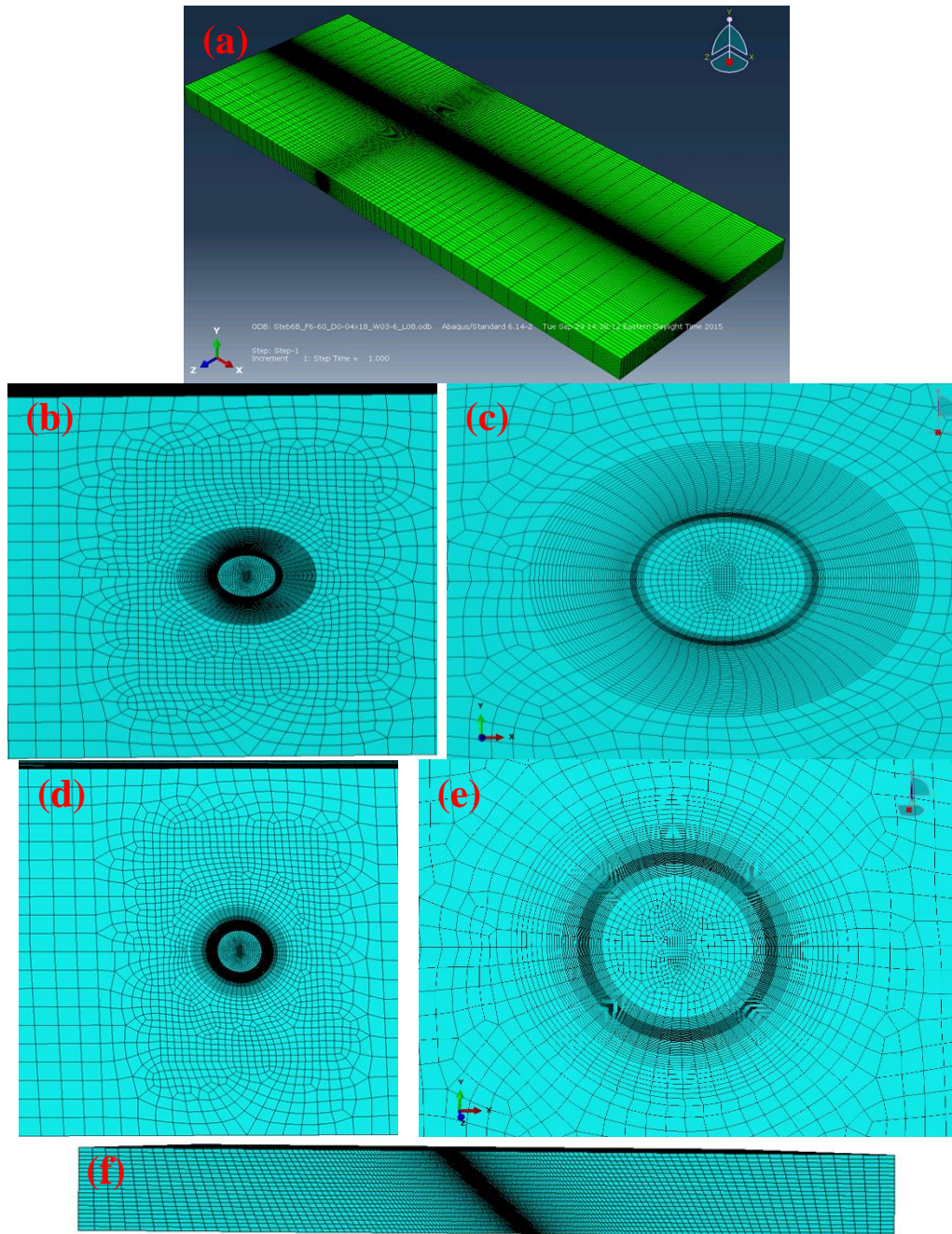


Figure E.26. Views of mesh for delamination-only model with partitions for a $t/5$ echelon crack oriented at 45° with code F5_CT6_W03-6_L08_45. (a) full view of model, (b) edge-view of refined region, (c) edge-view of near-tip region, (d) diagonal partition-view of refined region, (e) diagonal partition-view of near-tip region, (f) width-wise refinement view.

E.6.2. Results

Figure E.27 and Figure E.28 present graphical comparisons of the two models run for this step. For these figures, the horizontal axis represents the location along the delamination front in millimeters. The vertical axis is the component of ERR (in J/m^2) for G_I , G_{II} , G_{III} , and G .

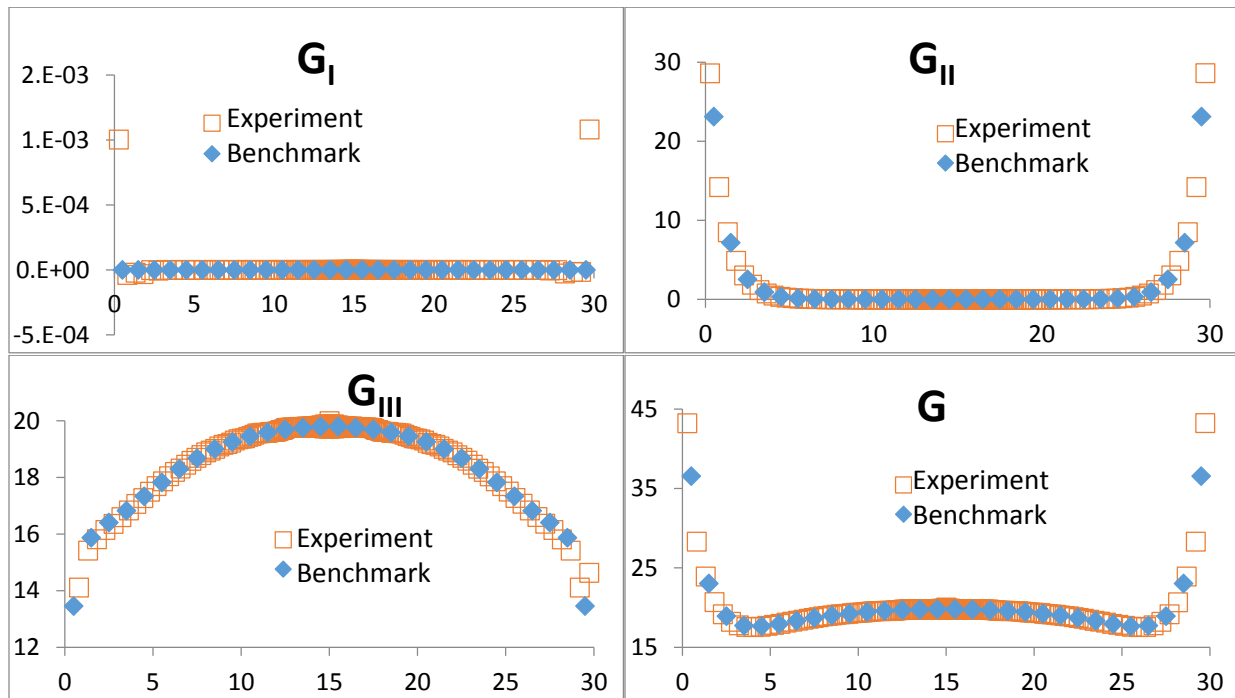


Figure E.27. Plot of ERRs for $t/20$ echelon crack.

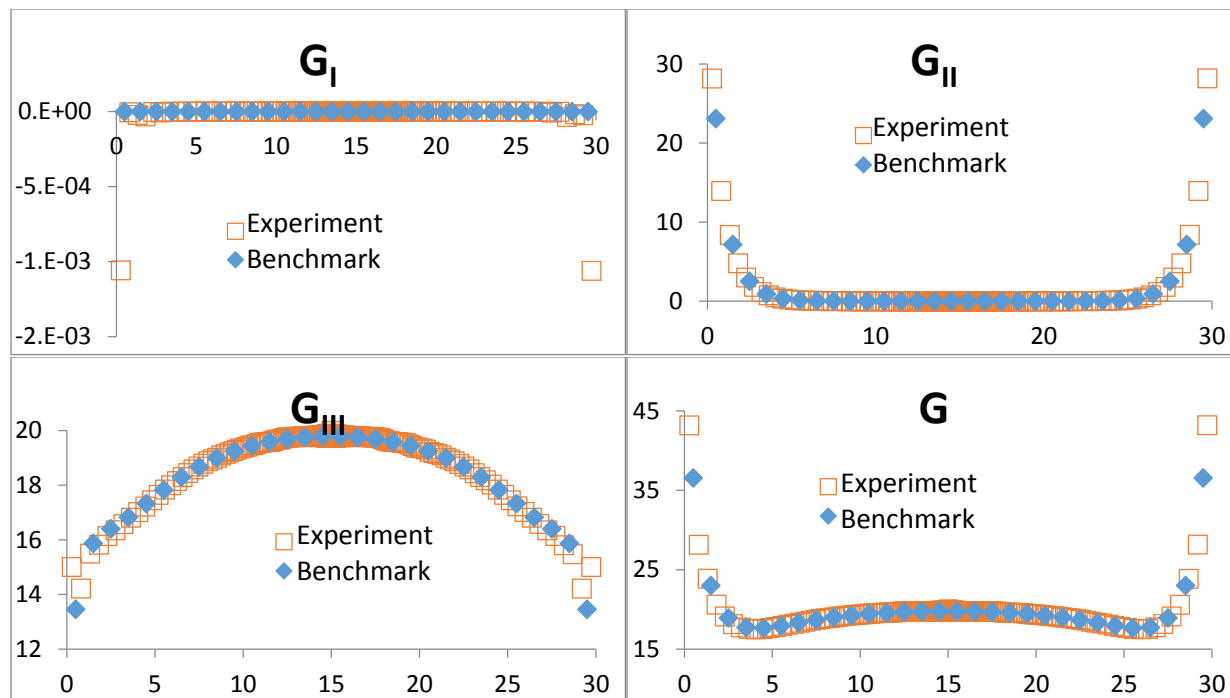


Figure E.28. Plot of ERRs for t/5 echelon crack.

For the two models run for this step, comparisons are given between the model result at a specific location along the delamination front and the ERRs at that location from the benchmark model as well as a simple comparison of the average value. The benchmark results for the STB model are given in Table E.1 (average values) and Table E.3 (local values). The percent differences between the experimental models and the benchmark are given in Table E.17 and Table E.18. As before, a negative percent difference indicates that the average value for the benchmark STB model was larger. The value of G_I is given since the benchmark STB model reports $G_I = 0$, and this results in an infinite percent difference between the two results. Because both these models contain a different number of elements across the width than the benchmark, linear interpolation was used to obtain the value of ERR at the locations of interest. For the average value, a linear weighting by element width was applied to the experimental results since

the models contain elements of variable lengths. This weighted average is then compared to the benchmark, which is inherently weighted due to the fact that every element is the same width.

Table E.17. Values of ERR components at select locations along the delamination front for a t/20 echelon crack in the combined model.

t/20 Echelon Crack	y-location (mm)	G_I (J/m ²)	G_{II} (%)	G_{III} (%)	G (%)
Average Value	--	3.51E-05	-2.43	0.184	-0.108
Center Element	14.5	1.07E-09	-79.5	-0.161	-0.161
Edge Element	29.5	6.14E-04	-2.79	7.07	0.842
Near-Edge Element	28.5	-2.00E-05	0.489	-1.95	-1.19

Table E.18. Values of ERR components at select locations along the delamination front for a t/5 echelon crack in the combined model.

t/5 Echelon Crack	y-location (mm)	G_I (J/m ²)	G_{II} (%)	G_{III} (%)	G (%)
Average Value	--	-4.09E-05	-3.89	0.276	-0.190
Center Element	14.5	-4.33E-09	-76.8	-0.126	-0.125
Edge Element	29.5	-6.18E-04	-4.25	9.02	0.634
Near-Edge Element	28.5	-2.36E-05	-0.884	-1.71	-1.46

E.6.3. Discussion

- Both meshes (t/20 echelon crack mesh and t/5 echelon crack mesh) show really good correlation to the benchmark STB results.
 - o Slight issues at the edges with G_I and G_{III} , although these same issues were seen previously, and the results here are in line with previous results from Section E.1.
 - o High error in G_{II} at the center element due to the very small value of G_{II} at that location, similar to that seen in Section E.1. Absolute error is very small.

E.6.4. Conclusions

The two models run for this section produce acceptably accurate ERR distributions on the delamination front. They will be used going forward.

E.7. Ellipsoidal Echelon Crack Model

E.7.1. Model Details

A single model was run with an embedded ellipsoidal echelon crack. The ellipsoidal echelon crack had a major to minor diameter ratio of 0.4. Eighteen ellipsoidal partitions were included on either side of the crack front. The length around echelon crack tip 0.02mm

Dimensions:

- 4mm width, 4mm thickness, 8mm length
- Echelon crack major diameter of $2c=0.75$ mm and minor diameter of $2a=0.3$ mm with the echelon crack center located 2mm from width and thickness edges and 4mm from length edge (center of model).

Boundary Conditions:

- Top and bottom faces (parallel to echelon crack faces) $U_1 = 0.001$ mm

Material Properties:

- Isotropic material properties based on IM7/8552
 - o $E = E_{22} = 11380$ MPa, $\nu=0.32$
 - o E' (plane strain) = 12680 MPa

Calculations for Analytical Solution (Newman and Raju 1983):

For ellipsoidal echelon crack of minor diameter $a = 0.15\text{mm}$, $a/c = 0.4$, $a/t = 0.075$, and $\sigma = 1$

MPa

$$M1 = 1$$

$$M2 = 0.05/(0.11+(a/c)^{1.5}) = 0.1377$$

$$M3 = 0.29/(0.23+(a/c)^{1.5}) = 0.600$$

$$F_w = \sqrt{1/\cos(\pi*c/2/b*\sqrt{a/t})} = 1.0004$$

$$g = 1-(a/t)^4/(1+4*(a/c))*\cos(\varphi) = \cos(\varphi)$$

$$F_\varphi = ((a/c)^2*\cos(\varphi)^2+\sin(\varphi)^2)^{0.25} = (0.16*\cos(\varphi)^2+\sin(\varphi)^2)^{0.25}$$

$$F_e = [M1 + M2(a/t)^2 + M3(a/t)^4]*g*F_\varphi*F_w$$

$$Q = 1+1.464*(a/c)^{1.65} = 1.323$$

$$K_I = \sigma* \sqrt{\pi*a/Q}*F_e$$

$$G_I = K_I^2/E'$$

$$K_{II} = K_{III} = G_{II} = G_{III} = 0$$

Mesh Details:

- Element length around echelon crack tip 0.002mm
- 60 elements around echelon crack
- Far field (horizontal edges, parallel to echelon crack) seeded biased towards center
0.04mm to 0.30mm at edges

- Far field (vertical edges, perpendicular to echelon crack) seeded biased towards center
0.01 mm to 0.20 mm at edges

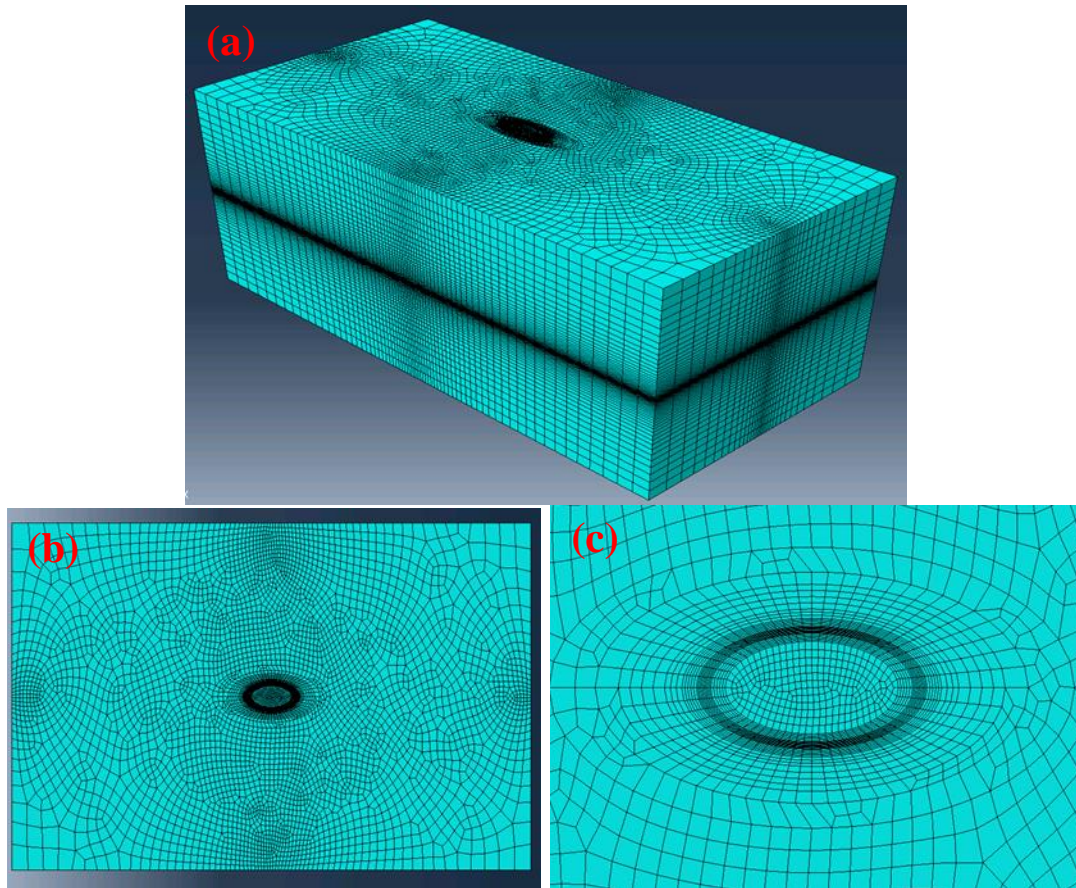


Figure E.29. Views of mesh for ellipsoidal crack model. (a) Full view of model, (b) planar view of model, (c) planar view of near-tip region.

E.7.2. Results

Figure E.30 presents a comparison between the analytical solution and the experimental results for the ellipsoidal echelon crack.

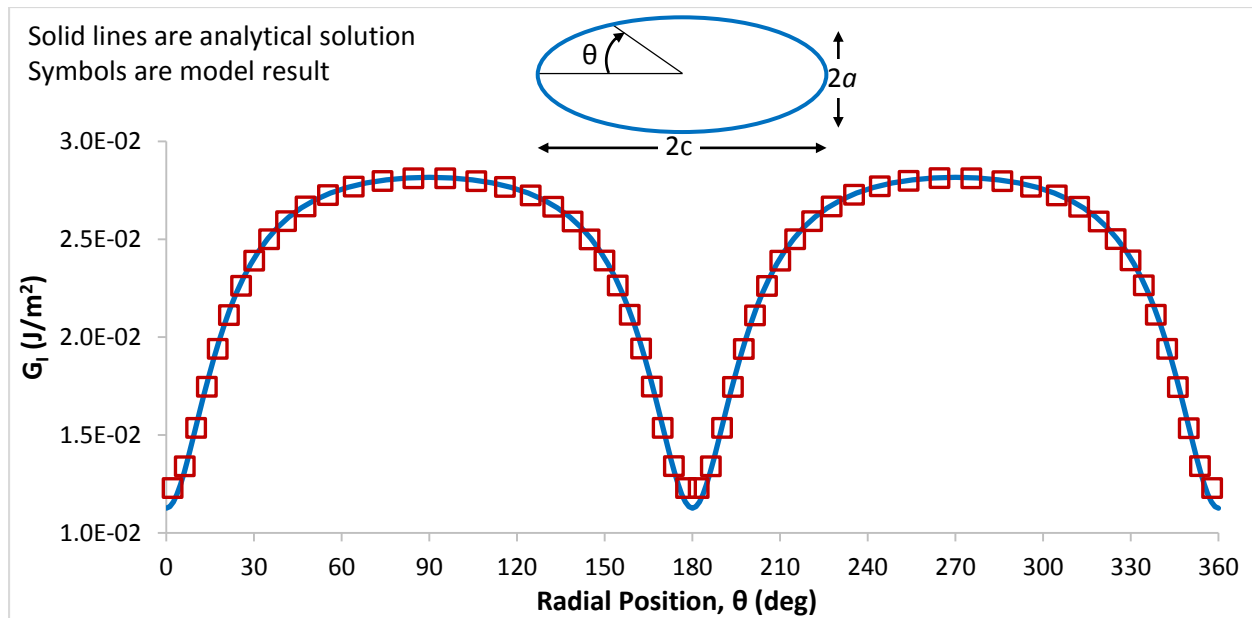


Figure E.30. Mode I ERR distribution for ellipsoidal model.

E.7.3. Discussion

The results are poorest at 0° and 180° while they are quite accurate everywhere else. At 0° the difference between the analytical solution and modeling result are 6.6% while the average across the entire crack front is 0.96%. As seen in Figure E.30, the results are overall very accurate.

E.7.4. Conclusions

The mesh for the ellipsoidal echelon crack was developed using element sizes known to be acceptable for a circular echelon crack. Based on the above results, this mesh is acceptable for modeling an ellipsoidal echelon crack as well.

E.8. Multiple Echelon Cracks Model

E.8.1. Model Details

Three models were created based on F20_CT6_W012-6_L04 from Section E.6, which is a $t/20$ echelon crack with a delamination tip partition that has 6 elements on each edge, a width-wise refinement from 0.012-0.6mm and a Level 2 refinement of 0.04mm. Recall that this model also has 60 elements around the echelon crack which are 0.001mm in length. For these models, instead of a single 45° plane, three planes spaced $3t/20$ apart were modeled. Outside of these planes the width refinement was from 0.012 mm – 0.6 mm while between the diagonal planes all width elements were 0.012 mm. The models created are as follows:

- Full mesh as described above but only delamination is modeled (partitions and mesh present for three echelon cracks, but cracks are not modeled).
- Full mesh as described above but only central echelon crack modeled (partitions and mesh for delamination and outside echelon cracks also present, but those entities not modeled).
- Full mesh as described above but only one outside echelon crack modeled (partitions and mesh for delamination and other two echelon cracks also present, but those entities were not modeled).

Dimensions:

- 30mm width, 3mm thickness, 80mm length, $t/20$ echelon crack diameter
- Middle echelon crack center located 30mm in length direction and in center of width and height such that, if there was a delamination tip, it would be centered on the tip in the middle of the specimen's width.

- Outside echelon cracks oriented similarly to middle crack, but spaced $3t/20$ on either side of middle echelon crack.

Boundary Conditions:

- For delamination only model
 - o Top and bottom (30mmx80mm) faces: $U_2 = 0$
 - o Upper mode III (1.5mm x 30mm) face $U_1 = 0, U_3 = 0.1\text{mm}$
 - o Lower mode III (1.5mm x 30mm) face $U_1 = U_3 = 0$
- For echelon crack only models
 - o Side (3mmx80mm) faces: $S_1 = 1\text{ MPa}$ (normal tractions)
 - o Mid-plane corner point at (-40mm, 0 mm, 0mm) pinned $U_1=U_2=U_3=0$
 - o Resultant stresses on 45° echelon crack is 0.5 MPa tension and 0.5 MPa shear

Material Properties:

- For delamination only model
 - o Orthotropic material properties for IM7/8552 given in Table 6.2.
- For echelon crack only models
 - o Isotropic material properties based on IM7/8552
 - o $E = E_{22} = 11380\text{ MPa}, \nu=0.32, G = 4311\text{ MPa}$
 - o $E' \text{ (plane strain)} = 12680\text{ MPa}$

Mesh Details:

See Figure E.21 for labels identifying different parts of the model

- Bonded region far-field element size: single biased 0.22mm near Level 1 region and 4.0mm at far end of specimen
- Unbonded region far-field: single biased 0.22mm near Level 1 region and 3.0mm at far end of specimen
- Level 1 refined regions horizontal element size: 0.20mm
- Level 1 refined regions vertical element size: 0.22mm
- Level 2 refined region all 4 edges element size of 0.04
- Delamination tip partition with 6 elements per edge
- 60 elements surrounding echelon crack
- Element length immediately around the echelon crack is 0.001mm
- Width-wise refinement: biased smallest at echelon crack 0.012-0.6mm

Example Calculation for Analytical Solution of Echelon Crack Models (Kassir and Sih, 1975):

For 45° echelon crack of diameter $t/20$, $\sigma = 0.5$ MPa, $\tau = 0.5$ MPa, and $a = 0.075$ mm

$$K_I = 2/\pi * \sigma * \sqrt{\pi*a} = 4886 \text{ N}\cdot\sqrt{\text{m}}$$

$$G_I = K_I^2/E' = 0.0018825 \text{ J/m}^2$$

$$K_{II} = 4/\pi/(2-\nu)*\tau*\sqrt{\pi*a}*\cos(\phi) = 5816 * \cos(\phi) \text{ N}\cdot\sqrt{\text{m}}$$

$$G_{II} = K_{II}^2/E' = 0.002667*\cos^2(\phi) \text{ J/m}^2$$

$$K_{III} = 4*(1-\nu)/\pi/(2-\nu)*\tau*\sqrt{\pi*a}*\sin(\phi) = 3955*\sin(\phi) \text{ N}\cdot\sqrt{\text{m}}$$

$$G_{III} = K_{III}^2/2/G = 0.001814*\sin^2(\phi) \text{ J/m}^2$$

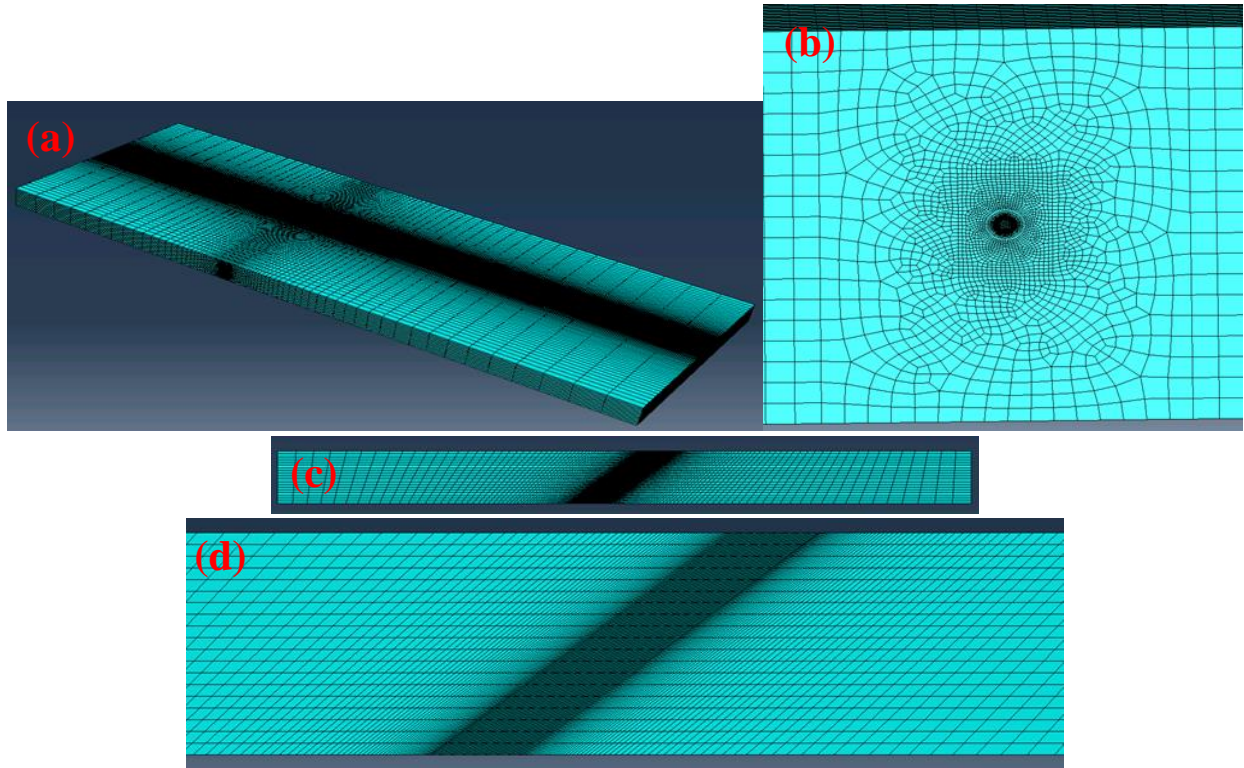


Figure E.31. Views of mesh for multiple echelon crack model. (a) Full view of model, (b) echelon crack plane-view, (c) width-wise refinement full view, (d) width-wise refinement at echelon crack planes.

E.8.2. Results

E.8.2.1. Delamination Only

Figure E.32 presents graphical comparisons of the delamination model and the STB benchmark. For these plots, the horizontal axis represents the location along the delamination front in millimeters. The vertical axis is the component of ERR (in J/m^2) for G_I , G_{II} , G_{III} , and G .

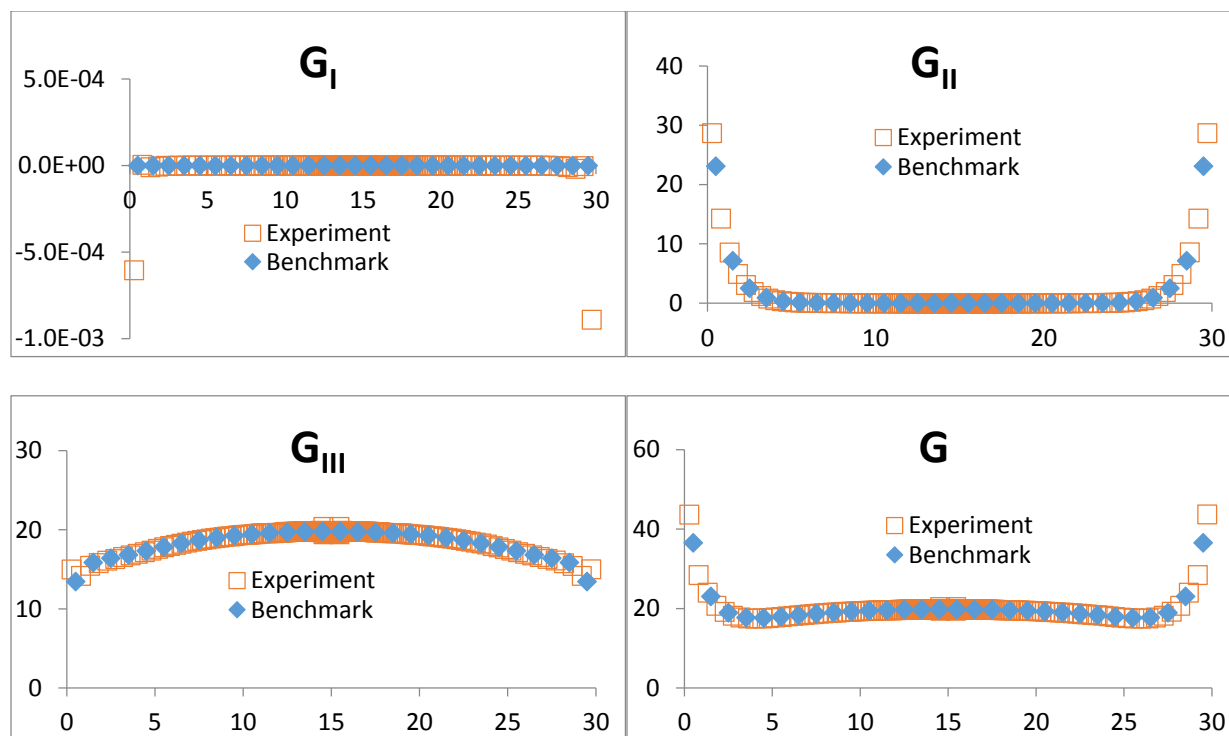


Figure E.32. ERR distributions for delamination model with multiple echelon cracks.

For the delamination models represented in Figure E.32, comparisons are given between the model result at a specific location along the delamination front and the ERRs at that location from the benchmark model. The benchmark results for the STB model are given in Table E.1 and Table E.3. The percent differences are given for the different models in Table E.19. As before, a negative percent difference indicates that the average value for the STB model was larger. The average value of G_I is given since the benchmark model reports $G_I = 0$, and this results in an infinite percent difference between the two results. Because this model contains a different number of elements across the width than the benchmark, linear interpolation was used to obtain the value of ERR at the locations of interest. For the average value, a linear weighting by element width was applied to the experimental results since the experimental models contain elements of different lengths. This experimental weighted average is then compared to the STB

benchmark average, which is inherently weighted due to the fact that every element is the same width.

Table E.19. Comparative results between benchmark STB model and experimental model ERRs at select locations along the delamination fronts for the multiple echelon crack delamination only model.

	y-location (mm)	G_I (J/m ²)	G_{II} (%)	G_{III} (%)	G (%)
Average Value	--	-2.79E-05	-2.45	0.142	-0.125
Center Element	14.5	-3.35E-09	-74.6	-0.308	-0.307
Edge Element	29.5	-5.08E-04	-2.69	8.94	1.59
Near-Edge Element	28.5	-1.52E-05	0.704	-1.91	-1.10

E.8.2.2. Echelon Cracks Only

Example analytical solutions for mixed mode loading of an embedded echelon crack are given above in Section E.8.1. These are used with the results from the models generated for this step to determine the percent difference for each mesh. The percent differences between the ERR components determined experimentally and the analytical solutions are given in Table E.20. The results given are an average percent difference across the entire front. Because of this averaging, it is not possible to use a sign to indicate whether the analytical solution or experimental results were larger or smaller, and so all percent differences are given as positive values.

Table E.20. ERR results for echelon cracks in multiple crack model

Model	G_I/G	G_I (%)	G_{II} (%)	G_{III} (%)	G (%)
Middle Echelon Crack	0.456	3.35	2.40	4.22	3.09
Outside Echelon Crack	0.457	3.33	2.42	4.23	3.08

Graphical results for the middle echelon crack only models are given in Figure E.33, while results for the outside echelon crack only model are given in Figure E.34. These results are

presented as polar plots where the circumferential axis is the angular position around the crack and the radial axis is the value of the ERR component.

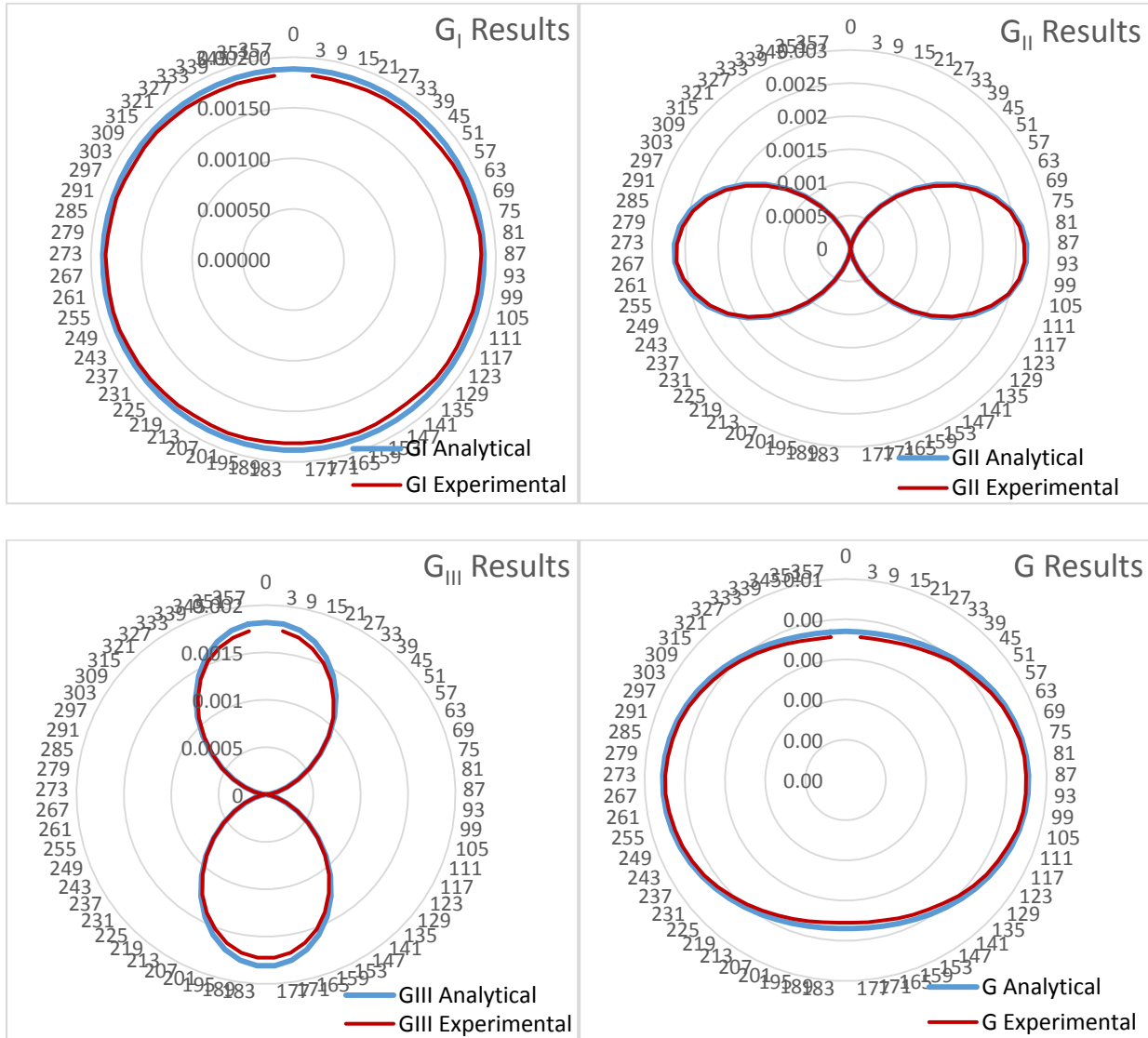


Figure E.33. ERR distributions for middle echelon crack in multiple crack model.

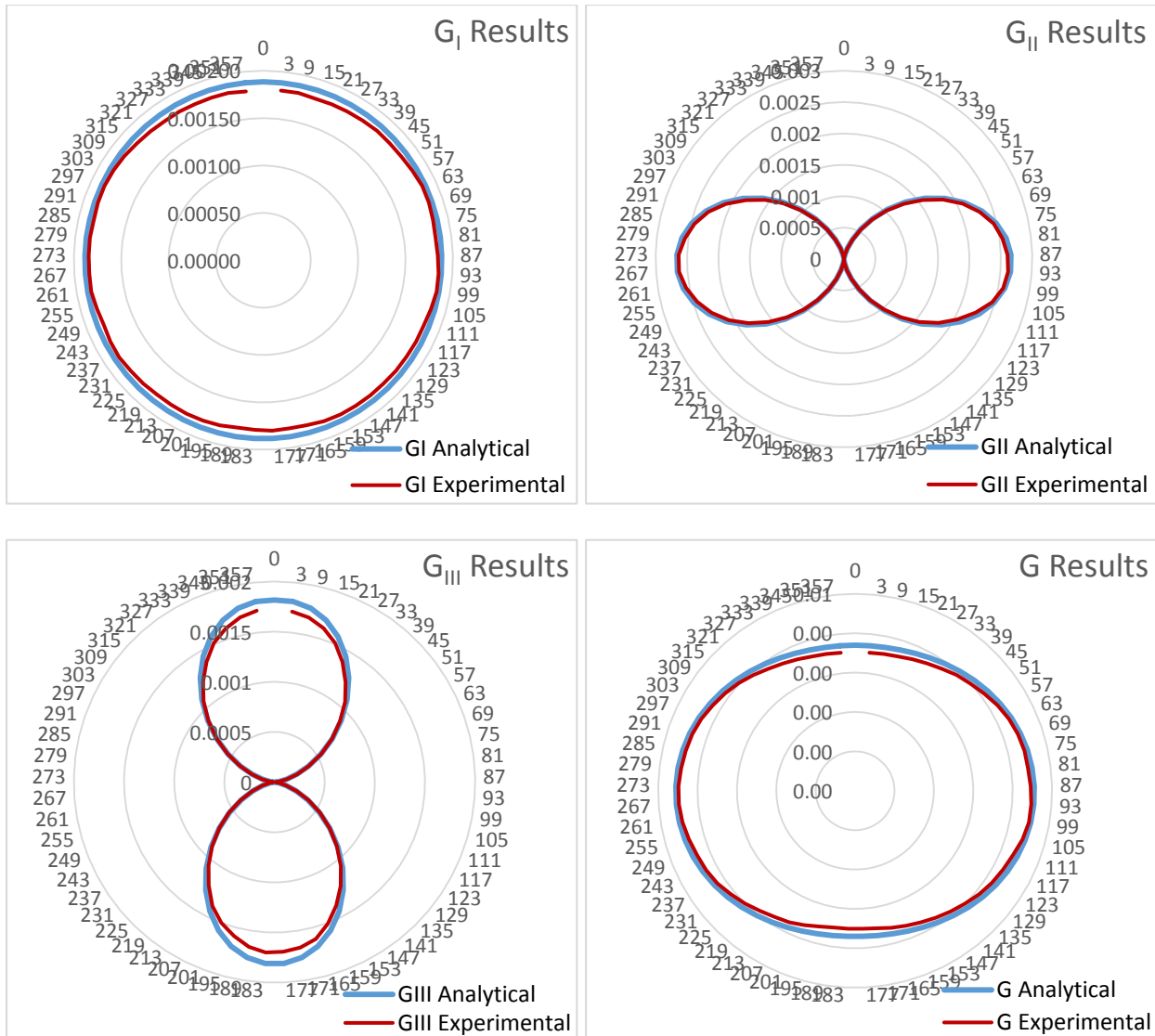


Figure E.34. ERR distributions for outside echelon crack in multiple crack model.

E.8.3. Discussion

The model of only the delamination gives results almost identically accurate to those in Section E.6. The models for only the central echelon crack and only the outside echelon crack give results almost identically accurate to those in Section E.5. There appears to be no new issues related to the modeling of multiple echelon cracks.

E.8.4. Conclusions

Based on the accuracy of the multiple crack models, no additional mesh refinement or study is necessary. The mesh recommendations given in Section E.6, along with using the smallest width-wise element size between the outside and middle echelon cracks, will result in acceptably accurate results.

References

A

Amestoy M, Leblond JB. Crack paths in plane situations – II. Detailed form of the expansion of the stress intensity factors. *Int J Sol Struct* 1992; 29(4):465-501.

ASTM Standard D3039. Standard test method for tensile properties of polymer matrix composite materials. ASTM International, West Conshohocken, PA, 2014. doi: 10.1520/D3039_D3039M-14.

ASTM Standard D4255. Standard test method for in-plane shear properties of polymer matrix composite materials by the rail shear method. ASTM International, West Conshohocken, PA, 2007.

ASTM Standard D5379. Standard test method for shear properties of composite materials by the v-notched beam method. ASTM International, West Conshohocken, PA, 2012. doi: 10.1520/D5379_D5379M-12.

ASTM Standard D5528. Standard test method for mode I interlaminar fracture toughness of unidirectional fiber-reinforced polymer matrix composites. ASTM International, West Conshohocken, PA, 2013.

ASTM Standard D6671. Standard test method for mixed mode I-mode II interlaminar fracture toughness of unidirectional fiber reinforced polymer matrix composites. ASTM International, West Conshohocken, PA, 2013.

ASTM Standard D7905. Standard test method for determination of the mode II interlaminar fracture toughness of unidirectional fiber-reinforced polymer matrix composites. ASTM International, West Conshohocken, PA, 2014.

B

- Bao G, Ho S, Suo Z and Fan B. The role of material orthotropy in fracture specimens for composites. *Int J Sol Struct* 1992; 29(0):1105-1116.
- Bažant ZP and Estenssoro LF. Surface singularity and crack propagation. *Int J Sol Struct* 1979; 15(5):405-426.
- Becht GJ and Gillespie JW Jr. Design and analysis of the crack rail shear specimen for mode III interlaminar fracture. *Compos Sci Technol* 1988; 31:143-157.
- Becht GJ and Gillespie JW Jr. Numerical and experimental evaluation of the mode III interlaminar fracture toughness of composite materials. *Polymer Compos* 1989; 10(5):293-304.
- Berto F, Elices M, Lazzarin P, and Zappalorto M Fracture behavior of notched round bars made of PMMA subjected to torsion at room temperature. *Eng Fract Mech* 2012A; 90:143-160.
- Berto F, Lazzarin P, and Ayatollahi MR. Brittle fracture of sharp and blunt V-notches in isostatic graphite under torsion loading. *Carbon* 2012B; 50:1942-1952.
- Browning G, Carlsson LA and Ratcliffe JG. Modification of the edge crack torsion specimen for mode III delamination testing. Part II- experimental study. *J Compos Mater* 2011; 45(25):2633-2640.
- Buchholz F-G, Chergui A and Richard HA. Fracture analyses and experimental results of crack growth under general mixed mode loading conditions. *Eng Fract Mech* 2004; 71(4-6):455-468.

C

Cambonie T and Lazarus V. Quantification of the crack fragmentation resulting from mode I+III loading. *Procedia Mater Sci* 2014; 3:1816-1821.

Canturri C, Greenhalgh ES and Pinho ST. The relationship between mixed-mode II/III delamination and delamination migration in composite laminates. *Compos Sci Technol* 2014; 105:102-109.

Carlsson LA, Adams DF and Pipes RB. Experimental Characterization of Advanced Composite Materials, 4th ed. Boca Raton, FL: CRC Press, 2014.

Cicci D, Sharif F and Kortschot MT. Data reduction for the split cantilever beam mode III delamination test. In: Proceedings of the 10th international conference on composite materials, Vol 1 (ICCM-10), British Columbia, Canada, 14–18 Aug 1995, pp. 189–96.

Cooke ML and Pollard DD. Fracture propagation paths under mixed mode loading within rectangular blocks of polymethyl methacrylate. *J Geophys Res* 1996; 101(B2):3387-3400.

Cotterell B and Rice JR. Slightly curved or kinked cracks. *Int J Fract* 1980; 16(2):155-169.

Cox SJD and Scholz CH. On the formation and growth of faults: an experimental study. *J Struct Geol* 1988; 10(4):413-430.

CYCOM® 977-3 toughened epoxy resin technical data sheet. Cytec Industries Inc.

www.cytec.com. Accessed 16 February 2012.

Czabaj MW and Ratcliffe JG. Comparison of intralaminar and interlaminar mode-I fracture toughness of a unidirectional IM7/8552 graphite/epoxy composite. *Compos Sci Technol* 2013; 89:15-23.

Czabaj MW, Ratcliffe JG and Davidson BD. Observation of intralaminar cracking in the edge crack torsion specimen. *Eng Fract Mech* 2014; 120:1-14.

D

Davenport JCW and Smith DJ. A study of superimposed fracture modes I, II and III on PMMA.

Fat Fract Eng Mater Struct 1993; 16(10):1125-1133.

Davidson BD. Delamination toughness characterization of composite materials, in: Blockley R. and Shyy W. (Eds.), *Encyclopedia of Aerospace Engineering*. John Wiley & Sons, Chichester, UK, 2010, pp. 1899-1910.

Davidson BD, Krüger R and König M. Three-dimensional analysis of center-delaminated unidirectional and multidirectional single-leg bending specimens. *Compos Sci Technol* 1995; 54(4):385-394.

Davidson BD, Krüger R and König M. Effect of stacking sequence on energy release rate distributions in multidirectional DCB and ENF specimens. *Eng Fract Mech* 1996; 55(4):557-569.

Davidson BD and Sediles FO. Mixed-mode I-II-III delamination toughness determination via a shear-torsion-bending test. *Compos Part A* 2011; 42(6):589-603.

Davidson BD and Schapery RA. Effect of finite width on deflection and energy release rate of an orthotropic double cantilever specimen. *J Compos Mater* 1988; 22:640-656.

Davidson BD, Sun X and Vinciguerra AJ. Influences of friction, geometric nonlinearities, and fixture compliance on experimentally observed toughnesses from three and four point bend end notched flexure tests. *J Compos Mater* 2007; 41(10):1177-96.

de Freminville C. *Revue de Metallurgie*, 1914; 971-1056.

de Morais AB and Pereira AB. Mode III interlaminar fracture of carbon/epoxy laminates using a four-point bending plate test. *Compos. Part: A* 2009B; 40:1741-1746.

de Morais AB, Pereira AB and de Moura MFSF. Mode III interlaminar fracture of carbon/epoxy laminates using the six-point edge crack torsion (6ECT). *Compos Part A* 2011; 42:1793-1799.

de Morais AD, Pereira AB, de Moura MFSF and Magalhães AG. Mode III interlaminar fracture of carbon/epoxy laminates using the edge crack torsion (ECT) test. *Compos Sci Technol* 2009A; 69(5):670-676.

Dhondt G, Chergui A and Buchholz F-G. Computational fracture analysis of different specimens regarding 3D and mode coupling effects. *Eng Fract Mech* 2001; 68(4):383-401.

Donaldson SL. Mode III interlaminar fracture characterization of composite materials. *Compos Sci Technol* 1988; 32(3):225-249.

E

Erdogan F and Sih GC. On the crack extension in plates under plane loading and transverse shear. *J Fluids Eng* 1963; 85(4):519-525.

F

Farshad M and Flüeler P. Investigation of mode III fracture toughness using an anti-clastic plate bending method. *Eng Fract Mech* 1998; 60(5-6):597-603.

G

Gao H. Three-dimensional slightly nonplanar cracks. *J Appl Mech* 1992; 59(2):335-343.

Gao H and Rice JR. Shear stress intensity factors for a planar crack with slightly curved front. *J Appl Mech* 1986; 53:774-778.

Geels K. Metallographic and materialographic specimen preparation, light microscopy, image analysis, and hardness testing: text. ASTM International, West Conshohocken, PA; MNL-26 2007.

Goldstein RV and Osipenko NM. Structures of fracture near a longitudinal shear main crack. In: Proceedings of the 19th European Conference on Fracture (ECF19), Kazan, Russia, 26-31 Aug, 2012A, pp. 1-10.

Goldstein RV and Osipenko NM. Successive development of the structure of a fracture near the front of a longitudinal shear crack. *Doklady Phys* 2012B; 57(7):164-167.

Goldstein RV and Osipenko NM. Development of multiple ordered fracture in an elastic homogenous, structured and layered medium. *Fat Fract Eng Mater Struct* 2014; 37:1292-1305.

Goldstein RV and Salganik RL. Brittle fracture of solids with arbitrary cracks. *Int J Fract* 1974; 10(4):507-523.

Greenhalgh ES. Delamination-dominated failures in polymer composites, in: Failure Analysis and Fractography of Polymer Composites. Woodhead Publishing Lmted., Oxford, 2009, pp. 164-237.

Gregory JR and Spearing SM. Modeling inelastic matrix crack tip deformation in a double cantilever beam specimen. *J Compos Mater* 2006; 40(2):143-56.

H

Hakim V and Karma A. Laws of crack motion and phase-field models of fracture. *J Mech Phys Sol* 2009; 57(2):342-368.

Hodgdon JA and Sethna JP. Derivation of a general three-dimensional crack-propagation law: a generalization of the principle of local symmetry. *Phys Rev B* 1993; 47(9):4831-4840.

Horner AL, Czabaj MW, Davidson BD and Ratcliffe JG. Three-dimensional crack surface evolution in mode III delamination toughness tests. *Eng Fract Mech* 2015; 149:313-25.

Hourlier F and Pineau A. Propagation of fatigue cracks under polymodal loading. *Fat Fract Eng Mater Struct* 1982; 5(4):287-302.

Hu H. Analytical determination of energy release rate and mode mix for interfacial cracks in layered elastic structures. Ph.D. Dissertation, Syracuse University, 1995.

Hull D. Tilting cracks: the evolution of fracture surface topology in brittle solids. *Int J Fract* 1993; 62:119-138.

Hull D. The effect of mixed mode I/III on crack evolution in brittle solids. *Int J Fract* 1995; 70(1):59-79.

Hysol® EA 9309.3NA Epoxy Paste Adhesive technical data sheet. Henkel Corporation.
www.aerospace.henkel.com. Accessed 22 October 2015.

J

Johnston AL and Davidson BD. Intrinsic coupling of near-tip matrix crack formation to mode III delamination advance in laminated polymeric matrix composites. *Int J Sol Struct* 2014; 51(13):2360-2369.

Johnston AL, BD Davidson and KK Simon. Assessment of split-beam-type tests for mode III delamination toughness determination. *Int J Fract* 2014; 185(1):31-48.

K

Kassir MK and Sih GC. Mechanics of fracture volume 2: three dimensional crack problems. Sih GC, ed. Noordhoff International Publishing, Leyden, the Netherlands, 1975.

Karma A, Kessler DA and Levine H. Phase-field model of mode III dynamic fracture. *Phys Rev Lett* 2001; 87:045501.

Khoshravan MR and Moslemi M. Investigation on mode III interlaminar fracture of glass/epoxy laminates using a modified split cantilever beam test. *Eng Fract Mech* 2014; 127:267-279.

Knauss WG. An observation of crack propagation in antiplane shear. *Int J Fract Mech* 1970; 6(2):183-187.

Krueger R. The virtual crack closure technique: history, approach and application. *Appl Mech Rev* 2004; 57(2):109-143.

L

Lai Y-S. A study of three-dimensional cracks. Ph.D. Dissertation, the University of Texas at Austin, 2002.

Laio WC and Sun CT. The determination of mode III fracture toughness in thick composite laminates. *Compos Sci Technol* 1996; 56:489-499.

- Lawn BR. Fracture of brittle solids, 2nd ed, Cambridge solid state science series. New York, NY: Cambridge University Press; 1993.
- Lazarus V, Buchholz F-G and Fulland M. Comparison of predictions by mode II or mode III criteria on crack front twisting in three or four point bending experiments. *Int J Fract* 2008; 153:141-151.
- Lazarus V and Leblond J-B. Crack paths under mixed mode (I+III) or (I+II+III) loadings. *Comptes Rendus de l'Académie des Sciences, Série II (Mécanique, Physique, Astronomie)* 1998; 326(3):171–177.
- Lazarus V, Leblond J-B and Mouchrif SE. Crack front rotation and segmentation in mixed mode I+III or I+II+III - part I: calculation of stress intensity factors. *J Mech Phys Sol* 2001A; 49:1399-1420.
- Lazarus V, Leblond J-B and Mouchrif SE. Crack front rotation and segmentation in mixed mode I+III or I+II+III - part II: comparison with experiments. *J Mech Phys Sol* 2001B; 49:1421-1443.
- Leblond J-B. Crack paths in three-dimensional elastic solids. I: two-term expansion of the stress intensity factors – application to crack path stability in hydraulic fracturing. *Int J Sol Struct* 1999; 36:79-103.
- Leblond J-B and Frelat J. Development of fracture facets from a crack loaded in mode I+III: solution and application of a model 2D problem. *J Mech Phys Sol* 2014; 64:133-153.
- Leblond J-B, A Karma and V Lazarus. Theoretical analysis of crack front instability in mode I + III. *J Mech Phys Sol* 2011; 59(9):1872–1887.
- Leblond J-B and Lazarus V. On the strong influence of imperfections upon the quick deviation of a mode I+III crack from coplanarity. *J Mech Mater Struct* 2015; 10(3):299-316.

- Lee SM. An edge crack torsion method for mode III delamination fracture testing. *J Compos Technol Res* 1993; 15(3):193-201.
- Li X, Carlsson LA and Davies P. Influence of fiber volume fraction on mode III interlaminar fracture toughness of glass/epoxy composites. *Compos Sci Technol* 2004; 64:1279–1286.
- Li S, He T, Teng C, Zheng X and Viktor K. Theoretical and experimental study of 3-D initial fracture and its significance to faulting. *Earthq Sci* 2011; 24(3):283-98.
- Li J, Lee SM, Lee EW and O'Brien TK. Evaluation of the edge crack torsion (ECT) test for mode III interlaminar fracture toughness of laminated composites. NASA-TM-1996-110264; 1996.
- Li J, and O'Brien TK. Simplified data reduction methods for the ECT test for mode III interlaminar fracture toughness. *J Compos Technol Res* 1996; 18(2):96-101.
- Lin B, Mear ME and Ravi-Chandar K. Criterion for initiation of cracks under mixed-mode I + III loading. *Int J Fract* 2010; 165:175–188.
- Liu S, Chao YJ and Zhu X. Tensile-shear transition in mixed mode I/III fracture. *Int J Sol Struct* 2004; 41:6147-6172.

M

- Makabe C, Anggit M, Sueyoshi T and Yafuso T. The formation mechanism of the factory-roof pattern in a torsional fatigue specimen with circumferential notch. *J Test Eval* 2006; 34(5):1-7.
- Marat-Mendes R and de Freitas M. Fractographic analysis of delamination in glass/fibre epoxy composites. *J Compos Mater* 2013; 47(12):1437-48.

Martin RH. Evaluation of the split cantilever beam for mode III delamination testing. In: O'Brien TK, editor. *Composite Materials: Fatigue and Fracture- Third Volume*, ASTM STP 1110, Philadelphia: American Society for Testing and Materials, 1991, pp. 243-266.

Movchan AB, Gao H and Willis JR. On perturbations of plane cracks. *Int J Sol Struct* 1998; 35(26-27):3419-3453.

Mróz KP and Mróz, Z. On crack path evolution rules. *Eng Fract Mech* 2010; 77:1781-1807.

N

Nakamura T and Parks DM. Antisymmetrical 3-D stress field near the crack front of a thin elastic plate. *Int J Sol Struct* 1989; 25(12):1411-1426.

Newman JC Jr and Raju IS. Analyses of surface cracks in finite plates under tension or bending loads. NASA TP-1578, 1979.

Newman JC Jr and Raju IS. Stress-intensity factor equations for cracks in three-dimensional finite bodies. *Fracture Mechanics: Fourteenth Symposium – Volume I: Theory and Analysis*, ASTM STP 79 1, Lewis JC and Sines G, eds. American Society for Testing and Materials 1983, pp. I-238-I-265.

Nuismer RJ. An energy release rate criterion for mixed mode fracture. *Int J Fract* 1975; 11(2):245-250.

Q

- O'Brien TK. Composite interlaminar shear fracture toughness, GIIC: shear measurement or sheer myth? *Composite Materials: Fatigue and Fracture, 7th Volume*. ASTM STP 1330, Bucinell RB, ed. American Society for Testing and materials 1998, pp. 3-18.
- O'Brien TK and Krueger R. Analysis of flexural tests for transverse tensile strength characterization of unidirectional composites. *J Compos Technol Res* 2003; 25(1):1-19.
- O'Brien TK, Johnston WM and Toland GJ. Mode II interlaminar fracture toughness and fatigue characterization of a graphite epoxy composite material. NASA-TM-2010-216838; 2010.

P

- Palaniswamy K and Knauss WG. On the problem of crack extension in brittle solids under general loading. *Mech Today* 1978; 4:87-148.
- Pennas D, Cantwell WJ and Compston P. The influence of strain rate on mode III interlaminar fracture of composite materials. *J Compos Mater* 2007; 41(21):2595-2614.
- Pereira AB, de Morais AB and de Moura MSFS. Design and analysis of a new six-point edge crack torsion (6ECT) specimen for mode III interlaminar fracture characterization. *Compos Part A* 2011; 42:131-139.
- Pernice MF, De Carvalho NV, Ratcliffe JG and Hallett SR. Experimental study on delamination migration in composite laminates. *Compos Part A* 2015; 73:20-34.
- Petrovic JJ. Mixed-mode fracture of hot-pressed Si₃N₄. *J Am Ceram Soc* 1985; 68(6):348-355.
- Pham KH and Ravi-Chandar K. Further examination of the criterion for crack initiation under mixed-mode I+III loading. *Int J Fract* 2014; 189:121-138.

Pollard DD, Segall P and Delaney PT. Formation and interpretation of dilatant echelon cracks.

Geol Soc Am Bull 1982; 93(12):1291-1303.

Pook LP. The significance of mode I branch cracks for combined mode failure. In: Radon JC,

editor. *Fracture and Fatigue: Elasto-Plasticity, Thin Sheet and Micromechanisms*

Problems, Oxford: Pergamon Press Ltd., 1980, pp. 143-153.

Pook LP. The fatigue crack direction and threshold behavior of mild steel under mixed mode I

and III loading. *Int J Fract* 1985A; 7(1):21-30.

Pook LP. Comments on fatigue crack growth under mixed modes I and III and pure mode III

loading. In: Miller KJ and Brown MW, editors. *Multiaxial Fatigue*, ASTM STP 853.

Philadelphia: American Society for Testing and Materials, 1985B, pp. 249-263.

Pons AJ and Karma A. Helical crack-front instability in mixed-mode fracture. *Nature* 2010;

464(4):85–89

R

Ratcliffe JG. Characterization of the edge crack torsion (ECT) test for mode III fracture

toughness measurement of laminated composites. NASA-TM-2004-213269; 2004.

Ren F, Wang JJ-A and Bertelsen WD. Fractographic study of epoxy under mode I and mixed

mode I/III loading. *Mat Sci Eng A* 2012; 532:449-455.

Ressel M and Theilig H. Finite element analysis of secondary cracks at a crack front under pure

mode III loading. *Key Eng Mater* 2012; 488-489:605-608.

Richard HA. In: Rossmann HP, editor. *Structural Failure, Product Liability and Technical*

Insurance: Proceedings of the 2nd International Conference, Geneva: Inderscience

Enterprises, 1987.

Richard HA, Fulland M and Sander M. Theoretical crack path prediction. *Fat Fract Engng Mater Struct* 2005; 28:3-12.

Richard HA, Schöllmann M, Fulland M and Sander M. Experimental and numerical simulation of mixed mode crack growth. In: de Freitas M, editor. Proc of 6th Int Conference of Biaxial/Multiaxial Fatigue and Fracture, Lisbon, Portugal, 2001, pp. 623-630.

Rizov V, Shindo Y, Horiguchi K and Narita F. Mode III interlaminar fracture behavior of glass fiber reinforced polymer woven laminates at 293 and 4 K. *Appl Compos Mater* 2006; 13:287-304.

Robinson P and Song DQ. The development of an improved mode III delamination test for composites. *Compos Sci Technol* 1994; 52:217-233.

Roering C. The geometrical significance of natural en-echelon crack-arrays. *Tectonophysics* 1968; 5(2):107-123.

Rybicki EF and Kanninen MF. A finite element calculation of stress intensity factors by a modified crack closure integral. *Eng Fract Mech* 1977; 9(4):931-938.

S

Schöllmann M, Richard HA, Kullmer G and Fulland M. A new criterion for the prediction of crack development in multiaxially loaded structures. *Int J Fract* 2002; 117(2):129-141.

Schroth JG, Hirth JP, Hoagland RG and Rosenfield AR. Combined mode I-mode III fracture of a high strength low-alloy steel. *Metallurgical Transact A* 1986; 18A:1061-1072.

Seifi R and Omidvar N. Fatigue crack growth under mixed mode I+III loading. *Marine Struct* 2013; 34:1-15.

- Shah RC. Fracture under combined modes in 4340 steel. In: fracture analysis, ASTM STP 560, Philadelphia: American Society for Testing and Materials, 1974, pp. 29-52.
- Sharif F, Kortschot MT and Martin RH. Mode III delamination using a split cantilever beam. In: Martin RH, editor. Composite materials: fatigue and fracture- Fifth Volume, ASTM STP 1230. Philadelphia: American Society for Testing and Materials, 1995; pp 85-99.
- Sih GC. Strain-energy-density factor applied to mixed mode crack problems. *Int J Fract* 1974; 10(3):305-321.
- Sih GC, Paris PC and Erdogan F. Crack-tip stress-intensity factors for plane extension and plate bending problems. *Int J Fract Mech* 1962; 29:306-312.
- Smekal AG. (translated) Fracture process behavior in brittle material under single and multiaxial stresses. *Österreichisches Ingenieur-Archiv* 1953; 7(1):4-71.
- Smith SA and Raju IS. Evaluation of stress-intensity factors using general finite-element models. Fatigue and Fracture Mechanics: 29th Volume, ASTM STP 1321, Panontin TL and Sheppard SD, eds. American Society for Testing and Materials 1999, pp. 176-200.
- Sommer E. Formation of fracture 'lances' in glass. *Eng Fract Mech* 1969; 1:539-546.
- Suemasu H. An experimental method to measure the mode-III interlaminar fracture toughness of composite laminates. *Compos Sci Technol* 1999; 59:1015-1021.
- Suo Z. Singularities, interfaces and cracks in dissimilar anisotropic media. In: *Proc R Soc Lond* 1990; A427:331-358.
- Suresh S and Tschegg EK. Combined mode I-mode III fracture of fatigue-precracked alumina. *J Am Ceram Soc* 1987; 70(10):726-733.
- Szekrényes A. Delamination fracture analysis in the G_{II} - G_{III} plane using prestressed transparent composite beams. *Int J Sol Struct* 2007; 44:3359-3378.

Szekrényes A. Improved analysis of the modified split-cantilever beam for mode-III fracture. *Int J Mech Sci* 2009; 51(9-10):682-693.

Szekrényes A. The influence of crack length and delamination width on the mode-III energy release rate of laminated composites. *J Compos Mater* 2011; 45(3):279-294.

T

Trakas K, and Kortschot MT. The relationship between critical strain energy release rate and fracture mode in multidirectional carbon-fiber/epoxy laminates. In: EA Armanios, editor. Composite materials: fatigue and fracture (6th vol.) ASTM STP 1285. Philadelphia: American Society for Testing and Materials, 1997, pp. 283-304.

U

Ueda Y, Ikeda K and Yao T. Characteristics of brittle fracture under general combined modes including those under bi-axial tensile loads. *Eng Fract Mech* 1983; 18(6):1131-1159.

W

Whitney JM. Structural analysis of laminated anisotropic plates. Lancaster: Technomic, 1987.

X

Xu G, Bower AF and Ortiz M. An analysis of non-planar crack growth under mixed mode loading. *Int J Sol Struct* 1994; 16:2167-2193.

Y

Yates JR and Miller KJ. Mixed mode (I+III) fatigue thresholds in a forging steel. *Fat Fract Eng Mater Struct* 1989; 12(3):259-270.

Z

Zehnder AT and Zella NK. Spiral to flat fracture transition for notched rods under torsional loading. *Int J Fract* 2015; 195(1):87-92.

Vita

Name of Author: Allison Lynne Horner

Place of Birth: Saint Cloud, Minnesota, USA.

Date of Birth: June 12, 1989

Schools Attended: The University of Tulsa, Tulsa, Oklahoma, USA
Syracuse University, Syracuse, New York, USA.

Degrees Awarded: Bachelor of Science in Mechanical Engineering (2011), The University of Tulsa.
Master of Science in Mechanical and Aerospace Engineering (2012), Syracuse University.